UNIVERSITAT POLITÈCNICA DE CATALUNYA BARCELONATECH

Neutronics analysis and thermodynamics studies of several DEMO breeding blankets for the development of the AINA safety code

Marco FABBRI

ADVERTIMENT La consulta d'aquesta tesi queda condicionada a l'acceptació de les següents condicions d'ús: La difusió d'aquesta tesi per mitjà del repositori institucional UPCommons (http://upcommons.upc.edu/tesis) i el repositori cooperatiu TDX (http://www.tdx.cat/) ha estat autoritzada pels titulars dels drets de propietat intel·lectual **únicament per a usos privats** emmarcats en activitats d'investigació i docència. No s'autoritza la seva reproducció amb finalitats de lucre ni la seva difusió i posada a disposició des d'un lloc aliè al servei UPCommons o TDX. No s'autoritza la presentació del seu contingut en una finestra o marc aliè a UPCommons (*framing*). Aquesta reserva de drets afecta tant al resum de presentació de la tesi com als seus continguts. En la utilització o cita de parts de la tesi és obligat indicar el nom de la persona autora.

ADVERTENCIA La consulta de esta tesis queda condicionada a la aceptación de las siguientes condiciones de uso: La difusión de esta tesis por medio del repositorio institucional UPCommons (http://upcommons.upc.edu/tesis) y el repositorio cooperativo TDR (http://www.tdx.cat/?locale-attribute=es) ha sido autorizada por los titulares de los derechos de propiedad intelectual **únicamente para usos privados enmarcados** en actividades de investigación y docencia. No se autoriza su reproducción con finalidades de lucro ni su difusión y puesta a disposición desde un sitio ajeno al servicio UPCommons No se autoriza la presentación de su contenido en una ventana o marco ajeno a UPCommons (*framing*). Esta reserva de derechos afecta tanto al resumen de presentación de la tesis como a sus contenidos. En la utilización o cita de partes de la tesis es obligado indicar el nombre de la persona autora.

WARNING On having consulted this thesis you're accepting the following use conditions: Spreading this thesis by the institutional repository UPCommons (http://upcommons.upc.edu/tesis) and the cooperative repository TDX (http://www.tdx.cat/?locale-attribute=en) has been authorized by the titular of the intellectual property rights **only for private uses** placed in investigation and teaching activities. Reproduction with lucrative aims is not authorized neither its spreading nor availability from a site foreign to the UPCommons service. Introducing its content in a window or frame foreign to the UPCommons service is not authorized (framing). These rights affect to the presentation summary of the thesis as well as to its contents. In the using or citation of parts of the thesis it's obliged to indicate the name of the author.

UNIVERSITAT POLITÈCNICA DE CATALUNYA

A THESIS SUBMITTED TO THE UNIVERSITAT POLITÈCNICA DE CATALUNYA FOR THE DEGREE OF DOCTOR OF PHILOSOPHY

Neutronics analysis and thermodynamics studies of several DEMO breeding blankets for the development of the AINA safety code

Author
M. FABBRI

Director
Dr. Javier DIES

Co-director
Dr. Alfredo DE BLAS

October 7, 2017

UNIVERSITAT POLITÈCNICA DE CATALUNYA
BARCELONATECH
Escola de Doctorat

Acta de calificación de tesis doctoral

Curso académico:

Nombre y apellidos

Programa de doctorado

Unidad estructural responsable del programa

Resolución del Tribunal

Reunido el Tribunal designado a tal efecto, el doctorando / la doctoranda expone el tema de su tesis doctoral titulada _____

_____.

Acabada la lectura y después de dar respuesta a las cuestiones formuladas por los miembros titulares del tribunal, éste otorga la calificación:

☐ NO APTO ☐ APROBADO ☐ NOTABLE ☐ SOBRESALIENTE

(Nombre, apellidos y firma) Presidente/a		(Nombre, apellidos y firma) Secretario/a
(Nombre, apellidos y firma) Vocal	(Nombre, apellidos y firma) Vocal	(Nombre, apellidos y firma) Vocal

_____, _____ de _____ de _____

El resultado del escrutinio de los votos emitidos por los miembros titulares del tribunal, efectuado por la Comisión Permanente de la Escuela de Doctorado, otorga la MENCIÓN CUM LAUDE:

☐ SÍ ☐ NO

(Nombre, apellidos y firma) Presidente/a de la Comisión Permanente de la Escuela de Doctorado	(Nombre, apellidos y firma) Secretario/a de la Comisión Permanente de la Escuela de Doctorado

Barcelona, _____ de _____ de _____

Acknowledgments

I would like to express my sincere gratitude to my advisors Prof. Javier Dies and Alfredo De Blas for the continuous support of my Ph.D study and related research, for his patience, motivation, and their knowledge. Their guidance helped me in all the time of research and writing of this thesis. The combination of the daily work with the PhD tasks was very demanding nevertheless my directors supported me also in this aspect.

I thank my fellow teammates for the stimulating discussions, for the overtimes we were working together before deadlines, and for all the fun we have had in the last four years. It was a unique and unforgettable journey.

Last but not the least, I would like to thank my family and of course my wife Beatriz: those wonderful people from whom I learned how to face sacrifices and to fight for what you believe in and what you really want to obtain: *om mani padme hum*.

Executive summary

By 2050 the energy consumption is expected to increase considerably. The production might be mostly based on a renewable energy mix driven by nuclear fusion which could potentially deliver continuous, large-scale power on a long-term basis without harming the environment. Regrettably, nuclear fusion still requires numerous developments, which are undergoing around the world, to prove the design feasibility and to evaluate the safety related aspects which are to some extent embraced within this thesis.

In light of this, during the last ten years the Nuclear Engineering Research Group (NERG-UPC) has been developing a safety code called AINA (acronym of Analyses of IN-vessel Accidents) to evaluate the magnetic fusion reactor plasma-wall transients in case of ex-vessel LOCA and overfuelling, determining thermal wall profiles as well as checking the integrity of in-vessel components (melting). Considering the evolution of technologies and related methodologies, a substantial renewal/improvement plan for AINA was established. Two specific development tasks are part of this PhD thesis. (i) The definition, standardization and validation of an enhanced methodology to develop new AINA versions in order to obtain robust models, estimating as accurately as possible the behaviour of the studied systems. (ii) The re-design, generalization and optimization of thermal-hydraulics routines for the determination of the AINA thermal-wall distributions both in normal and accident scenarios in substitution of the former unverified/unqualified ones. In addition, the thermal-hydraulic routines have been validated against commercial software as ANSYS Fluent.

Consequently, the code has been almost rewritten, improved and consolidated giving special attention on document, comment and Verification & Validation according to the current software standard requirements. Indeed, several novel features have been introduced to extend the modelling capacity of the AINA application solver and to estimate the errors. Afterwards, two specific AINA blanket thermal-wall models have been developed: the Water Cooled Pebble Bed JAPANESE-DEMO and the Helium Cooled Pebble Bed EUROPEAN-DEMO. According to the established methodology, the complete process of design, improvement and validation has included a full set of compulsory radiation transport analyses, thermal-hydraulic studies and AINA thermal-wall model tuning. Furthermore, preliminary assessments of the transient accident scenarios and sensibility studies have also been performed. So, starting from fully detailed neutronics and thermal-hydraulic results, a simplified and conser-

vative wall model has been implemented in AINA, obtaining reliable results in a short calculation time validating the approach proposed. Indeed, simplified models have been iteratively built and adjusted, achieving a good agreement with the fully detailed simulation and yielding maximum absolute temperature differences of approximately 10%. The determination and coherence of the temperature distribution obtained using independent tools and approaches, ANSYS® Fluent® vs AINA thermal-hydraulic routines, supports the proposed methodology, hence validating all the results obtained. Nevertheless, the 1D non-conservative temperature field, where present, could be compensated by the application of scaling functions, obtaining a perfect match with the most conservative 3D distribution. In this innovative approach, the scaling functions correspond to the ratios between the most conservative radial distribution in the fully detailed and the 1D simulations. Moreover, thanks to the simplified and endorsed model, sensitivities and screening assessment can be easily performed showing how the system reacts as a consequence of loads, boundary conditions and perturbations. In light of this, the detailed number of studies can be significantly reduced.

To conclude, this multidisciplinary activity has requested the establishment of a specific framework, including skills and tools.

Objective of this PhD thesis

The main objectives of this PhD are hereinafter described:

- Contribution to the general development of AINA code, a safety code for the study of plasma wall transients in nuclear fusion reactors like ITER or DEMO.
- Definition and validation of a standard methodology to develop new AINA versions. This want to obtain robust and peer reviewed models which predict as accurately as possible the behavior of the studied system in a short-time but establishing a boundary for the worst scenarios that are useful in obtaining results in a safety analysis.
- Creation, generalization and optimization of thermal-hydraulics routines for the determination of the AINA thermal-block temperature distribution both in steady state and transient regimes. In addition, their validations against commercial software as ANSYS Fluent have been performed.
- Design, improvement and validation of the Japanese Water Cooled Pebble Bed DEMO AINA new blanket thermal-block model.
- Generation, set-up and endorsement of the European Helium Cooled Pebble Bed DEMO AINA blanket thermal-block model.
- Radiation transport and adjoin flux calculations in support to the AINA DEMO developments.
- Thermal-hydraulic assessments and analyses in support to the AINA DEMO developments.
- Contribution to DEMO safety studies by performing studies of plasma related bounding events with AINA code. The objective is to analyze loss of plasma control transients and thermo-hydraulic transients providing useful result in support to the safety analysis.
- Technical support to the *EuroFUSION contracts* and to the *Secondment expert from UPC-FEEL to IFERC Japan.*

Contents

Chapter 1: Introduction

The more important energy issues worldwide are discussed and the nuclear fusion is placed in context with the rest of energy generation alternatives. Therefore, a brief history of plasma and nuclear fusion research is exposed. Moreover, ITER and the future fusion demonstration reactor characteristics are described. Safety studies and AINA software are briefly explained.

Chapter 2: Computational Methods and methodologies

The computational methods used in this thesis (e.g. radiation transport and adjoin flux calculations, thermal-hydraulic and AINA analyses) are described. In addition, the consolidated and best-practice methodologies employed are detailed.

Chapter 3: Thermal-hydraulic routines

The creation, generalization and optimization of thermal-hydraulics routines for the determination of the AINA thermal-block distributions are reported. In addition, their validations against commercial software as ANSYS Fluent are characterized. To conclude, the novel features introduced are explained.

Chapter 4: Water Cooled Pebble Bed (Japanese-DEMO)

The complete process of design, improvement and validation carried out for the Japanese Water Cooled Pebble Bed DEMO AINA blanket thermal-block model is described. Moreover, the radiation transport analyses, thermal-hydraulic studies and AINA thermal-wall model tuning performed are reported.

Chapter 5: Helium Cooled Pebble Bed (European-DEMO)

The generation, set-up and endorsement done for the European Helium Cooled Pebble Bed DEMO AINA blanket thermal-block model are characterized. Furthermore, a preliminary assessment of the HCPB AINA safety analysis and sensibility study is included.

Chapter 6: Conclusion

This chapter contains the conclusion and the main achievements.

Contents

List of Figures

List of Tables

Nomenclature

BSS	Breeding blanket supporting structure
NIF	National Ignition Facility
ADVANTG	AutomateD VAriaNce reducTion Generator
AINA	Analysis of in-vessel accidents
BB	Breading Blanket
BC	Boundary Conditions
CFD	Computational fluid dynamics
CFD-3D	Fully detailed 3D Thermal-hydraulics analysis
CFD-DOM	2D CFD WCPB BB Assessment
CFD-NHD	3D CFD Nuclear sensitivity assessment
CFD-POLY	3D CFD Mesh independence assessment
FEEL	Fusion Energy Engineering Laboratory
HCPB	Helium Cooled Pebble Bed
HTC	Heat Transfer Coefficient
IFERC	International Fusion Energy Research Centre
ITER	International Thermonuclear Experimental Reactor
ITER	International Thermonuclear Experimental Reactor
JAERI	Japan Atomic Energy Research Institute
LOCA	Loss Of Cooling Accidents
LOCA	Loss of Coolant Accident
MC	Monte Carlo

MCNP Monte Carlo N Particle

NERG Nuclear Engineering Research Group

NHD Nuclear Heating Density

NWL Neutron Wall Loading

OF Over-fuelling accident

TBM Test Blanket Modules

TBM Test Blanket Modules

TBR Tritium Breeding Ratio

TE Truncation Error

TFC Tally Fluctuation Chart

UDF User Defined Function

UDM User-Defined Memory

UPC Technical University of Catalonia

VRT Variance Reduction Techniques

VTK Visualization Toolkit

VV Vacuum Vessel

WCPB Water Cooled Pebble Bed

WW weight windows

Scientific production

Peer reviewed papers

- M. Fabbri,A. de Blas, A. Riego, J. Dies, I. Zamora, E.Baeza, Methodology for the improvement of the AINA Code wall-model applied to DEMO WCPB blanket, Fusion Engineering and Design, *http://dx.doi.org/10.1016/j.fusengdes.2017.05.027*

- J.C. Rivas, M. Nakamura, Y. Someya, K. Hoshino, N. Asakura, H. Takase, Y. Miyoshi, H. Utoh, K. Tobita, J. Dies, A. de Blas, A. Riego, M. Fabbri, Safety studies of plasma-wall events with AINA code for Japanese DEMO, Fusion Engineering and Design, Volumes 109–111, Part B, 1 November 2016, Pages 1653-1657, ISSN 0920-3796, *http://dx.doi.org/10.1016/j. fusengdes.2015.10.037.*

- César Hueso, Marco Fabbri, Cristina de la Fuente, Albert Janés, Joan Massuet, Imanol Zamora, Cristina Gasca, Héctor Hernández, J. Ángel Vega, Methodology for the nuclear design validation of an Alternate Emergency Management Centre (CAGE), EPJ Nuclear Sci. Technol. 3, 5 (2017), *10.1051/epjn/2017004*

- J. Fradera, C. Colomer, M. Fabbri, M. Martín, E. Martínez-Sabán, I. Zamora, A. Alemán, J. Izquierdo, R. Le Barbier, Y. Utin, Thermal-hydraulic analysis of an irregular sector of the ITER vacuum vessel by means of CFD tools, Fusion Engineering and Design, Volume 92, March 2015, Pages 69-74, ISSN 0920-3796, *http://dx.doi.org/10.1016/j.fusengdes..2015.01.049.*

- J. Fradera, M. Velarde, J. M. Perlado, C. Colomer, P. Briani, E. Martínez-Saban, I. Zamora, M. Fabbri, A. Janés, and A. Alemán. Multiscale integral analysis of tritium leakages in fusion nuclear power plants. In 2015 IEEE 26th Symposium on Fusion Engineering (SOFE), pages 16, May 2015,
DOI: 10.1109/SOFE.2015.7482334.

- Fire analysis with fire dynamics simulator (FDS) software in NPP areas, I. Zamora, J. Valls, J. Fradera, C. Colomer, B. Hermosa, M. Fabbri, J.

Salellas, E. Martínez, M. Salvat, European Nuclear Conference Proceedings, 2016, *www.euronuclear.org/events/enc/enc2016/transactions/_ENC 2016-transactions.pdf*

Peer reviewed papers (still under publication process)

- Radiation transport calculation of the UGXR collimators for the Jules Horowitz reactor, 3th International Conference on Radiation Shielding (ICRS-13) & 19th Topical Meeting of the Radiation Protection & Shielding Division of the American Nuclear Society -2016 (RPSD-2016), "under-review"
- Overview of Nuclear Integration Activities for Mitigation of Radiation Loads to ITER Superconducting Magnets, ANS Annual Meeting 2017, Special Session on Neutronics Challenges of Fusion Facilities San Francisco (CA), June 11-16, 2017, Transactions of ANS, "invited contribution, already submitted"
- The ITER tokamak neutronics reference model C-Model, ISFNT-13, 2017, "submitted to Fusion Engineering and Design"
- Nuclear heat analysis for the ITER Vacuum Vessel, ISFNT-13, 2017, "submitted to Fusion Engineering and Design"
- Development of the safety code AINA for the European DEMO designs , ISFNT-13, 2017 (or Fusion Engineering and Design still to be decided), "to be submitted"

Posters

- The ITER tokamak neutronics reference model C-Model, ISFNT-13, 2017
- Nuclear heat analysis for the ITER Vacuum Vessel, ISFNT-13, 2017
- Development of the safety code AINA for the European DEMO designs, ISFNT-13, 2017
- Desarrollo del código de seguridad para reactores de fusión AINA 4 para DEMO, Sociedad Nuclear Española, 2017
- Methodology for the improvement of the AINA Code wall-model applied to DEMO WCPB blanket, M. Fabbri, A. de Blas, A. Riego, J. Dies, I. Zamora, E. Baeza. Symposium on Fusion Technologies, SOFT, 2016
- Multiscale integral analysis of tritium leakages in nuclear power plant, J.Fradera, M.Velaverde, P.Briani, E.Martinez-Saban, I.Zamora, M.Fabbri, A.Janes, A.Alemán, J.M.Perlado. Symposium on Fusion Engineering, SOFE, 2015.

- CFD meshing methodology for large computational domains applied to an irregular sector of the ITER vacuum vessel. R. Le Barbier, Y. Utin, J. Izquierdo, C. Colomer, J. Fradera, M. Fabbri, M. Martín, A. Alemán. Symposium on Fusion Technologies, SOFT, 2014.
- MCNPX/ANSYS Fluent automatic coupling software, M. Fabbri, C. Colomer, J. Fradera, M. Martín, A. Alemán International Synopsys Nuclear Fusion Technologies, ISFNT, 2013.

Presentation in congress/workshop

- ADVANTG applications to ITER (EU experience), ADVANTG Workshop at JET, 2016
- Neutronics Activities at Fusion For Energy, International Energy Agency "Neutronics Workshop" held at SOFT-2016.
- Progress on a ITER Nuclear Analysis Framework, ITER Neutronic Meeting, 2016.
- New ITER torus sector reference model, ITER Neutronic Meeting, 2016.
- In-vessel modelling updates for C-lite, ITER Neutronic Meeting, 2016.
- iMesh-A program for the post processing of vtk radiation maps. ITER Neutronic Meeting, 2015.
- Metodología de análisis radiológico de la habitabilidad del centro alternativo de gestión de emergencias (CAGE) en caso de accidente severo Sociedad Nuclear Española, 2015.
- Optimización de la inversión económica en PCI mediante la metodología de diseño prestacional en el análisis de la propagación de incendios con FDS (Fire Dynamics Simulator) en áreas de fuego de Centrales Nucleares , Sociedad Nuclear Española, 2015.
- Safety Studies For Japanese Demo Design With Aina Code. 2nd Plasma Conference, Niigata, 2014.
- Análisis de simulación de la propagación de incendios mediante el programa Fire Dynamics Simulator FDS en áreas de fuego de Centrales Nucleares. Sociedad Nuclear Española, 2014.
- Estudio de un sistema out-core para la caraterización de combustible durante una operacion de recarga de una central nuclear PWR. Sociedad Nuclear Española, 2013.
- Aproximación al cálculo de la deposición energética en un contenedor de combustible irradiado mediante el acoplamiento de códigos neutrónico fluido-dinámicos. Sociedad Nuclear Española, 2013.

- MCNPX/ANSYS Fluent automatic coupling software. ITER Neutronics meeting, 2013.

Chapter 1

Introduction

1.1 Nuclear Fusion

By 2050 the energy consumption is expected to increase dramatically due to world's population growth (e.g. 9.7 billion people estimated [20]), better living standards and the developing countries become more industrialized. Furthermore, considering also the environmental requirements for zero or low CO_2 emission sources to limit the global Earth temperature increase, the worldwide community need to invest in a sustainable, balanced and efficient energy mix, because no single technology will fulfill the necessities. Of course, renewable technologies as wind, wave, solar, hydro energy offering long-term and clean energy production must be part of it although they are not the solution. Indeed, they are characterized by low energy density, a large environmental footprint and their fluctuations in time require storage systems and back-up power plants. We must develop new sustainable energy sources that can deliver continuous, large-scale power for the long-term without harming the environment. For these reasons, Nuclear Fusion energy has to be part of the "mix" of energy for the second half of the 21th century as stated by the European Council of Ministers in its decision on the Euratom FP6:

> *"Fusion energy could contribute in the second half of the century to the emission-free large-scale production of base-load electricity. The advances made in fusion energy research justify the further pursuit of a vigorous effort towards the long-term objective of a fusion power plant."*

The most optimistic road-map foresee the provision commercial electricity in about 30 years having the potential to supply up to 20% of the world's energy by the year 2100, nevertheless nowadays delays are foreseen.

The main advantages of fusion are [21]:

- No emission of any CO_2 greenhouse gases neither of acid ones
- Abundant and economic fuel sources and potential very efficient

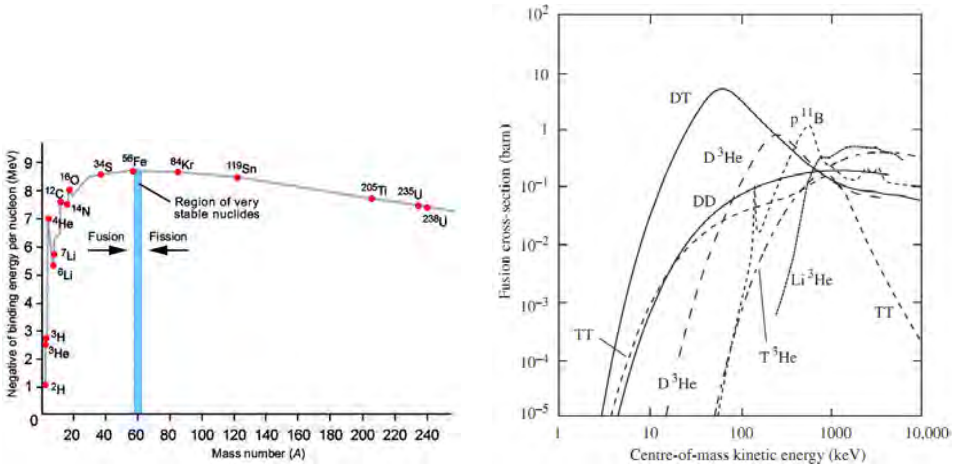

Figure 1.1.1: Energy per Nucleon and Fusion Cross Sections [1]

$$
\begin{aligned}
&{}^2_1H + {}^3_1H \rightarrow {}^4_2He + {}^1_0n + 17.59MeV \\
&{}^2_1H + {}^2_1H \rightarrow {}^3_2He + {}^1_0n + 3.27MeV \\
&{}^2_1H + {}^2_1H \rightarrow {}^3_1H + {}^1_1H + 4.03MeV \\
&{}^2_1H + {}^3_2He \rightarrow {}^4_2He + {}^1_1H + 18.3MeV
\end{aligned}
$$

Table 1.1.1: Fusion Reactions [1]

- Power excursions of the plasma are self-limited to low levels by intrinsic processes
- No long-lived radioactive waste with rapid decay

The European agency for the Fusion Development mission is "bringing the power of the Sun to the Earth". But what is Fusion really and how does it work?

The fusion[1] is a nuclear reaction in where two lights nuclei, such as Hydrogen isotopes Deuterium and Tritium, are merged together, leading to an heavier nuclei and releasing a substantial amount of energy is liberated as consequence of the mass defect [22]by means of kinetic energy to particle. The main fusion reactions are reported in Table 1.1.1.

The most feasible reaction on the earth is Deuterium(D) + Tritium(T) since it needs a relatively low energy to reach the maximum probability to take place the fusion process, the Deuterium isotopes can be extracted from see water and the Tritium directly in the fusion reactor using the produced high energy neutron by means of breeding in-vessel components called Breeding Blanket. Different technologies (i.e. HCPB, HCLL, WCLL and DCLL) are going to be tested toward the selection and implementation in the future commercial fusion reactor.

[1]It is the opposite of the nuclear fission in which a heavy nucleus, as the Uranium or Plutonium, is divided in two parts.

Unfortunately having fusion is not so simple. Indeed, it happens at very elevated temperature in fully ionized gas named plasma where the particles have enough energy to overcome the Coulomb threshold. To obtain viable and efficient production of fusion energy three main requirements must be fulfilled simultaneously in a very important fusion parameter, the triple product.

- High density of the plasma, to achieve high density rate
- Large confinement time, to achieve large power
- High temperature of the plasma of about $2e8°C$, to improve the reaction probability

Nowadays, no materials could afford the plasma temperature so the hot fuel particles are kept away from the walls of the container by creating a magnetic "cage" made by strong magnetic fields which prevent the particles from escaping. Depending on the magnetic confinement of the reactor, two main developments lines have being developing along the last decades: Magnetic Fusion and Inertial Fusion [1]. More than 200 Tokamaks have been built around the world as for instance T-10 (Russia), STOR-M (Canada), JET (European Union), Tore Supra (France), DIII-D (U.S.A), FTU (Italy), ASDEX Upgrade (Germany), MAST (United Kindom), EAST (China), KSTAR (South Korea).

The fusion progress can be measured by means of the Lawson Criteria which defines the minimum value of the triple product,$nT\tau_E > 3 \cdot 10^2 keV * s * m^{-3}$, to reach the ignition condition. From this point ahead, the fusion reaction products are themselves able to maintain the required plasma temperature and balance all the power losses generated without the insertion of external power. Currently no fusion reactor has been reached yet neither the ignition, $Q = \infty$, nor the breakeven condition, representing a physic gain factor, Q=1, equal to one so an equivalence between the produced power and the introduced one.

By the way, these are the some of the main fusion achievements along the history:

- JET, 1983, the world's first controlled release of fusion power [23]
- JET, 1994, the biggest fusion power pick, 17 MW [23]
- Tore Supra, 2003: the record for the longest plasma duration time of any Tokamak: six minutes and 30 seconds [24]
- JT-60, 1998: the highest value of fusion triple product equal to $1.53 \cdot 10^{21} keV * s * m^{-3}$[24] (being JT-60 a D-D reactor it would have reached the breakeven point).

ITER and DEMO are the forthcoming fusion reactor and they should be able to prove the suitability of the fusion energy as an electrical power source in the future.

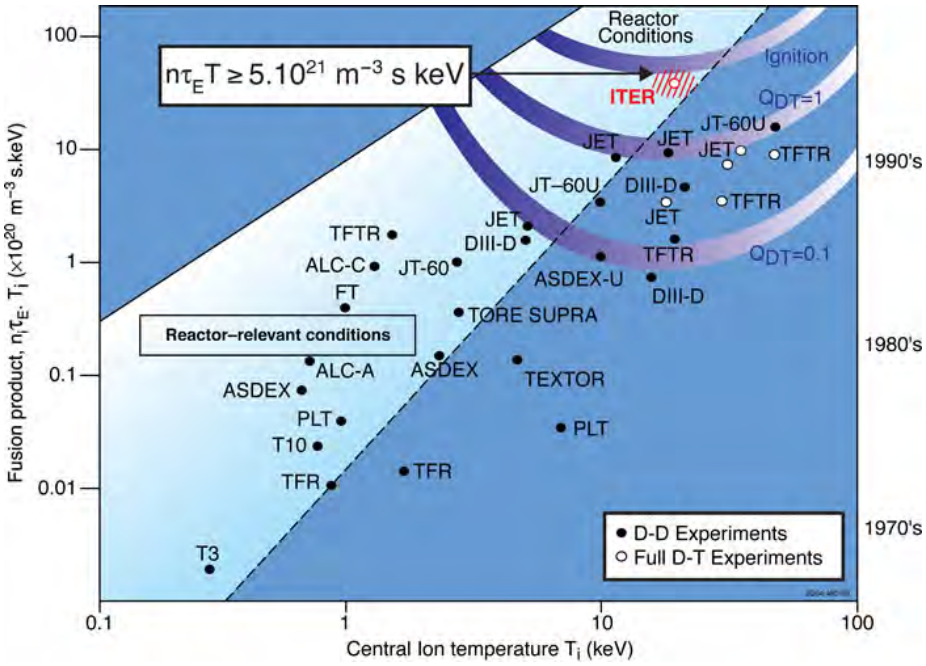

Figure 1.1.2: Triple Product evolution [2]

		Magnetic Fusion	Inertial Fusion
Ion density	$[m^3]$	10^{20}	10^{30}
Temperature	$[K]$	10^{8}	10^{8}
Confinement Time	$[s]$	10^{0}	10^{-9}

Table 1.2.1: Fusion parameters

1.2 Reactor Design: Magnetic or Inertial Fusion Reactors?

As commented before, two very different approaches being investigated toward the ignition conditions: the *inertial* and the *magnetic* confinement system. Whereas, the first one the confinement time is very short and the plasma density very elevated the second one relies on bigger pulse and smaller pressure.

Indeed, in the *inertial* confinement a small spherical pellet fuel is flash-irradiated by a number of extremely intense and calibrated laser beams which compress the external layer producing evaporation against the internal part of the target. Thus, the density is increased and the reaction elements reaching the fusion conditions. Therefore, it is the inertia which avoids the plasma to escape. Finally, the energy, by means of high-energy beams of laser light, electrons or ions, is released and evacuated by the external wall cooling systems. Nowadays,

the most advanced and famous inertial fusion experiment is the National Ignition Facility(or NIF) at the Lawrence Livermore National Laboratory in California [25].

On the other side, since the plasma is an excellent and fully ionized conductor, a combination of strong magnetic field is used to confine the plasma in the magnetic confinement devices having the particle moving around a spiral. Depending on the magnet configuration type two main configurations are possible: mirror confinement and the toroidal confinement being the second one the most efficient and suitable.

Therefore, we distinguish between two main magnetic devices: Tokamak and stellarator. Whereas, the first one uses a combination of poloidal and toroidal coils in addition to a central solenoid (transformer) inducing a current inside the plasma, the second does not need it. Indeed, the stellarator uses only a very complex and challenging magnets configuration being the absence of the transformer is great advantage which allows a continuous usage. Although stellarators are very promising as commercial reactors, the research in this direction is still in an earlier phase due to its complex engineering. For the time being, the German Wendelstein-7X is the most advanced and promising world stellarator. Nevertheless, other pioneer experiments are located all over the world [26]: TJ1U stellarator and TJII Heliac (CIEMAT, Spain), Helically Symmetric Experiment (HSX)(University of Wisconsin, U.S.A.) and he National Compact stellarator Experiment (Princeton, U.S.A.).

In contrast, the TokamakS are simpler but they work on pulses because the transformer has to be recharged as Faraday's law describes having in the plasma instability is main disadvantages. The construction of larger devices, and therefore large volume to surface plasma ratios, allows the confinement so the control having great improvements. In addition, diagnostics are fundamental in fusion experiments to be able to understand plasma physics and configuration. Nowadays, the worldwide fusion community attentions are focused on ITER (International Thermonuclear Experimental Reactor), the biggest ever seen Tokamak reactor which is under construction and ready to be operated since 2025 [27]. It is worth reminding ITER has the scope to demonstrate the feasibility of fusion toward the construction of a fully commercial and economically viable reactor, DEMO.

1.3 ITER: International Thermonuclear Experimental Reactor

ITER, meaning "the way" in Latin, is the culmination of decades of fusion research: more than 200 Tokamaks built the world over to demonstrate the scientific and technical feasibility of fusion as an energy source, and in particular[5]:

- Produce 500 MW of fusion power[2] for pulses of 400 s

[2]Please note that ITER will not produce electrical energy because it is not provided by an

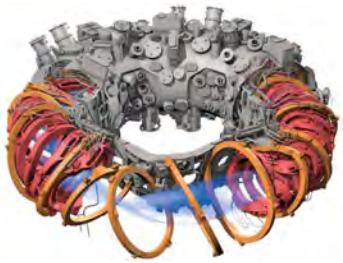

Figure 1.2.1: NIF [3]and W-7X [4]

- Demonstrate the integrated operation of technologies for a fusion power plant
- Achieve a deuterium-tritium plasma in which the reaction is sustained through internal heating
- Test tritium breeding
- Demonstrate the safety characteristics of a fusion device

Nowadays, the ITER project involves seven parties (or members) (European Union, United States of America, People's Republic of China, Russian Federation, Japan, South Korea and India), representing 50% of the World population and 80% of the world gdp (or gross domestic product"), nevertheless accession by or co-operation with other countries are possible under the scrutiny of the ITER Council. The parties contributes to the ITER project providing manufactured components (in-kind contribution) or economical support (in-cash contribution): E.U. as host party has the biggest contribution equal to ~45% whereas the remaining six member ~9% each. ITER is a very challenging project both for the technical and managerial point of view. Currently, the ITER construction estimated cost is around 13000 M€ which is comparable with the budget of projects like the Apollo and International Space Station. The idea of ITER was initially proposed back in 1985 as collaboration between the former Soviet Union, the United States, the European Union and Japan below the IAEA [5] umbrella. Presidents Gorbachov, Reagan & Mitterrand proposed the set-up of an international peaceful collaboration for the development of fusion energy. Since then, several member has joint the agreement (and in one case also left as Canada), the main design done and ITER authorized to operate thanks to the creation of the ITER Installation Nucléaire de base (INB) in the Journal Official de la République Française on 10 November 2012 being the first fusion nuclear installation (not considered as research one for the standard point of view). Indeed, since 2007 ITER is being constructed at Cadarache in the South

alternator hence the fusion power produced will be evacuated to the external cooling system without producing steam.

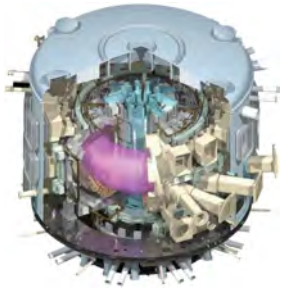

(a) ITER machine

(b) ITER Cross Section

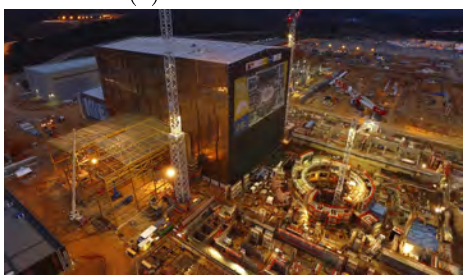

(c) Assembly Hall @ 2017/03

(d) Tokamak pit @ 2017/03

Figure 1.3.1: ITER reactor and its site [5]

of France and starting to operate from late 2025, ready to D-T operation in late 2035 [27].

- To understand the importance of the project please find next some peculiar facts:
- The ITER machine will weigh 23000 ton, as three Eiffel Towers.
- The ITER plasma will reach $1.5e8^{\circ}C$, or 10 times the temperature of the core of the Sun
- The Tokamak building will measure 73 m as the Arc de Triomphe in Paris. ITER will be composed by 107 elements, 4 times those present in a shuttle
- The magnetic field generated will be approximately 6 times that of the Earth (5.3 T vs 1 T)
- Plasma Toroidal D shaped chamber measures 6.2 m of major radius

1.4 DEMO: The DEMOnstrating Fusion Reactor

ITER is not the end of the fusion development but one of the main milestones of the fusion roadmap. It will contribute to the design of the next-generation

machine, named DEMO, which aims to be the prototype of the future commercial reactor fusion reactor. The experience and the know-how gained from the ITER project will be the basis for designing the DEMOnstrating machine which aims to have continuous (or at least close) operation, testing the Tritium self-sufficiency (the so called Tritium Breeding) and the production of large-scale electrical power. DEMO will have a simpler design than ITER, with less diagnostics and more focused in the employment of the fusion energy than the investigation of the plasma regimes. Different Tritium Blanket technologies (e.g. WCPB, HCPB, WCLL, DCLL), which should be able to employ the neutron produced by the fusion reactor to generate Tritium and evacuate at the same time the fusion power, are under study being part of R&D lines. The EUROfusion consortium, which is the '*European Consortium for the Development of Fusion Energy*', manages and funds European fusion research activities on behalf of Euratom [28], is focused on four breeding blanket concepts:

- HCPB (Helium Cooled Pebble Bed) [29]: He is used as coolant, Be as neutron multiplier and LiSiO4 as breeding material.
- HCLL (Helium Cooled Lithium Lead) [30]: He is used as coolant, PbLi as breeding material and multiplier.
- DCLL (Dual Coolant Lead Lithium) [31]: He and PbLi are used as coolant, PbLi as breeding material and multiplier.
- WCLL (Water Cooled Lithium Lead) [32]: Water is used as coolant, PbLi as breeding material and multiplier.

The Tritium self-sufficiency is challenged by engineering rather than by physics. Indeed, the selection of materials (structural, breeding, multiplier and coolant), the necessity of diagnostics and system as well as the space limitation (particularly inboard) are, currently, some of the main concerns. Furthermore, the three crucial functions must be fulfilled by a DEMO Breeding Blanket:

- Capacity to convert the neutron energy in heat, collect it and reach high conversion efficiency
- Achievement of the Tritium breeding self-sufficiency and it confinement
- Afford an effective neutron and gamma shielding to the superconductive coils

Nowadays, different conceptual DEMO project are under elaboration and evaluation by different parties because no clear cohesion is foreseen as for ITER. Therefore, it is worth reminding that the seven ITER members have the possibility to test different DEMO BB mock-up in the ITER Test Blanket Modules (or TBM) program which is developed individually by the ITER Domestic Agencies representing an unique possibility to test it. Several concept, both with liquid breeders (e.g. Helium-Cooled Lithium Lead (EU, China), Dual Coolant "He/Pb17Li¨ by USA/China, Dual Coolant "He/Molten Salt¨

by USA/China ...) and solid ones (e.g. Helium-Cooled Ceramic Breeder by China/EU/Japan/RF/Korea/USA), are going to the tested in three equatorial ports (No. 02, 16 and 18) approximately from 2025.

For all these reasons, DEMO represent a concept than a specific machine. Nevertheless, the construction phase could be estimated around 2030s and the operation in late 2040s being now under conceptual design aimed having fusion electricity production well before 2050 [33, 28]. Nevertheless, European fusion program has already defined the top-level fusion objective of DEMO [34]:

- To protect workers, the public and the environment from harm
- To ensure in normal operation that exposure to hazards within the facility and due to release of hazardous material from the facility is controlled, kept below prescribed limits and minimized to be as low as reasonably achievable
- To ensure that the likelihood of accidents is minimized and that their consequences are bounded
- To ensure that the consequences of more frequent incidents, if any, are minor
- To apply a safety approach that limits the hazards from accidents such that in any event there is no need for public evacuation on technical grounds
- To minimize radioactive waste hazards and volumes and ensure that they are as low as reasonably achievable.

To conclude, DEMO requires a significant amount of innovation and research in critical areas such as heat removal, materials development and activation, machine operation, remote handling, standard and regulation, tritium management and breeding. Additional research facility for the material development as IFMIF [35, 36, 37], which is part of the Broader Approach agreement [33], are fundamental in the fusion road-map. During the last ten years, the FEEL-UPC group has being contributing to the fusion development in several international projects mainly devoted in Safety .

1.5 Fusion Safety

Starting back in 1990, an independent Fusion Evaluation Board [38] listed the basic safety and environmental objectives for fusion power claiming that nuclear fusion has an "inherent environmental and safety advantages over all current alternatives for base load electricity generation", added that a "convincing demonstration" of these advantages was necessary and emphasized two "central points", considering the research a fundamental milestone of the process:

Figure 1.4.1: DEMO Plant [6]

- "It must be clearly shown that the worst possible fusion accident will constitute no major hazard to populations outside the plant perimeter that might result in evacuation."
- "Radioactive wastes from the operation of a fusion plant should not require isolation from the environment for a geological time-span and therefore should not constitute a burden for future generations."

The main conclusions are endorsed by the very low fuel inventory necessary inside the plasma chamber, the inherent passive shutdown in case of unplanned functioning with the absence of chain reactions so dangerous and typical of the fission power plant. The only potential radiological hazard to consider will be the Tritium (with an half-life of 12.32 years [39]) and the materials activated by neutron collision but with a short half-life apt to reduce its activity in approximately 100 years [21]. The safety point has to be considered and embedded in all stages of the fusion power plant life-cycle from the conceptual design up to final decommission, propagating the System Design Requirements (or SRD) top-bottom within all the supply chain.

For this reasons, until now numerous, independent and extensive safety and environmental investigations have been carried out for ITER and for DEMO. Nevertheless, it is worth reminding that the DEMO Safety analysis could be supported and take benefit from ITER assessments although not replaced because the plant will have different systems, requirements and materials.

The safety analysis must cover all the accidents types and possibilities, starting from the postulation following all possible the event sequences. To achieve this, Postulated Initiating Events (PIEs) must be identified using systematic methods such as Failure Modes and Effects Analysis (FMEA) or Hazard and Operability (HAZOP) studies. The outcomes constitute the PIE-PIT matrices, where frequency category and radiological consequences are assigned and the plant state determined at the end of each sequence. Therefore, using the information generated, components can be classified or redesigned according to the system requirements. Nowadays, numerous computers codes and models, depending on the application area, are used to perform deterministic safety analyses of the fusion facilities. These mush pass a rigorous V&V (or Validation & Verification) process in order to be authorized by the nuclear operator [40].

It is worth reminding that during the last ten years, the Fusion Energy Engineering Laboratory (FEEL), a division of the Nuclear Engineering Research Group (NERG) of the Technical University of Catalonia (UPC) has being developing a safety code called AINA (acronym of Analyses of IN-vessel Accidents). It evaluates the magnetic fusion reactor plasma-wall transients in case of ex-vessel LOCA and overfuelling, determining thermal wall profiles as well as checking the integrity of in-vessel components (melting). The code, which is currently the reference European safety code [41]to perform the analysis of plasma-wall interaction, has been already successfully applied in different projects to different fusion reactors designs as ITER [42, 43, 44, 45, 46, 47, 8] and the Japanese DEMO design WCPB [48, 8, 49]. Along the years, the AINA Safety Code has being constantly developed and improved thanks to several PhD and Master Thesis. Indeed, this thesis mainly focuses on the peer review, consolidation and validation of code with special attention to Thermal Block which computes the thermal evolution of the in-vessel components during the accident scenarios [8]. In particular, thermal-hydraulics routines, for both 1D and 2D models , have been developed, optimized and cross-checked by means of CFD commercial software, Chapter. No. 3. Furthermore, a suited methodology for the development of further AINA versions and the implementation of new in-vessel components has been defined, Sec. 2.1. Indeed, this has been successfully applied for the generation of Japanese DEMO WCPB blanket version, Chapter. No. 4, as well as the European DEMO HCPB, Chapter. No. 5, requiring the execution of Radiation Transport Calculations and CFD simulations. Accordingly, the complete set of methodologies have been reported and described in Chapter No. 2.

Chapter 2

Computational methods and methodologies

2.1 AINA: Analysis of IN-vessel Accident

AINA, which stands for Analyses of IN-vessel Accidents, is currently the reference European safety code [41]to perform the analysis of plasma-wall interaction in magnetic fusion reactor such as ITER and European DEMO. Furthermore, it has been also employed for Japanese fusion applications as the Japanese DEMO being as well once reference code in that country. It establishes boundary for the worst scenario of ex-vessel LOCA and overfuelling, determining thermal wall profiles as well as checking the integrity of in-vessel components (melting) during accidents scenarios. The safety studies performed intend to provide information for decision making using simplified models for plasma dynamics, plasma-wall interaction and wall thermal evolution.

AINA is the direct evolution of the SAFALY code [50], developed by Takuro Honda at HRL, Hitachi, Ltd. in the frame of a JAERIcontract. Its development and usage have been one of the main research lines in the FEEL department of the Universidad Politecnica de Catalunya being topic of, at least, three PhD thesis ([51], [52] and this) and several master thesis and generating a long list of international and peer reviewed publications [42, 43, 53, 44, 45, 46, 47, 54]. In addition, AINA has been successfully involved in several international projects as:

- ITER loss of plasma control event evaluations related to the Generic Site Safety Report (2007, ITER Organization)
- Passive plasma termination for Be evaporation in LOCA transients (2008, ITER Organization)
- ITER safety studies: Development of quality management system for AINA code (2009, ITER Organization)

- Development of AINA code for ITER (EFDA-2013)
- Secondment expert from UPC-FEEL to IFERC Japan, development of AINA code for Japan DEMO (2014, Fusion for Energy)
- Secondment expert from UPC-FEEL to IFERC Japan, development of AINA code for Japan DEMO (2015, Fusion for Energy)
- Safety studies for DEMO with AINA code (2014-2018, EUROFusion, still on-going)

AINA code is composed by three main core sections linked one to each other:

- *The plasma block:* the plasma solver is based upon 0-dimensional multi-fluid approach of the mass and energy balance of the plasma core calculated through volume integrals and radial profiles of plasma density and temperature. Particle conservation is considered for fuel ions and alpha particles and every type of impurity (e.g. Xenon and Wolfram), treating the ions and electrons separately. A steady state scenario is computed using an average ion temperature and specified power fusion as inputs and solving the system by the Newton method.
- *The plasma wall interaction:* it evaluates the interaction between the plasma and the in-vessel components. It is focused on two aspects which are the estimation of energy fluxes for the thermal equilibrium calculation of the wall and the surface sublimation and erosion of the impurities on the wall and impurity fluxes to core plasma, on the basis of particle and energy fluxes hitting the wall.
- *Thermal block:* it composed by several independent blocks which contain the simplified in-vessel blanket and the divertor representation (1D or 2D); the material temperature distribution is determined solving the heat equation, Equ.3.3.1, by means of the finite different technique[13] both in steady state and transient regimes using the correspondent boundary conditions (e.g. NWL, imposed temperature VV), coolant conditions (e.g. HTC, fluid bulk temperature, velocity) and accident hypothesis (e.g. typology and magnitude). It is worth reminding that each thermal block is computed separated but at the same time linked to the others by the radiation process caused by the temperature difference of the first wall.

In a very simplified manner, the plasma model computes the radiative energy fluxes over the plasma wall components, at the same time, the wall-model determines the thermal profile and so the first wall temperature which influences the impurities fluxes produced by erosion processing and sputtering into the plasma, perturbing the plasma balance. With the computed input, the thermal analysis of in-vessel components is computed using suited finite difference approach and considering separately first wall and divertor modules and performing a thermal analysis for each one retrofitting back the FW temperature and restarting again

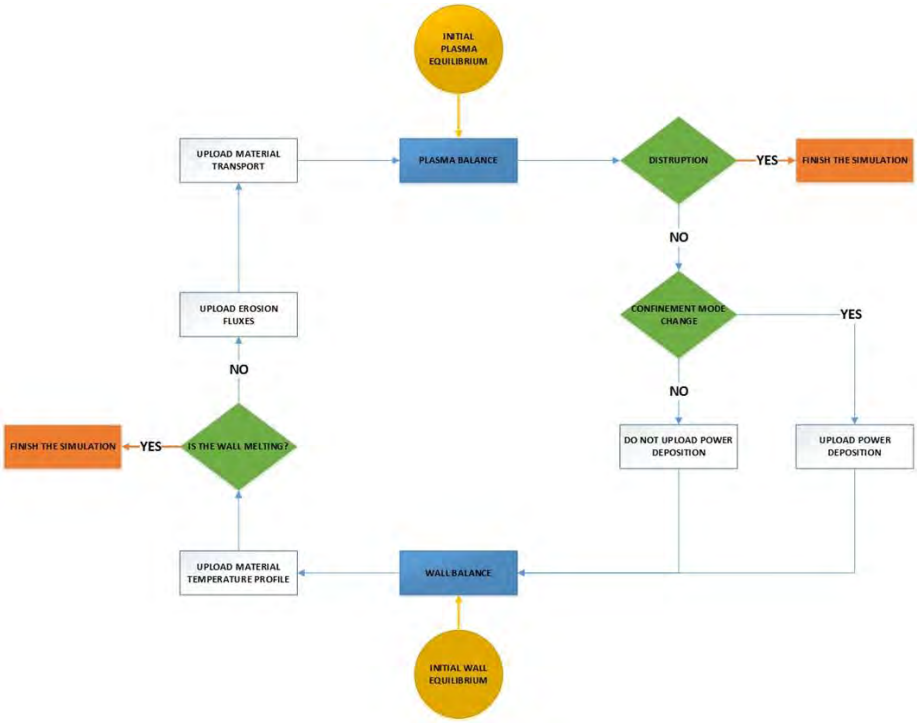

Figure 2.1.1: AINA CORE main loop schematics[7]

the loop. Using this semi-transient approach, AINA estimates the plasma-wall accidents [7]. For more information you could refer to [7].

As typical in a safety code, uncertainties originated form design of the reactor, from plasma physics or from material properties can be properly estimated by means of parametric studies and added if necessary to the final outcomes which can be visualized.

One of the main goals achieved during this thesis has been the definition and application of this standard methodology to develop and implement new in-vessel components (e.g. HCPB BB, WCPB BB, divertor model, etc.) and/or the change of magnetic Tokamak reactor. This methodology aims to build consistently from now on new AINA version, robust from a safety point of view with proper margins to guarantee that the computed temperature suites the realistic physical model. This approach has been already applied to the Japanese DEMO Water Cooled Pebbled Bed blanket case and to the European DEMO Helium Cooled Bebble Bed which are respectively reported in chap.4 and in chap5.

2.1.1 Methodology for the development for new AINA versions

The development and insertion of new in-vessel components in the AINA Safety Code could require the modification of the three main areas (Plasma block, Plasma-Wall interaction and Thermal Block). Depending on the specific requirements of the project, the methodology could be mainly focused on specific blocks but, for sake of completeness, the hereinafter described approach is the most extensive and complete one. The definition and application of this standard approach wants to obtain robust and peer reviewed models which predict as accurately as possible the behavior of the studied system in a short-time but establishing a boundary for the worst scenarios that are useful in obtaining results in a safety analysis. In certain cases, the usage of simplified models could lead to the determination of non conservative parameters thus the application of safety factors or conservatism is foreseen and necessary.

The development strategy, reported in Fig.2.1.2, is subdivided in fours sequential stages. In the Stage No.1, all the blocks are generated, improved and checked in parallel to improve the time schedule. Further details are provided Sec.2.1.1, Sec.2.1.1 and Sec.2.1.1.

Then, in Stage No.2, the Plasma Block and the Plasma-Wall interaction one are connected and the plasma steady-state scenario computed thus possible errors, if present, corrected.

Stage No.3 consists in coupling the thermal blocks, starting from one single poloidal position up to reaching the complete configuration. Specific time setting can be imposed to optimize the interactions between core domains hence limiting some parameter computations only at defined moments. Doing this, difficulties can arise due to the contrasting sensibility to perturbation induced of Plasma Block vs Thermal one.

Afterwards, employing the beta version of the new AINA Safety Code version several scenarios should be determined including at least the state-state case, two overfuelling accidents (50%, 150% of the NWL), two LOCA (50%, 100%) and further assessments changing the coolant parameters (e.g. variation of HTC and coolant bulk temperature). All the obtained results shall be checked with publications, existing safety reports or previous studies. The review and endorsement of the models concludes the Stage No.4 and so the development.

Plasma block For the time being, the Plasma Block is quite simple and requires small computational requirements. It is based on a 0D code which solves the mass and energy global balance of the fusion plasma core whereas the transport problem is done by means of semi-empirical scaling, IPB98 [7]. Further developments as the implementation of a more accurate treatment of plasma processes should not be discarded a priori. In addition, a peer review and verification of the whole Plasma Block is suggested every AINA Safety Code refurbishment.

Anyway, the development of a new AINA Safety Code version specific to a Tokamak machine requires the change and adjustment of the main plasma parameters as the geometry (e.g. volume, minor and major radius, triangularity, etc ...) and the physics ones (e.g. DD, TT, DT, etc ...). Mass balances and power losses methodology should be checked and improved, if necessary. Indeed, the presence of some specific elements, as Tungsten[1], could lead to extremely high *line power losses*.

A parameter cross-check by external software as, PROCESS [55] or PRETOR [56], is recommended to confirm the validity and applicability of the implemented modifications. It is worth reminding that this external verification was already performed in the past moving to the ITER to the European DEMO model [57].

To conclude, the Plasma Block modification and consolidation requires a lot of expertise and should be assigned to Plasma Physic Engineers or at least to people involved previously in this kind of tasks. Considering this, the specific development of this area is not part of this thesis and it will not treated here. You could refer to [7] for more information.

Plasma-Wall interaction Although in Tokamak fusion reactor the plasma is confined by a combination of magnetic fields generated by external conductor and by currents flowing in the fully-ionized gas, it has a limited contact with the first wall layers that strongly influences its characteristics and performance. Indeed, the application of limiters or divertors is required to minimize contact with the wall and recollect the impurities for the plasma[1] avoiding unnecessary energy losses. The interaction of plasma with first wall surfaces will have a considerable impact on the performance of fusion plasmas, the lifetime of plasma-facing components and the retention of tritium in next step burning plasma experiments. Fig.2.1.3 illustrates how the impurity production change in JET due to the usage of limiters or divertors [9].

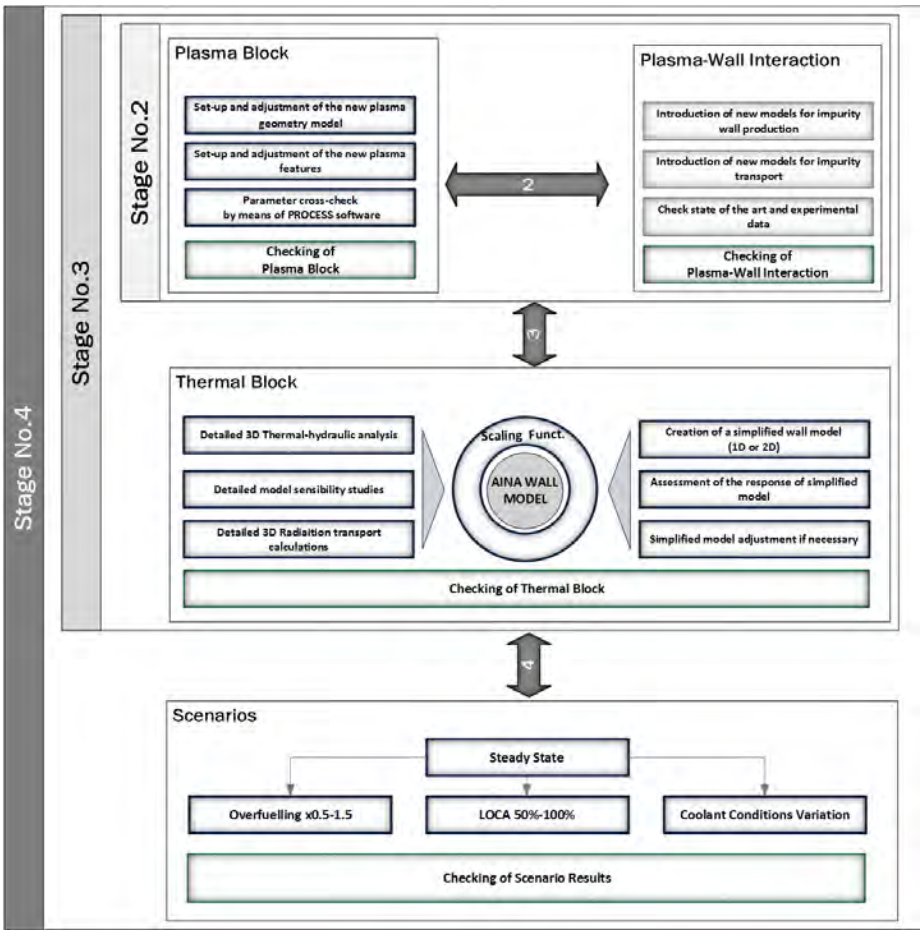

Figure 2.1.2: Methodology for the development of new AINA versions [8]

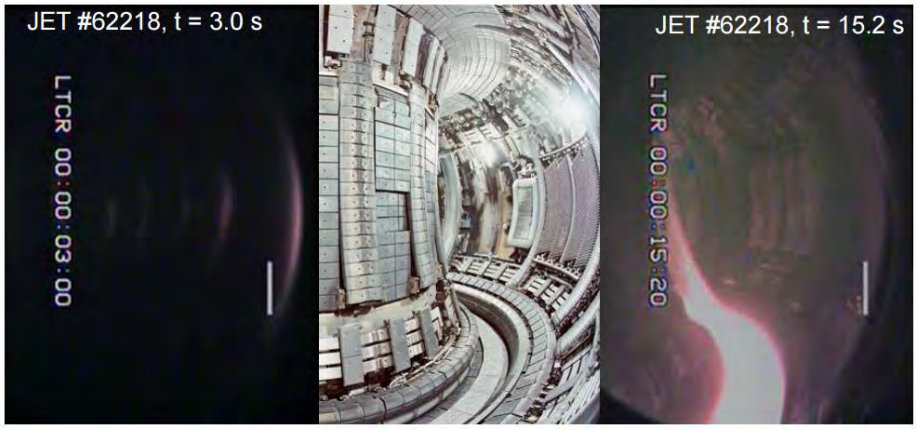

Figure 2.1.3: JET Plasma-Wall Interaction with a limiter (left) and a divertor (right)[9]

Depending on the plasma configuration of the machine, the plasma-wall interaction processes, as *Sputtering* or Scrape-off Layer (or SOLS), importance can variate. In addition, the insertion of the new in-vessel components could require the necessity of generation of new impurity models and transport.

For this reason, as for the plasma block, a peer review of the updated models is strongly recommended by means of external software (e.g. PROCESS[55]) checking also the state of the art of the plasma-surface interaction and experimental data. For almost ten years now, AINA Safety Code has being developed thus, for now on, a constant and rigorous update should be an essential part of the proposed methodology.

To conclude, whereas, the development of this area has been supported, it is not the main focus of this thesis so not treated here. For more detailed information refer to [7].

Thermal Block The Thermal Block, included in the AINA Safety Code, computes the temperature distribution of each in-vessel poloidal region for the imposed scenarios by means of finite difference routines, both 1D and 2D, developed and largely validated within this thesis, see Sec.3.

The usage of approximate but conservative wall-models instead of fully detailed 3D ones is preferred to optimize the running time and the computational resources. Its application shall be supported by clear evidences which confirms the coherency of operational scenarios obtained by the accurate modeling. So, firstly the fully detailed radiation transport calculation has to be carried out to compute the total nuclear power deposition in the components due to neutron and photon heating by means of combinations tally or mesh as described in Sec.2.2.6. Using these data, the steady-state thermal-hydraulic analysis is performed as detailed in Sec.2.3.1. In addition, sensibility analysis should be

done to understand how the systems react to imposed perturbation or to model assumptions to obtain a complete picture of the system behavior. Therefore, starting from the detailed results, simplified thermal-models are drafted and compared using the same boundary conditions. The NHD distribution applied shall be the most conservative over the 3D domain resulting for a rigorous analysis. Depending on the project requirements (e.g. computational effort, accuracy, time response needed, etc...), diverse options can be developed and tested. Iterations and adjustments could be necessary to achieve an optimized and analogous configuration which, at the same time, represents the most conservative of the model. Moreover, it is also recommended to create a simplified radiation transport model in order to cross-check results, perform sensibility and parametric studies (e.g. cross sections and temperature impact analysis) in standard workstations without using super-computer [58].

Unfortunately, at this stage, it could happen that the AINA wall model might not conservatively represent the detailed behavior of the components due to the simplifications carried out, the different NHD distribution applied, the diverse thermal response or by intrinsic modeling features which cannot be adjusted by further iterations. To cope with this, the AINA temperature field distribution once computed is compensated by the application of scaling functions determined as $T_{3D}(x,y,z)/T_{1D}(x)$ ratios for different operational levels (e.g. NWL equal to 80%, 100%, 120% of the nominal power) which are interpolated depending on the scenarios. To enhance the safety margin, the temperature field distribution should be adjusted only if the $T_{3D}(x,y,z) > T_{1D}(x)$.

The described methodology has been successfully applied to Japanese DEMO Water Cooled Pebble Bed blanket as reported in Sec.4.

2.1.2 Short and mid term AINA expected development

For almost ten years now, the AINA Safety Code has being constantly evolved and improved. Several PhD candidates and Master Thesis students with a diverse know-how had given their meaningful support achieving numerous international and peer reviewed publications. Unfortunately, the development was done in a not fully harmonized way, missing a clear and coherent road-map. Considering also the evolution of software and methodologies, the code required a substantial refurbishment.

For these reasons, in late 2014, the kick-off of the *Safety studies for DEMO with AINA code* project within the EUROfusion framework triggered a critical and peer review of the whole AINA Safety Code. Since then, actions were taken thus the code has been almost rewritten, improved and consolidated. In addition, a great effort has been dedicated to document, comment and V&V (when possible) in line with the current software development standard requirement, applying also the so called *waterfall* approach[59]. A collection of the possible development tasks has been detailed in Table 2.1.1 assigning an estimated priority (* low, ** medium and *** high).

Development Tasks	Priority
Plasma Model validation by PRETOR	**
Updating AINA Manual	*
AINA in C++ programming language	*
DEMO Divertor Thermal Wall Model	***
HCLL BLK Thermal Wall Model	***
DCLL BLK Thermal Wall Model	***
AINA Plasma Block using PRETOR	*
WCLL BLK Thermal Wall Model	***

Table 2.1.1: AINA Safety Code expected development

2.2 Radiation Transport

Fusion neutronics aims for the knowledge of neutrons and photons distribution in space and energy starting from the nuclear cross-section data describing the interaction processes of particles and atomic nuclei: thus the mathematical transport problem needs to be solved. The transport of radiation through a material can be described using the Boltzmann transport equation[22]:

$$\frac{1}{v}\frac{\partial\phi(\vec{r},E,\vec{\Omega},t)}{\partial t}+\vec{\Omega}\cdot\nabla\phi(\vec{r},E,\vec{\Omega},t)+\Sigma_t(\vec{r},E,\vec{\Omega},t)\phi(\vec{r},E,\vec{\Omega},t)= \\ +\int_{\Omega'}\int_{E'}\Sigma_s(\vec{r},E'\to E,\vec{\Omega}'\to\vec{\Omega},t)\phi(\vec{r},E',\vec{\Omega}',t)dE'd\Omega'+S(\vec{r},E,\vec{\Omega},t) \quad (2.2.1)$$

where:

- $\frac{1}{v}\frac{\partial\phi(\vec{r},E,\vec{\Omega},t)}{\partial t}$ is the particle flux variation rate in time caused by phenomena such as isotopes decay or delayed neutrons production
- $\vec{\Omega}\cdot\nabla\phi(\vec{r},E,\vec{\Omega},t)$ is the streaming term, representing the dependence of the particle flux gradient on the direction
- $\sum_t(\vec{r},E,\vec{\Omega},t)\phi(\vec{r},E,\vec{\Omega},t)$ is the total reaction rate, including the scattering and absorption interactions and neutron production
- $\int_{\Omega'}\int_{E'}\sum_s(\vec{r},E'\to E,\vec{\Omega}'\to\vec{\Omega},t)\phi(\vec{r},E',\vec{\Omega}',t)dE'd\Omega'$is the scattering term which describes the interaction of particles from some direction $\vec{\Omega}'$and energy E' into direction $\vec{\Omega}$ and energy E
- $S(\vec{r},E,\vec{\Omega},t)$ represents the external particles source in E, $\vec{\Omega}$ and at location $\vec{r}$

Equ.2.2.1 is an integro-differential equation in six independent variables (three in space and energy, one in energy and time)[1]. In a limited number of simple cases the Boltzmann transport equation is solvable analytically, but for most cases, when considering complex systems as a fusion reactor, it can be only solved numerically, in an approximate manner. The two main approaches that can be used to attempt to solve the Boltzmann transport equation numerically are:

- Non-stochastic or deterministic approach: perform the balance of particles gains and losses, solving the integro-differential Boltzmann transport equation for flux density in infinitesimal phase space elements
- Stochastic or probabilistic approach: simulation of real physical process on microscopic level, tracking the individual particle histories from its generation (in nuclear reactions) to its disappearance (by absorption or leakage), with interaction probabilities obtained by nuclear cross sections

Both approaches can achieve the same level of accuracy because, after all, they solve the Boltzmann equation using a numerical solution which converges to the exact solution [60]. In Monte Carlo algorithms, where the convergence is stochastic, an higher history number allows having a numerical solution closer toward the exact solution only in probability. This does not avoid having systematic error associated with some variance reduction methods which of course can be further reduced or eliminated despite the increased computational cost. In deterministic algorithms, bringing a numerical solution closer to the exact solution involves increasing the resolution of computing grids and increasing the number of iterations in iterative procedures.

2.2.1 Deterministic approach

Only for very simple radiation transport cases analytical equation and exact solution can be obtained. Concerning complicated systems, only approximate numerical solutions of the Boltzmann equation can be derived by means of discretization in the phase space, the so called the deterministic methods. Deterministic methods typically employ one or more of these techniques:

- Discretization in angle (discrete ordinates, S_n)
- Spherical harmonics expansion of the scattering term using the Legendre Polynomials, P_n
- Discretization in energy (multigroup approximation)

The discrete ordinates discretizes the angular variation of the direction vector, $\vec{\Omega}$, into finite directions in space with associated solid angle elements [61]. The

[1] The Boltzmann equation can be written in several different forms such as integral, even/off parity, Green's function and multiple collisions. Each form having it particular mathematical property facilitates a class of solutions hence applied for different applications.

number of directions considered must be sufficient to describe the possibly highly anisotropic angular flux and to avoid the "ray effect" problem [62] (Fig.2.2.1) which could be seen in problems where a localized source is positioned within a low scattering medium.

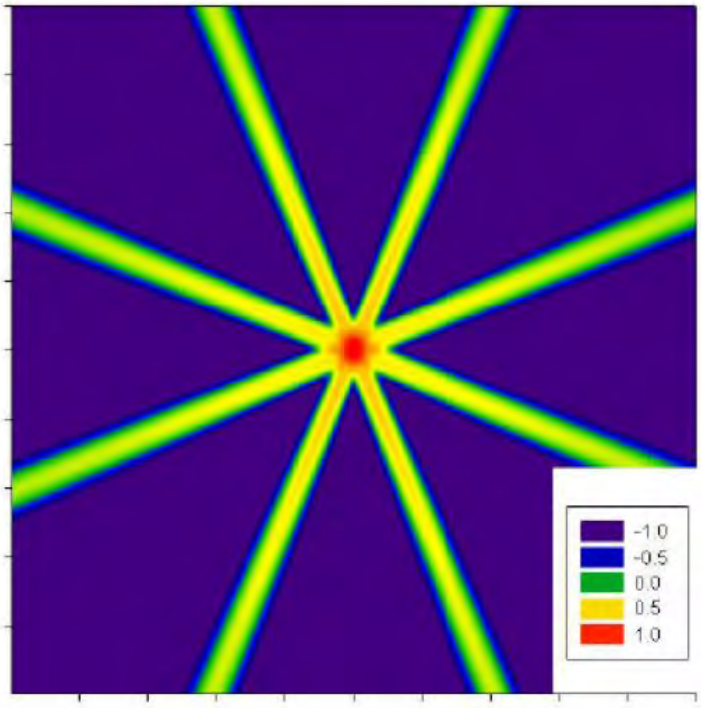

Figure 2.2.1: Severe ray effects exhibited in a 2-D scalar flux solution to a point source using 8 discrete ordinates

Consider that a large amount of group allows a better accuracy but at the same time an increased computational cost.

On the other hand, the spherical harmonics expansion by means of the using the Legeandre Polynomials [63], P_n, are used for instance to develop the scattering term of the Boltzmann equation removing the dependence by the scalar product between two particle direction. Moreover, they can be applied to the whole Boltzmann equation to further simplify it. In the multigroup approximation[64], all the energy depend variables, as for instance the nuclear cross section and the source, are split in a number of discrete energy group where the centroid determines the interaction energy. A typical energy group used in fusion application is the VITAMIN J, which has 175 bins [65]. As commented for the S_n, approximation, the accuracy of this method is strongly related to the numbers of energy division assumed. The user has to employ a sufficient number of groups in order to represent all the main resonance avoiding a clear

under/over-estimation of the result.

To conclude, the most important deterministic software currently used in nuclear fusion are:

- ATTILA [66, 67]
- DENOVO [68]

2.2.2 Probabilistic approach

What exactly is the Monte Carlo method? Metropolis and Ulam (1949) described the method as *"a statistical approach to the study of differential equations, ormore generally, of integro-differential equations that occur in various branches of the natural sciences"*[69]. Focusing on fusion neutronics, the basic idea is not solve the transport equation as such. Instead, the algorithm simulates the microscopic physics of every particle collision, energy and direction change. Each particle is simulated according to a source distribution and interaction coefficients and is tracked through its history until it is absorbed or escapes the system. When enough of these particle histories are tracked the answer can be considered statistically significant. Computational techniques that, in simplistic terms, predict particles events with repeated random sampling (actually the generation of random numbers in a computer) are called Monte Carlo methods. Whereas, the *discretized method* are based upon phase space boxes approximation, the MC codes do not need such. It is worth highlighting that the modern version of the Monte Carlo method was invented by Fermi in 1934 at the University of Rome [70]. However this technique was not published until the late 1940s by Stanislaw Ulam within the Manhattan Project at the Los Alamos National Laboratory. At this point, Ulam and John Von Neumann suggested that aspects of research into nuclear fission at Los Alamos could be aided by use of computer experiments based on chance [71]. The project was top secret so Metropolis chose the name Monte Carlo in reference to the Casino in Monaco [72] . Later he also developed computing devices to manage such intensive calculations [73].

A Monte Carlo code reproduces theoretically a statistical process, such as the interaction of nuclear particles with materials, and it is particularly useful for complex problems that cannot be properly and efficiently modeled by means of *deterministic methods*. The individual probabilistic events of a process are simulated sequentially with probability distributions governing these events that are statistically sampled to describe the total phenomenon. In general, the simulation is performed on high performance computing devices because the number of trials necessary to adequately describe the phenomenon is usually quite large [58, 74]. The statistical sampling process is based on the selection of random numbers (analogous to throwing dice in gambling, hence the name 'Monte Carlo'). In particle transport, the Monte Carlo technique consisting in following each of many particles from a source throughout its 'life' to its 'death' by absorption or escape phenomena from the interested domain. The probabil-

ity distributions are randomly sampled using transport data to determine the outcome at each step of its life.

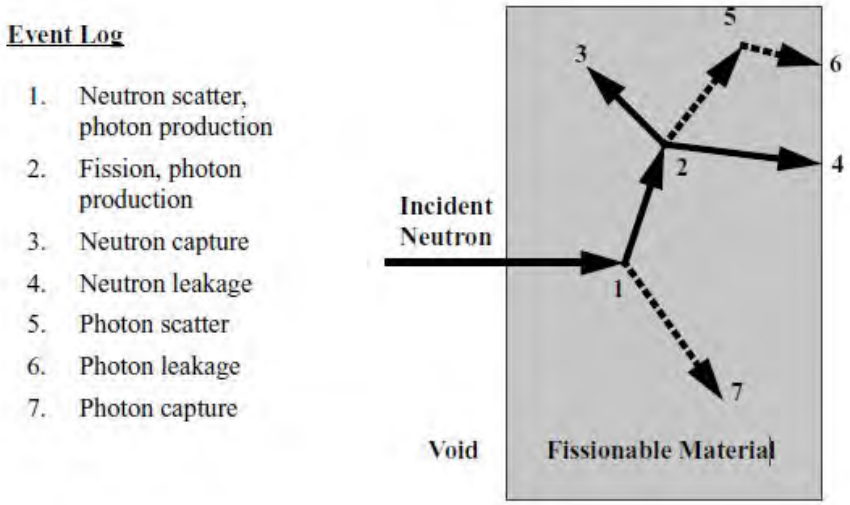

Figure 2.2.2: History of a MC neutron transport

Fig.2.2.2- [75] illustrates a random history of a neutron incident on a slab of material that can undergo fission. Numbers between 0 and 1 are selected randomly to determine what (if any) and where interaction takes place, based on the rules (physics) and probabilities (transport data) governing the processes and materials involved. In this particular example, the following events occur:

1. The neutron undergoes an inelastic scattering reaction and is deflected through some angle, which is determined from the physical scattering distribution stored in the nuclear data. A photon was created, which is temporarily stored in memory for later analysis.

2. The neutron is captured in some nuclide capable of a (n,2n) fission reaction: two neutrons and one photon are generated, with related energies and directions to the reaction. Again, one neutron and the photon are stored for later analysis.

3. The first fission neutron generated previously suffers an absorption reaction and its life is terminated.

4. The banked neutron, retrieved from memory, leaks from the system.

5. The fission-produced photon collides and,

6. leaks out of the slab.

7. The remaining photon, created in at stage 1, is captured, completing the neutron history.

To conclude, the uses of MC software is continuously increasing worldwide in several fields. Next, the most important software in nuclear fusion are reported:

- MCNP, "Monte Carlo N-Particle" [75]
- GEANT, "Generation of Events ANd Tracks" [76]
- PENELOPE, "PENetration and Energy LOss of Positrons and Electrons" [77]
- SuperMC [78, 79]

MCNP has been the software employed along this PhD thesis and it is described in detail in chapter 2.2.4.

2.2.3 Monte Carlo, deterministic method and hybrid codes

The Monte Carlo and the Deterministic methods are very different techniques which both aim to resolve the transport equation. The accuracy of the methods can be similar and depend mainly on the user options. By the way, if calculations are set up correctly nonphysical response are unlikely in MC, nevertheless negative flux or heating can appear in deterministic codes because they are accepted in the iteration converge process. In these cases, the user expertise is fundamental and might avoid erroneous results.

Whereas, the deterministic code solves the transport equation for the average particle behavior, the Monte Carlo code simulate individual particles and recording some features (tallies) of their average behavior [75]. Using the central limit theorem, the average behavior of particles in the physical system is then derived from the average behavior of the simulated particles. The Monte Carlo particularly well suited to solve complicated three-dimensional, time-dependent problems, allowing detailed representations of all aspects of physical data. Whereas, the MC transports particles between events (e.g. collision) which are separated in time and space, the Deterministic code involves time and space derivative because it starts from an integral-differential form of the Boltzmann equation. In addition, the Deterministic codes require a large amount of memory to resolve the large set of equations whereas the MC could be operated in standard workstation and easy parallelized thanks to the history independence. Despite these disadvantages, discrete ordinates techniques are still very largely used in fusion neutronics and can produce useful results in many cases where large volumes and amounts of materials can be reliably simplified reducing at the same time the computing time needed. They provide complete information, such the particle flux, in the whole phase space of the problem however Monte Carlo supplies information only about specific tallies requested by the user. Although the MC techniques feasibility to solve very complicated phase space, determine a response far away from the source where the flux is several order of magnitude

attenuated is very challenging. Indeed considering a neutron which travels up to distance x where the flux is 10^6 times decreased, only one particle within a million will reach that position. A large amount of tracks is needed in order to obtain valid statistics at that position causing a not feasible computational time. Variance reduction techniques (or VRT), which are mathematical treatments of the transport, are required to speed up the simulation hundreds of times obtaining statistically valid results in a reasonable time. Nowadays, the MC codes are internally provided by several VRT which can be set-up and adjusted by the user depending on the specific application. This operation requires a lot of expertise, it is very time-consuming and it could be iterative. For these reason, the recent neutronics fusion tendency is to compute in a semi-automatic way these parameters all over the phase/space by means of an external deterministic software which resolves the adjoin Boltzmann equation as for instance ADVANTG [80]. This methodology, worldwide named as Hybrid methods, is also described hereinafter (see sec.2.2.5).

2.2.4 MCNP: Monte Carlo N-Particle

MCNP is the acronym of Monte Carlo N-Particle. It was produced under a U.S. Government by Los Alamos National Laboratory. It can be used in several transport modes including the capacity to calculate the eigenvalues for critical systems : neutron only, photon only, electron only, combined neutron/photon transport where the photons are produced by neutron interactions, neutron/photon/electron, photon/electron, or electron/photon. The code treats an arbitrary three-dimensional configuration of materials in geometric cells described by first and second-degree surfaces and fourth-degree elliptical tori [81, 75]. MCNP has particle energy limitations in the transport: the neutron energy regime is from 10-11 MeV to 20 MeV for all isotopes and up to 150 MeV for some isotopes, the photon energy regime is from 1 keV to 100 GeV, and the electron energy regime is from 1 keV to 1 GeV. Important features that make MCNP very versatile include a powerful general source, criticality source, and surface source, a set of variance reduction techniques; a flexible tally structure and an extensive collection of cross-section data. Moreover the code contains numerous flexible tallies: surface current and flux, volume flux (track length), point or ring detectors, particle heating, fission heating, pulse height tally for energy or charge deposition, mesh tallies, and radiography tallies. All these important features makes MCNP the reference tool for the neutronic analyses in the frame of the ITER/EUROfusion project and for this reason has been used in the studies carried out in this thesis [82]. MCNP makes use of ENDF (Evaluated Nuclear Data File [83]) pointwise cross section formatted data which means that no approximation or averaging has been applied and hence a very good representation of transport is maintained.

2.2.4.1 Geometry description

MCNP makes use of the combinatorial geometry to define the three-dimensional space where the particles transport is simulated: canonical surfaces are combined using Boolean operators to create a volume, thus cells are defined by the intersections, unions, and complements of the regions bounded by the surfaces. Furthermore, surfaces are defined by supplying coefficients to the related analytic equations or known points on the considered surfaces. The combination of surfaces defines a cell and requires the specification of a 'sense' of all points in a cell with respect to a bounding surface, which is either positive or negative. Cells are defined by cell cards. Each cell is described by a cell number, material number and material density followed by a list of operators and signed surfaces. The manual generation of the MNCP geometry description (both surfaces and cells) is very tedious and time-consuming hence currently limited only to very simple models. Nowadays, the generation and debugging of complex 3D models is done by means of external software as SuperMC [78, 79] or MCAD [84, 85] which converts simplified geometrical 3D model (e.g. stp, iges, sat) into MCNP surface and cell cards. The usage of these tools reduce significantly the amount of time required for the model generation and at the same time grant the implementation of very detailed geometry details such as the ITER First Wall blanket channels.

2.2.4.2 Boundary conditions

Four types of external boundary conditions can be imposed to the MCNP geometry surfaces. Hereinafter, they are described and their functions illustrated by means of a simple example: a particle track "a" is with trajectory angle α impinges surface No.1 which changes its nature case-by-case:

- Absence of boundary conditions, Fig.2.2.3-(a): *no special treatment is applied to the particles crossing this type.* Indeed, in the example reported, once the track "a" passes the surface, which defines the model's graveyard, it is killed.

- Periodic boundary conditions, Fig.2.2.3-(b): *periodic boundary conditions can be applied to pairs of planes to simulate an infinite lattice. Although the same effect can be achieved with an infinite lattice, the periodic boundary is easier to use, simplifies comparison with other codes having periodic boundaries, and can save considerable computation time,* cit.[75]. In the example reported, the surface No.1 is coupled to the No.2: the track "a" exits from surface No.1 with angle α hence it enters as track "b" from surface No.2 preserving the inclination α.

- White boundary conditions, Fig.2.2.3-(c): *A surface can be designated a white boundary surface by preceding its number on the surface card with a plus. A particle hitting a white boundary is reflected with a cosine distribution, $p(\mu) = \mu$, relative to the surface normal; that is,$\mu = \sqrt{\xi}$, where ξ is a random number. They also can be used to approximate a boundary with*

an infinite scatterer. They should always be used with caution, cit.[75]. In the example, the track "a" once strikes over the surface No.1 is reflected with a random sampled direction.

- Reflecting boundary conditions, Fig.2.2.3-(d): *a surface can be designated a reflecting surface by preceding its number on the surface card with an asterisk. Any particle hitting a reflecting surface is specularly (mirror) reflected. Reflecting planes are valuable because they can simplify a geometry setup (and also tracking) in a problem, however they can make difficult to correct the correct answer,* cit.[75]. In the described example, the track "a" once strikes over the surface No.1, it is reflected with the same angle α.

Depending on the specific application, simulation needs and medium, one or more type could be applied. For instance, the impact of the BC has been assessed for the WCPB BB, Sec.4.2.2.4.

2.2.4.3 Source specification

MCNP's generalized user-input source capability allows the user to specify a wide variety of source conditions without having to make a code modification. Independent probability distributions may be specified for the source variables of energy, time, position, and direction, and for other parameters such as starting cells or surfaces. In addition to input probability distributions for source variables, certain built-in functions are available. These include various analytic functions for fission and fusion energy spectra such as Watt, Maxwellian, and Gaussian spectra; Gaussian for time; and isotropic, cosine, and mono-directional for direction. Biasing may also be accomplished by special built−in functions. A surface source allows particles crossing a surface in one case to be used as the source for a subsequent problem by means of the SSQ/SSR command cards. The decoupling of a calculation into several parts allows detailed design or analysis of certain geometrical regions without having to rerun the entire problem from the beginning each time.

2.2.4.4 Tallies

The code automatically creates standard summary information that gives the user a better insight into the physics of the problem and the adequacy of the Monte Carlo simulation including a complete accounting of the creation and loss of all tracks and their energy, the number of tracks entering and reentering a cell plus the track population in the cell, the number of collisions in a cell, the average weight, mean free path, etc. In addition, response in specific regions of the model, where specific nuclear responses are needed, can be estimated, the so called *tally*. Several typologies of tallies are available in MCNP as well as the particle flux in cell and in surface (F4), the current crossing a surface (F2), the particle flux at a point detector (F5), the detector spectra response (F8) and the particle heating (F6). For each tally a Tally Fluctuation Chart (or TFC)

in present automatically in the MCNP output resuming the tally estimation, statistics checks and trends to help the user in the results validation.

Moreover, MCNP allows the superimposition of a mesh (e.g. cylindrical, rectangular or spherical) over the problem geometry, the so called FMESH tally, to compute particle flux and its by product such as nuclear heating, Tritium production, etc using proper converting parameters and correspondent cross sections. The last release of MCNP, MCNP6.1, permits also the implementation and transport over unstructured mesh generated by finite-element methods software as ABACUS [86], facilitating the coupling with other codes such as CFD ones.

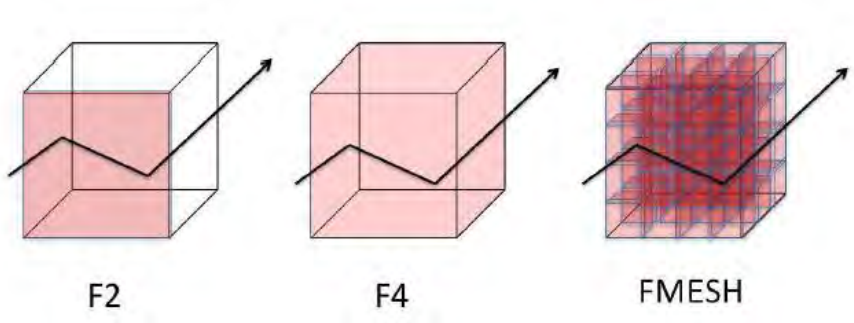

Figure 2.2.4: MCNP tally typology

Mesh tally Nuclear heating distribution could be obtained by converting flux mesh tallies with the help of tally multiplier. Two different set of results can be obtained:

1. *Implicit Type*: the tally multiplier converts neutron and photon flux to nuclear heating in the material where particle is being currently tracked. Using this approach, the tracks in voided regions do not contribute to the tally whilst the reported value is still averaged in the whole voxel. Thus, for elelments containing some void areas, this tally results in a decreased heating value, since the heating in material "seen" in the mesh element is smeared over volume. This effect leads to non conservative results in the FW layer and so it is discarded.

2. *Explicit Type*: the tally multiplier converts neutron and photon flux to nuclear heating using a specific imposed material cross section all over the mesh (e.g. 316L(N)-IG) avoiding no conservatism on the external boundaries. This set describes the heating accurately only for the specific applied material, requiring the usage of different mesh tallies to cover the whole set of materials. Although this approach is more demanding, it is strongly recommended and applied hereinafter.

2.2.4.5 Variance reduction techniques

Variance-reducing techniques in Monte Carlo calculations want to reduce the computer time required to obtain estimated nuclear response of sufficient precision[2] and the simultaneous decrease in the computer time, non-affecting the physical result. The fundamental idea is to minimize the transportation of particle in areas away for the region of interest increasing at the same time the contribution to the interested response in an unbiased way. It is worth reminding than the *"Successful use of MCNP variance reduction techniques is often difficult, tending to be more art than science"*, cit. [75]. There are several variance reduction techniques, with their own advantages, problems, and peculiarities, which can be classified in three categories [87, 75]:

- *Truncation Methods:* truncation of parts of phase space that do not, theoretically, contribute significantly to the solution. Geometry, energy and time cutoff are possible.

- *Population Control Methods:* control the number of samples taken in various regions of phase space. In important regions many samples of low weight are tracked, while in unimportant regions few samples of high weight are tracked. Specific population control methods available in MCNP are geometry splitting and Russian roulette, energy splitting/ roulette (see Fig.2.2.5), time splitting/roulette, weight cutoff, and weight windows (or WW). The WW are widely used method in fusion neutronics thanks to its feasibility with very complex 3D geometry and its possibility to be applied to as mesh or cell based. The WW can be generated manually, by the MCNP internal generator or by means of ADVANTG [80] (see Sec.2.2.5).

- *Modified Sampling Methods:* alter the statistical sampling of a problem to increase the number of tallies per particle. For any Monte Carlo event it is possible to sample from any arbitrary distribution rather than the physical probability as long as the particle weights are then adjusted to compensate. Thus with modified sampling methods, sampling is done from distributions that send particles in desired directions or into other desired regions of phase space such as time or energy, or change the location or type of collisions. Modified sampling methods in MCNP include the exponential transform, implicit capture, forced collisions, source biasing, and neutron-induced photon production biasing.

- *Partially-Deterministic Methods:* these methods, which are very complex, substitute the standard MC random walk with more deterministic-like techniques as for instance the next event estimator (e.g. F5 tally). Point detector, DXTRAN sphere and correlated sampling techniques belong to this category.

[2]Note that precision is only one requirement for a good Monte Carlo calculation. Even a zero variance calculation cannot accurately predict natural behavior if other sources of error are not minimized.

2.2.4.6 Nuclear data

In this PhD thesis, coupled neutron-photon simulation have been carried out by means of the Fusion Evaluated Nuclear Data Libraries (FENDL2.1 [88] and FENDL3.1b [18]). The FENDL library is a comprehensive, validated, and extensively tested nuclear data repository developed specifically for thermonuclear fusion applications. Indeed, nowadays they are the recommended libraries for the ITER project. The library contains ENDF formatted pointwise cross section data for various neutron-induced reactions with fusion relevant nuclides no requiring resonance correction factors and approximations of the angular and emitted particle spectra. For more information you could refer to the IAEA web page.

2.2.5 ADVANTG: AutomateD VAriaNce reducTion Generator

As commented previously, ADVANTG is becoming a standard tool in fusion neutronics to generate automatically variance reduction parameters for fixed-source continuous-energy Monte Carlo simulations with MCNP5 v1.60. The weight window generated are based on an approximate 3-D multigroup discrete ordinates adjoint transport solutions generated by means of the DENOVO software [68]. Space and energy-dependent weight-window bounds and biased source distributions are generated and exported in a format which is directly usable with MCNP5. ADVANTG can be applied to numerous typology of radiation transport as neutron, photon, and coupled neutron-photon simulations of real-world radiation detection and shielding scenarios. In addition, the WW can be optimized both for individual tally (e.g. F1, F2, F4, F5, F6, F8) and Cartesian mesh tally (e.g. FMESH), applying the CADIS or FW-CADIS methodology [10].

In order to run the tool, the user has to set up a very user friendly input file where several options have to be specified as well as the MCNP model, $S_n$order, model discretization, maximum No. of iteration etc. Hence, ADVANTG reads the MNCP input file, mix the multigruop cross section and map material regions onto the deterministic spatial mesh as well as the tally regions. Once the model is discretized, the adjoint sources is computed. At this point, DENOVO runs parallel 3-D S_n calculation to estimate the adjoint fluxes over the domain using the Consistent Adjoint Driven Importance Sampling (or CADIS) or the Forward CADIS (or FW-CADIS) approach, depending if the VRT optimization is toward a localized detector (tally) region or a distribution of tallies and multiple localized detector regions.

The CADIS method wants to estimate the scalar importance of particle to some objective, hence the response R, and then compute the biased source distribution, $q^+(\vec{r}, E)$, as:

$$R = \int \int q(\vec{r}, E)\phi^+(\vec{r}, E)d\vec{r}\,dE \tag{2.2.2}$$

$$q^{+}(\vec{r},E) = \frac{\phi^{+}(\vec{r},E)\, q(\vec{r},E)}{R} \tag{2.2.3}$$

where $\vec{r}$ is the vector which defines the phase space position, $q(\vec{r},E)$ is the unbiased source and $\phi^{+}(\vec{r},E)$ is the the scalar adjoint flux.

Considering the parameter c is the ratio between the WW upper and lower bounds, $c = w_u/w_l$, the space/energy dependent WW are determined as:

$$w_l(\vec{r},E) = \frac{R}{\phi^{+}(\vec{r},E)\left(\frac{c+1}{2}\right)} \tag{2.2.4}$$

In order to have consistent source biasing parameters and WW, the statistical weight, w_0, is given to the source particle:

$$w_0(\vec{r},E) = \frac{q(\vec{r},E)}{q^{+}(\vec{r},E)} = \frac{R}{\phi^{+}(\vec{r},E)} \tag{2.2.5}$$

On the other side the FW-CADIS methodology is more complex and computational demanding than the CADIS one, because it also requires the determination of function that represents the importance of particles to achieving uniform MC particle density all over the problem phase-space ahead the response step. Indeed, the calculation of the adjoint source, $q^{+}(\vec{r},E)$, is based on the forward solution of the flux, $\phi(\vec{r},E)$. For instance, if the purpose is to compute some response function on a mesh tally (e.g. He PPM production, $\sigma_d(\vec{r},E)$, the adjoint source is calculated as:

$$q^{+}(\vec{r},E) = \frac{\sigma_d(\vec{r},E)}{\int \phi(\vec{r},E)\, \sigma_d(\vec{r},E)\, dE} \tag{2.2.6}$$

In both approaches, weight-window bounds are generated and exported as well as the estimated biased source probabilities in two formats: one compatible with MCNP and the other with Visit for a proper visualization [89].

As an example, consider the following problem of where the dose radiation map has to be determined within the whole PWR facility. Considering the deep-penetration problem, this is a very challenging MCNP calculation. Indeed, running an analogy simulation for about 10 billion histories requires about 25 cpu*days obtaining a very poor and unacceptable results for almost all of the area outside the containment (Fig. 2.2.6 (a)). By the way, using an hybrid methodology, e.g. MCNP+ADVANTG, and investing 0.75 cpu*days in the ADVANTG calculation plus 20cpu*days in the MCNP calculation, we obtain almost only non-zero over most of the facility and range over 30 orders of magnitude (Fig. 2.2.6 (b)). This results is very impressive showing how powerful the hybrid method can be if used in the proper way after a quite steep learning curve.

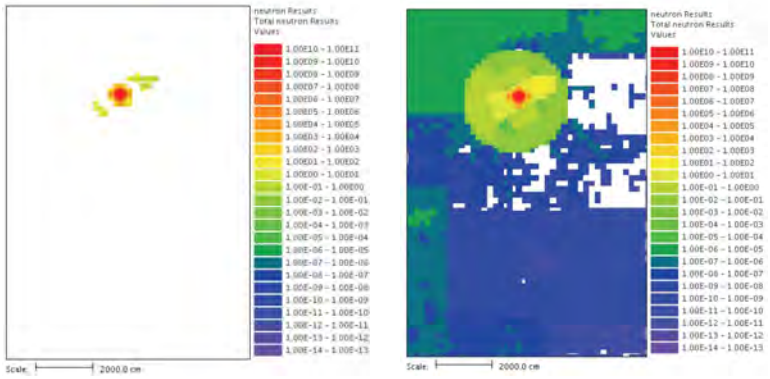

(a) *(b)*

Figure 2.2.6: ADVANTG example [10]

2.2.6 Methodology

The radiation transport calculations has required the development and refinement of a suited methodology to fulfill both the technical and quality requirement imposed. The consolidated approach, based on the state-of-art technique, has been reported in Fig.2.2.7 and detailed hereinafter.

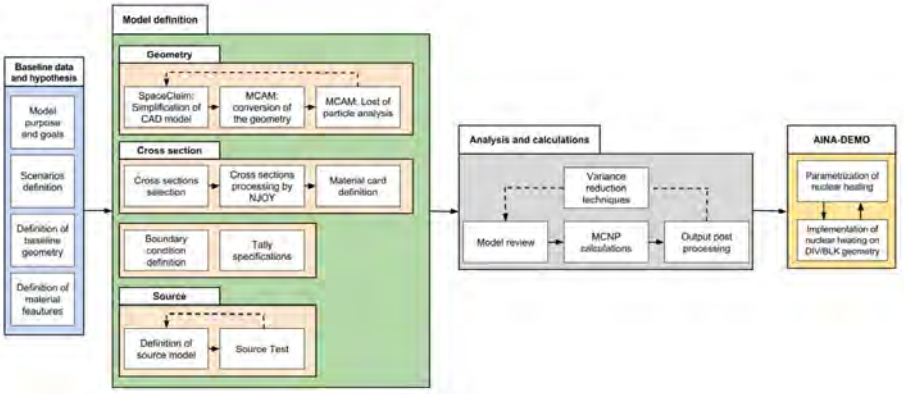

Figure 2.2.7: Radiation Transport Methodology

The methodology, which requires the application of different software, is composed by several sequential phases:

1. Baseline data and hypothesis
2. Model definition
3. Analysis and calculations

4. Post-processing and preparation of data for AINA Safety2.2.8 Code

Baseline data and hypothesis This phase consists the definition of model purposes, the definition of scenario (i.e. type of plasma DD or DT, fusion power, etc...) and the definition of all the input data (e.g. model version, material type and its compositions).

Model definition Once all the baseline data and hypothesis are fixed, the modeling work can start. Commonly, CAD engineering model contains too much geometry details (e.g., fillets, chamfers, bolts, springs, screw holes and threads), incompatible surfaces (e.g., splines) or with complex structures which are not important for neutronics analysis and significantly increases calculation times. These features will make the translation to MCNP file more difficult or impossible. Therefore, it requires necessary and appropriate simplifications and modification of geometry by proper software as SpaceClaim [90] or CATIA [91]. The objective is to remove details which are not important for transport calculations. One example of common simplification is reported hereinafter, Fig.2.2.8, where the rounding cut-outs have been replaced by sharped corners.

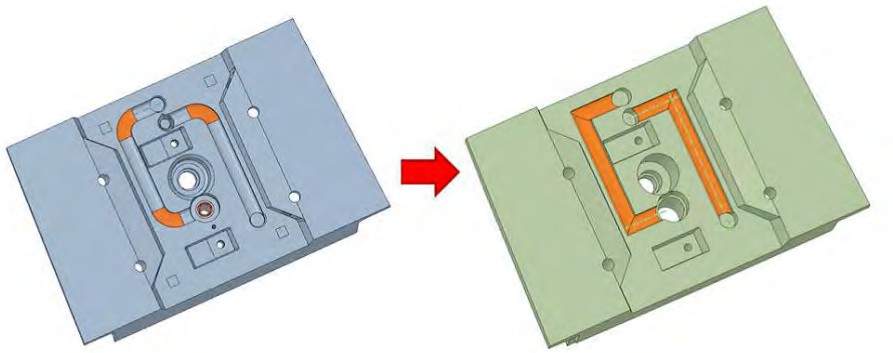

Figure 2.2.8: Geometrical simplifications on a blanket module

Gross simplification of components may also be desirable, for example when dealing with a collection of small detailed components, or a large component with intricate internal structures. In these cases, it may be appropriate for the details to be removed entirely in favor of an envelope volume representation. In order to maintain the correct mass of materials, such simplification is always accompanied by homogenization of materials and a density correction. By approximating the bodies, the radiation transport behavior of the system (i.e. the capability to shield photons) shall be preserved or sufficient similar to the original representation. This is obtained preserving the overall mass of main materials within approximately 2% and with particular attention to retain the streaming paths.

For this reason a mass checking and a visual original-simplified component comparison should be done for each component. Generally, it is desirable to retain more detail of channels, penetration or where strong gradients are present. In case of modification a proper justification shall be provided by the analyst. Once the MCNP has been simplified and checked, the complex solids shall be decomposed into a combination of simple convex solids like box or sphere to allow the proper conversion to MCNP by means of SuperMC/MCAM [78, 79]. Therefore, manually assisted decomposition with SpaceClaim is adopted and the whole model is decomposed into a number of convex solids which can be converted to MCNP files rapidly. During the SuperMC/MCAM conversion, the solids are translated into cells, to which can be assigned a material card, and surfaces descriptions, and void spaces around the solids created. The graveyard can be generated manually or automatically using the SuperMC functions changing construction type and related limits. Parameter sensitivity analysis is recommended to optimize the number of MCNP cell and surfaces hence improving the computational performances. Finally, the converted MCNP file has to be validated with MCNP utilities and real particle tracing with void options for detecting possible geometry errors. SuperMC software could be employed for the 3D visualization of lost particles (e.g. lost position known and cosine directories).

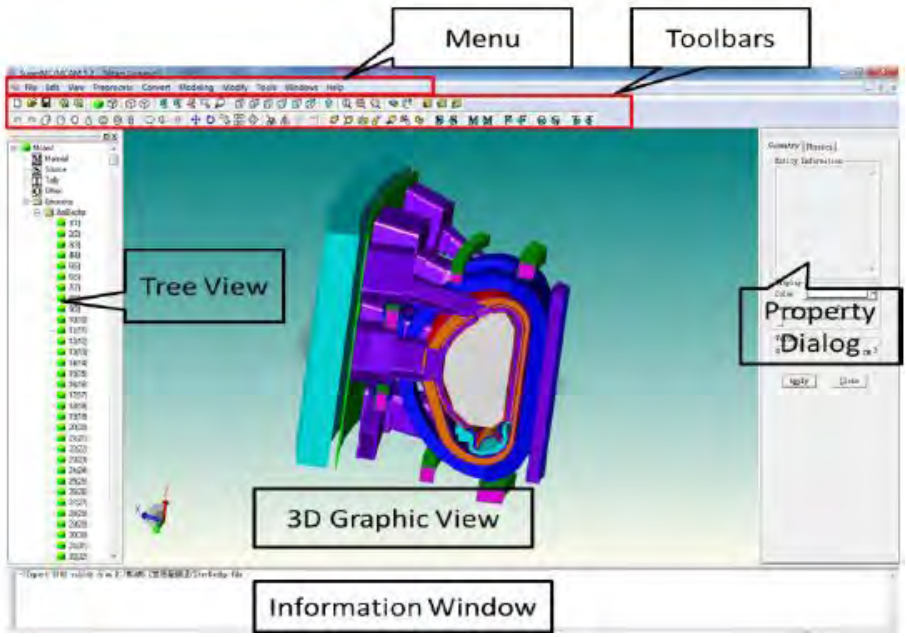

Figure 2.2.9: SuperMC Software [11]

In general, lost particle could be found where with multiple surface inter-

sections are present and cannot be avoid due to the geometry complexity of some components. These errors, which are caused by the truncation error of coefficients in the translation, the surfaces offset of small distances, the CAD approximation in the step conversion, engender tiny interference or empty area between the adjacent solids, as showed in Fig.2.2.10, and for the time being they have to be repaired manually.

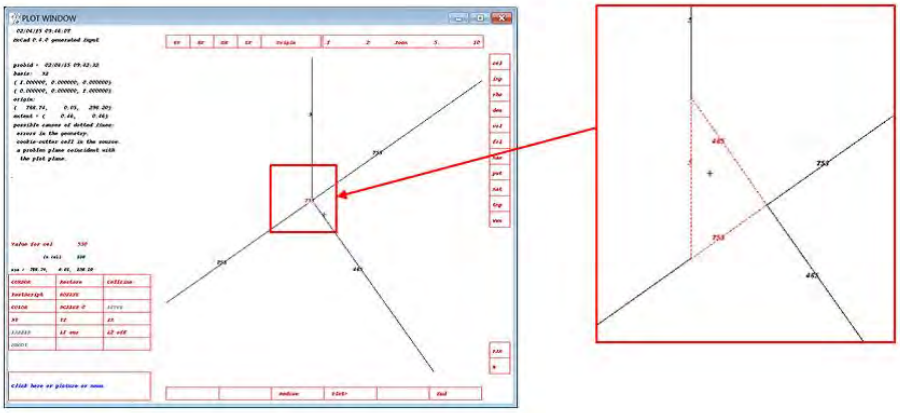

Figure 2.2.10: MCNP lost particle errors

Once the geometry is converted and tested, the material card assigned to each MCNP cell has to be prepared according to the isotopic composition and applying the selected fusion cross sections, such as the FENDL, which are not contained in the standard MCNP installation package. For this reason, following the MCNP manual instructions, they have been added manually to the XDIR file. To automatize this very time consuming operation, a suited C++ routine, named "XDIR_Add.exe", has been developed to copy and add all the isotopes. Moreover, it is important to remember that the cross sections are specific for a certain temperature (e.g. 300 K). Indeed, the nuclear interactions are also function of the temperature, in particular in the thermal range, the application of the cross sections in conditions not close to the nominal zone should be proper justified. For this reason, NJOY software[92] has been requested to the NEA Data Bank and properly compiled to assess this possible need.

In addition, the source (e.g. plasma neutron, activated material, etc...) and the boundary have to be implemented and possible tested by means of basic cases or in void mode.

To conclude, proper tally and mesh tally have to be defined according to the simulations purpose and to evaluate the goodness of there results. It is strongly suggest to cross check the results by different tallies because the variace reduction technique could influence differently them.

Analysis and calculations As soon as the model has been prepared, it has to be independently reviewed to check the presence of possible source of error. Then, the simulation can be done and results obtained. Depending on the specific usage, the application of variance reduction techniques could be necessary to fulfill and accomplish all the statistical requirement of the MCNP tally fluctuation charts. According to Sec.2.2.4.5, the standard MCNP VRT can be implemented or the ADVANTG software used to produce optimized weight windows. It is worth reminding than this process could require several iterations. Indeed, the *"Successful use of MCNP variance reduction techniques is often difficult, tending to be more art than science"*, cit. [75].

Post-processing and preparation of data for AINA Safety Code To conclude, the data produced have to be normalized for a specific plasma scenario and shaped in a format compatible with AINA safety code or subsequent engineering analysis as the thermal-hydraulic one, which depending on the specific application could be in table, approximated by a functions or in VTK files. To convert the mesh tally output to the VTK format, the *msh2vtk[93]* script has been employed for the structured mesh whereas the *um-post-op[75]* utility for the unstructured one. It is worth reminding that a MCNP bug in this routine has been discovered and communicated to the MCNP forum on the 01/09/2015 18:30. To conclude, it is suggested to store the information in very structured way defining a proper nomenclature for the cases, input and output.

2.3 Computational fluid dynamics

Fluid (gas and liquid) flows are governed by partial differential equations which represent conservation laws for the mass, momentum, and energy. Computational Fluid Dynamics (CFD) is the methodology to replace partial derivative equation (or PDE) systems with set of algebraic equations in order to be solved numerically in massive form by digital computers. It is for the first applied in the 50s at Los Alamos National Laboratory [94]. CFD provides a quantitative and qualitative estimation of the fluid flows using mathematical modeling, numerical methods (e.g. discretization and solution techniques) and software (e.g. solvers, pre/post utilities). It predicts several parameters as flow patterns, temperature distribution, pressure drops, turbulences which are problematic, expensive or impossible to study using traditional (experimental) techniques. For these reasons, this approach is widely used in numerous applications: weather forecast, space mission design (Fig. 2.3.1(a)), improving of cycling performance (Fig. 2.3.1(b)), enhancement of F1 aerodynamic penetration (Fig. 2.3.1(c)), nuclear reactor detailed study (Fig. 2.3.1(d)) and others. By the way, it is important to highlight that the CFD shall be used a complement to the experimental part because it is not error-proof even if it is more feasible, cheaper, fast and multiple-purpose. Indeed, several entities have been working since a decade on procedures to standardize the estimation and verification of uncertainty in CFD applications [95, 96]which take into account factors as domain discretization, computer

round-off error, physical approximation error and iterative convergence error .

Next, some of the most used CFD software are listed:

- ANSYS CFX [97]
- ANSYS FLUENT [98]
- STAR-CCM+ [99]
- OPEN-FOAM [100]

ANSYS FLUENT has been the software employed along this PhD thesis for CFD study and it is used described in detail hereinafter.

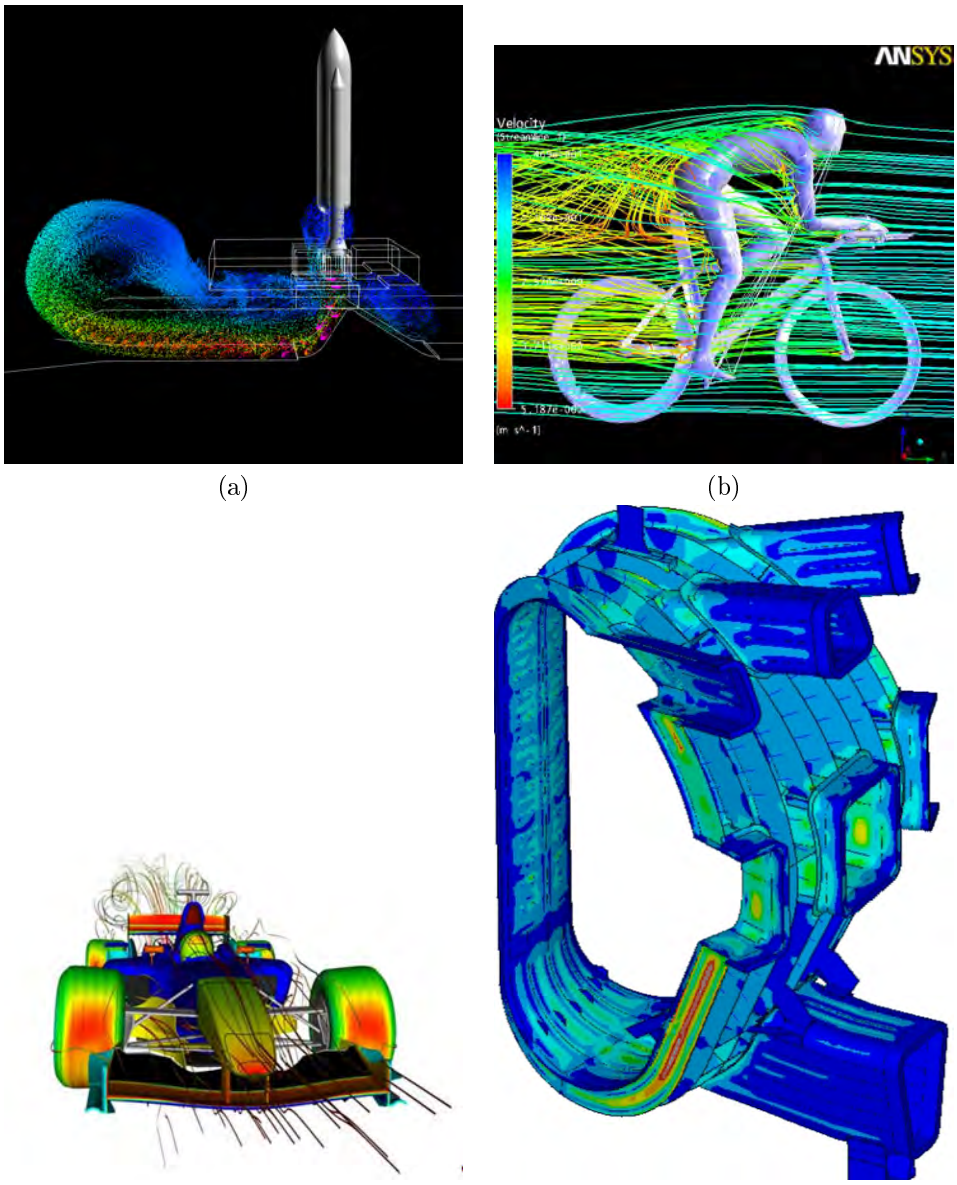

(a) (b)

(c) (d)

Figure 2.3.1: Some CFD applications

2.3.1 Methodology

A suited computational fluid dynamics (or CFD) methodology has been implemented to fulfill both the technical and quality requirement imposed. The consolidated approach, based on the state-of-art technique [98, 95, 101], has

been reported in Fig.2.2.7 and described hereinafter.

Problem identification The first stage consists in the definition of model purposes, the definition of scenario (i.e. steady-state, transient, etc...) and the definition of all the input data (e.g. model version, material type and its properties, HTC, etc ...). Depending on the goals, the level of accuracy requested, the expected overall simulation time, the simplifying assumptions shall be decided. In addition, the CFD software has to be pointed as the appropriate tool for the specific use.

Once the domain of interest has been selected, it is important to check how to isolate it from the complete physical system, hence defining proper boundary conditions (e.g. adiabatic, flux imposed, temperature imposed, etc ...) and their typologies (e.g. symmetrical, periodical or standard). For instance the European DEMO-HCPB example is hereinafter described, Fig.2.3.3. Even if the CFD analysis aims to determine the detailed temperature distribution only inside the blanket, it is important to consider how to interface it with the global Vacuum Vessel Primary Heat Transfer (or VV PHTS) with proper boundary conditions which also depend on the behavior of the specific system. The requirements and the design should be done top-down propagating the conditions step-by-step from generic system to specific ones by means of different software.

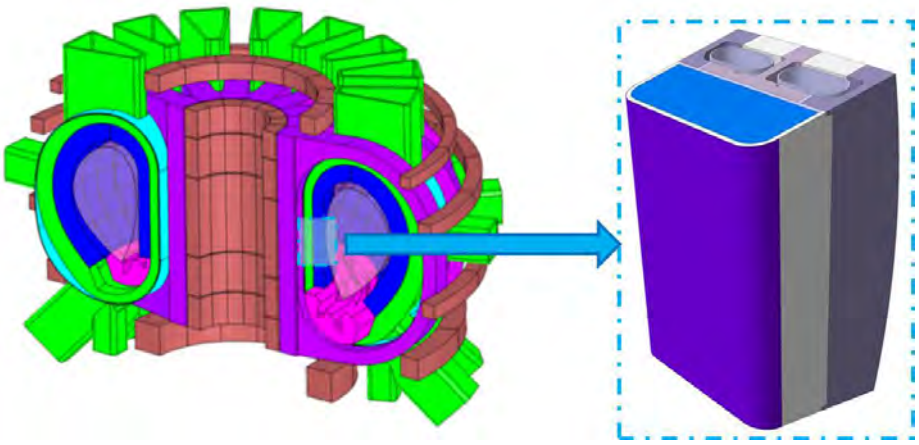

Figure 2.3.3: Domain selection[12]

Pre-Processing Once all the baseline data and hypothesis are fixed, the modeling work can start. Commonly, CAD engineering model contains too much geometry details (e.g., fillets, chamfers, bolts, springs, screw holes and threads), or complex structures which are not important for CFD calculations and significantly increases the model complexity. Indeed, they could prevent the mesh generation or at least slow down the speed of the process. Therefore, the model requires necessary and appropriate simplifications and modification of geome-

try by proper software as SpaceClaim [90] or CATIA [91]. The objective is to remove details which are not important the analysis but preserving as much as possible the coolant paths.

The correct mass of materials shall be preserved or sufficient similar to the original representation: for this reason original-simplified CAD comparison shall be done. Using the simplified and checked geometry, the meshing phase can be started by means of a specific meshing tools, as Pointwise [102] Fig.2.3.4. Within this thesis, the use of automatic meshing has been discarded in favor of manual ones in order to achieve a better control of parameters and mesh regarding the tiny details contained inside first wall components as channels and pipes. By the way, this procedure guaranties better results if applied properly afterwards a considerably path inside the learning curve.

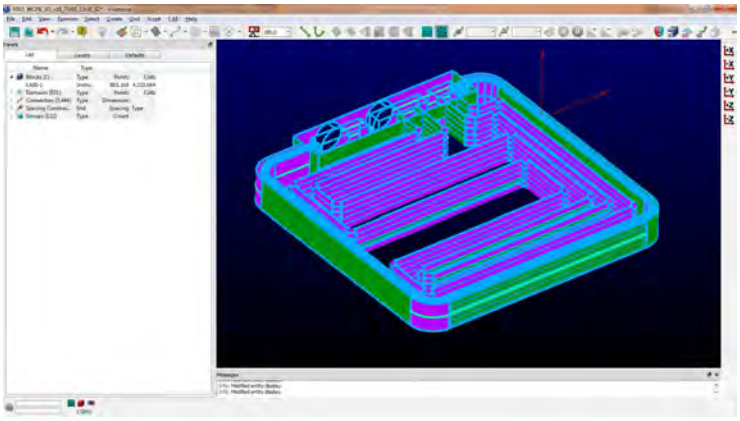

Figure 2.3.4: Meshing and elements

Depending on the mesh resolution required, the gradient expected, the turbulent model, the boundary layer requirements and the computer resources allocated, the mesh type and element are selected, Fig.2.3.5-(b). Indeed, structured or unstructured mesh can be selected or combined (e.g. hybrid mesh), Fig.2.3.5-(a). Knowing that the first one is more suitable when the domain is orthogonal nevertheless not adapted to curved ones. Afterwards, the edges are nodalized, the single face domain meshed hence the control volume obtained. To finalize the meshing phase, mesh parameters (i.e. skewness, smoothness, non-orthogonally, aspect ratio, etc ...) have to be checked to guaranty proper quality features and if not fulling it has to be adjusted accordingly. The polyhedral elements are recommended because they intrinsically fulfill some quality requirements as the skewness and non-orthogonality.

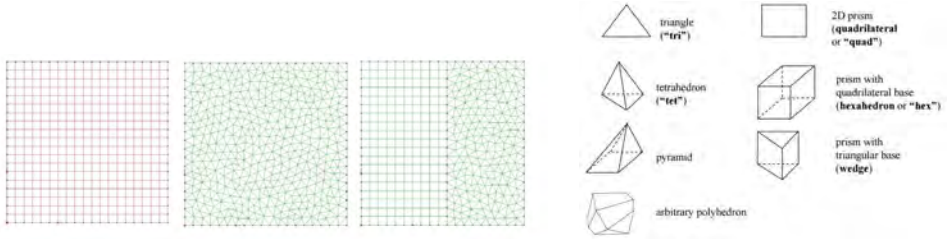

(a) (b)

Figure 2.3.5: Meshing type and elements

At this point, the materials have to be defined and assigned to the corresponded domains using User Defined Function (or UDF) if necessary, the physical models selected (i.e. type of turbulence, mono-phase, etc...), the boundary and initial conditions imposed and the solver controls applied. The NHD, produced by means of radiation transport calculations according to the approach described in Sec.2.2 or by predefined equations, is introduced to the CFD models using specific semi-automatized routines developed and described in Sec.2.3.2 allowing parametric studies or scaling if necessary. At this stage, the model is ready to be solved.

Solve The specific scenario is considered converged, and iteration stopped, only when:

- The changes in solution variables (i.e. temperature distribution) between subsequent iteration are negligible
- The global properties are conserved such as mass and energy balance
- The quantities of interest have reached stable values (e.g. pressure drop, temperature)

It is worth reminding that the solution accuracy depends mainly on the BC and IC, the model applied, the mesh resolution and its independence.

In addition, each final analysis should be complemented by a proper uncertainty evaluation following the V&V standards [95, 103].

Post-Processing At this point the results have to be examined extracting the useful data by means of post-processing tools as Paraview [104, 105]. Again, the model results should be checked and the assumption challenged: typical questions could be "Are the physical models appropriate?" or "Is the mesh adequate and refined enough to catch the detailed response of interest". To conclude, it is suggested to store the information in very structured way defining a proper nomenclature for the cases, input and output.

2.3.2 ANSYS Fluent User Defined Functions

Because of the ANSYS Fluent standard interface cannot be programmed to anticipate all needs, it is possible to interact with the code by a sort of C functions named User Defined Function (or UDF) [98]. This very powerful tool allows, for instance, the customization of boundary conditions and physical models, source terms, reaction rates, material properties and the execution on Demand functions only when requested. Along this thesis, several UDFs have been developed in order to mapping and applying the NHD to the CFD models and to introduce the physical properties (e.g. thermal conductivity, density, specific heat) in function of the temperature for each specific material. The application of UDF requires either the compilation or interpretation within the specific model; within this thesis we decided to go the compiled one to have a more efficient function and shared libraries which can be used by different simulations.

Detailed description of the developed UDF, how to compiled an UDF and how to use an UDF is described in the next sections.

How to compile an UDF? The following steps shall be executed to properly compile the UDF by means of the ANSYS Fluent interface[3], Fig.2.3.6(a)-(b):

1. Go to *DEFINE* $\Rightarrow$ *USER Define* $\Rightarrow$ *Functions* $\Rightarrow$ *Compiled*
2. Browse and select "UDF_Filename.c" source file to compile $\Rightarrow$ *Add*
3. Type a proper UDF *Library Name*
4. Press *Build*
5. *Load* the compiled UDF

[3]Otherwise, the UDF could be also externally compiled using the command *nmake* in a MS Windows SDK 7.1 x64 creating a directory "3ddp" ANSYS Fluent case folder.

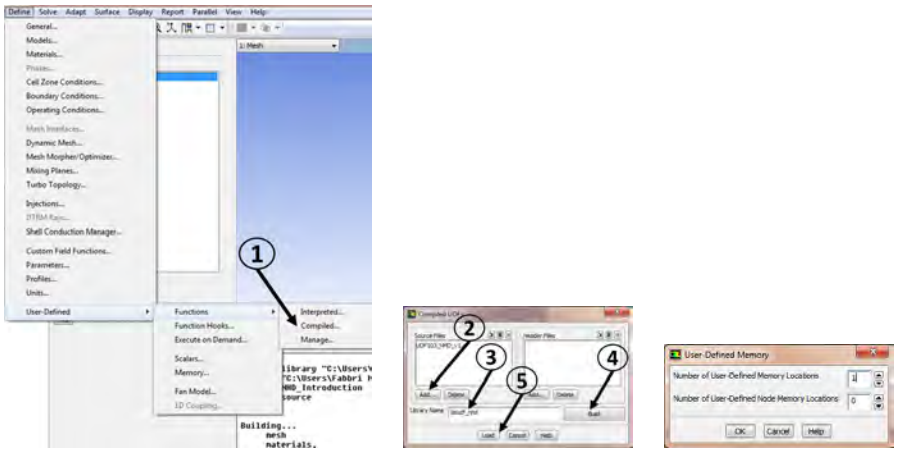

(a) (b) (c)

Figure 2.3.6: UDF and UDM

How to use an UDF? Before applying any UDF developed, you need to allocate the proper number of memory location(s) for each cell and/or node element contained in your model. This reserved space is named User-Defined Memory (or UDM) and it can be imposed though the control menu going to *DEFINE* $\Rightarrow$ *USER Define* $\Rightarrow$ *Memory* (Fig.2.3.6-(c)). Then, once the UDM is initialized and selected in the interested *Cell ZoneID*[4], the UDF can be run: depending on the typology of the macro it can be Executed on Demand, as for the NHD one, or loaded as for the material features. To conclude, the usage of in-line text comments during the UDF running is strongly recommended to judge the proper working of the routines as well as the post-processing of the UDM.

How to check an UDF outcomes? Although the UDF have been largely tested and validated for the whole set of options, it is recommended to double check the produced outcomes. Internal evaluation and external ones can be combined or alternated, they mainly consists:

- *Internal checks:* they are done internally by means of the CFD program interface. For instance, minimum, maximum and average value of the filled UDM (e.g. NHD) can be determined using the *Reports* utility in a short-notice. In addition, the visual inspection can be carried out in a quite tedious way and not efficiently in particular for huge models.

- *External checks*: they are performed using external software once the model and related results have been exported in a native or neutral format. As for the internal options, minimum, maximum and average value of the

[4]The ANSYS Fluent mesh could be divided in multiple zones internally named *Cell ZoneID* in order to distinguish different materials, properties or for other solutions needs.

filled UDM (e.g. NHD) can be determined as well of the other filed (e.g. materials, conductivity, specific heat). Furthermore, the visual inspection is very efficient and many options can be applied as computation of gradients, contour plots, equation along lines, slices, clips. This approach is suggested for heavy model or very detailed post-processing.

2.3.2.1 UDF@Physical Material Property

Following the ANSYS Fluent manual instruction [98], a dedicated UDFs has been set up in order to introduce for each specific material present in the model the physical properties as the thermal conductivity, the density, and the specific heat in function of the temperature. The material features can be specified by means of piece-wise functions, predefined intervals or interpolate between points. In this way, during the solving process and after each iteration until reaching convergence, the code automatically updates the properties basing upon the cell material and temperature.

2.3.2.2 UDF@Nuclear Heat Density Introduction

The Nuclear Heating Density is a fundamental parameter in the determination of the temperature field as results of CFD calculations. It is historically a bottleneck inside the CFD methodology because the ANSYS Fluent code is quite poor of suitable tools. For this reason, a flexible and robust *Execute on Demand* UDF has been developed to import in semi-automatized way the NHD avoiding unnecessary mistakes and saving time. In-line comments are generated automatically by UDF to check the proper functioning of the macro. Thus, it is composed by three main parts which correspond to different ways to implement the different NHD formats in the CFD model covering all the specific needs:

1. Equation mode: it allows introducing the NHD using a predefined equations

2. Discrete intervals mode: it allows introducing the NHD using spatial discrete intervals

3. Mapping mode: it allows interpolating a generic 3D VTK mesh into a 2D or 3D CFD mesh selecting if necessary a specific *Cell ZoneID*

The mapping type and related options are provided by means of an external text file, named *IN_NHD.txt*, which is loaded during UDF execution and depending upon the methodology used the data has to be structured in slightly different way. Moreover, a log file, named *OUT_NHD.txt*, containing a list of the cell with the NHD introduced, is generated just before the UDF conclusion as well as in-line comments in the ANSYS Fluent command window to probe the proper macro functioning.

One of the main advantages of the approach implemented is the possibility to selected the most suited technique for each Zone_ID without interfere with the

others as well the capability apply sequentially the routine to different material, revisiting it if necessary.

A complete descriptions of the three approaches is given in the following sections.

Option No.1: Equation mode The *equation mode* allows inserting the NHD in function of the plasma distance using a generic six order equation as in Equ.2.3.1, in which the NHD is assumed in function of the X coordinate of the cell centroid.

$$NHD(x) = a_1 * X^6 + a_2 * X^5 + a_3 * X^4 + a_4 * X^3 + a_5 * X^2 + a_6 * X + a_7 \quad (2.3.1)$$

For each specific zone_ID, a equation has to be specified; there are not any limitation in the No. of zone_ID to be filled in the same run. More complex equations, also bi-dimensional, could be easily implemented modifying the UDF@NHD; by the way, for the PhD proposal, this complexity fulfills all the needs.

The *IN_NHD.txt* shall be formatted as follow when the *equation mode* is selected, Fig.2.3.7:

- [1] UDF Option which in this case is 1
- [2] Total number of ANSYS Zone_ID to fill
- [3] ANSYS Zone_ID to fill (No. 2)
- [4] Equation parameters from $a_1$to a_7 to use within Zone_ID No.2
- [5] ANSYS Zone_ID to fill (No. 5) [5]
- [6] Equation parameters from $a_1$to a_7 to use within Zone_ID No.5

[5]Step [3] and [4] are repeated for all the ANSYS Zone_ID to fill, as for the case of [5] and [6]

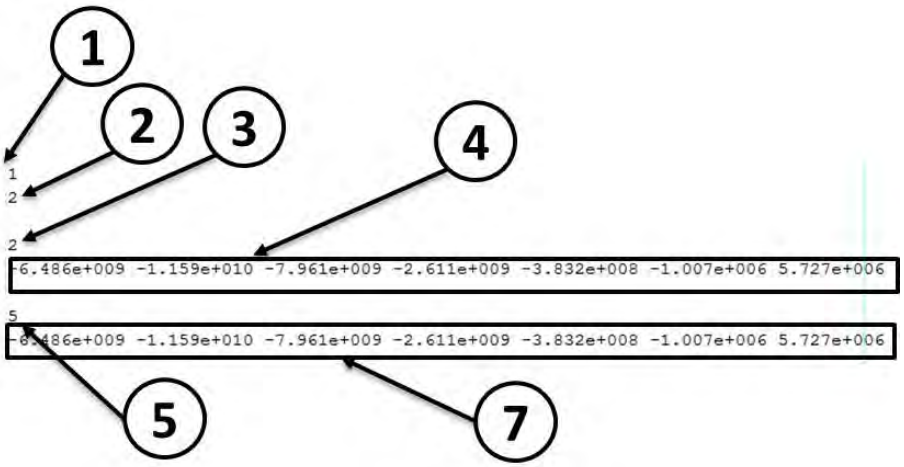

Figure 2.3.7: UDF@Equation mode

For instance, the *equation mode* approach has been tested to the 2D European HCPB DEMO model version. The mesh has been generated by means of Pointwise, Fig.2.3.8-(a), and it is composed by several Zone_ID, distinguishable by different colors in Fig.2.3.8-(b). In this was, distinct materials can be applied as well as various mapping techniques used. The NHD equation implemented, $NHD(x) = 10^4x^6 + 10^5x^2 + 5 * 10^6x + 4 * 10^6$, has been plotted in Fig.2.3.8-(d) and applied only to the internal breeding zone, Fig.2.3.8-(c).

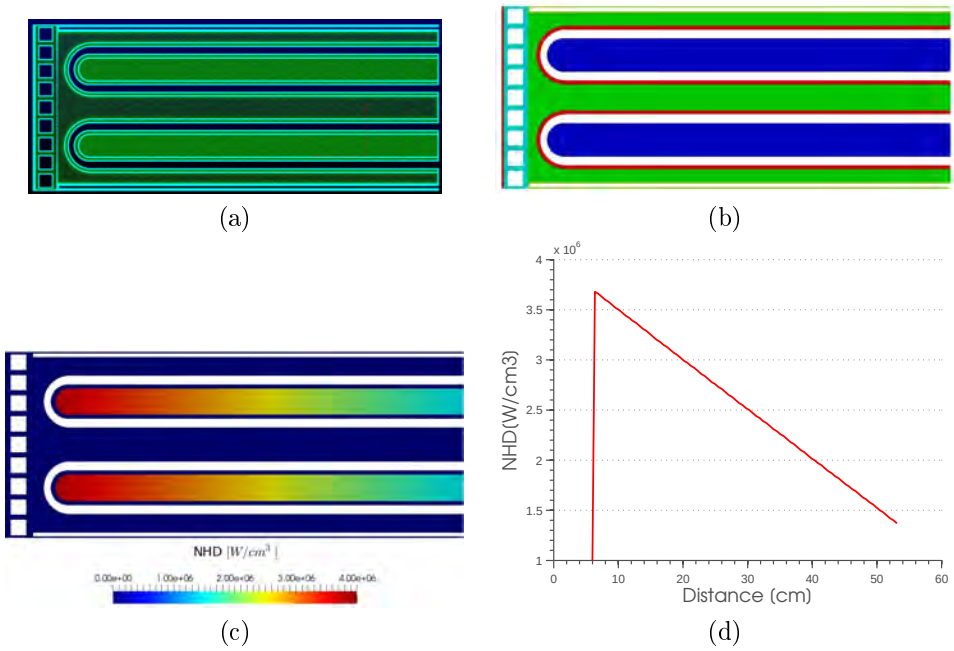

Figure 2.3.8: Discretized mode example

Option No.2: Discrete interval mode The *discrete interval mode* allows implementing the NHD using a stair distribution, so a bin discretization using as reference the cell centroids, along one direction. There are neither limitation in the No. of zone_ID to be filled in the same run nor in the No. of interval. In addition, a scaling factor, different from one (1), could be introduced for each material to perform sensibility studied.

The *IN_NHD.txt* shall be formatted as follow when the *discrete interval mode* is used, Fig.2.3.9:

- [1] UDF Option which in this case is 2
- [2] Total number of ANSYS Zone_ID to fill
- [3] Vector containing the ANSYS Zone_ID to fill
- [4] Vector containing the NHD scaling factor for each ANSYS Zone_ID to fill (i.e. if 1 the input are not modified)
- [5] Total number of bins defining the NHD
- [6] Vector containing the upper bound coordinate of the bins$[m]$
- [7] Vector containing the NHD $[W/cm^3]$ of the bins

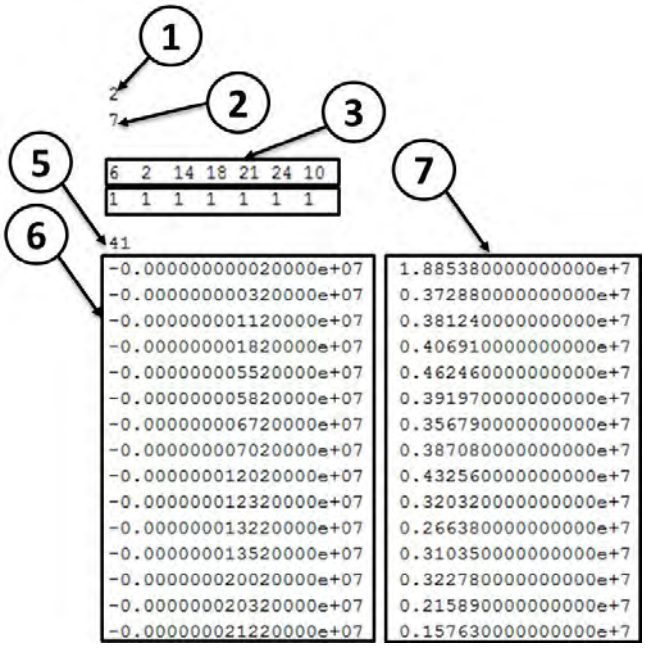

Figure 2.3.9: UDF@Discrete interval mode

To give a clear example, the *discrete interval mode* approach was applied to the 2D European HCPB DEMO model version for a preliminary thermal-hydraulic assessment to support an debugging stage of AINA-DEMO which was presented in an EUROfusion progress meeting [106]. A NHD stairs distribution, Fig.2.3.10-(b), was applied to the whole 2D model, obtaining the NHD field of Fig.2.3.10-(a).

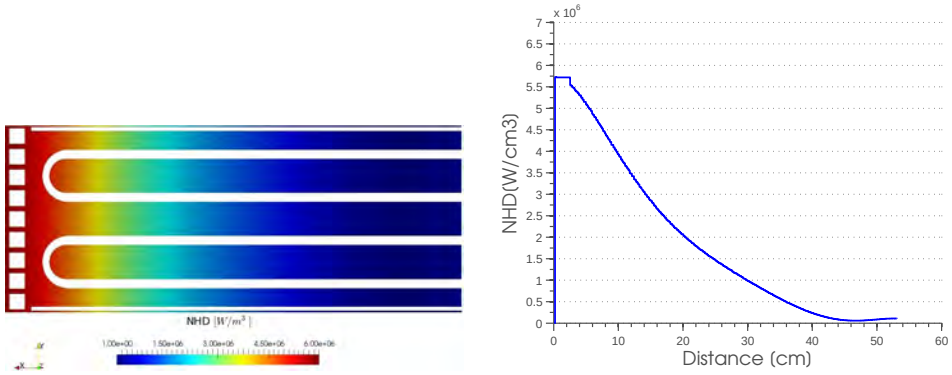

(c) (d)

Figure 2.3.10: Discretized mode example

Option No.3:Mapping mode The *mapping mode* allows implementing the NHD by the interpolation of a VTK scalar structured format into the 2D/3D ANSYS Fluent mesh one using a in-house developed technique. Only a subset of the domain can be selected giving the possibility to combine this option with No.1 and 2 in sub sequential runs. As well as for the previous option the data can be scaled using a correction factor, which has to be specified for each zone_ID. In case of the usage of a 2D mesh a VTK Z plane has to be chosen.

The *IN_NHD.txt* shall be formatted as follow when the *mapping mode* is used, Fig.2.3.11:

- [1] UDF Option which in this case is 3
- [2] Type of target mesh: 2 for 2D, 3 for 3D one
- [3] Total number of ANSYS Zone_ID to fill
- [4] Vector containing the ANSYS Zone_ID to fill
- [5] Vector containing the NHD scaling factor for each ANSYS Zone_ID to fill (i.e. if 1 the input are not modified)
- [6] Domain boundary of the VTK to map [m]: $X_{min}X_{max}Y_{min}Y_{max}Z_{min}Z_{max}$
- [7] Voxel dimension of VTK to map [m]: $\triangle X \triangle Y \triangle Z$
- [8] Z plane to use for the interpolation[6]
- [9] Column vector containing the voxel NHD $[W/cm^3]$ ordered as $X_- \Longrightarrow X_+/Y_- \Longrightarrow Y_+/Z_- \Longrightarrow Z_+$

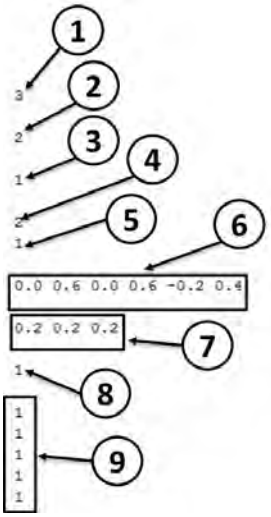

Figure 2.3.11: UDF@Mapping mode

[6]This parameter is inserted only if the target mesh is 2D.

The UDF routines works for each cell contained in the target ANSYS Fluent mesh performs the following steps:

1. It evaluates if the mesh cell centroid coordinates are contained inside the volume boundary defined in the *"IN_NHD"* file, yellow point in Fig.2.3.12. .

2. If the Point No.1 if fulfilled, the distance of the VTK cell centroid to the volume boundaries is computed as No. of VTK cells ($parameters\ x, y, z$) otherwise to code move to Point No.1 analyzing the next cell.

3. At this point, the macro knows the correspondence between the ANSYS Fluent mesh and the VTK ones hence its relative position which may overlap different voxels ($parameters\ xx, yy, zz$). Then, the routine defines the distribution of the NHD ($parameters\ q_{000}, q_{100}, q_{010}, q_{110}$, $q_{001}, q_{101}, q_{011}, q_{111}$)according to the relative volume disposals along all directions ($parameters\ v_{000}, v_{100}, v_{010}, v_{110}, v_{001}, v_{101}, v_{011}, v_{111,}$), Fig.2.3.12.

4. If negative NHD are generated by Point No.3, the whole set of parameter computed for the specific cell are printed in the ANSYS Fluent console for a proper preliminary visual comparison otherwise the mesh cell coordinates and the applied NHD are written in a new line of the *"OUT_NHD"* file for V&V proposal.

5. To conclude a final check about the relative volume disposals along all directions ($parameters\ v_{000}, v_{100}, v_{010}, v_{110}, v_{001}, v_{101}, v_{011}, v_{111}$) is done. If the sum of the contribution is bigger than an imposed tolerance, which normal could be imposed as fraction of the VTK voxel volume, a message is printed automatically in ANSYS Fluent console to warn about a possible error.

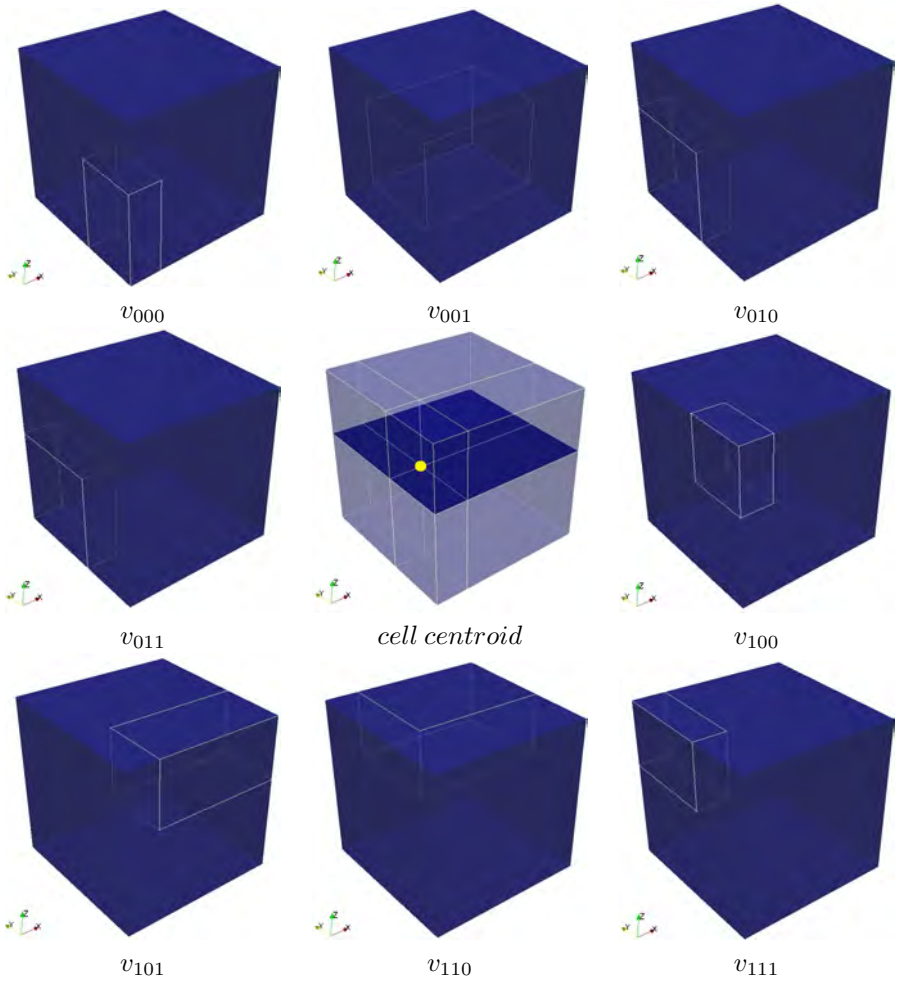

Figure 2.3.12: Mapping mode@volume contributions

In addition, the *mapping mode* approach has been largely tested, therefore an example of those is reported hereinafter. A VTK rectangular cube mesh (0.6 m side, 27 cells with a value of 10) which is not completely overlap to an unstructured one (1 m side, 192392 cells with a value of 0), Fig.2.3.13-(a) is assumed. Thanks to the developed UDF, the values of the first cubes are mapped into the second, preserving the NHD maximum and the integral within the 1% of error. In Fig.2.3.13 several slides highlights how the interpolation is applied only to a subset of the domain, within of the given boundaries.

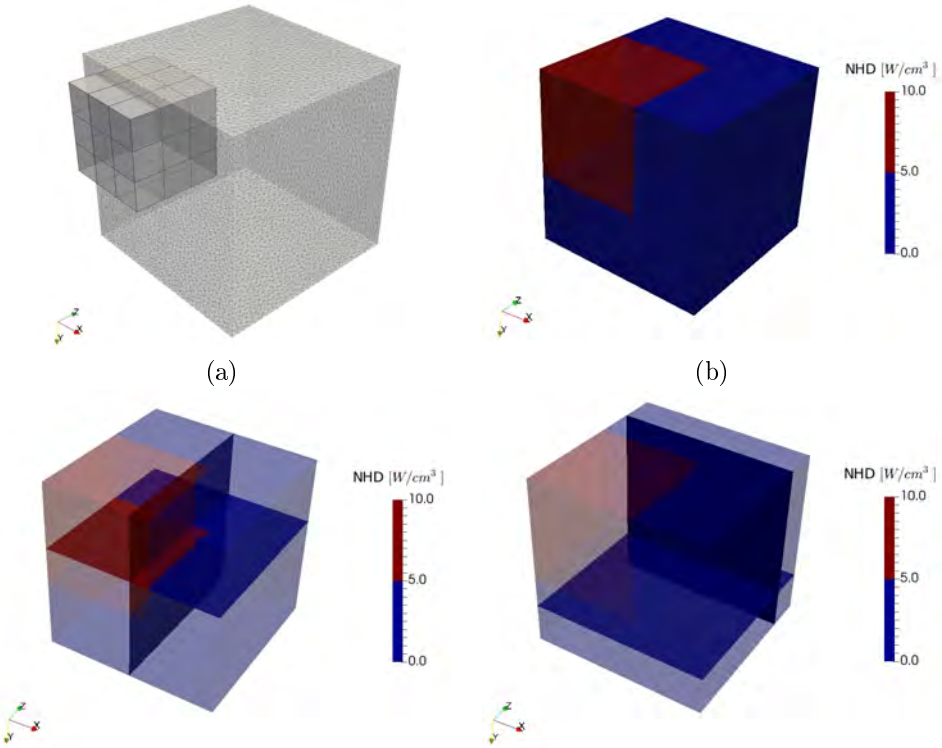

Figure 2.3.13: Mapping mode example

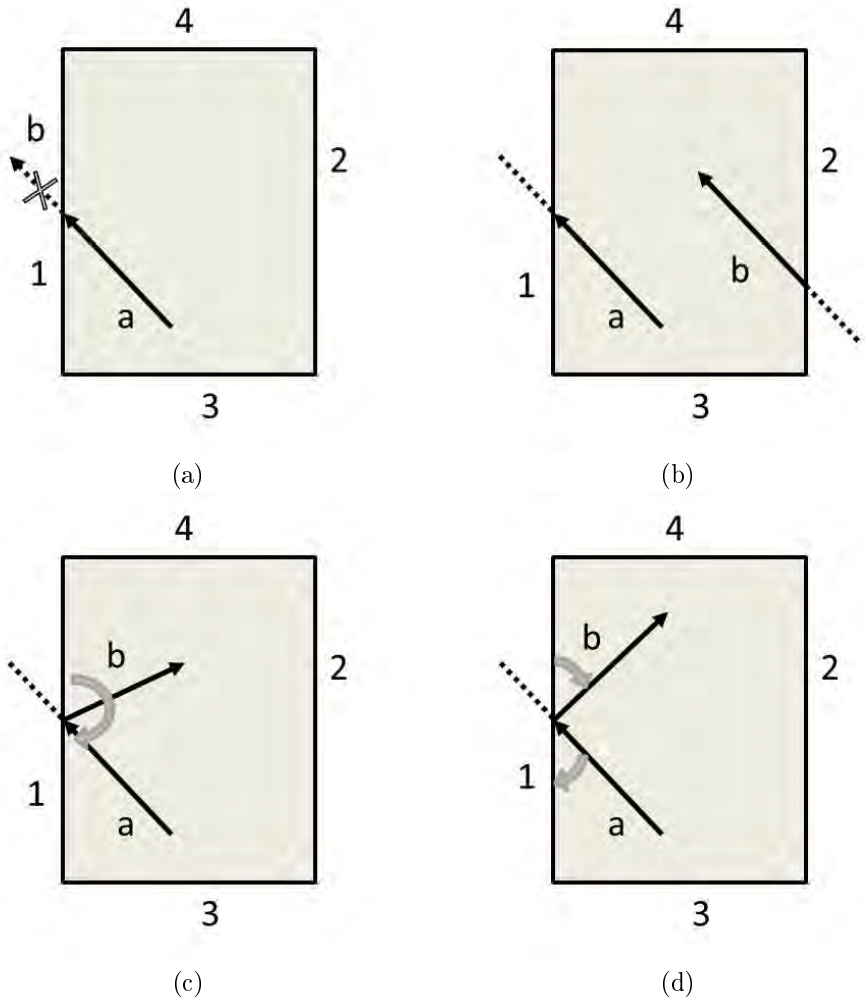

Figure 2.2.3: MCNP Boundary Conditions

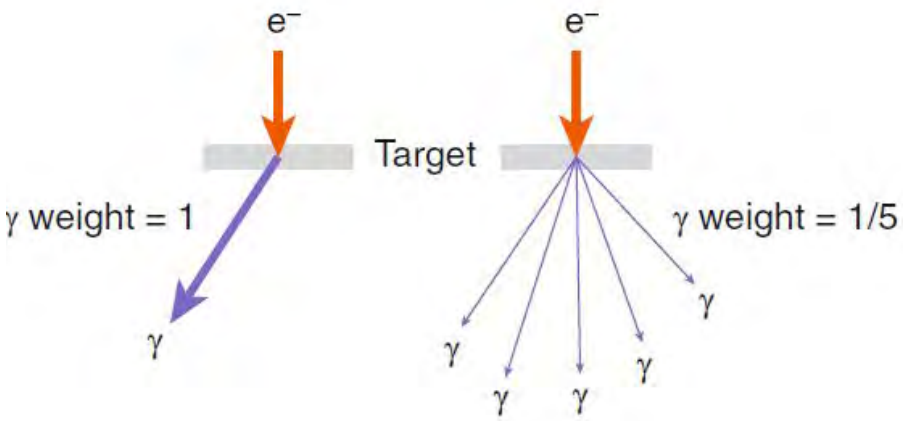

Figure 2.2.5: Particle splitting

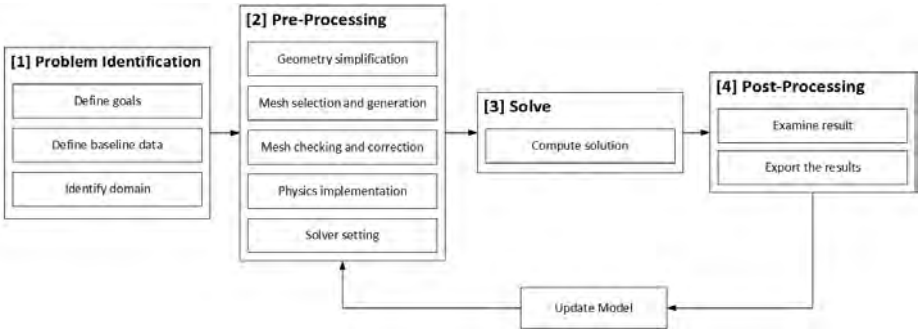

Figure 2.3.2: Computational fluid dynamics methodology

Chapter 3

Thermal-hydraulic routines

The magnetic nuclear fusion reactors, as ITER, are very complex and composed by numerous systems which contributes to the machine operation, maintenance and decommissioning[107]. The breeding blanket is one of the most challenging and innovative components: it is composed by thousands of internals which face huge magnetic field, mechanical stresses, high temperature and radiation damages caused by the knocking of 14.1 MeV DT neutrons and the production of secondary gamma. The several cooling loops present maintain the temperature within reasonable regimes and extract the tritium produced. The determination of 3D detailed temperature distribution by means of analytic method is not feasible thus it requires the application of the usage of the numerical tools as CFD ones (e.g. ANSYS FLUENT©[98]) which are very computational demanding (both time and memory, 200 GB of RAM for two week and 200 cpu[101]) and require the use of super-computer [58]. In addition, considering the large time required for the model preparation and its poor flexibility, its usage in the AINA software is not the best option. For these reasons a series of flexible thermal-hydraulics routines, based on the finite different technique[1], have been developed in order to obtain reliable, approximate but conservative thermal-wall results in a short-notice using a standard workstation. It is worth highlighting that these routines do no aim to substitute the 3D CFD studies whereas to take advantage of their outcomes and characterized the system behavior in a simplified way.

The routines, hereinafter described, are composed by a master program and several branches which are intrinsically controlled by the selection done by the user.

The program allows an easily tuning the following parameters hence to implement to any blanket types or geometries:

- Model dimension: 1D or 2D
- Type of solution: Steady-state or transient

[1]The thermal-hydraulics routines have been developed in MATLAB language but they can be easily converted in further programming languages.

- Material identification and thickness: definition of the spatial domain discretization and the correspondent material type
- Nodal discretization: definition the number of nodes for each material layer linearly or in following a Gaussian distribution
- Nuclear Heating: definition of the NHD in form of vector, equation or material type.
- Boundary conditions: all the types of BC can be imposed (e.g. adiabatic, imposed flux, imposed temperature)
- Implementation of cooling channels (please ref to Sec.3.3.1.1 for more information).
- Cooling channels parameter (e.g. mass flow rate, heat transfer coefficient and bulk temperature of the coolant)
- Convergence criteria which could be an imposed node temperature difference iteration i and i+1 (e.g. 0.1 K) and the maximum number of the iteration allowed
- Definitions of the transient typology and its characteristics such as type (overfuelling or LOCA), time (interval evolution and total) and combination of them

The routines determine the heat equation solution using the 1D/2D finite difference solution. The detailed mathematical treatment is reported in sec. 3.3 whereas the steady-state or transient routine approach in section 3.1and 3.2. As output a text file report containing the minimum, the maximum and the each node location is provided as well as a VTK file [108]including the NHD, the material node identifier, temperature and the thermal properties using a point mesh or a structure one depending on the user needs. In this way, a proper comparison of data with any external CFD or analytical tool can be carried out using for example Paraview software[104, 105], which is a the very versatile and flexible open tool created by INL and LANL.

Along this thesis, two main DEMO blanket designs have been studied using this routines and validated against the ANSYS FLUENT© commercial tool: the Japanese DEMO Water Cooled Pebble Bed (or WCPB) (section 4) and the European DEMO Helium Cooled Pebble Bed (or HCPB) (section 5).

The routines has been successfully implemented in the AINA-DEMO 4.0 code[7].

3.1 Steady-steady approach

The steady-state approach employed by the thermal-hydraulic routine is reported in Figure 3.1.1 and hereinafter described.

The steady-state solver requires three main inputs:

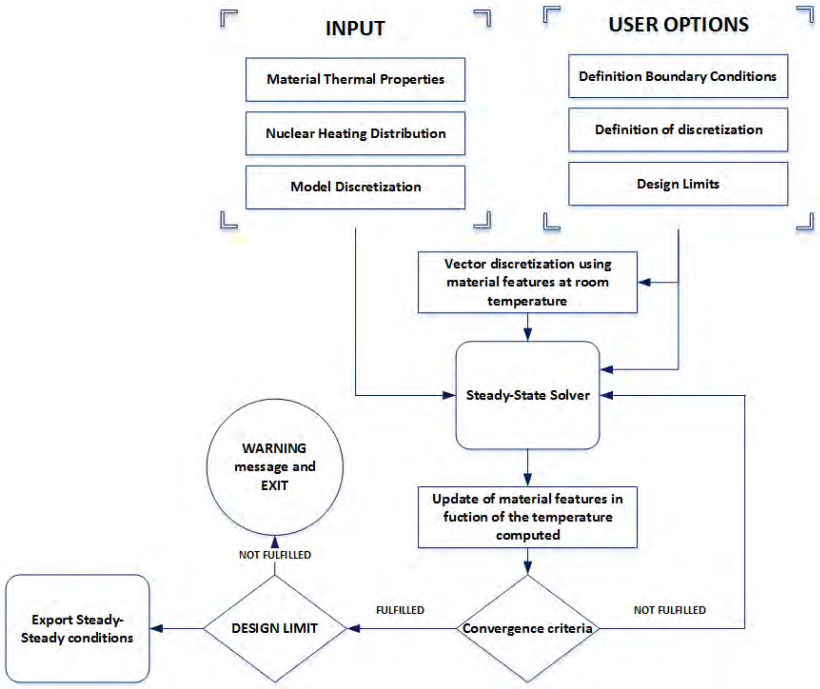

Figure 3.1.1: Steady-state solver approach

1. The input: material thermal properties, the nuclear heating distributions and the model discretization
2. The simulation options : the boundary condition definition, the nodalization of each material layer and the design limits
3. Material domain discretization (e.g. definition of area associated to a specific material or a cooling channel)

Firstly, the model domain is discretized in nodes to which depending on the position the NHD and the material properties at room temperature are assigned. Secondly, the SS solver computes a tentative solution (e.g. temperature distribution) which allows the update of the material thermal properties. Until the convergence criteria, imposed previously by the user , is not fulfilled the solver continues iterating updating the blanket properties or the maximum number of iteration is achieved.

Once the criteria is passed, the design limits are checked: if they are met, the program will end normally exporting the steady-state model solution, if not it will warn the user using a pop-up disclaimer indicating the also the affected materials. An example of this message is reported in Figure 3.1.2.

Figure 3.1.2: Example of warning message for not accomplished design limits

3.2 Transient approach

The transient approach employed by the thermal-hydraulic routine is reported in Figure 3.2.1 and hereinafter described.

The transient solver requires two main inputs:

1. The simulation options: the definition of the transient type, the time intervals, the transient total duration and the design limits
2. The input: material thermal properties, the updated of the NHD/coolant conditions based on the perturbation imposed and the state-state solution computed as reported in section 3.1

Firstly the solver computes a tentative transient solution (e.g. temperature distribution) using as initial condition the SS solution computed previously according to sec.3.1. Then the material thermal properties are updated. Until the convergence criteria is not fulfilled the solver continues iterating updating the blanket properties or the maximum number of iteration is achieved.

Once the convergence criteria is passed, the design limits are checked: if they are met, the program will continue normally, if not it will warn the user using a pop-up disclaimer indicating the also the affected materials as reported in Figure 3.1.2. Later the routine checks the transient time and exports the solution: if the t_i is within the time interval defined by the user, the solution at t_i is imposed as initial condition for the solution at t_{i+1}entering again in the transient loop solution whereas if it is not the program stops.

3.3 Finite difference methodology

In general terms, the temperature distribution of a fusion blanket module is very articulated and it cannot be fully represented by simplified model.

Concerning safety analysis, approximated models should be representative of the most relevant and conservative conditions. Besides the correct mathematical treatment of the heat transfer equation and assumptions, it could happen that the temperature distribution obtained is not conservative if compared with the 3D detailed one. In this case, a scaling function shall be applied to the resulting distribution to achieve at least the same conditions found in the detailed studies as done in (Sec.4). Moreover, the analysis should have associated its error estimation and stability analysis (Sec.3.5).

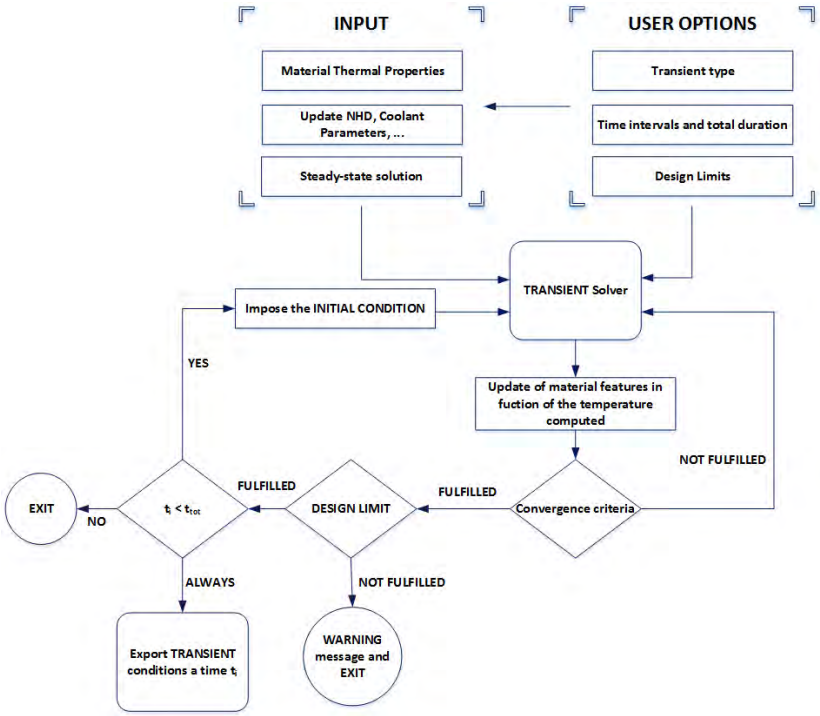

Figure 3.2.1: Transient solver approach

The generation of a simplified model is a sort of iteration process where the several options should be tested until reaching the configuration which best fits the needs. In addition, the selection of the 1D or 2D solution is not normally clear a priori but it depends on several factors which have to be taken into account:

- The computational resources: the 1D solution is several times less demanding that the 2D one thanks to the limited matrix dimensions
- The possibility to approximate the system in a simplified way both in steady-state and in transient response
- The presence of cooling channels and its disposal
- The spatial distribution of the NHD
- The accuracy of the solution

Both the 1D and the 2D solution have been obtained starting from the 3D heat transfer equation at a point $\vec{r}$[13]:

$$\rho(T,\vec{r})c(T,\vec{r})\frac{\delta T(\vec{r,t})}{\delta t} - \nabla(k_T(T,\vec{r})\nabla T) = +\ddot{q}(\vec{r},t) \tag{3.3.1}$$

where ρ is the material density , c the heat capacity, k_T the thermal conductivity and $\ddot{q}$ the volumetric nuclear heat deposition. The problem is solved in a matrix form:

$$A * T = b \tag{3.3.2}$$

where A is the temperature coefficient matrix, T the temperature vector and b the known vector, hence obtaining T as:

$$T = A^{-1}b \tag{3.3.3}$$

To conclude, please consider that historically in AINA Safety code the water explicit flow has been never modeled whereas the HTC is externally computed, analytical or numerically using a CFD code, hence implemented. Along this line, it has not been a priority of the author to develop this feature because it is considered as secondary and not really useful and coherent with the software usage.

3.3.1 1D Solution

The simplification from 3D model to 1D one is done considering each region as a cuboid, where the only conducting surfaces are the one facing the plasma and the opposite, so the rest can be seen (at least by symmetry considerations) as adiabatic. The different materials in each module are arranged in layers parallel and discretized.

A 1D parabolic, non-linear and in-homogeneous partial differential equation derived from Equ.3.3.1 is used

$$\rho(T,x)c(T,x)\frac{\delta T(x)}{\delta t} = \frac{\delta}{\delta x}\left(k_T(T,x)\frac{\delta T}{\delta x}\right) + \dddot{q}(x,t) \tag{3.3.4}$$

where ρ is the material density, c the heat capacity, k_T the thermal conductivity and $\dddot{q}$ the volumetric nuclear heat deposition.

Applying to Equ.3.3.4 a implicit first order discretization and a forward methodology and at the same time considering the ρ, c and q_V variables only dependent on x, we obtain for a generic internal node$i$ [2]:

$$\begin{aligned}\frac{\rho_i c_i}{\Delta t}(T_i^{n+1} - T_i^n) = &\frac{k_i - k_{i-1}}{\Delta x_i}\,\frac{T_i^{n+1} - T_{i-1}^{n+1}}{\Delta x_i} \\ &+ k_i\,\frac{T_{i+1}^{n+1} - 2T_i^{n+1} + T_{i-1}^{n+1}}{\Delta x_i^2} + \dddot{q}_i\end{aligned} \tag{3.3.5}$$

Diving Equ. 3.3.5 both side by$\gamma = \frac{\rho_i c_i}{\Delta t}$:

$$\begin{aligned}T_i^n + \frac{\dddot{q}_i \Delta x_i}{\gamma} = &-T_{i+1}^{n+1}\left(\frac{k_i}{\Delta x_i^2\gamma}\right) \\ &- T_i^{n+1}\left(\frac{k_i - k_{i-1}}{\Delta x_i^2\gamma} - \frac{2k_i}{\Delta x_i^2\gamma} - 1\right) \\ &- T_{i-1}^{n+1}\left(-\frac{k_i - k_{i-1}}{\Delta x_i^2\gamma} + \frac{k_i}{\Delta x_i^2\gamma}\right)\end{aligned} \tag{3.3.6}$$

obtaining

$$T_i^n + \frac{\dddot{q}\,\Delta x_i}{\gamma} = T_{i+1}^{n+1}\,\alpha_0 + T_i^{n+1}\,\alpha_1 + T_{i-1}^{n+1}\,\alpha_2 \tag{3.3.7}$$

where $\alpha_0 = -\frac{k_i}{\Delta x_i^2\gamma}$, $\alpha_1 = \frac{k_i + k_{i-1}}{\Delta x_i^2\gamma} + 1$ and $\alpha_2 = -\frac{k_{i-1}}{\Delta x_i^2\gamma}$.

At this point the boundary conditions shall be applied. Depending on the BC type we can distinguish four different types:

1. Temperature imposed $T(0,t) = T_o$
2. Flux imposed $-k_T(T,x)\frac{\delta T}{\delta x} = \ddot{q}$
3. Adiabatic $k_T(T,x)\frac{\delta T}{\delta x} = 0$
4. Convention $-k_T(T,x)\ \frac{\delta T}{\delta x}\big|_{X=0} = h(T(x) - T_\infty)$

Independently from the BC applied in the solution, the matrix A (see Equ.3.3.8 and Equ.3.3.3) is tridiagonal with m rows which are the total number of nodes

[2] For sake of simplicity in the following equation the dependence of $k = k(T)$, $\rho = \rho(T)$ and $c = c(T)$ have been omitted.

1. Constant surface temperature

$$T(0, t) = T_s \qquad (2.29)$$

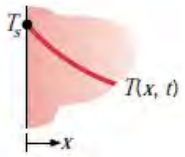

2. Constant surface heat flux

(a) Finite heat flux

$$-k\frac{\partial T}{\partial x}\Big|_{x=0} = q_s'' \qquad (2.30)$$

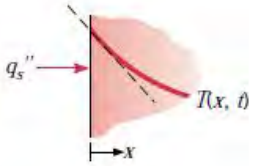

(b) Adiabatic or insulated surface

$$\frac{\partial T}{\partial x}\Big|_{x=0} = 0 \qquad (2.31)$$

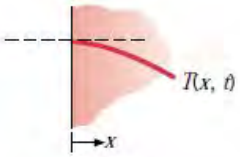

3. Convection surface condition

$$-k\frac{\partial T}{\partial x}\Big|_{x=0} = h[T_\infty - T(0, t)] \qquad (2.32)$$

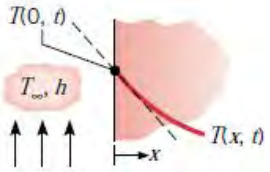

Figure 3.3.1: Boundary conditions for the heat diffusion equation at the surface (x=0) [13]

present in the model so the solution points. The boundary conditions are applied modifying the terms $(\alpha_{0\rfloor_{BC}}, \alpha_{1\rfloor_{BC}}, \alpha_{2\rfloor_{BC}})$ placed in the matrix first and last row.

$$\begin{bmatrix} \alpha_{1\rfloor_{BC}} & \alpha_{0\rfloor_{BC}} & 0 & 0 & 0 \\ \alpha_2 & \alpha_1 & \alpha_0 & 0 & 0 \\ 0 & \alpha_2 & \alpha_1 & \alpha_0 & 0 \\ \dots & \dots & \dots & \dots & \dots \\ 0 & 0 & \alpha_2 & \alpha_1 & \alpha_0 \\ 0 & 0 & 0 & \alpha_{2\rfloor_{BC}} & \alpha_{1\rfloor_{BC}} \end{bmatrix} \begin{bmatrix} T_1^{n+1} \\ T_2^{n+1} \\ T_3^{n+1} \\ \dots \\ T_{n-1}^{n+1} \\ T_n^{n+1} \end{bmatrix} = \begin{bmatrix} T_1^n \\ T_2^n \\ T_3^n \\ \dots \\ T_{n-1}^n \\ T_n^n \end{bmatrix} + \begin{bmatrix} \frac{\ddot{q}_1 \Delta x_1}{\gamma_1} \\ \frac{\ddot{q}_2 \Delta x_2}{\gamma_2} \\ \frac{\ddot{q}_3 \Delta x_3}{\gamma_3} \\ \dots \\ \frac{\ddot{q}_{n-1} \Delta x_{n-1}}{\gamma_{n-1}} \\ \frac{\ddot{q}_n \Delta x_n}{\gamma_n} \end{bmatrix} \tag{3.3.8}$$

To conclude, starting from the mathematical approach described and imposing the time derivative to zero the steady-state formulation can be easily obtained.

3.3.1.1 Coolant channel treatment

The coolant channel numerical treatment is a key point in the approximate solution and a distinguishing feature of the AINA Safety Code. For instance please consider the blanket example reported in Fig.3.3.2 the model is composed by FW layer facing the plasma then followed by a main body which respectively contain the FW channels (i.e. square light blue channel) and internal ones (i.e. rectangular grey channel).

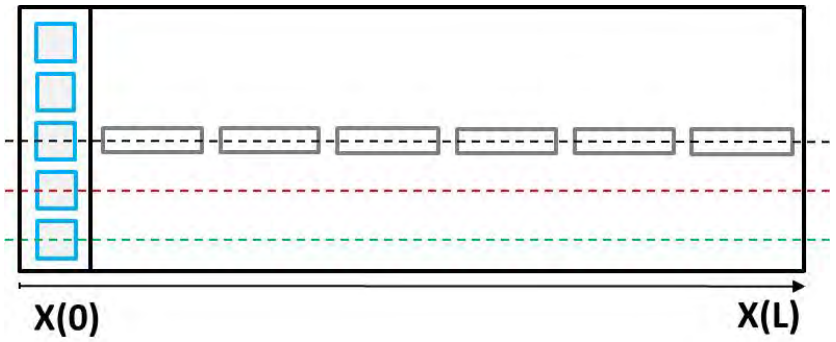

Figure 3.3.2: Coolant channel treatment

The coolants channel depending on its structure and the modelling position selected (e.g. in Fig.3.3.2 black, red or greed dotted ones) can be treated as:

- Type A: Unique-node layers at different depths parallel the first wall if along the 1D discretization. They are considered as planar and occupy-

ing only one node[3]. In this way, heat transfer can be modeled strictly from a one-dimensional approach, by weighting the conductive and convective contributions to heat transfer with a surface coefficient, using the f_{COOL}factor which is equal to the relative surface of the coolant tubes to the total surface of the module section:

$$f_{COOL,j} = \frac{Surface_{COOLED}}{Surface_{TOT}} \tag{3.3.9}$$

Coming back to the example reported in Fig.3.3.2, the main body channels can be assumed as Type A only for black modelling direction whereas FW ones in all the cases.

- Type B: Negative weighted convective flux if not along 1D discretization as in Fig.3.3.2 for main body channels along red and green lines. This effect is not limited to a single node but to the entire area affected by the convection. To take into consideration the detrimental response in function of the radial distance from the coolant and from poloidal distance from the 1D discretization line, $f_{WGT,R}$ and $f_{WGT,P}$are employed, resulting the convective heat flux for a generic tube k at the position x

$$q_{Type,B,k}(x) = f_{WGT,R,i}\, f_{WGT,P,i}\, h_k \left(T(x) - T_{k,\infty}\right) \tag{3.3.10}$$

where h is the heat transfer coefficient the thermal conductivity, $T(x)$ the material temperature a x and $T_{i,\infty}$ the coolant bulk temperature for the tube i. Indeed, increasing the poloidal distance for the coolant channel line, the detrimental effect of $f_{WGT,P}$ is higher as in Fig.3.3.2 moving from red to green line.

Thus introducing in the Equ.3.3.4, the coolant effects we obtain:

$$\begin{aligned}\rho(T,x)c(T,x)\frac{\delta T(x)}{\delta t} = & \\ & + \frac{\delta}{\delta x}\left(\left(1 - f_{COOL,j}\right) k_T(T,x)\,\frac{\delta T}{\delta x} + f_{COOL,j}\, h_j \left(T(x) - T_{j,\infty}\right)\right) \\ & + f_{WGT,R}\, f_{WGT,P}\, h_k \left(T(x) - T_{k,\infty}\right) + q_V(x,t)\end{aligned} \tag{3.3.11}$$

where f_{COOL}, $f_{WGT,R}$and $f_{WGT,P}$ are discrete function, taking values only at the specified coolant positions:

$$\begin{aligned} f_{COOL,j}(x) &= \sum \delta_j(x) \tfrac{Surface_{COOLED}}{Surface_{TOT}} \\ f_{WGT,R}(x) &= \sum \delta_k(x)\, f_{WGT,R} \\ f_{WGT,P}(x) &= \sum \delta_k(x)\, f_{WGT,P} \end{aligned} \tag{3.3.12}$$

[3]The multi-node approach has been tested but it is not physically valid because the energy balance is not fulfilled.

with δas the Dirac Δ function and j as a radial cooling node.[4]

Applying to Equ.3.3.1 a implicit first order dicretization and a forward methodology and considering at the same time the ρ, c and q_V variables only dependent on x, we distinguish three different case for a node i :

- Node before the type A coolant node[5]

$$\frac{\rho_i c_i}{\Delta t}(T_i^{n+1} - T_i^n) = \frac{T_{i-1}^{n+1} - T_i^{n+1}}{\Delta x_{i-1}} k_{i-1} +$$
$$(1 - f_{COOL,j}) \left(T_{i+1}^{n+1} - T_i^{n+1}\right) \frac{k_{i+1}}{\Delta x_{i+1}} \tag{3.3.13}$$
$$+ f_{COOL,j}\, h_j \left(T_i^{n+1} - T_{j,\infty}^{n+1}\right)$$
$$+ f_{WGT,R}\, f_{WGT,P}\, h_k \left(T_i^{n+1} - T_{k,\infty}^{n+1}\right) + \dddot{q}\, \Delta x_{i-1} \tag{3.3.14}$$

- Type A coolant node

$$\frac{\rho_i c_i}{\Delta t}(T_i^{n+1} - T_i^n) =$$
$$+ (1 - f_{COOL,j}) \left(\left(T_{i+1}^{n+1} - T_i^{n+1}\right) \frac{k_{i+1}}{\Delta x_{i+1}} + \left(T_{i-1}^{n+1} - T_i^{n+1}\right) \frac{k_{i+1}}{\Delta x_{i+1}} \right)$$
$$+ f_{COOL,j}\, h_j \left(T_i^{n+1} - T_{j,\infty}^{n+1}\right)$$
$$+ f_{WGT,R}\, f_{WGT,P}\, h_k \left(T_i^{n+1} - T_{k,\infty}^{n+1}\right) + \dddot{q}\, \Delta x_{i-1} \tag{3.3.15}$$

- Node after the type A coolant node

$$\frac{\rho_i c_i}{\Delta t}(T_i^{n+1} - T_i^n) = \frac{T_{i-1}^{n+1} - T_i^{n+1}}{\Delta x_{i-1}} k_{i-1}$$
$$+ (1 - f_{COOL,j}) \left(T_{i+1}^{n+1} - T_i^{n+1}\right) \frac{k_{i+1}}{\Delta x_{i+1}}$$
$$+ f_{COOL,j}\, h_j \left(T_i^{n+1} - T_{j,\infty}^{n+1}\right)$$
$$+ f_{WGT,R}\, f_{WGT,P}\, h_k \left(T_i^{n+1} - T_{k,\infty}^{n+1}\right) \tag{3.3.16}$$
$$+ \dddot{q}\, \Delta x_{i-1} \tag{3.3.17}$$

Equation 3.3.14, 3.3.15 and 3.3.17 could be determined also by the thermal balance methodology[13].

In case of complete loss-of-coolant accident (or LOCA) transient, the radiation effect, described by the Stefan-Boltzmann law, is considered to be dominant in an empty tube so complete the Equation No.3.3.14, 3.3.15 and 3.3.17.

[4] From now on to simplify the mathematical treatment only one coolant channel type A and one of type B is considering acting on node i

[5] $T_\infty$is the bulk temperature of the coolant element.

Considering our 1D modelization, the power radiated between the two nodes surrounding a j type A coolant node is:

$$q_{irr} = f_{COOL,j}\varepsilon\sigma(T_{i+1}^4 - T_{i-1}^4) \tag{3.3.18}$$

where ε is the material emissivity of the material which characterizes the energy the fraction of the energy absorbed by the body assumed as grey body[6] and σ is the Stefan-Boltzmann constant equal to $5.67037310^{-8}\frac{W}{K^4m^2}$. Using this approach it is not possible to implement the irradiation term in type B coolant node; no taking into account that this term is considered as conservative.

3.3.1.2 Gaussian node discretization

The default material finite different discretization is the linear one so a equal spacing between neighbors nodes. Knowing that the greater thermal gradients are generally located close to the material boundaries due to the material thermal characteristics differences, a smaller node distance could improve the solution precision. Therefore, two possible solutions are set-up: a finer linear discretization or a Gaussian discretization. The first solution could improve the solution nevertheless requiring more computational effort. On the other hand, the Gaussian placement optimizes the node disposition requiring the same computational effort.

In conclusion, depending on the application, the user can select the most suited technique.

3.3.2 2D Solution

Due to the complexity of the system in analysis, the 1D solution could not be enough accurate or could not be an accurate representation of the domain in analysis. For this reason, a more complex routine has been developed to provide a 2D solution for rectangular region. Several approaches can be used to solve the 2D heat equation such as the analytical, the graphical and numerical (e.g. finite-difference, finite-element, or boundary element) approaches. Although several techniques are available for solving such equations, the solutions typically involve complicated mathematical series and functions and may be obtained for only a restricted set of simple geometries and boundary conditions. Indeed, conduction shape factors and dimensionless conduction heat rates are compilations of existing solutions only for a subset of geometries that are commonly encountered in engineering practice. In contrast to the analytical methods, which provide exact results at any point, graphical and numerical methods can provide only approximate results at discrete points. To automatize, speed up and generalize the solver the finite difference method has been implemented to operate with a wide range of boundary conditions.

The approaches described in sec.3.1 and 3.2 are mostly valid however they need some modifications in the model preparation as reported in Figure 3.3.3.

[6] The material emissivity, ε, is considered as constant and independent for the temperature.

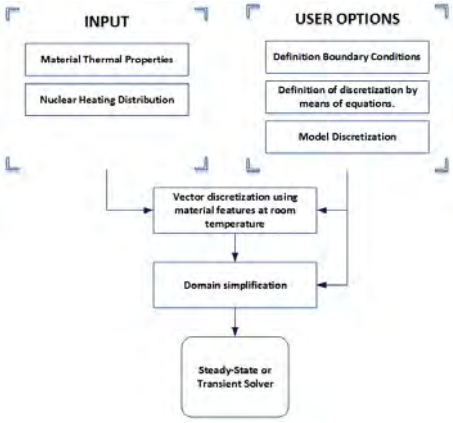

Figure 3.3.3: 2D Domain approach

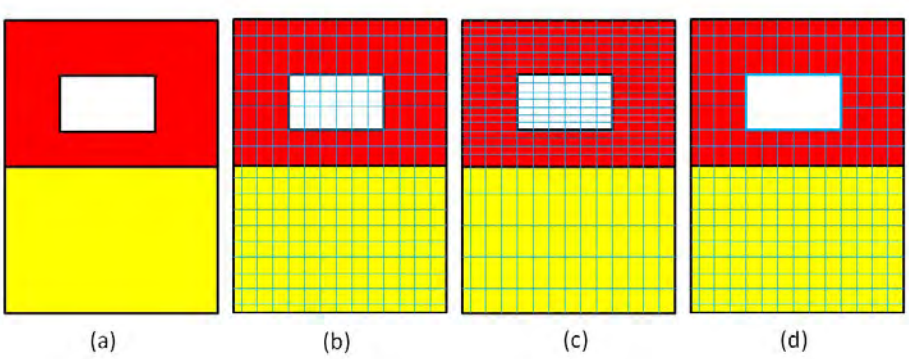

Figure 3.3.4: Example of a 2D domain

Firstly the user has to specify the domain in analysis (e.g. materials type, material discretization, the coolant areas ...) by means of equations. As example please consider the domain reported in 3.3.4(a) which is composed by two material zones (e.g. red, No.1, and yellow, No.2). and No.2 has a hole in the center.

Secondly, the domain, following the user specification, is divided in a structure way in small areas assigning to each reference point that is at its center. The reference point is frequently termed a nodal point (or simply a node). The aggregate of points is termed a nodal network or mesh. Each voxel is categorized and depending on the position the correspondent materials features and NHD is assigned.[7]

[7] Nowadays, the unstructured discretization is not possible but it is not discarded a priori in the AINA development. By the way the Gaussian node distribution presented in sec.3.3.1.2 is also applicable to the 2D domains.

As illustration two different approaches are reported in Fig.3.3.4: (b) employs a uniform grid whereas (c) an optimized division over the hole area where the highest gradient should be placed. The nodes are classified in four categories:

1. Nodes placed on the external boundary conditions
2. Nodes defining internal areas (e.g. hole in domain No.1 Fig.3.3.4) hereinafter defined as internal boundary condition nodes.
3. Nodes contained inside a bounded area.
4. Generic internal nodes which are all the remaining nodes which do not belong to the previous categories

The internal nodes contained inside a bounded area are removed from the computational domain because they are not useful for the solution. For instance, starting from domain (b) (Fig.3.3.4), the simplified final nodalization is obtained (Fig.3.3.4 (d)).

3.3.2.1 Generic internal nodes

The simplification from 3D model to 2D one is done considering each region rectangular region. The different materials in each module are arranged in layers parallel and discretized. Considered this the Equ.3.3.1 is further simplified as:

$$\rho(x,y,t)cp(x,y,t)\frac{\delta T(x,y,t)}{\delta t} = \nabla k(x,y,t)\nabla T(x,y,t) + q(\dddot{x},y,t) \tag{3.3.19}$$

Considering a state-state scenario, the thermal conductivity and the NHD constant and implementing a second order solution, we obtain:

$$\frac{\delta^2 T(x,y)}{\delta x^2} + \frac{\delta^2 T(x,y)}{\delta y^2} + \frac{\delta^2 T(x,y)}{\delta x \delta y} + \frac{\dddot{q}}{k} = 0 \tag{3.3.20}$$

$$\frac{T_{m+1,n} - 2T_{m,n} + T_{m-1,n}}{\Delta x_{m,n}^2} + \frac{T_{m,n+1} - 2\dddot{T}_{m,n} + T_{m,n-1}}{\Delta y_{m,n}^2} + \frac{-T_{m-1,n+1} + T_{m-1,n-1} + T_{m+1,n+1} - T_{m+1,n-1}}{4\Delta x \Delta y} + \frac{\dddot{q}}{k} = 0 \tag{3.3.21}$$

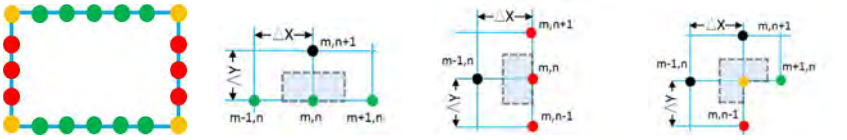

Overall Type#01 Type#02 Type#03

Figure 3.3.5: Internal Boundary Conditions

$$T_{m+1,n}\left(\frac{1}{\Delta x_{m,n}^2}\right)+T_{m,n+1}\left(\frac{1}{\Delta y_{m,n}^2}\right)+T_{m-1,n}\left(\frac{1}{\Delta x_{m,n}^2}\right)$$
$$+T_{m,n-1}\left(\frac{1}{\Delta y_{m,n}^2}\right)+-T_{m-1,n+1}\left(\frac{1}{\Delta x\Delta y}\right)+T_{m-1,n-1}\left(\frac{1}{\Delta x\Delta y}\right)$$
$$+T_{m+1,n+1}\left(\frac{1}{\Delta x\Delta y}\right)-T_{m+1,n-1}\left(\frac{1}{\Delta x\Delta y}\right)+$$
$$+T_{m,n}\left(-\frac{2}{\Delta x_{m,n}^2}-\frac{2}{\Delta y_{m,n}^2}\right)+\frac{\ddot{q}}{k}=0 \tag{3.3.22}$$

3.3.2.2 Boundary condition nodes

The 2D boundary condition treatment is more complex than for the 1D one. Indeed not all the internal boundary condition nodes are treated equal but the approach depends on the relative positions. As illustration, the domain obtained in Fig.3.3.4 (d) has been taken defining row index m and column one n.

Therefore, consider the internal hole as a Dirichlet BC with a heat transfer coefficient h and a fluid bulk temperature T_∞ consistent along the perimeter). Three main types of internal boundary conditions[8] are distinguished along the perimeter (see Fig.3.3.2.2):

- Nodes on the vertical sides (red circle)
- Node on the corners (orange circle)
- Nodes on the horizontal sides (greed circle)

Type#01

[8] A first order solution have been implemented. A second order one, using the polynomial approach[63], has been extensively tested but unfortunately has not resulted beneficial and so discarded. This was probable caused by the employment of ghost nodes technique.

$$\begin{aligned}
&\dddot{q}\frac{\Delta x\Delta y}{2} + h\Delta x\left(T_\infty - T_{m,n}\right)\\
&+k_{m+1,n}\frac{\Delta y}{2\Delta x}\left(T_{m+1,n} - T_{m,n}\right)\\
&+k_{m-1,n}\frac{\Delta y}{2\Delta x}\left(T_{m-1,n} - T_{m,n}\right)\\
&+k_{m,n+1}\frac{\Delta x}{\Delta y}\left(T_{m,n+1} - T_{m,n}\right) = 0
\end{aligned} \tag{3.3.23}$$

Type#02

$$\begin{aligned}
&\dddot{q}\frac{\Delta x\Delta y}{2} + h\Delta y\left(T_\infty - T_{m,n}\right)\\
&+k_{m,n+1}\frac{\Delta x}{2\Delta y}\left(T_{m,n+1} - T_{m,n}\right)\\
&+k_{m,n-1}\frac{\Delta x}{2\Delta y}\left(T_{m,n-1} - T_{m,n}\right)\\
&+k_{m+1,n}\frac{\Delta y}{\Delta x}\left(T_{m+1,n} - T_{m,n}\right) = 0
\end{aligned} \tag{3.3.24}$$

Type#03

$$\begin{aligned}
&\dddot{q}\frac{3\Delta x\Delta y}{4} + h\left(\frac{\Delta y}{2} + \frac{\Delta x}{2}\right)\left(T_\infty - T_{m,n}\right)\\
&+k_{m,n+1}\frac{\Delta x}{2\Delta y}\left(T_{m,n+1} - T_{m,n}\right)\\
&+k_{m-1,n}\frac{\Delta y}{\Delta x}\left(T_{m-1,n} - T_{m,n}\right)\\
&+k_{m+1,n}\frac{\Delta y}{2\Delta x}\left(T_{m+1,n} - T_{m,n}\right) = 0
\end{aligned} \tag{3.3.25}$$

On the other side if the temperature T is imposed over the hole perimeter, we obtain independently from the position:

$$T_{m,n} = T \tag{3.3.26}$$

As well as the internal ones the external boundary condition approach depends on the relative position. The user can select between temperature imposed (refer to Equ.3.3.26), flux imposed (refer to Equ.3.3.27, 3.3.28 and 3.3.29) or adiabatic ones.

Type#01

$$\begin{aligned} &\dddot{q}\frac{\Delta x\Delta y}{2}+\ddot{q}\Delta x \\ &+k_{m+1,n}\frac{\Delta y}{2\Delta x}\left(T_{m+1,n}-T_{m,n}\right) \\ &+k_{m-1,n}\frac{\Delta y}{2\Delta x}\left(T_{m-1,n}-T_{m,n}\right) \\ &+k_{m,n+1}\frac{\Delta x}{\Delta y}\left(T_{m,n+1}-T_{m,n}\right)=0 \end{aligned} \tag{3.3.27}$$

Type#02

$$\begin{aligned} &\dddot{q}\frac{\Delta x\Delta y}{2}+\ddot{q}\Delta y \\ &+k_{m,n+1}\frac{\Delta x}{2\Delta y}\left(T_{m,n+1}-T_{m,n}\right) \\ &+k_{m,n-1}\frac{\Delta x}{2\Delta y}\left(T_{m,n-1}-T_{m,n}\right) \\ &+k_{m+1,n}\frac{\Delta y}{\Delta x}\left(T_{m+1,n}-T_{m,n}\right)=0 \end{aligned} \tag{3.3.28}$$

Type#03

$$\begin{aligned} &\dddot{q}\frac{\Delta x\Delta y}{4}+\ddot{q}_y\frac{\Delta y}{2}+\ddot{q}_x\frac{\Delta x}{2} \\ &+k_{m,n+1}\frac{\Delta x}{2\Delta y}\left(T_{m,n+1}-T_{m,n}\right) \\ &+k_{m+1,n}\frac{\Delta y}{2\Delta x}\left(T_{m+1,n}-T_{m,n}\right)=0 \end{aligned} \tag{3.3.29}$$

The equation for adiabatic condition can be obtained starting from the Neumann ones and imposing the flux $\ddot{q}$ equal to zero.

3.4 Routine validation

3.4.1 1D domain

The 1D routines has been broadly cross-checked comparing the results against the 3D CFD detailed model results obtained by means of ANSYS FLUENT© as for the case of Japanese DEMO Water Cooled Pebbled Bed blanket (or WCPB) and the European DEMO Helium Cooled Pebbled Bed (or HCPB) one. The results shows a good agreement within the 10% of discrepancy and so largely within the initial requirement and expectation[9]. The discrepancies could be

[9] In this chapter the relative temperature difference is always computed as : (ReferenceValue - Computed)/ReferenceValue

anyway adjusted applying a scaling function to the numerical solution obtained depending on the operation conditions. Considering all the simplifications and assumption used in the models, the thermal-wall routines completely fulfill the AINA safety code needs and confirm the new approaches implemented. For the detailed information please refer to chapter 4 for the WCPB and chapter 5 for the HCPB.

3.4.2 2D domain

As done for the the 1D routines, 2D ones have been cross-checked and validated comparing the several sets versus:

- Analytic result where possible
- 1D in-house routine
- 2D CFD model computed by means of ANSYS FLUENT©
- 3D CFD detailed model results obtained by means of ANSYS FLUENT© as done in for the WCPB (chapter 4)

Hereinafter, the two groups of cases analyzed are listed :

1. Group-A (see Fig.3.4.1)
   (a) Case#01: Temperature (X-, X+, Y-, Y+) imposed on external BC, no internal hole
   (b) Case#02: Temperature (X-, X+, Y-, Y+)/Flux(Y+) imposed on external BC, no internal hole
   (c) Case#03: Temperature (Y-, Y+)/Adiabatic(X-, X+) imposed on external BC, no internal hole
   (d) Case#04: Temperature (Y-)/Adiabatic(X-, X+)/Flux(Y+) imposed on external BC, no internal hole
   (e) Case#05: Temperature (Y-)/Adiabatic(X-, X+, Y+) imposed on external BC, no internal hole
2. Group-B(see Fig.3.4.2)
   (a) Case#06: Temperature (X-,Y-)/Adiabatic(X+)/Flux(Y+) imposed on external BC, with internal internal holes with fixed temperature
   (b) Case#07: Temperature (X-,Y-)/Adiabatic(X+)/Flux(Y+) imposed on external BC, with internal internal holes with Direchlet BC
   (c) Case#08: Temperature (Y-)/Adiabatic(X-,X+)/Flux(Y+) imposed on external BC, with internal internal holes with Direchlet BC

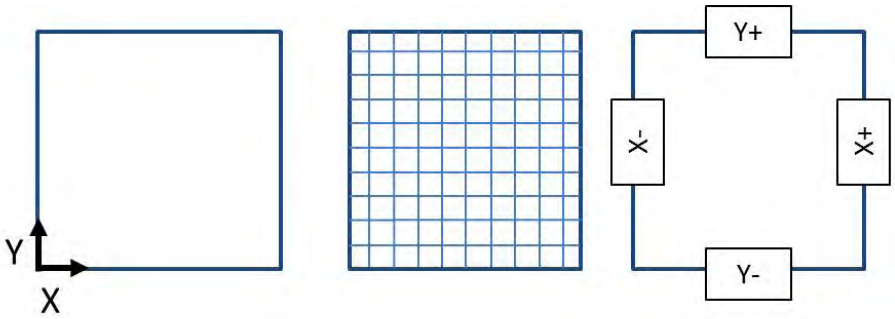

Figure 3.4.1: Group-A 2D domain

Type	Description
BC@X-	T imposed at 300K
BC@X+	T imposed at 300K
BC@Y-	T imposed at 300K
BC@Y+	T imposed at 600K
Nuclear Heating	Equally distributed $10W/m^3$

Table 3.4.1: Case#01-Assumptions

Whereas, group-A uses a 1 m square domain of aluminum ($e.g. k = 202.4W/m^2/K$) discretized uniformly with 100 nodes for side, without internal holes (Fig.3.4.1), group-B works on a 0.3x0.6 m domain of Aluminum containing eighteen internal holes of 8x50 mm homogeneously distributed in Y and separated by 87.8mm starting form Y- (Fig.3.4.2). The group-B's domain discretization changes case by case. Both for group-A and group-B the thermal conductivity is assumed constant and so the temperature dependence neglected.

The eight cases proposed intends to progressively validate one by one the BC implement, both internal and external, the NHD application and the coolant pipe functions.

3.4.2.1 Case#01

The Case#01 assumptions are reported in Table 3.4.1.

The 2D steady-state macroscopic temperature results are detailed in Table 3.4.2.1 whereas the 2D temperature field in Fig.3.4.2.1. Both the macroscopic and the local results shows a very good agreement between the in-house routine and the commercial software for this specific application. The maximum relative local difference is within -1/+1% reaching a maximum close to the external sides and considered completely acceptable. The discrepancy could be mostly addressed to the more accurate mathematical solution implemented in the commercial software and to the different treatment of BC element. Due to this effect

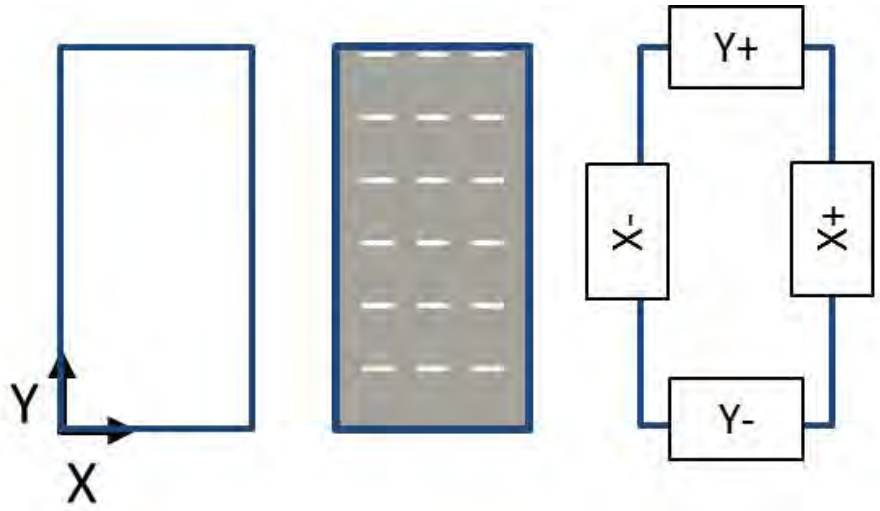

Figure 3.4.2: Group-B 2D domain

	T_{min}	T_{max}	$\overline{T}$
AINA	300.00 K	600.00 K	375.03 K
AINA SIM.	300.00 K	600.00 K	375.03 K
ANSYS	300.00 K	596.97 K	375.02 K

Table 3.4.2: Case#01-Macroscopic results

hereinafter denominated "boundary effect" and described in section 3.4.2.1, the commercial software does not match the BC Y+ value (596.97 K instead of 600 K, with 0.5% relative error) whereas that is the case for the in-house routine.

Moreover, the routine allows implementing symmetrical BC to optimize the computational effort and the time-span of the solution. For instance the domain used in case#01 can be halved using the symmetry plane X=0.5m without affecting any of the outcomes.

The case#01 validates the in-house implementation of the temperature imposed BC, the heat term imposed along the domain and the usage of symmetric boundary conditions.

The Boundary Effect Please consider Fig.3.4.5 where four types of different BC condition elements are reported: polyhedral element (a), structured rectangular element (b), tetrahedral one (c), structured one node cell (d). Type (a), (b) and (c) are the most common cell used in CFD codes whereas (d) one is the AINA element.

In contrast to element (a,b,c), the AINA one (d) has only one node which re-

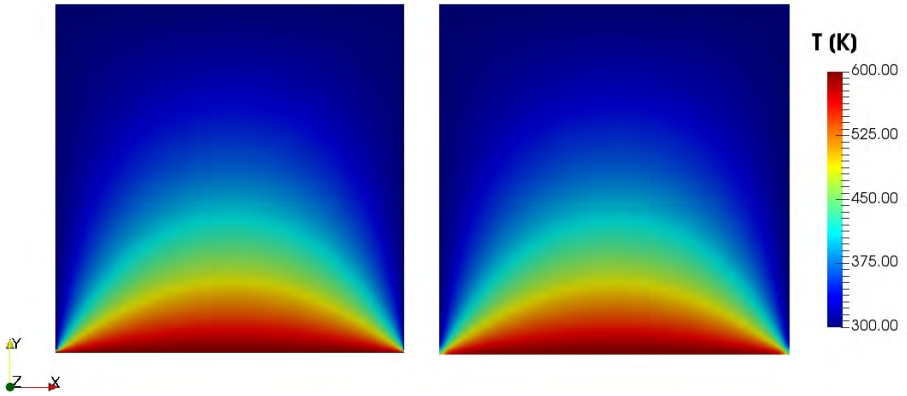

Figure 3.4.3: Case#01-AINA (left) vs ANSYS Fluent (right)

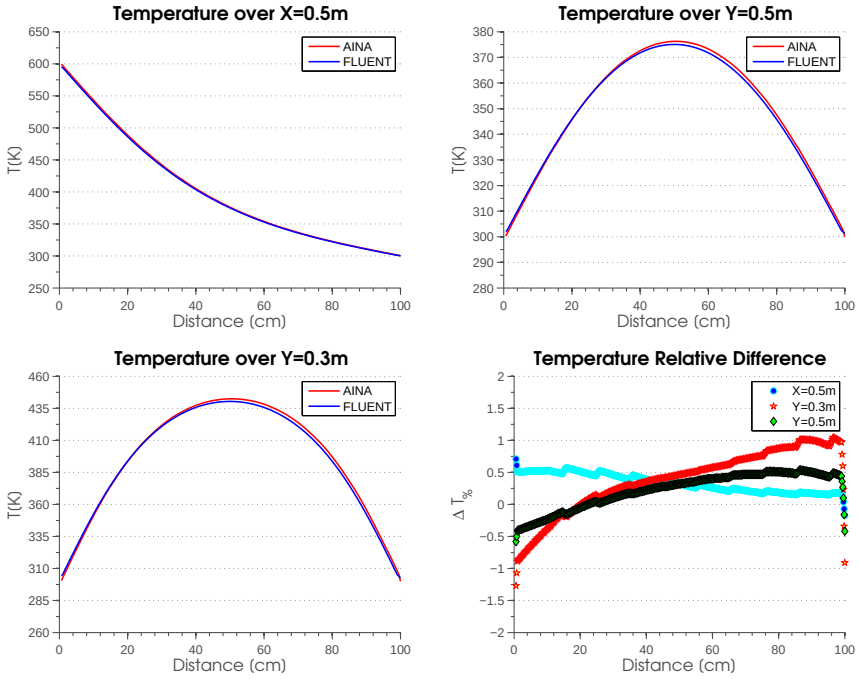

Figure 3.4.4: Case#1-Results along lines

lies on the BC. The cell temperature computed by in-house routine corresponds to the nodal one whereas the ANSYS Fluent to the weighted average between the elements with bound the element. Considering that the BC is applied only to the nodes which relies on the axis, it is evident why the commercial CFD software does not match the BC value. The boundary effect is one of the main reason of discrepancy and it is present both in internal and external BC.

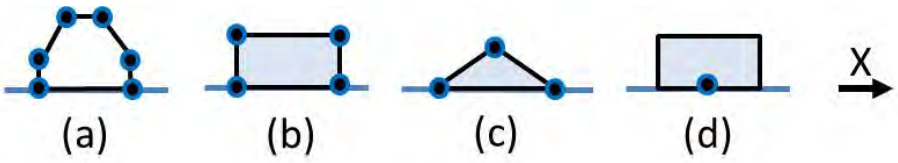

Figure 3.4.5: BC Comparison: ANSYS Fluent (left and middle) vs AINA (right)

3.4.2.2 Case#02

The Case#02 assumptions are reported in Table 3.4.3.

Type	Description
BC@X-	T imposed at 300K
BC@X+	T imposed at 300K
BC@Y-	T imposed at 600K
BC@Y+	Flux imposed$10^4 W/m^2$
Nuclear Heating	Equally distributed $10 W/m^3$

Table 3.4.3: Case#02-Assumptions

The 2D steady-state macroscopic temperature results are detailed in Table 3.4.2.2 whereas the 2D temperature field in Fig.3.4.2.2. Both the macroscopic and the local results shows a very good agreement between the in-house routine and the commercial software for this specific application. The maximum relative local difference is about 1.5% close to the external sides and completely acceptable. The discrepancy could be completely addressed to the more accurate mathematical treatment implemented in the commercial software's solver algorithm employed and to the boundary effect (see section 3.4.2.1). As for the Case#01, the commercial software does not obtain the BC Y+ value (596.97 K in place of 600K, with 0.5% relative error) whereas this is the case for the in-house routine.

The case#02 validates the in-house implementation of the Neumann BC with the heat term imposed over the domain.

	T_{min}	T_{max}	$\overline{T}$
AINA	300.00 K	600.00 K	383.95 K
ANSYS	300.00 K	596.97 K	384.84 K

Table 3.4.4: Case#02-Macroscopic results

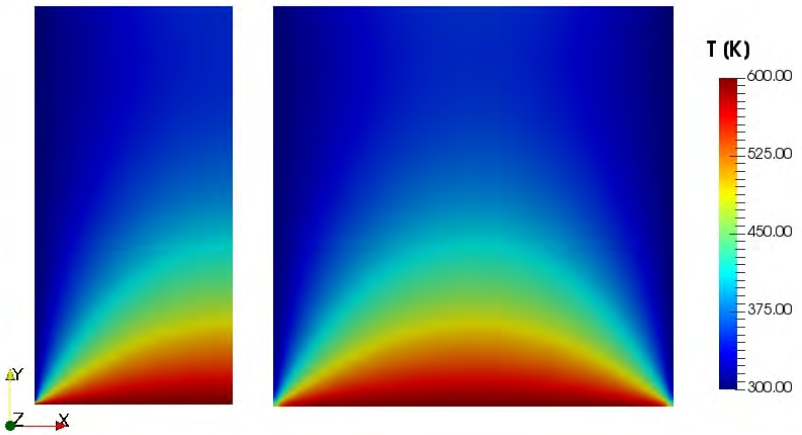

Figure 3.4.6: Case#02-AINA (left) vs ANSYS Fluent (right)

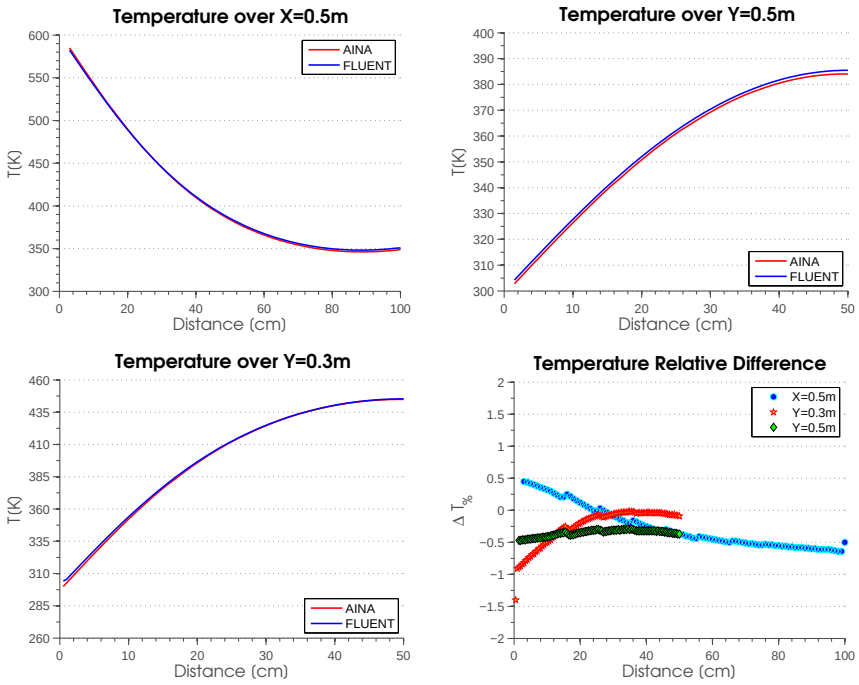

Figure 3.4.7: Case#02-Results along lines

3.4.2.3 Case#03

The case#03 assumptions are reported in Table 3.4.5.

Type	Description
BC@X-	Adiabatic
BC@X+	Adiabatic
BC@Y-	T imposed at 600K
BC@Y+	T imposed at 300K
Nuclear Heating	Equally distributed $10W/m^3$

Table 3.4.5: Case#03-Assumptions

The 2D steady-state macroscopic temperature results are detailed in Table 3.4.2.3 whereas the temperature field in Table 3.4.8, in conjunction with the AINA-1D field, the ANALYTIC results and the AINA-2D to 1D, which is the post processed 2D temperature averaged along Y axis.

Both the macroscopic and the local results show a very good agreement in comparison with the analytical exact solution, see Figure 3.4.2.3. The maximum relative local difference is less than 0.5% and constant along the domain. As for the case#01, the commercial software does not obtain exactly the BC fixed

temperature values (595.50 K in place of 600 K) whereas this is the case for the in-house routine because of the boundary effect (see section 3.4.2.1). The case#01 validates the in-house implementation of the combination of Neumann BC with temperature imposed ones.

	T_{min}	T_{max}	$\overline{T}$
AINA-1D	300.00 K	600.00 K	450.00 K
AINA-2D	300.00 K	600.00 K	450.02 K
AINA-2D to 1D	300.00 K	600.00 K	450.02 K
ANSYS	301.49 K	598.50 K	449.90 K
ANALYTIC	300.00 K	600.00 K	450.00 K

Table 3.4.6: Case#03-Macroscopic results

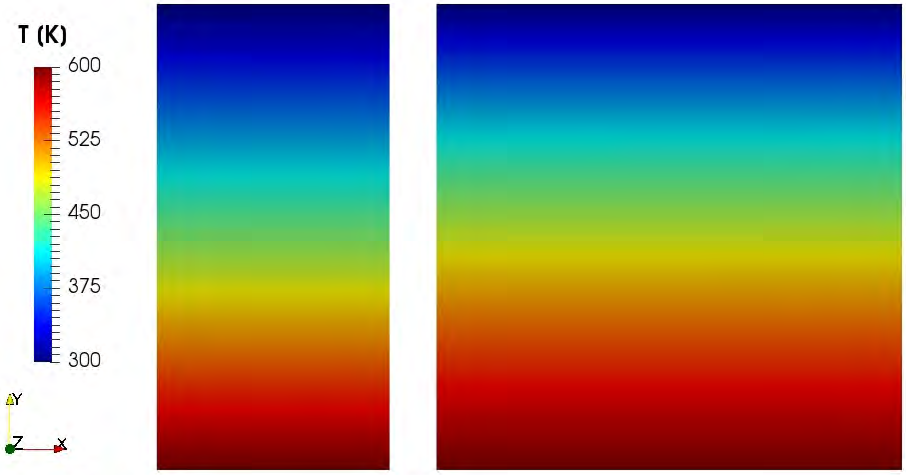

Figure 3.4.8: Case#03-AINA (left) vs ANSYS Fluent (right)

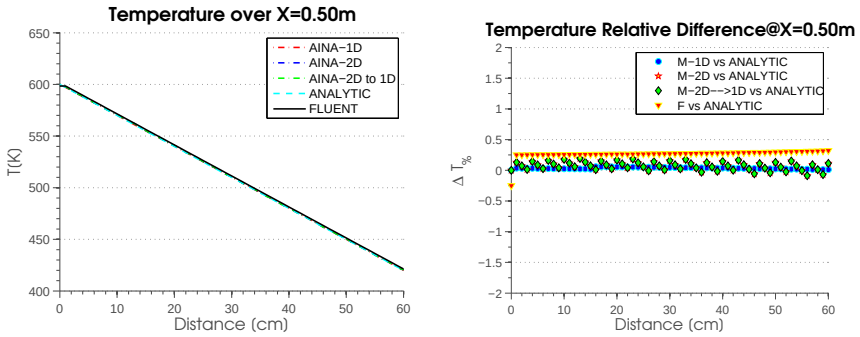

Figure 3.4.9: Case#03-Results along lines

3.4.2.4 Case#04

The Case#04 assumptions are reported in Table 3.4.7.

Type	Description
BC@X-	Adiabatic
BC@X+	Adiabatic
BC@Y-	T imposed at 300K
BC@Y+	Flux $10^4 W/m^2$
Nuclear Heating	Equally distributed $10^5 W/m^3$

Table 3.4.7: Case#04-Assumptions

The 2D steady-state macroscopic temperature results are detailed in Table 3.4.2.4 whereas the temperature field in Table 3.4.10, in conjunction with the AINA-1D field, the ANALYTIC results and the AINA-2D to 1D, which is the post processing temperature averaging of 2D data along Y axis.

Both the macroscopic and the local results show a very good agreement in comparison with the analytical exact solution, Figure 3.4.2.4, having the line plot pratically superimposed. The maximum relative local difference is for the commercial software and less than 1.00%. These small discrepancies could be mostly addressed to the boundary effect (see section 3.4.2.1) and different order of solution.

The case#04 validates the in-house implementation of the combination of Neumann BC, temperature imposed and adiabatic ones.

	T_{min}	T_{max}	$\overline{T}$
AINA-1D	300.00 K	600.00 K	489.11 K
AINA-2D	300.00 K	596.44 K	489.24 K
AINA-2D to 1D	300.00 K	596.44 K	489.24 K
ANSYS	302.71 K	596.21 K	489.40 K
ANALYTIC	300.00 K	596.44 K	489.35 K

Table 3.4.8: Case#04-Macroscopic results

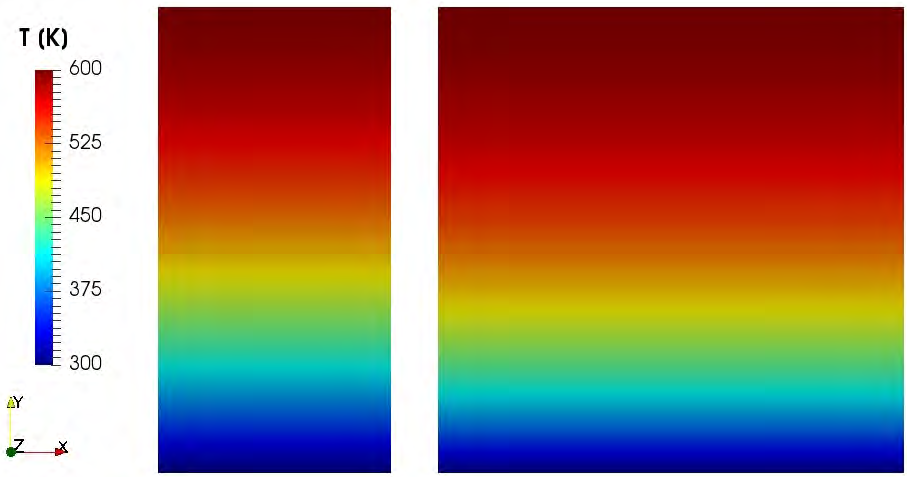

Figure 3.4.10: Case#04-AINA (left) vs ANSYS Fluent (right)

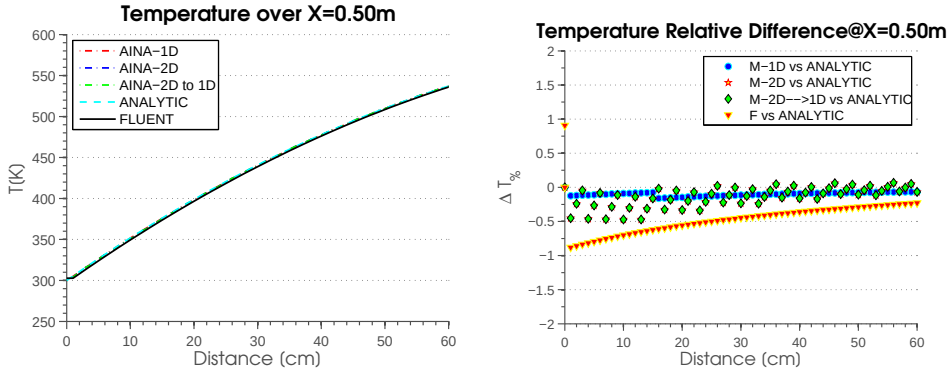

Figure 3.4.11: Case#04-Results along lines

	T_{min}	T_{max}	$\overline{T}$
AINA-1D	300.00 K	546.60 K	464.38 K
AINA-2D	300.00 K	547.04 K	464.54 K
AINA-2D to 1D	300.00 K	547.04 K	464.54 K
ANSYS	302.47 K	547.47 K	464.97 K
ANALYTIC	300.00 K	547.04 K	464.65 K

Table 3.4.10: Case#05-Macroscopic results

3.4.2.5 Case#05

The Case#05 assumptions are reported in Table 3.4.9.

Type	Description
BC@X-	Adiabatic
BC@X+	Adiabatic
BC@Y-	T imposed at 300K
BC@Y+	Adiabatic
Nuclear Heating	Equally distributed $10^5 W/m^3$

Table 3.4.9: Case#05-Assumptions

The 2D steady-state macroscopic temperature results are detailed in Table 3.4.2.5 whereas the temperature field in Table 3.4.12, in conjunction with the AINA-1D field, the ANALYTIC results and the AINA-2D to 1D, which is the post processing temperature averaging of 2D data along Y axis.

Both the macroscopic and the local results show a very good agreement in comparison with the analytical exact solution, Figure 3.4.2.5, having the line plot almost superimposed as found for previous cases. The maximum relative local difference is for the commercial software and less than 1.00%. These small discrepancies could be mostly addressed to the boundary effect (see section 3.4.2.1).

The case#05 completes the in-house validation for the in-house routine for all the BC types applied a domain without internal holes.

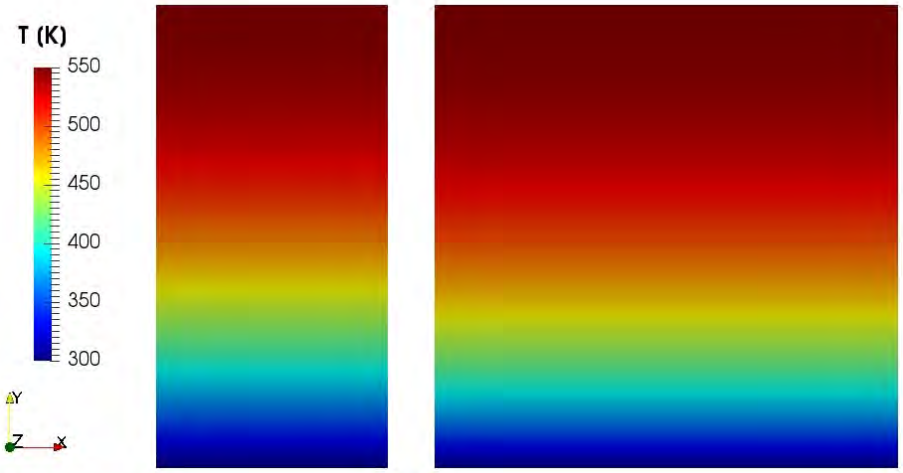

Figure 3.4.12: Case#05-AINA (left) vs ANSYS Fluent (right)

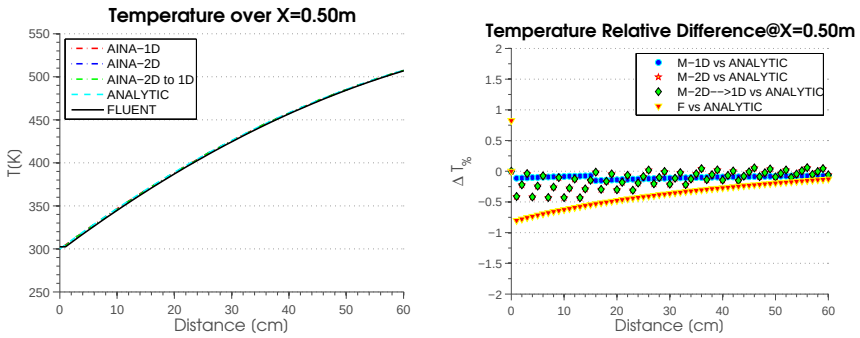

Figure 3.4.13: Case#05-Results along lines

3.4.2.6 Case#06

The Case#06 assumptions are reported in Table 3.4.11.

Type	Description
BC@X-	T imposed at 300K
BC@X+	Adiabatic
BC@Y-	T imposed at 600K
BC@Y+	Flux, $10^4 W/m^2$
BC@Internal Holes	T imposed at 400K
Nuclear Heating	Equally distributed $50 W/m^3$

Table 3.4.11: Case#06-Assumptions

Different mesh set-up has been tested both for ANSYS Fluent (Fig.3.4.2.6) and AINA in order to check the mesh sensibility of the two approached, generating in total six different simulations named respectively F-R1, F-R2, F-R3 and M-R1, M-R2, M-R3[10]. All the mesh quality standards has been checked by means of the Pointwise[102] and ANSYS Fluent internal tools.

A tetrahedral unstructured mesh has been used for the CFD code: F-R1 has the smallest cell dimension which is increased up to F-R3. Mesh F-R1 has about 15 times more cells that F-R2 and 50 times than F-R3. The mesh specification (e.g. dimension, type and order) should be decided according to the problem specifications and the requested output. In most cases, a finer discretization allows a better accuracy but also it need a bigger computational effort.[11]

Regarding the in-house routine simulations the three slightly different meshes have been used:

- M-R1 is an uniform course structured grid which is not adapted to the internal coolant holes.
- M-R2 is an uniform fine structured grid which is adapted to the internal coolant holes.
- M-R3 is an uniform fine structured grid and more fine close to Y- and X+which is adapted to the internal coolant holes.

The 2D steady-state macroscopic temperature results are detailed in Table3.4.2.6 whereas the 2D temperature field in Fig.3.4.15 and Fig.3.4.16.

Although the Fluent meshes are various, the average macroscopic temperature results show a good agreement whereas the minimum and maximum temperatures are affected up to about 5% mainly to do the boundary effect (see section 3.4.2.1). The temperature domains obtained are similar but, as logical, with different resolutions. The main discrepancies are gathered close to the external boundaries and to the internal pipes where the major gradients are located (see Fig.3.4.2.6). Indeed, the maximum local per cent difference found is about 8% close to X- between F-R1 and F-R3, which overestimates the gradient[12].

On the other hand, the AINA cases comparison shows important differences both in the macroscopic and local results. Due to the course mesh employed by AINA-R1, the temperature domain computed differs substantially from the other two cases and not physically valid. This is caused by the mismatch of cooling pipe with the real geometry. On the contrary, the M-R2 and M-R3 are quite in agreement and close to F-R1 even if the average temperature differs up

[10]Although, the coolant pipes seems to be slightly smaller than the ANSYS Fluent one they have exactly the same dimensions. This visual effect is caused by the impossibility for structured mesh to halve boundary internal cell without modifying the others.

[11]For instance, the most advanced thermal-hydraulic application to Vacuum Vessel ITER fusion reactor, [101], has reached the huge quantity of the $10^8 - 10^9$mesh elements, which depends upon super-cluster with hundreds of cpu and Gb of RAM for weeks.

[12]Hereinafter, the ANSYS-R1 case is assumed as reference for the comparison with AINA.

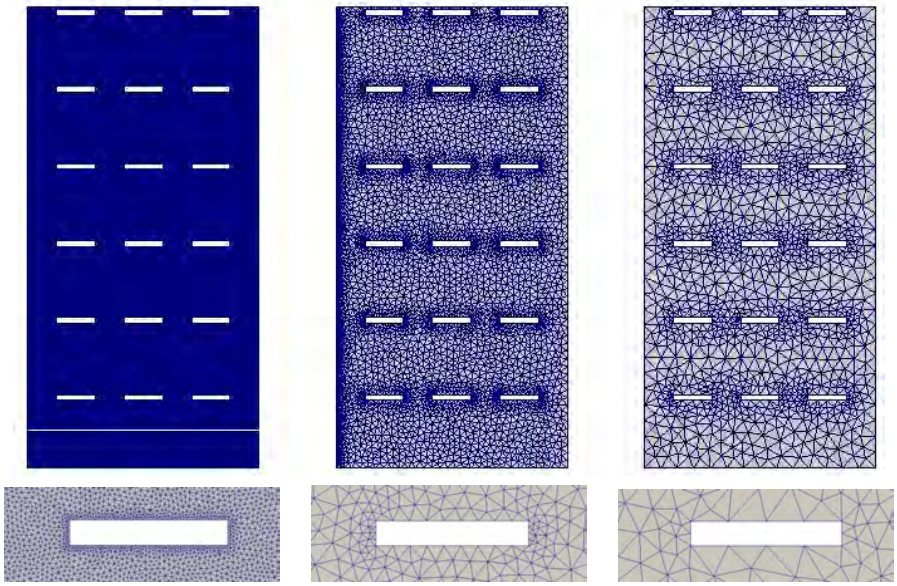

Figure 3.4.14: Case#06-Results along lines

to about 5 K. Minor adjustments and refinement in the AINA mesh discretization carried out in the M-R3 case, has allowed some improvements despite of more computational costs. Indeed, the in-house routine has required for up to 12 Gb of RAM and about 200 s whereas the commercial software 10 s and 4 times less of RAM. This could be partially caused by MATLAB itself and so reduced once the routine will be passed to C++.

Excluding M-R1, the visual comparison of the temperature distribution confirms the validity of the in-house routine versus ANSYS Fluent. The local temperature analysis at different locations highlights a good agreement of the data and relative difference maximum of 4% (M-R3). Considering the mesh discretization difference, the discrepancies found between case M-R3 and F-R1 are within the ANSYS Fluent mesh sensibility and so completely acceptable.

	No. Cell	T_{min}	T_{max}	$\overline{T}$
ANSYS-R1 (or F-R1)	146636	300.45 K	599.35 K	403.77 K
ANSYS-R2 (or F-R2)	10938	300.50 K	596.87 K	403.73 K
ANSYS-R3 (or F-R3)	2870	305.51 K	591.55 K	403.63 K
AINA-R1 (or M-R1)	5000	69.38 K	600.00 K	286.83 K
AINA-R2 (or M-R2)	20070	300.00 K	600.00 K	401.92 K
AINA-R3 (or M-R3)	20592	300.00 K	600.00 K	398.10 K

Table 3.4.12: Case#06-Macroscopic results

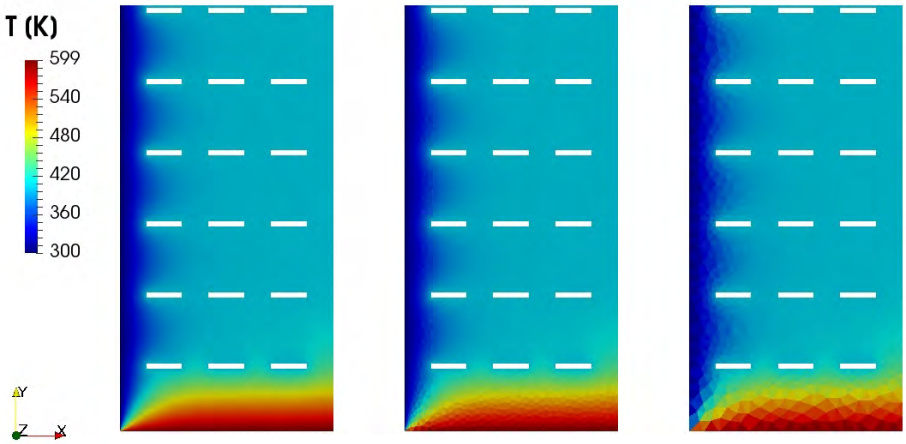

Figure 3.4.15: Case#06-ANSYS Fluent Temperature (from left F-R1, F-R2 and F-R3)

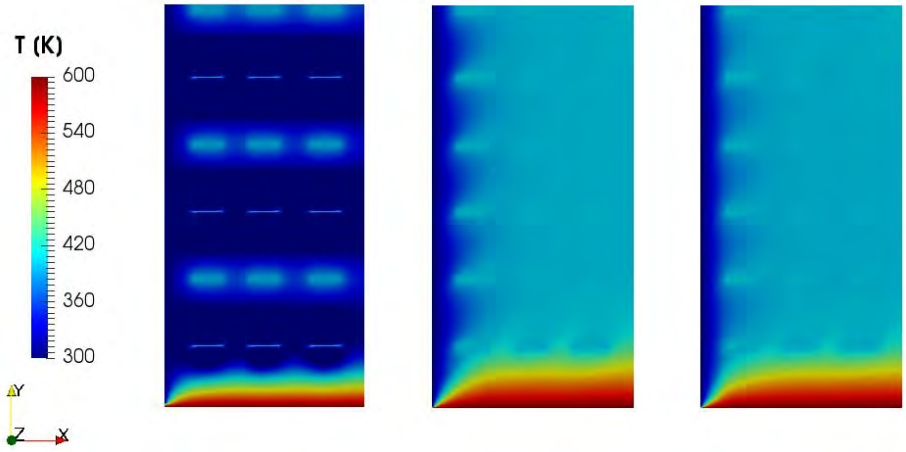

Figure 3.4.16: Case#06-AINA (from left M-R1, M-R2 and M-R3)

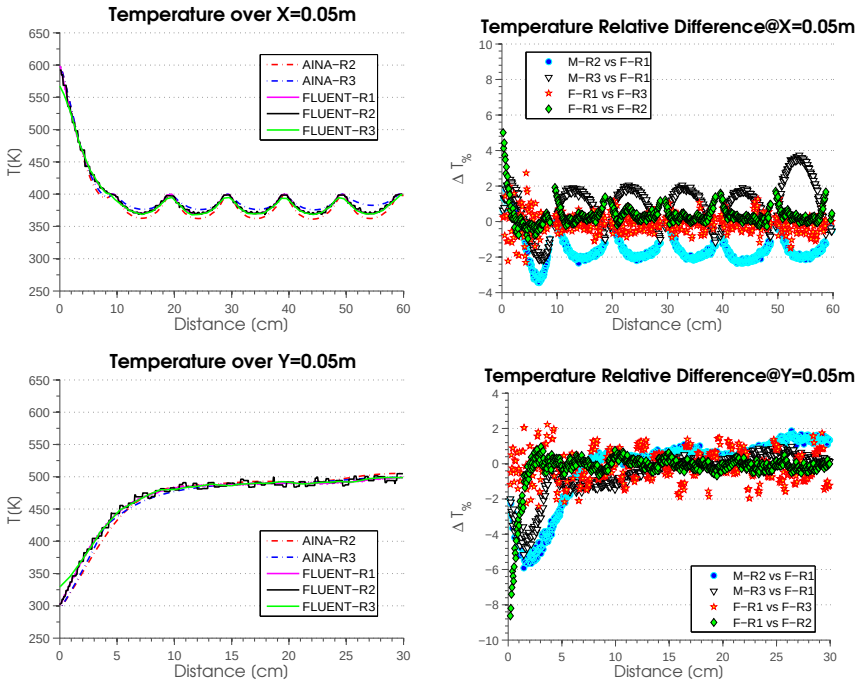

Figure 3.4.17: Case#06-Temperature and its relative difference at different locations

The case#06 validates the in-house routine with internal hole and fixed temperature applied.

3.4.2.7 Case#07

The Case#07 assumptions are reported in Table 3.4.13. The ANSYS Fluent mesh is the same employed in "case#06:F-R1" whereas the AINA one correspond to the "case#06:M-R3".

Type	Description
BC@X-	T imposed at 300K
BC@X+	Adiabatic
BC@Y-	T imposed at 600K
BC@Y+	Flux, $10^4 W/m^2$
BC@Internal Holes	HTC $10^3 W/K/m^2$, T imposed at 300K
Nuclear Heating	Equally distributed $500 W/m^3$

Table 3.4.13: Case#07-Assumptions

The 2D steady-state macroscopic temperature results are detailed in Table 3.4.2.7 whereas the local temperature field in Fig.3.4.18.

	No. Cell	T_{min}	T_{max}	$\overline{T}$
ANSYS	146636	336.26 K	599.99 K	456.73 K
AINA	20592	356.46 K	600.00 K	455.56 K

Table 3.4.14: Case#07-Macroscopic results

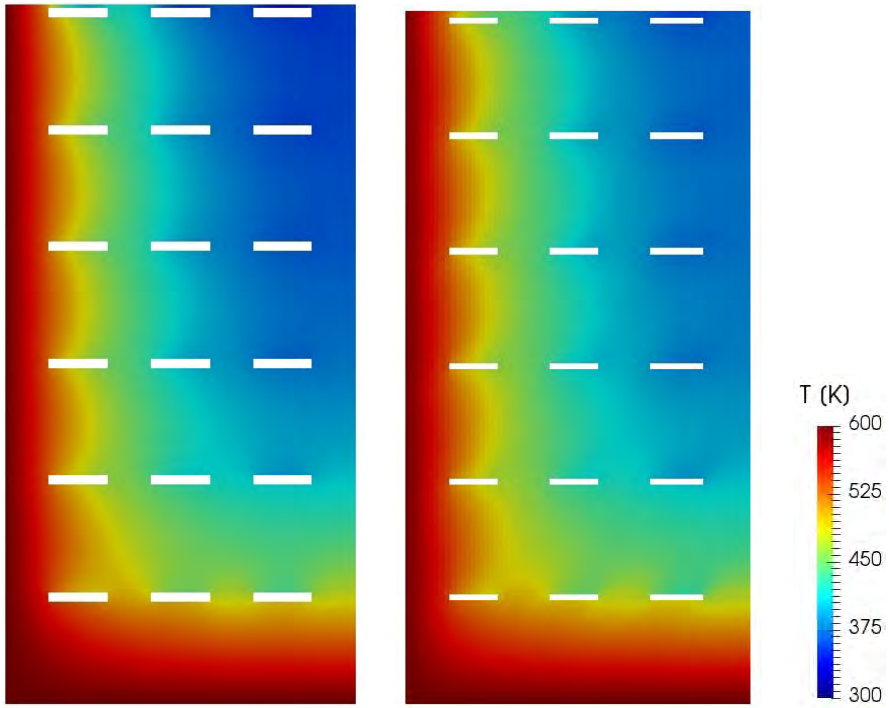

Figure 3.4.18: Case#07-ANSYS Fluent and AINA temperature

Both the macroscopic and the local results show a good agreement; the difference found 3.4.2.5 could be mostly addressed to the boundary effect (see section 3.4.2.1) and difference mesh sizes as showed in sect.3.4.2.6. The maximum relative local difference is below the 5.00% and seems to increase passing through the coolant pipes (Fig.3.4.2.5). There is not a clear under or overestimation of the in-house routine.

The case#07 validates the in-house routine with internal hole and Dirichlet BC applied.

3.4.2.8 Case#08

The Case#08 assumptions are reported in Table 3.4.15. The ANSYS Fluent mesh adopted is the same employed in "case#06:F-R1" whereas the AINA-2D one correspond to a slightly variation of the "case#06:M-R3" with a similar

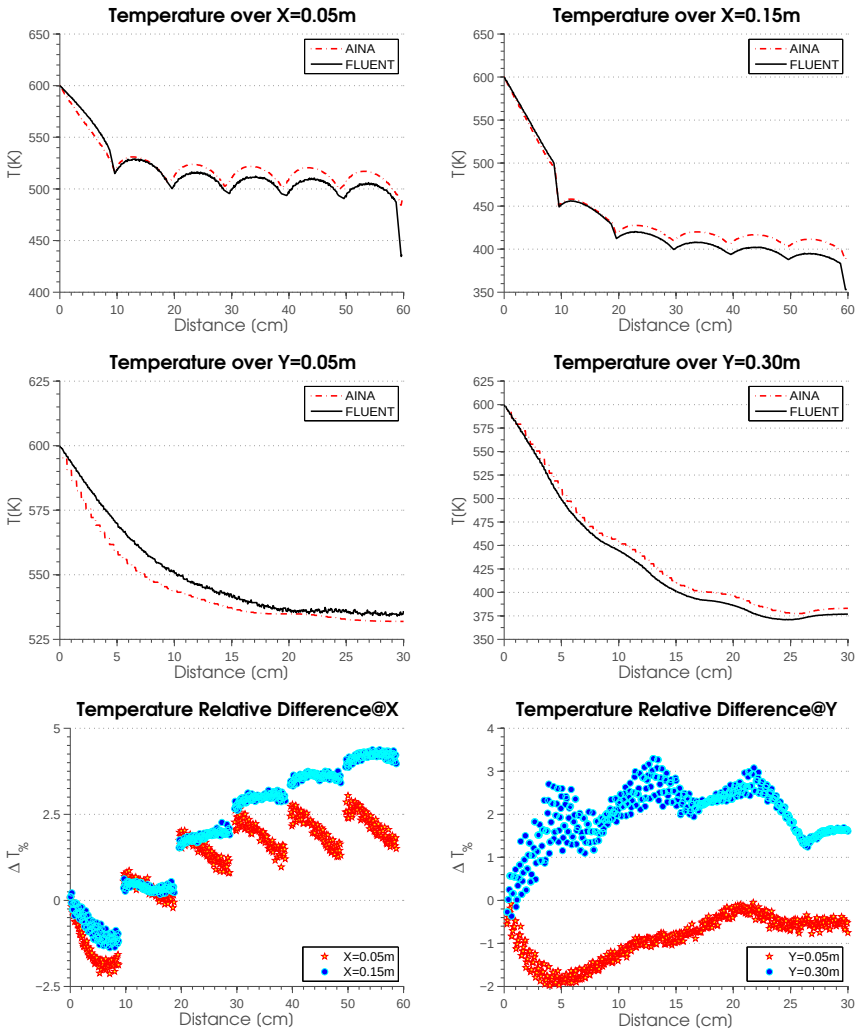

Figure 3.4.19: Case#07-Temperature and relative difference at different locations

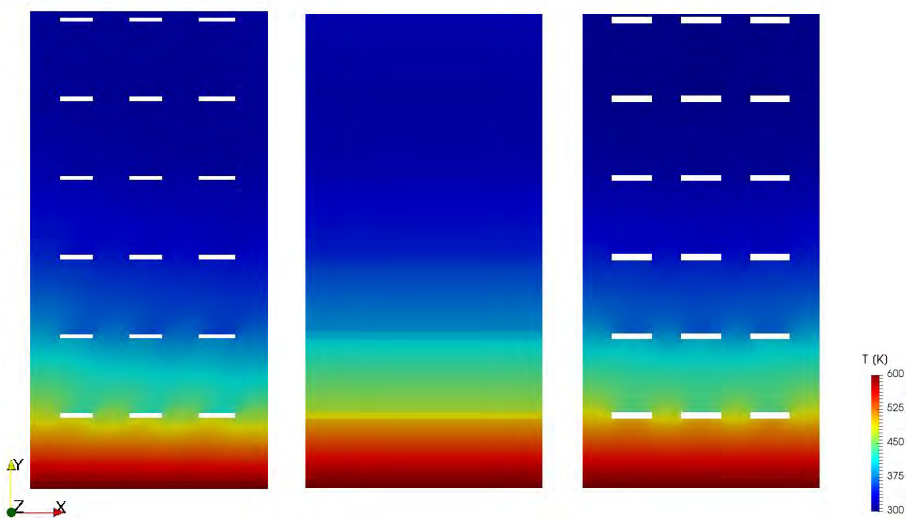

Figure 3.4.20: Case#08- AINA (2D,1D) and ANSYS Fluent temperature

resolution reaching X- and X+ boundaries. On the other hand, AINA-1D is the 1D model computed averaging the material characteristics over Y axis.

The 2D steady-state macroscopic temperature results are detailed in Table 3.4.2.8 whereas the local temperature field in Fig.3.4.20.

Both the macroscopic and the local results show a good agreement; the difference found could be mostly addressed to the boundary effect (see section 3.4.2.1) and difference mesh sizes as showed in sect.3.4.2.6. Fig.3.4.2.8 contains the temperature comparison along different locations including the "AINA-2D to 1D" parameter, which is the post processing temperature averaging of 2D data along Y axis. The post processing highlights a minor temperature overestimation of the in-house routine at different locations. In addition, the "AINA-1D" trend is very close to the "AINA-2D" although both the computational time and the memory requirements are at least one order of magnitude less. This wants to demonstrates that depending on the specific application all the in-house routine typologies shall be tested and suited before selecting the one which will be part of the AINA safety code because more complexity in the algorithm does not always correspond to more result accuracy and overall benefit.

The maximum relative local difference is below the 8.00% and seems to increase passing through the coolant pipes.

The case#08 validates the in-house routine for generic approximation of 1D model with the presence of internal pipes.

Type	Description
BC@X-	Adiabatic
BC@X+	Adiabatic
BC@Y-	T imposed at 600K
BC@Y+	Flux, $10^4 W/m^2$
BC@Internal Holes	HTC $10^3 W/K/m^2$, T imposed at 300K
Nuclear Heating	Equally distributed $500 W/m^3$

Table 3.4.15: Case#08-Assumptions

	No. Cell	T_{min}	T_{max}	$\overline{T}$
ANSYS	146636	306.71 K	599.56 K	367.77 K
AINA-2D	21600	314.33 K	600.00 K	376.60 K
AINA-1D	521351	314.33K	600.00 K	375.38 K

Table 3.4.16: Case#08-Macroscopic results

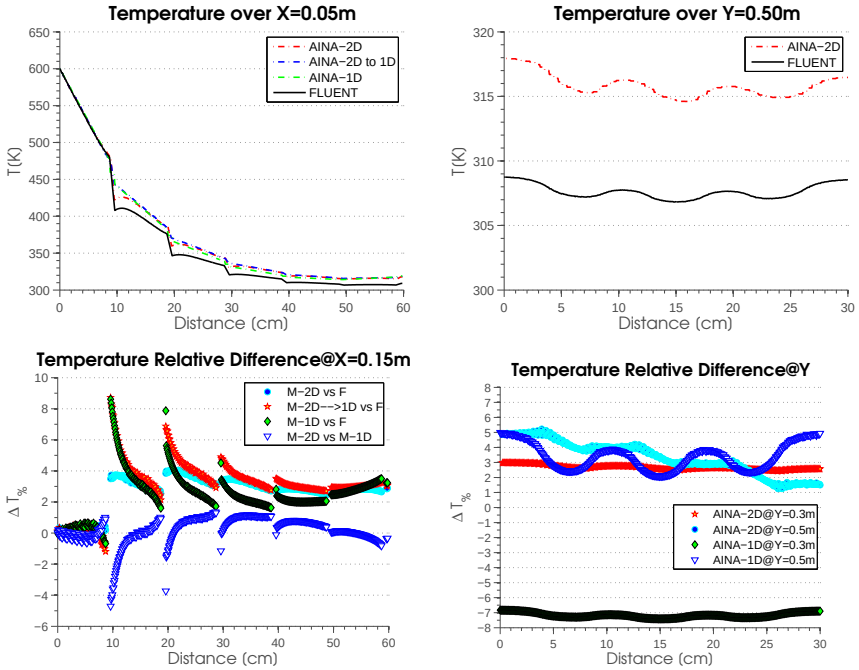

Figure 3.4.21: Case#08-Temperature and its relative difference at different locations

3.5 Error estimation and stability analysis

Analytical solutions, thus exact solutions, to heat transfer problems are restricted due to complexity to simple geometries and boundary conditions. For this reason, the thermal wall routines developed are based on the finite-difference method over a structured mesh. As described in Sec.3.3, the solution is computed and depends over a nodal net which covers the whole domain, averaging the solution over the single element of dimension $\Delta x \Delta y$ and in time, Δt. The source of errors which could be involved in the application of the FD are listed and rated in Table3.5.1(* low impact, ** medium impact, *** high impact).

Type	Rating	Chapter No.
Convergence (material properties)	**	3.5.1
Convergence (discretization)	**	3.5.1
Truncation Error	*	3.5.2
Numerical round off	*	3.5.3
Problem and domain simplification	***	3.5.4

Table 3.5.1: Possible source of error in FD

To conclude, a suited stability analysis has been carried out to bound the parameter for a valid and stable numeric solution.

3.5.1 Convergence Analysis

The problem discretization, both in time and space, could be one of the main source of error when the finite-difference method is used. Indeed, although the stability criteria is fulfilled (Sec.3.5.5), the model could lead to very inaccurate if the model discretization is not enough to couch the variation of the response functions as the temperature distribution.

For this reason, please consider the following 1D heat distribution SS example with the boundary conditions reported in Table 3.5.2.

Type	Description
BC@X(0)	Flux $5 * 10^5 W/m^2$
BC@X(L=0,6m)	T imposed at 225 K
Material	Eurofer
Coolant Channels Position	FW channel + eight equally spaced
Coolant Channels: $T_{BULK}[K]$	498
Coolant Channels: $HTC[W/m^2/K]$	1300
Nuclear Heating	Equally distributed $10^7 W/m^3$

Table 3.5.2: BC Convergence Analysis

To evaluate the convergence of the numerical method, the integral of the radial temperature profile as well its distribution have been computed for different

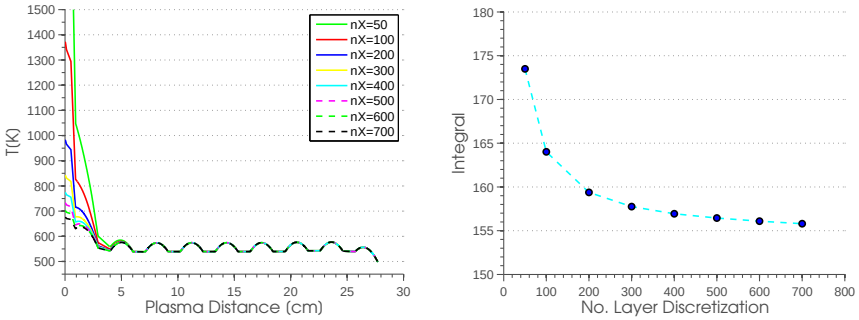

Figure 3.5.1: Grid density vs integral and temperature distribution

space discretization, Δx. As shown in Fig.3.5.1-(a), the temperature distribution evolves depending on the layer node discretization meanwhile its integral seems to converge to a finite value as the number of steps grows, Fig.3.5.1-(b). Indeed, larger space discretization, and so higher TE, causes very inaccurate temperature distribution mostly close to the FW where the conditions are the most restrictive. Similar conclusions can be obtained changing the time discretization, Δt.

In addition, as described in Sec.3.3, the solution scheme includes iterations to converge to the correspondent material properties in function of the nodal temperature starting from an initial assumption: the nodal temperatures depends on the material properties which variate with the temperature. This modus operandi, which avoids the presence of the material properties temperature derivatives, is concluded once both by a maximum number of iterations or an imposed precision is reached. In Fig.3.5.1-(a), the temperature distribution evolution of previous case with 400 nodes is reported with its step by step iteration convergence due to the material properties changes. Through the iterations, the temperature evolves progressively diminishing the variation from the previous estimation up to the final distributions, Fig.3.5.1-(b). Again, the most prominent difference as placed close to the FW where the highest temperature is present. To conclude, it is important to set a sufficient number of iteration or restrictive criteria to achieve a proper convergence.

3.5.2 The truncation error

The discrepancy that arises from performing a finite number of steps to approximate a process with infinitely many steps is defined as the truncation term error. This source of error, which is not only present in the finite difference scheme but also in several other fields as the truncation of infinite series and differential equations, is generated by the truncation of the Taylor Series up to a level n. To evaluate the numerical solution accuracy the residual $\Re$, which is the difference between the exact solution and the numerical solution at point x, has been computed.

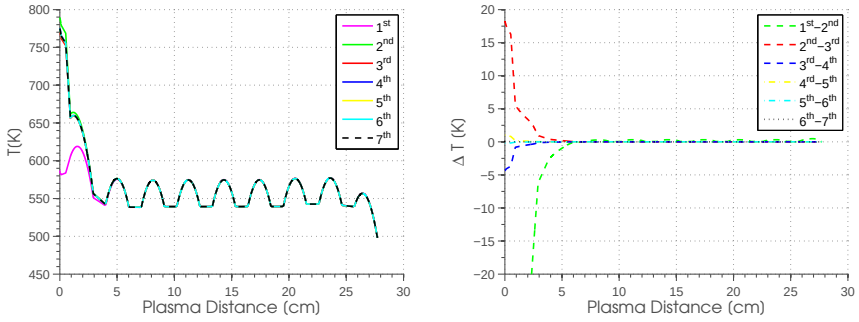

Figure 3.5.2: Temperature distribution vs material temperature

For sake of simplicity please consider a 1D heat equation applied to an internal point[13]:

$$\frac{\delta T(x)}{\delta t} = \alpha \frac{\delta^2 T}{\delta x^2} + \ddot{q}(x,t) \tag{3.5.1}$$

where α is thermal diffusivity and $\ddot{q}$ the volumetric nuclear heat deposition.

Applying to Equ.3.3.4 a implicit second order discretization in space and first one in time and at the same time considering the α and $\ddot{q}$ variables only dependent on x, we obtain for a generic internal node i

$$\frac{T_i^{n+1} - T_i^n}{\Delta t} = \alpha \frac{T_{i+1}^{n+1} - 2T_i^{n+1} + T_{i-1}^{n+1}}{\Delta x^2} + \ddot{q} + \Re \tag{3.5.2}$$

where the truncation error, $\Re$, is composed by the time derivative contribution and the space one and it is equal to:

$$\Re_{1D} = \Re_{time,1D} + \Re_{space,1D} \tag{3.5.3}$$

$$\Re_{time,1D} = \left(\frac{\delta^2 T(x)}{\delta t^2}\right)_i \frac{\Delta t}{2} + \mathcal{O}(\Delta t) \tag{3.5.4}$$

$$\Re_{space,1D} = \alpha \left(\frac{\delta^4 T(x)}{\delta x^4}\right)_i \frac{\Delta x^4}{12} + \mathcal{O}((\Delta x)^2) \tag{3.5.5}$$

Whereas, $\Re_{time}$ is of first order in time, proportional to Δt and present only for transient analysis, $\Re_{space}$ is second order in space, proportional to Δx and it appears both for transient and steady-state analysis. In order to reduce the truncation error, small discretization in time and space shall be used, however

[13] Most of the nodal point are classified as internal and only a minor part as boundary ones. For this reason, computing the truncation error all over the domain as reported is a good approximation.

this will increase the computational effort. Depending on the calculation requirements these parameter shall be changed and optimized taking always into account the numerical solution stability.

In the same way applying the same methodology to the 2D heat equation, 3.3.19, we obtain the following truncation error:

$$\Re_{2D} = \Re_{time,2D} + \Re_{space,2D} \tag{3.5.6}$$

$$\Re_{time,2D} = \left(\frac{\delta^2 T(x)}{\delta t^2}\right)_i \frac{\Delta t}{2} + \mathcal{O}(\Delta t) \tag{3.5.7}$$

$$\Re_{space,2D} = \alpha \left(\frac{\delta^4 T(x)}{\delta x^4}\right)_i \frac{\Delta x^4}{12} + \alpha \left(\frac{\delta^4 T(y)}{\delta y^4}\right)_i \frac{\Delta y^4}{12} \mathcal{O}((\Delta x, \Delta y)^2) \tag{3.5.8}$$

Equ.3.5.6 contains the same time truncation error but a bigger one in space due to the double space derivative. It is worth reminding that the convention term has been not considered in this paragraph because it does not have any impact on the truncation error as the coolant nodes are considered only applied to a single nodes.

To conclude, a specific routine has been developed for the TE determination and parameter screening to help the selection of the proper discretization $(\Delta x, \Delta y, \Delta t)$. For illustration, the script has been applied to the example reported in Sec.3.5.1 imposing an overfuelling accident equal to 1.5 times the nominal power over the initial 40s of transient and testing different discretizations in space (e.g. 50, 100, 200, 300, 400, 500, 600 and 700 discretization per layer) and time (time interval of 1s, 2s, 5s and 10s). As expected for all the simulations, starting for the steady-state condition, at t=0s, the temperature distribution evolves progressively toward more critical conditions, reaching at t=40s a similar state which seems to be close to another SS configuration (Fig.3.5.2-(a)). Indeed, at higher times the time temperature derivative is less pronounced. In addition, the time TE diminishes progressively using smaller time intervals (Fig.3.5.2-(b)) as for the space error employing finer nodal meshes. Both the integral space TE and the single TE at 0.2m from the plasma decrease using more nodes (Fig.3.5.2-(c,d)) as illustrated in the previous mathematical treatment. Summarizing we can conclude that smaller TE, both in time and space, corresponds to finer dicretization hence an heavier computation effort. Please remember that the smallest nodalization does not always mean the best solution. Indeed, smart nodalization can be employed refining the solution where the derivatives are bigger while relaxing in other zones. For instance, the time TE can be optimized applying shorter time step in [0, 20s] hence relaxed in [20, 40s] and the space TE using a more accurate mathematical treatment. In general, please consider the application of compromise between precision and computational error as for the showed example could be $\Delta x = 500, \Delta t = 2s$.

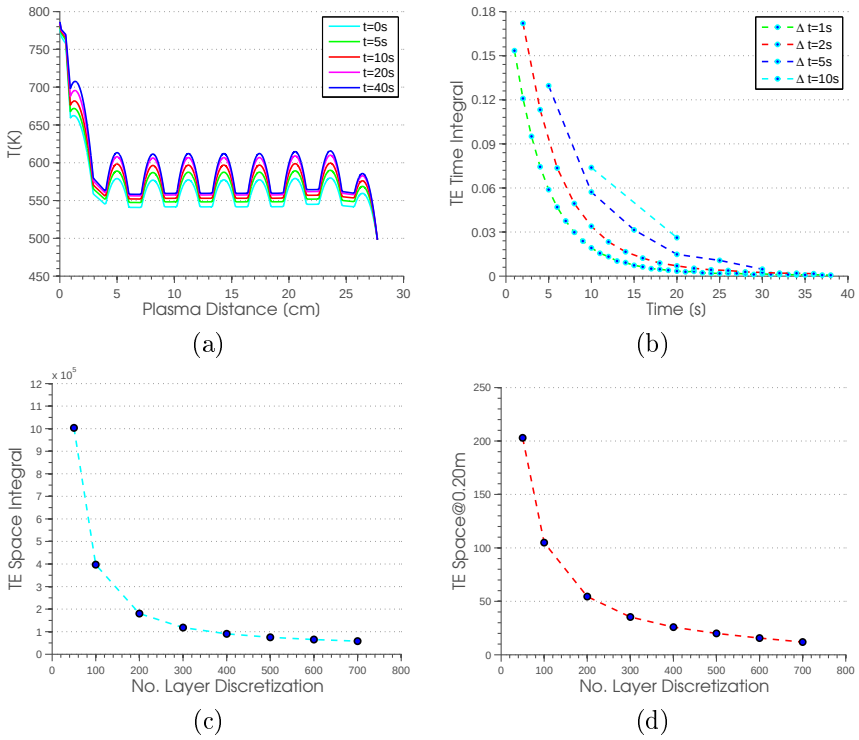

Figure 3.5.3: Truncation Error

3.5.3 Numerical round-off

A round-off error, [109], is defined as the difference between exact mathematical value and the calculated one due to rounding approximation. This error is present every time a computer is involved in the calculation process and many digits are involved. However, this effect has low impact on the final result, it is should be monitored in particular when a sequence of calculations is done or in ill-conditioned problems because errors may accumulate and propagate.

3.5.4 Problem and domain simplification

One of the main source of error in any numerical resolution is the "problem and the domain simplification". Indeed, each case has to be approximated in terms of suitable boundary conditions, initial conditions, domain of interest and material properties. The transposition and simplification of real conditions to the problem ones shall be controlled and its impact estimated as much as possible hence corrected if possible. For this reason, the verification and validation process, [103], shall be nested in each problem from the problem formulation to the peer review. Simplified models should be used, if possible, once more detailed ones have been tested to avoid any erroneous physical effect or underestimation. It is

worth reminding that when the consolidated and final results is reported both the accuracy and the precision has to be taken into account and differentiated.

3.5.5 Stability Analysis

Starting from the 3D heat equation, Equ.3.3.1, finite difference are used to replace both the time and space derivatives using a implicit first order discretization in time and second one in space (Equ.3.3.4, Equ.3.3.19).

Doing so both the time and spatial discretization specifications, the so called *stability criterion*, are needed to have numerical *stability*, avoiding nonphysical and numerical induced oscillations, preventing erroneous results. The implicit method has the great advantage to be unconditionally stable whereas the explicit one not requiring the definition of a stability criterion. In this way any discretization can be implemented without affecting the stability but, of course, having an impact on the accuracy as detailed in Sec.3.5.1.

On the other side, the implicit method is more resource demanding than the explicit one because the unknown nodal temperatures at time t has to be solved simultaneously and iteratively.

3.6 Conclusion and future developments

A series of flexible thermal-hydraulics routines have been built in order to obtain reliable, approximate but conservative thermal-wall results in a short-notice using a standard workstation. It is worth highlighting that these routines do no want to substitute the 3D CFD studies whereas to take advantage of their outcomes and characterize the system behavior in a simplified way. A detailed description has been provided both for the methodology and for the proposed mathematical treatment. The routines, which are based on the finite difference technique, can be easily tuned to allow the implementation to any blanket types or geometries. Model dimension (1D or 2D), type of solution (steady-state or transient), material identification and mesh spatial domain, presence of the cooling areas and implementation of any type of BC are some of settable options. Post-processing tools have been created to automatize the production of a series of outputs in the standard VTK format which can be employed in numerous external software. The thermal routines have been verified and cross-checked against analytic solutions (when possible) and the commercial CFD software ANSYS Fluent ones. Macroscopic and local temperature results have been compared finding a very good agreement and a maximum local difference of 8% that can be mainly attributed to the different treatment of boundary condition and to the different accuracy of the numerical solution, the so called "boundary effect" (see sec.3.4.2.1). Specific studies have been done highlighting that the discrepancy could be considered within the mesh sensibility. In addition, the in-house thermal routines shown a better agreement to the reference data once minor adjustments and refinement are done in the AINA mesh discretization despite of the more computational costs needed. Indeed, the 2D developed

routine requires at least one order of random-access memory and time more than ANSYS Fluent; normally it is not possible to achieve the number of CFD mesh element due to the memory constrains. On the other hand, the 1D in-house routine is more fast and less memory demanding than the 2D one thanks to the limited matrix dimension and a comparable performance to the CFD code.

Depending on the specific application all the in-house routine typologies (1D and 2D domain) shall be tested and suited before selecting the one which will be part of the AINA safety code because more complexity does not always correspond to a better accuracy. The collapse of a blanket model into the AINA thermal block is not a one-shot process but a complex and iterative one. A detailed methodology has been developed and it shall be from now on followed (see sec.2). Several adjustments, as the application of safety functions, could be needed if the results are not conservative.

It is worth reminding that the described routines have been already employed in several studies and presented to the Fusion community obtaining a very positive feedback[110]. Considering all the verification process carried out and the new features implemented, the AINA thermal block is more flexible, conservative and manageable than the previous one version.

Future development should be focused in conversion of the routine to external programming language (e.g. Python, C++, etc...), the improvement of its performance and the incorporation of a correction term which takes into account the TE thus increasing the solution accuracy.

Chapter 4

Water Cooled Pebble Bed (Japanese-DEMO)

4.1 Introduction

In this chapter, the work done regarding the Water Cooled Pebbled Bed Japanese DEMO blanket concept is presented and its main features described, Sec.4.1.1. In the frame of the *Broader Approach Program* [33], the collaboration between Japan-EU related to the ITER project, a specific version of AINA code has been developed for the WCPB Japanese DEMO design. This has triggered the realization of the safety studies and the publication of several peer-reviewed contributions, *"Safety studies of plasma-wall events with AINA code for Japanese DEMO"* [54] , *"Safety studies for Japanese demo design with AINA code"* [111] and "*Methodology for the improvement of the AINA Code wall-model applied to DEMO WCPB blanket*" [112].

Within the several tasks carried out, my support has been mainly focused on:

- Endorsement of the proposed methodology for the AINA development (Sec.2.1)
- Radiation transport analysis and sensibility assessments (Sec.2.2)
- Thermal-hydraulic analysis and sensibility assessments (Sec.2.3)
- Blanket collapse[1] toward the creation of the AINA thermal-wall model (Sec.4.4)
- Support to *Secondment expert from UPC-FEEL to IFERC Japan, 2014-2015,* [51]

[1] This operation is defined as *"blanket collapse"* because it aims to obtain to move from the a fully detailed model to a simplified one retaining the characteristic features of the systems as much as possible.

As described in Sec.2.1, the first stage in the development of the AINA wall model is the determination of the neutron/photon power deposition and tritium production by means of the radiation transport calculations, Sec.4.2. Therefore, fully detailed 3D models have been generated according to the methodology described in Sec.2.2. In addition, the results have been double checked and compared with those obtained by simplified 1D model, which are less resource demanding. Thus, several assessments have been performed determining the impact of the model definition (1D heterogeneous vs homogeneous layers definition, Sec.4.2.2.3), influence of boundary conditions (Sec.4.2.2.4), cross-sections typology (FENDL2.1 vs FENDL3.1b, Sec.4.2.2.6) and the effect of operational conditions due to density variation and resonance broadening, Sec.4.2.2.7.

At this point, a fully detailed 3D CFD model has been generated, defeaturing the original CAD and meshing it according to the approach described in Sec.2.3.1. Then, the nuclear heating density has been applied to the model taking advantage of the ANSYS Fluent UDF developed hence the thermal-hydraulics simulation carried out. Furthermore, additional meshes (e.g. polyhedral elements) have been generated and run to exclude any possibility of mesh independence and the NHD sensitivity checked as recommended by [95]. Likewise, a 2D CFD model with even finer discretization has been also created to reject any probability of having material temperatures depending on the model topology and geometrical assumptions.

Therefore, having a consolidated he 3D WCPB BB temperature field and nuclear power deposition, the first AINA wall model concept has firstly drafted hence iterated reaching a configuration which best represents the detailed behavior. Indeed, thanks to the good toroidal NHD and geometrical symmetry, a 1D configuration has been finally selected obtaining at nominal conditions a good temperature agreement within the 10% and so largely within the initial requirement and expectation endorsing the new approaches implemented. Nevertheless, at some locations the temperature distribution computed by the AINA WCPB thermal-model resulted not conservative once if compared with the outcomes obtained for the 3D fully-detailed ones (e.g. 20°C less in temperature peak). This is a consequence of the 1D bigger cooling surface/volume ratio, the mayor distance between the cooling tubes than the 3D modelling and the absence influence of the nearby zone. These features are model intrinsic. Thus a scaling approach has been employed instead to match the responses only where the results are non-conservative and increasing the safety-margins. These distributions, which are the ratio between the most conservative 3D radial distribution and the 1D AINA wall model one, have been computed for the different operational levels (80%, 100%, 120%). To enhance the safety margin, the scaling functions are applied only if the $f_{T_{3D}}(X) > f_{T_{1D}}(X)$. Besides, sensitivity studies of the AINA wall model temperature distribution versus NHD type, HTC variation and water bulk temperature have been carried out as well as preliminary study regarding LOCA and LOFT accidents.

To conclude it is worth reminding that all the analysis performed has employed the WCPB configuration of 2014 [113] and the related data [14] provided by International Fusion Energy Research Centre (or IFERC) team.

4.1.1 System description

As anticipated in Sec.1, nowadays different conceptual DEMO projects are under elaboration and scrutiny by different parties because no clear cohesion is foreseen in the ITER project. The experience and the know-how gained from the ITER project is shared among the seven parties apart from the Test Blanket Modules (or TBM) technologies. It is developed individually by the Domestic Agencies and it represents an unique possibility to test DEMO BB mock-ups in real fusion conditions.

The Japanese DEMO activities are carried out on a Japan-wide basis involving seventy researcher, sixteen university and laboratories also with the support of Fusion for Energy within the *Broader Approach Program* [33].

Since the beginning, one of the Japanese DEMO BB concept has been the Water Cooled Pebble Bed, Fig.4.1.1, based upon the solid ceramic breeder, the lithium metatitanate, Li_2TiO_3, embedded in a F82H structure, which is a reduced activation ferritic/martensitic steel developed in particular for fusion applications. The breeder in form of pebbles is mixed uniformly with a neutron multiplier, the $Be_{12}Ti$, to enhance the Tritium Breeding Ratio but avoiding any reaction with hot water in the case of breaking of the coolant as if only Beryllium is used. A water coolant pipes system (155 bar and about 2.6 m/s of velocity) is placed inside the BB to export the heat deposited inside the mixed breeder as well as a nested cooling channels inside the First-Wall, which is coated by a very small of Wolfram layer to improve its resistance. In addition, an independent extraction system is used to collect the Tritium produced within the BB [14, 114, 115, 116]. Moreover, the cooling channels are also nested in the side walls and top/bottom plates.

4.1.2 Material specifications: thermo-physical properties and correlations

The thermo-physical properties and correlations of the material employed for the WCPB analysis have been reported hereinafter:

- Water, Sec.4.1.2.1
- Wolfram, Sec.4.1.2.2
- F82H, Sec.4.1.2.3
- Breeder material, Sec.4.1.2.4

4.1.2.1 Water

Steam and water properties employed are taken from the "International Association for Properties of Water and Steam Industrial Formulation 1997 (IAPWS IF-97). Th complete IF-97 standard, which provides a very accurate steam and water properties in ranges from 0-1000 bar and 0-2000°C, have been used by means of a database [117] to automatize the thermal-routines.

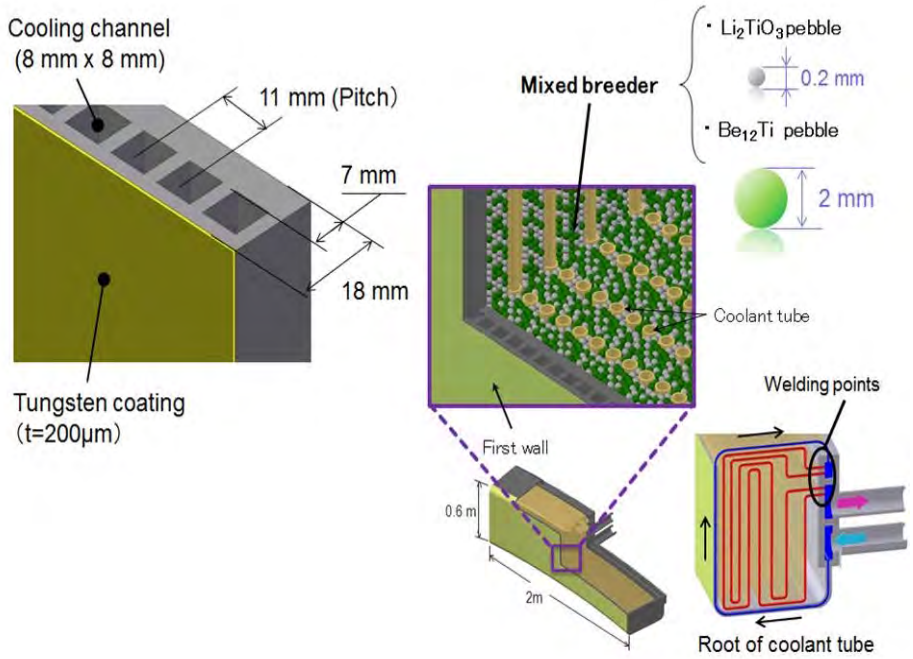

Figure 4.1.1: WCPB Concept [14, 15]

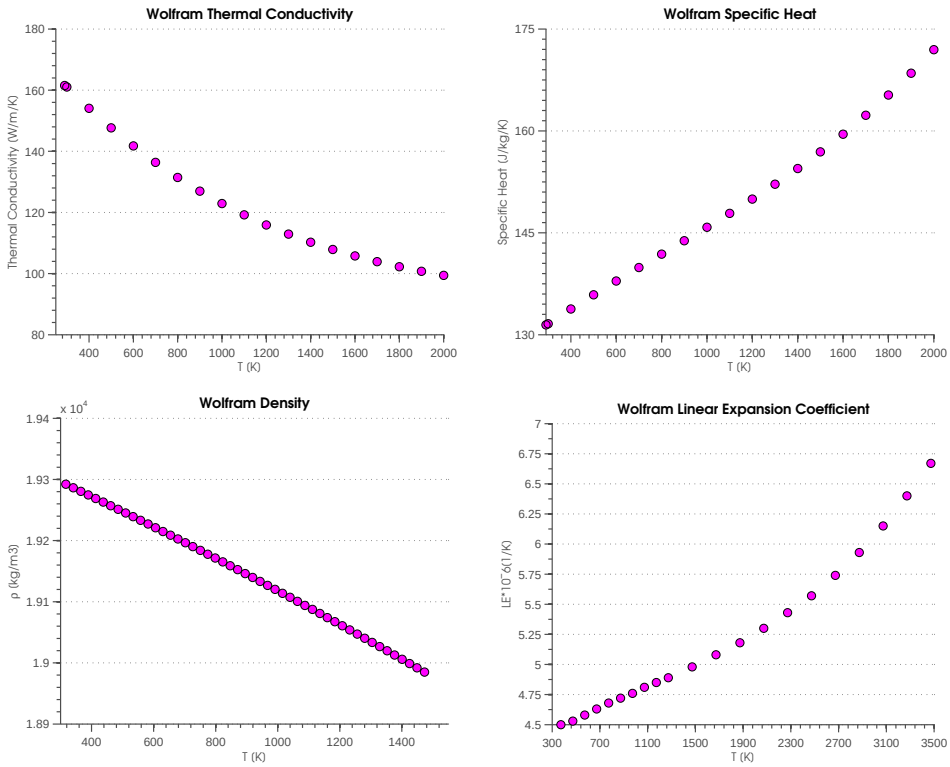

Figure 4.1.2: Wolfram properties [14, 15]

4.1.2.2 Wolfram

The WCPB approach utilizes pure Wolfram coating as FW material. The material properties assumed have been reported in Fig.4.1.2.

4.1.2.3 F82H

F82H is a the reduced activation ferritic/martensitic steel (Fe_8Cr_2W) with small additions of C, Si, Mn, Ti, V and Ta. It has being developed since 1980 as the structural material for the fusion demonstration reactor DEMO [118]. The content of all impurities and in particular the high activation elements are kept very low to limit as much as possible the Shutdown Dose Rate and the plant occupation dose. The F82H composition is reported in Table 4.1.1 whereas its features in Fig.4.1.3. It is worth reminding that its composition and features are very similar to the EUROFER Steel [119] developed by the EUROfusion community qualified by the RCC-MRx code and used in the ITER Test Blanket Models.

Element	Quantity
Fe	8.78E-01
Cr	8.40E-02
Nb	5.00E-05
Cu	5.00E-04
Mo	5.00E-04
Mn55	5.00E-03
Sn	4.00E-05
P	4.00E-04
B	3.00E-05
S	3.00E-04
V	3.00E-03
N	2.00E-04
Si	2.00E-03
Al	2.50E-04
O	1.00E-04
Ti	1.00E-04
Co	1.00E-04
Ni	1.00E-03
Ta	1.00E-03
C12	1.20E-03
W	2.20E-02

Table 4.1.1: F82H Elemental composition [14]

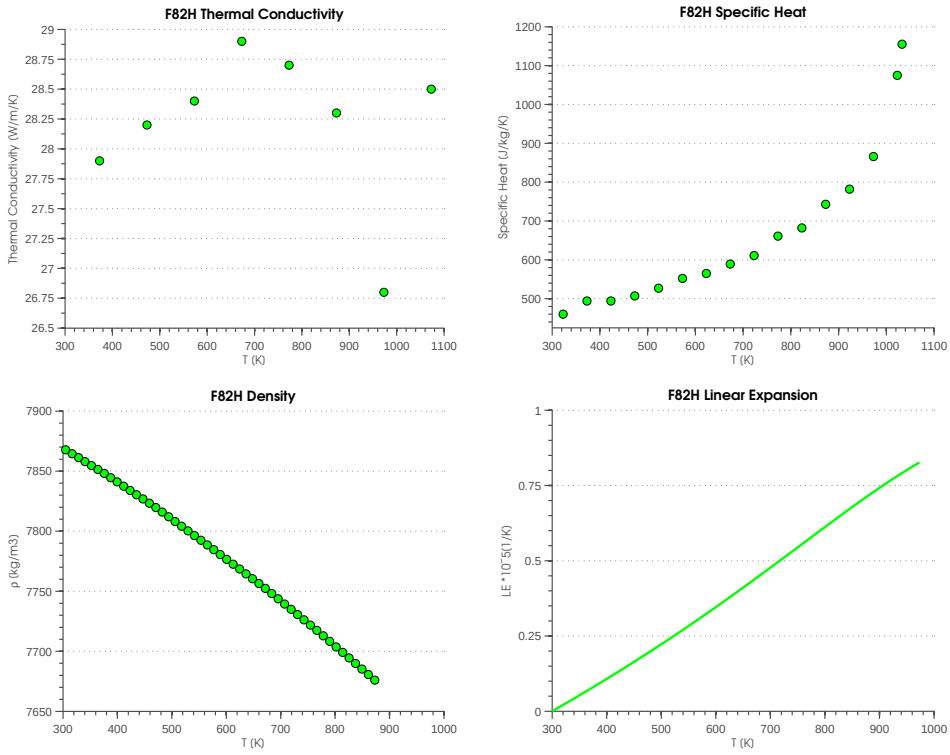

Figure 4.1.3: F82H properties [16, 14]

Element: $Be_{12}Ti$	Quantity
Be	6.93E-01
Ti	3.07E-01

Element: Li_2TiO_3	Quantity
Ti	4.43E-01
Li_7	1.30E-02
Li_6	1.00E-01
O	4.44E-01

Element: $Breeder$	Quantity
Li_2TiO_3	1.60E-01
$Be_{12}Ti$	6.40E-01
$He-gas$	2.00E-01

Table 4.1.2: Breeder Elemental Composition [14]

4.1.2.4 Mixed breeder : Li_2TiO_3 & $Be_{12}Ti$

The WCPB design employs a mixed ceramic breeder which is composed by $Li_2TiO_3$and $Be_{12}Ti$ pebbles of 0.2 mm and 2 mm of diameter aiming to have the Tritium self-sufficiency hence a Tritium Breeding Ratio (or TBR) major than one. The Litium is used as *breeder* material thanks to its capacity to to produce Tritium by (n,T) or (n,n'T) reactions:

- ${}^6Li + n \rightarrow T + {}^4He + 4.78\ MeV$
- ${}^7Li + n \rightarrow n' + T + {}^4He - 2.47\ MeV$

In addition, the process efficiency is improved by the introduction of a *multiplier*, the Beryllium, which is a material prone to undergo (n,2n) reactions thus able to increase the neutron field so the Tritium Breeding Ratio.

The breeder composition is reported in Table 4.1.2 whereas its features in Fig.4.1.4.

4.2 Radiation Transport Analysis

Three-dimensional radiation transport calculations have been performed employing the MCNP6.1 (Monte Carlo N-Particle Transport Code) [75] with special attention to the neutronic performance of the WCPB blanket, focusing on the nuclear heating density, the tritium production and the neutron/gamma field. Coupled neutron/gamma transport calculations have been carried out using the reference cross-section library for the ITER Project, FENDL3.1b@300 K (Evaluated Nuclear Data Library for Fusion Applications) [18], at room temperature densities. A MCNP fully detailed blanket stand-alone model has been created using state-of-the-art methodology. SpaceClaim [90] and CATIA [91] software have been employed for the geometry defeaturing to allow the generation of MCNP geometry by means of SuperMC [78, 79], limiting the volume

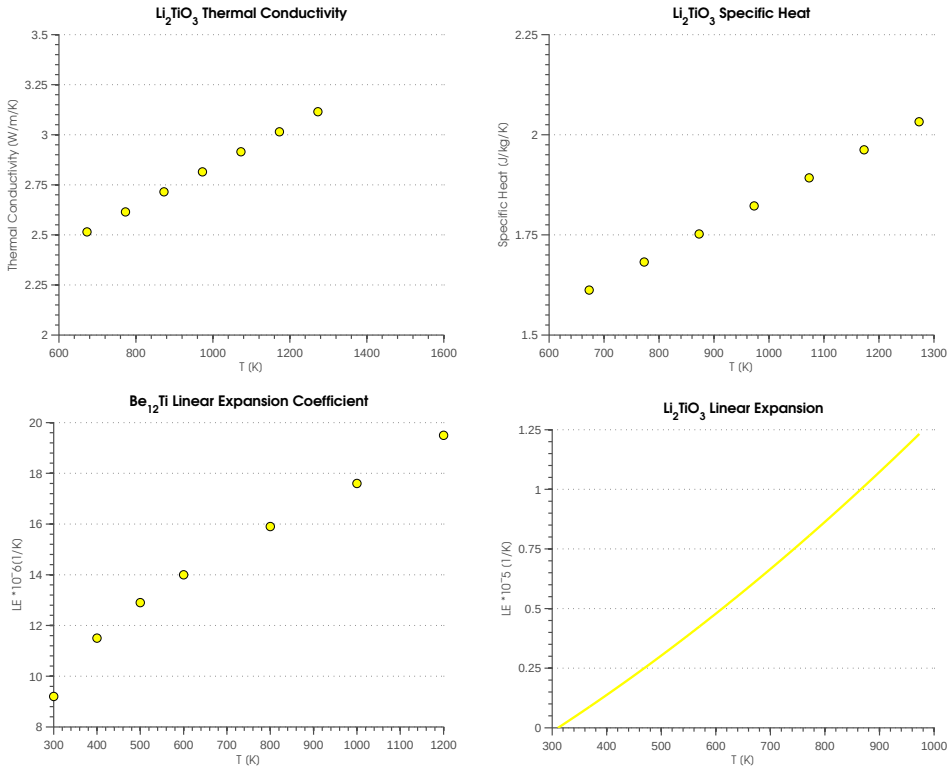

Figure 4.1.4: Breeder properties [14, 15, 17]

differences due to simplification to less than 1% preserving the details as much as possible. Volumetric Deuterium-Tritium Gaussian fusion source has been assumed and the Neutron Wall Loading (NWL) normalized to $1\,MW/m^2$. Reflective boundary conditions have been imposed on the blanket lateral sides for conservatism. The energy-dependent weight window variance reduction technique, generated by ADVANTG deterministic code [10, 80], has been employed to obtain the quantities of interest with the desired statistical uncertainty and optimizing the computational effort. Results have been obtained and evaluated by means of tally and mesh-tally features.

In addition, two 1D blanket simplified MNCP models have been generated in order to further optimize and reduce the computational effort enabling multiple assessments (e.g. boundary condition impact Sec.4.2.2.4, temperature impact Sec.4.2.2.7, cross section impact Sec.4.2.2.6). Starting from the 3D WCPB representation, forty-seven radial parallel layers have been created to preserve the in-vessel features as far as possible. In the end, they differ only in the material composition of the slices. Indeed, whereas one model employs the most representative material of the segmentation, the other uses a homogenized material mixture corresponding to the effective cell composition. They are therefore identified as the heterogeneous (1D-HET) and the homogeneous (1D-HOM) model. After a meaningful comparison, the first model has been preferred due to the greater integrated power deposition as well as the preservation of the NHD peaking profile. Moreover, 1D-HET results have been used as reference radiation transport data for thermal-hydraulic analyses because they imply the most conservative temperature distribution.

4.2.1 Fully detailed 3D MCNP model

4.2.1.1 Model generation: geometrical simplification, CAD conversion and material card generation

As detailed in Sec.2.2, the first stage in the creation of a MCNP model is the geometry simplification. Commonly, the CAD engineering model contains too much geometry details (e.g., fillets, chamfers, bolts, springs, screw holes and threads), incompatible surfaces (e.g., splines) or with complex structure which is not important for neutronics analysis. These features will make the translation to MCNP file more difficult or impossible. Therefore, it has required appropriate simplifications and modification of the provided geometry using state-of-the-art software as SpaceClaim [90] and CATIA [91]. Considering the enormous number of elements contained in the original CAD (e.g. about 10000), the defeaturing and the homogenization of some components were clearly necessary to achieve an manageable MCNP model. Moreover, to preserve as much as possible the radiation transport behavior (mainly along the radial direction), simplifications have been applied only where strictly necessary, limiting the volume simplification differences to less than 1%. All the water pipes have been maintained as heterogeneous (e.g. water and F82H tube separated cells) replacing only the round with shaped corners. On the other hand, the FW

	Cell No.			Surface No.		
	From	To	Total	From	To	Total
Main parts	1	1411	1411	1	1367	1367
Universe No.1	10000	12153	2154	10000	12601	2601
Universe No.2	20000	22828	2829	20000	23455	3455
Universe No.3	30000	31905	1906	30000	32312	2312

Table 4.2.1: MCNP cell and surface distribution

(Wolfram, water and F82H) has been split in multiple bodies as well as the back plate to enhance the MCNP conversion by means of SuperMC [78, 79]. Besides, the cooling channels nested inside both the BB walls and the top/bottom plate have been removed, representing these components as homogenized bodies with the correspondent water/F82H ratio mixture. In addition, a simplified Vacuum Vessel has been implemented by on the back of the WCPB BB to preserve the back-scattering provided by the components, Fig.4.2.3. It is composed by three different layers: inner and outer shells are made by F82H while the inner part by a mixture of F82H+H20 (60%/40%) to indicate the presence of metallic structure as the in-wall shielding or VV ribs.

The MCNP material cards have been generated using the element composition reported in Sec.4.1.2 and applying the FENDL3.1b cross section with the photon transport data from MCPLIB84 libraries.

Then, the CAD-MCNP conversion has been carried out with the SuperMC [78, 79], assigning to each cell the correspondent material definitions and densities at room temperature (300 K). In order to optimize the model generations and to limit the geometrical operations, the CAD conversion have been carried out in two main blocks: the BB case and the BB area, which has been further divided in three additionally zones with a lower level universes. Thus, only the heterogeneous pipes were modeled in the simplified CAD and the mixed breeding area obtained by the automatic void generation function of SuperMC using the convex cell algorithm and a surface No. limitation equal to 300. In Fig.4.2.2, the MCNP universe representation is detailed as well as the top-level universe filling cells. Therefore, using this enhanced modeling approach, further modifications over the BB area could be implemented without the necessity to replace or re-model other components. Several iterations between the simplified CAD and the MCNP model have been performed to adjust surfaces, empty space and interference in order to achieve a suitable lost particle rate. The consolidated fully detailed 3D MNCP model is composed by very large number of cells and surfaces, respectively 8303 and 9735, as detailed in Table 4.2.1.

Several cross sections of the fully detailed MCNP model are reported in Fig.4.2.3:

- Fig.4.2.3-(a): Z cross section over the whole model. All the major components are marked as well as the plasma source position. The articulated pipe shape is preserved as well as its connection to the back-plate.

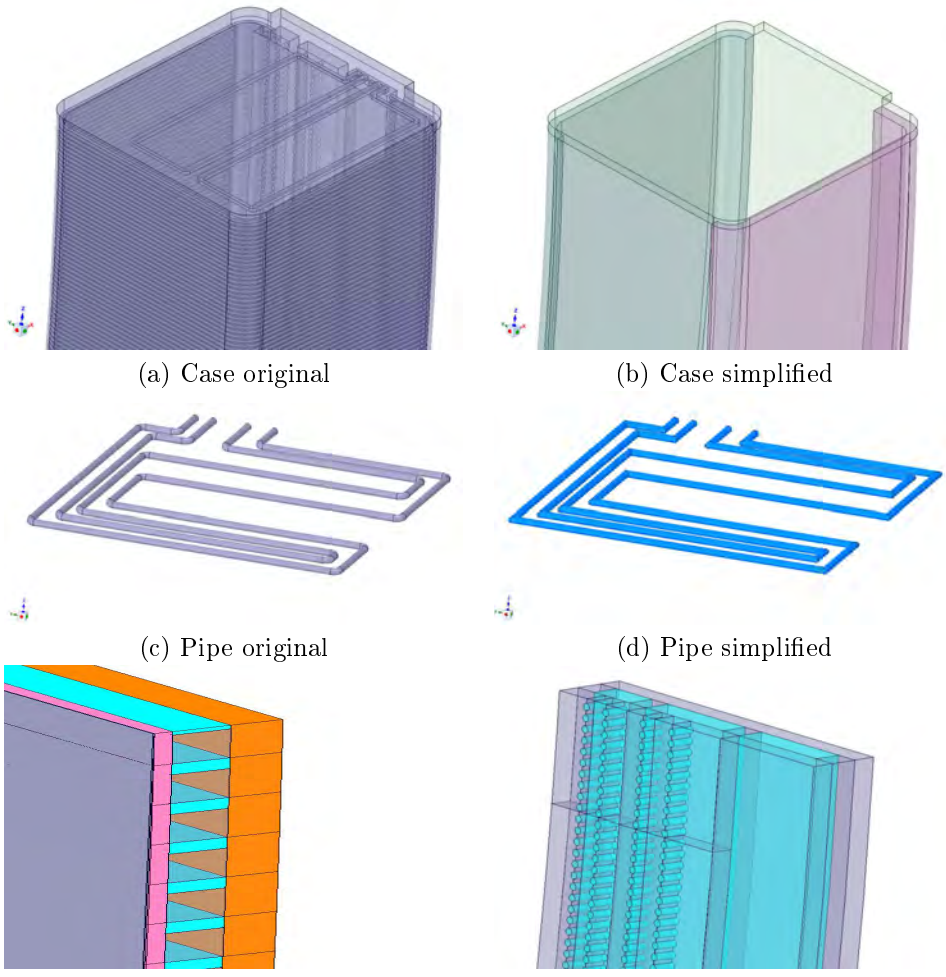

(a) Case original

(b) Case simplified

(c) Pipe original

(d) Pipe simplified

(e) FW simplified

(f) Back plate simplified

Figure 4.2.1: CAD to MCNP Simplifications

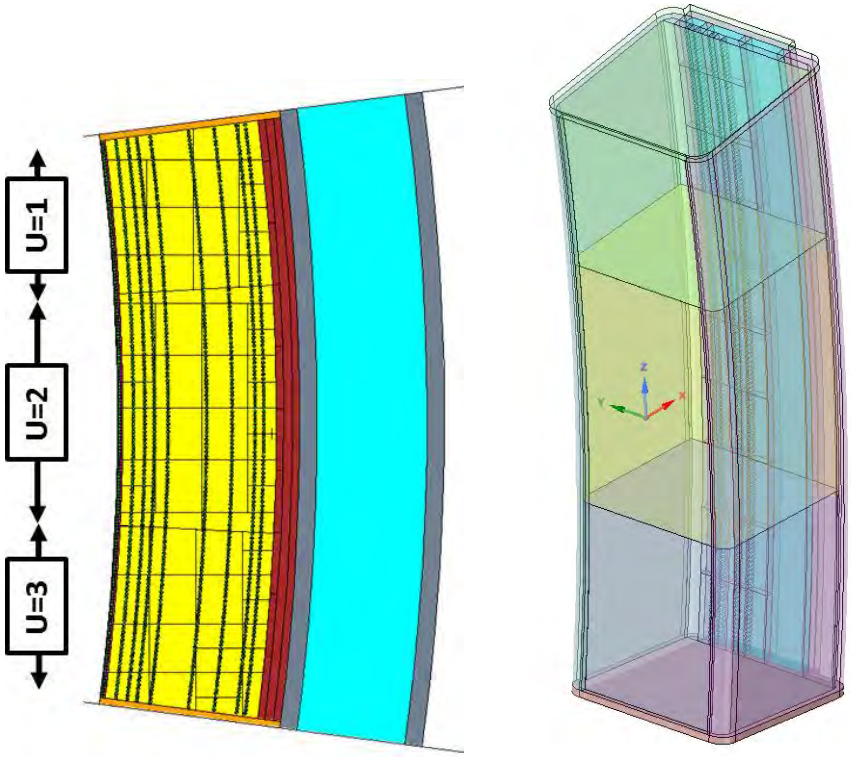

(a) (b)

Figure 4.2.2: MCNP universe structure: 2D (a) vs 3D (b)

- Fig.4.2.3-(b): X cross section over the FW area pointing out the presence of the cooling paths and the Wolfram layer on its top. In addition, the pipes heterogeneity is observed.
- Fig.4.2.3-(c): X cross section over the pipe connection with the back-plate showing the large number of detailed maintained in the model.
- Fig.4.2.3-(d): X cross section over the BB region revealing the constant thickness of the manifold elements.

4.2.1.2 SDEF definition and normalization

A volumetric and isotropic Deuterium-Tritium neutron Gaussian fusion source has been assumed in front of the whole WCPB FW. The mean energy spectrum and full width at half maximum (FWHM) have been imposed equal to 14.0791 MeV and 0.53415 MeV as in [120]. The results have been normalized to a Neutron Wall Loading (NWL) of 1 MW/m^2 using the neutron current impinging FW. An optimized random number and stride [2] have been employed according to [120].

4.2.1.3 Variance reduction techniques and tally definitions

Primary nuclear responses of interest are the WCPB integral nuclear heating and detailed 3D heat deposition maps due to plasma neutrons and secondary prompt photons. These have been obtained by implementation of the MCNP tally cards described in Table 4.2.2[3]. The following typologies have been applied:

- F4[4] over the first wall to determine surface neutron current
- F4 over the breeding material to estimate the tritium production using type and 205 MT ENDF reaction within a dedicated FM card[5]
- F6[6] over the major components (e.g. first wall, side walls, back plate) to determine the nuclear heating by the neutrons and the photons

To accelerate convergence of nuclear heat response tallies at the required locations, optimise computer resources and achieve meaningful statistical errors within a reasonable timescale, weight window mesh and biasing parameters

[2] RAND GEN=2 SEED=501932527452161 STRIDE=152917 HIST=5518120

[3] The WCPB BB model aims to provide result during plasma irradiation; regarding additional contributions due to activation or components or heating systems are not considered in this work because their design is still immature and commonly of minor impact during the plasma scenario operation.

[4] As explained in Sec.2.2.4.4, this estimator uses the fundamental definition of the flux as the number of particle-track lengths per unit of volume [75].

[5] It is a tally multiplier card [75]. It can be used to estimate a specific reactions or response as the d.p.a., doses or He ppm production.

[6] As explained in Sec.2.2.4.4, this estimator is a track-lengths estimators of the flux with a energy-dependent multiplier. Therefore, the F4 tallies with a proper energy dependent multiplier, FM card, can be equivalent to F6 tallies [75].

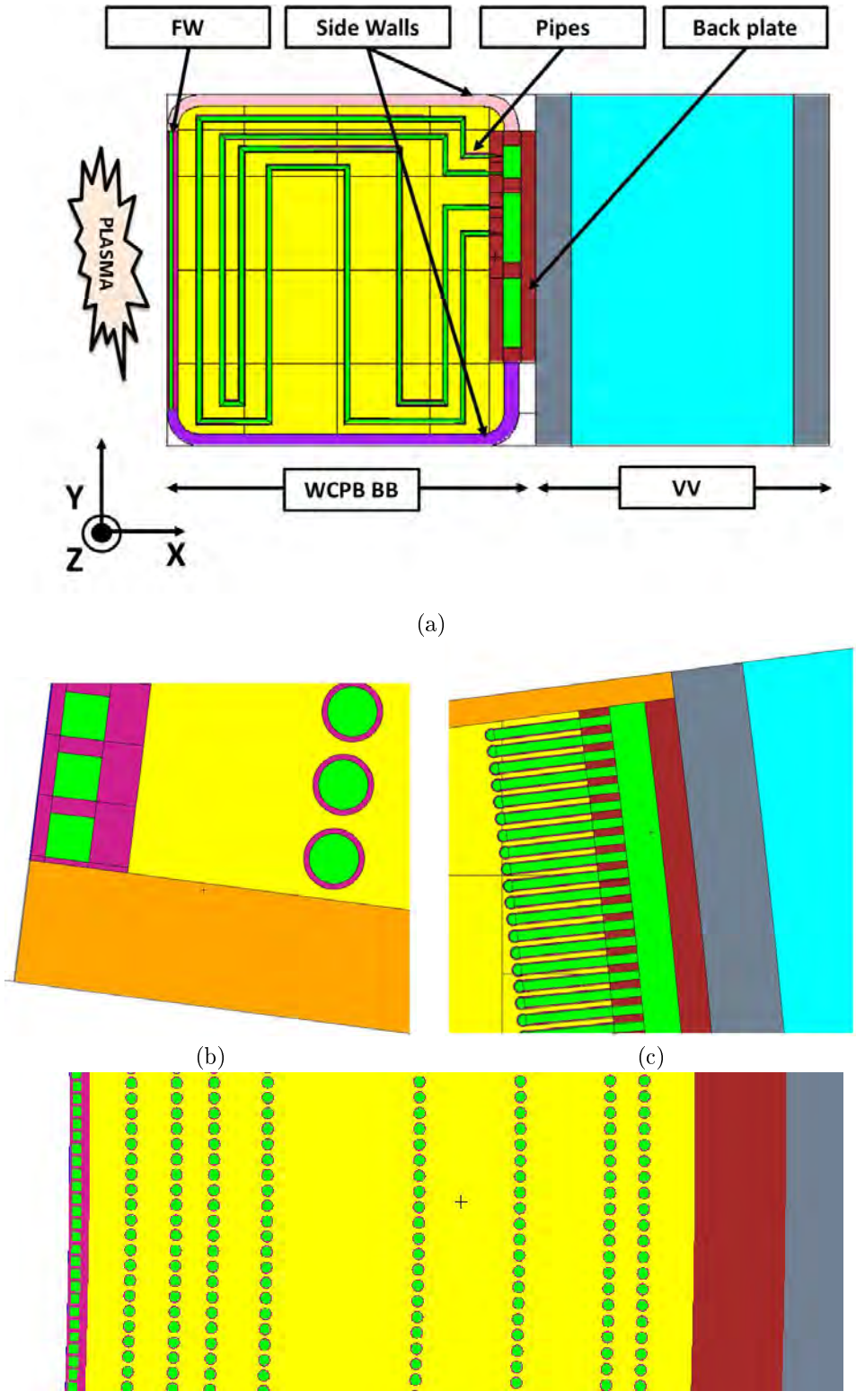

(a)

(b)

(c)

(d)

Figure 4.2.3: Fully detailed 3D MCNP

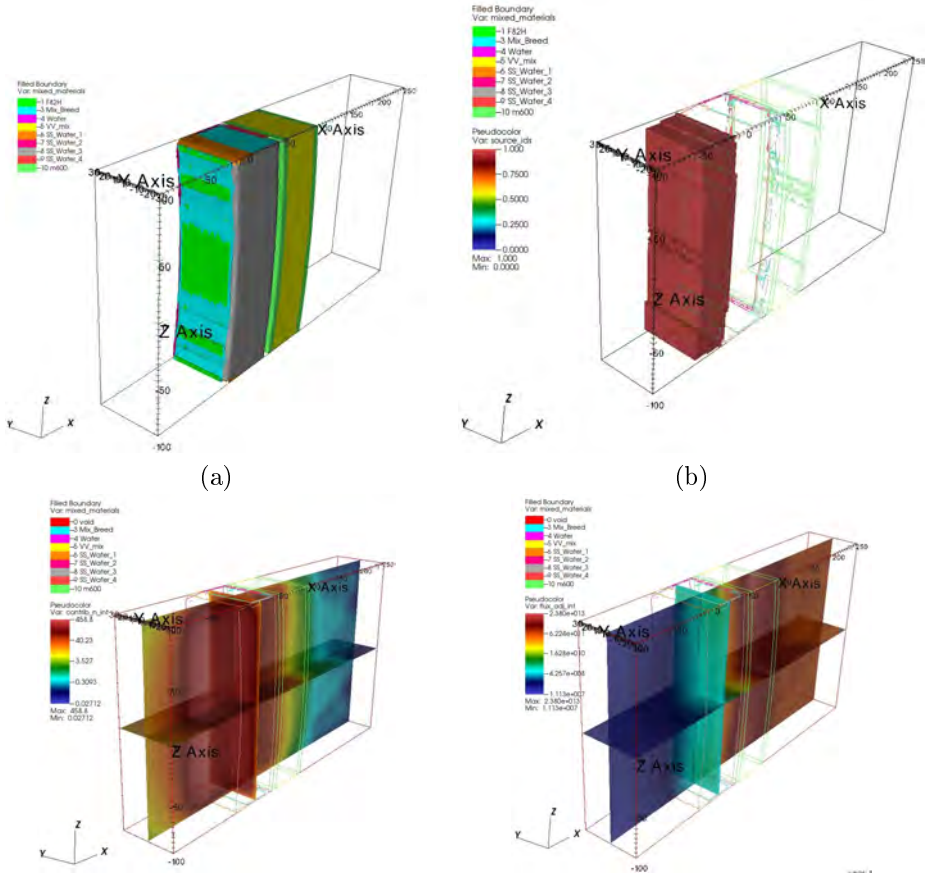

Figure 4.2.4: ADVANTG Weight Window

for MCNP were generated with ADVANTG [10, 80], Fig.4.2.4. As detailed in Sec.4.2, this code creates voxelised geometry and source from the MCNP input, Fig.4.2.4-(a,b), and calculates forward and adjoins deterministic neutron fluxes, Fig.4.2.4-(c,d), to subsequently derive source biasing and weight window parameters.

In addition, the VV region was covered with three, superimposed, rectangular, F4-type mesh-tallies of 1x1x2 cm resolution, hence in the level of the model details preserved as required by the ITER guidelines. The distribution of the explicit mesh-tallies is shown in Fig.4.2.5. FM cards, reported in Table 4.2.2, have been used to obtain the neutron and photon flux, the nuclear heat deposition in the F82H material and the tritium production. The resulting mesh-tally output files were added up, processed and converted to .vtk for visualization, result analysis and storage. The results reported hereinafter are based on 1e9

	Neutrons	*Photons*
F82H NHD (in m100)	8.475123E-2 100 1 -4	8.475123E-2 100 -5 -6
Tritium production (in m300)	-1 300 205	-

Table 4.2.2: MCNP FM Multiplier

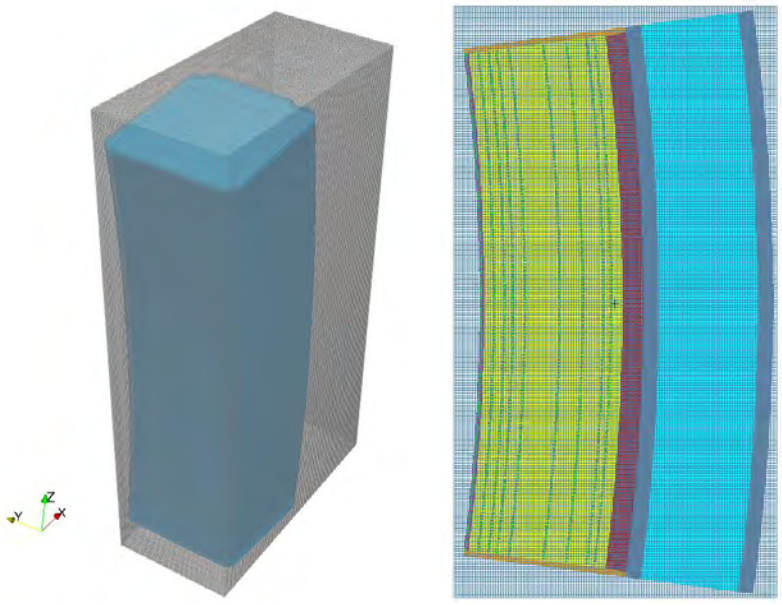

(a) (b)

Figure 4.2.5: MCNP FMESH: 3D visualization (a) and MCNP plotter (b)

histories and they have required 80000 min of running time. All the MNCP main tally statistical requirements have been fulfilled.

4.2.1.4 Results

A selection of the fully detailed MCNP simulation responses post-processed by means of Paraview software has been reported hereinafter in conjunction with the model geometry only for visualization purposes:

- Neutron flux in Fig.4.2.6, Fig.4.2.7
- Photon flux in Fig.4.2.8, Fig.4.2.9
- 3D Flux gradients in Fig.4.2.10
- Neutron and photon power deposition densities in Fig.4.2.11, Fig.4.2.12 and Fig.4.2.13
- Tritium volumetric production in Fig.4.2.14

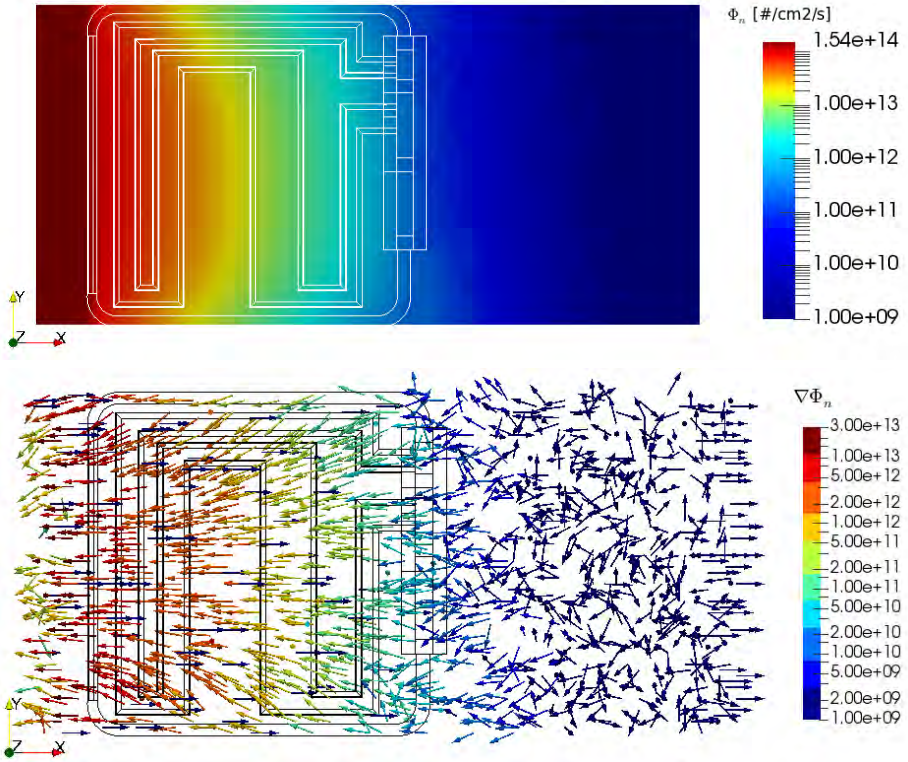

Figure 4.2.6: MCNP 3D - Neutron Flux@Z=0

Flux As expected the neutron flux has a decrease trend with the radial distance (e.g. almost six orders of magnitude over the WCPB BB), Fig.4.2.7. The reduction on the boundary sides seems to be more accentuated that the central one. Indeed, observing the gradient vectors this behavior is confirmed. In addition, thanks to the geometry poloidal symmetry, the trend observed over the Z middle plane is repeated over the whole geometry, Fig.4.2.7: no major differences are observed neither in the Y planes analysis nor in the 3D flux gradient having almost all the vector parallel to the radial direction, Fig.4.2.10, apart from the area beyond the WCPB BB (e.g. VV) where a lot of scattering is present.

Accordingly to the neutron flux, the gamma flux has a decrease trend with the radial distance with a peak close to the FW (e.g. almost four orders of magnitude over the WCPB BB), Fig.4.2.8. In contrast to the neutron flux, the gamma flux on the boundary sides appears similar to the central zone as supported by the gradient vectors.. In addition, thanks to the geometry poloidal symmetry, the trend observed over the Z middle plane is repeated over the whole geometry, Fig.4.2.9. No major differences are observed neither in the Y planes analysis nor in the 3D flux gradient having almost all the vector parallel to the

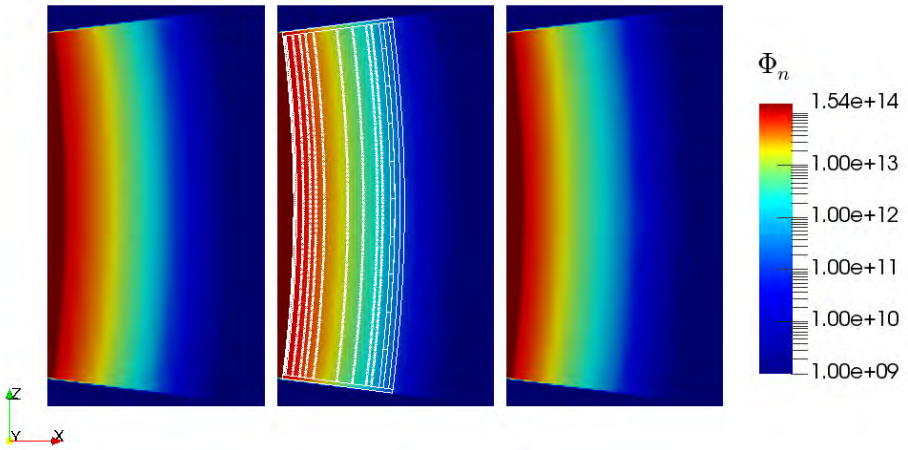

Figure 4.2.7: MCNP 3D - Neutron Flux@Y

radial direction, Fig.4.2.10, apart from the area beyond the WCPB BB (e.g. VV) where a lot of scattering is present.

Power deposition density The neutron and photon power densities over several planes (e.g. Z=-20 cm, Z=0 cm and Z=20 cm) have been reported in Fig.4.2.11 [7]. The neutron distribution is dominant over the photon one which is a secondary radiation produced only by the primary particle interactions. Thanks to the very fine FMESH[8] (e.g. 1 cm of resolution), the impact of the material typologies over the distribution can be observed. Indeed, the neutron NHD is peaked over the low atomic number material regions as the water whereas the photon in the F82H components as the pipes or the WCPB external box. In addition, a slightly increased neutron deposition of the front part of the side WCPB case is denoted due to the homogeneous mixture employed in the MCNP modelling, Sec.4.2.1. Once again, as observed in the flux analysis, no major discrepancies can be denoted among the different sections. Summing the neutron and photon distribution, the total power deposition due to the plasma radiation is obtained, Fig.4.2.12. Moreover, for illustration purposes using the Paraview resampling tool, the obtained field has been applied to the whole simplified CFD geometry and only to the F82H part to distinguish the contribution to the components, Fig.4.2.13.

[7] The FMESH reported here are implicit ones for a better understanding of the different contribution, whereas those implemented in the CFD calculations are the explicit one because more conservative as detailed in Sec.2.2.

[8] As commented in Sec.2.2.4.4, FMESH tally is a special MCNP features which allows the superimposition of a mesh (e.g. cylindrical, rectangular or spherical) over the problem geometry to compute particle flux and its by product such as nuclear heating, Tritium production, etc using proper converting parameters and correspondent cross sections.

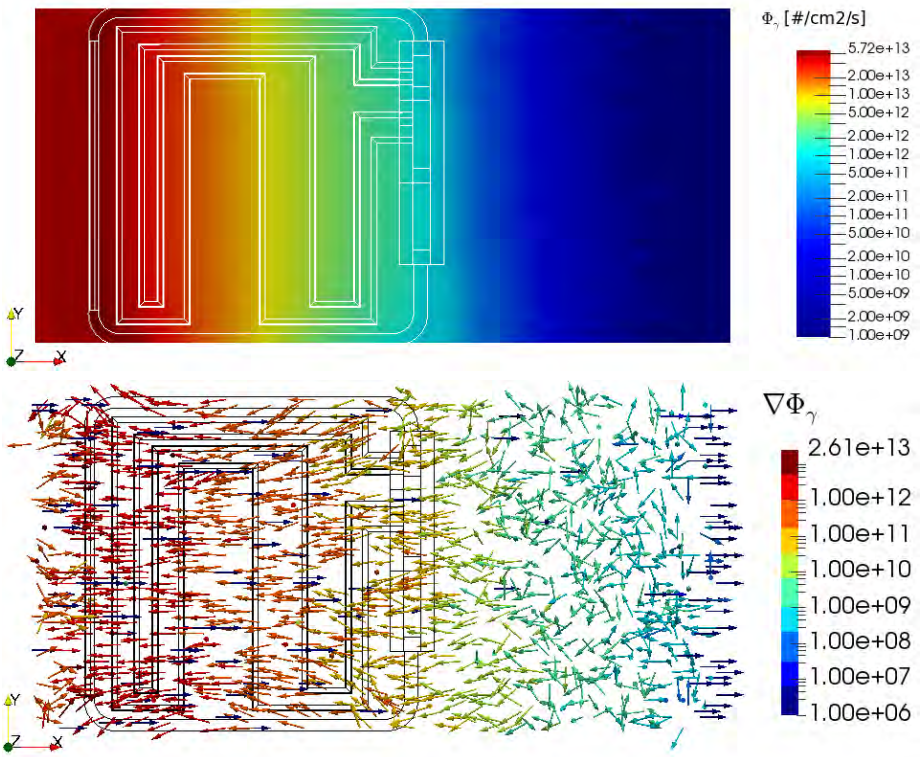

Figure 4.2.8: MCNP 3D - Photon Flux@Z=0

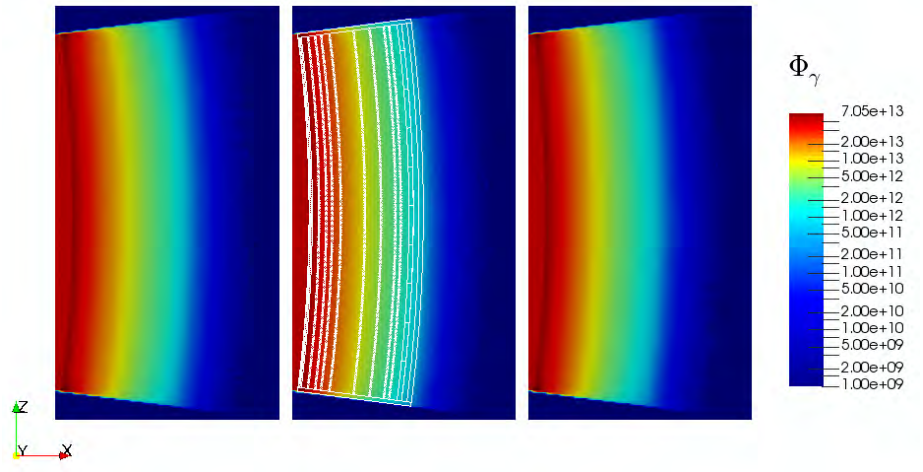

Figure 4.2.9: MCNP 3D - Photon Flux@Y

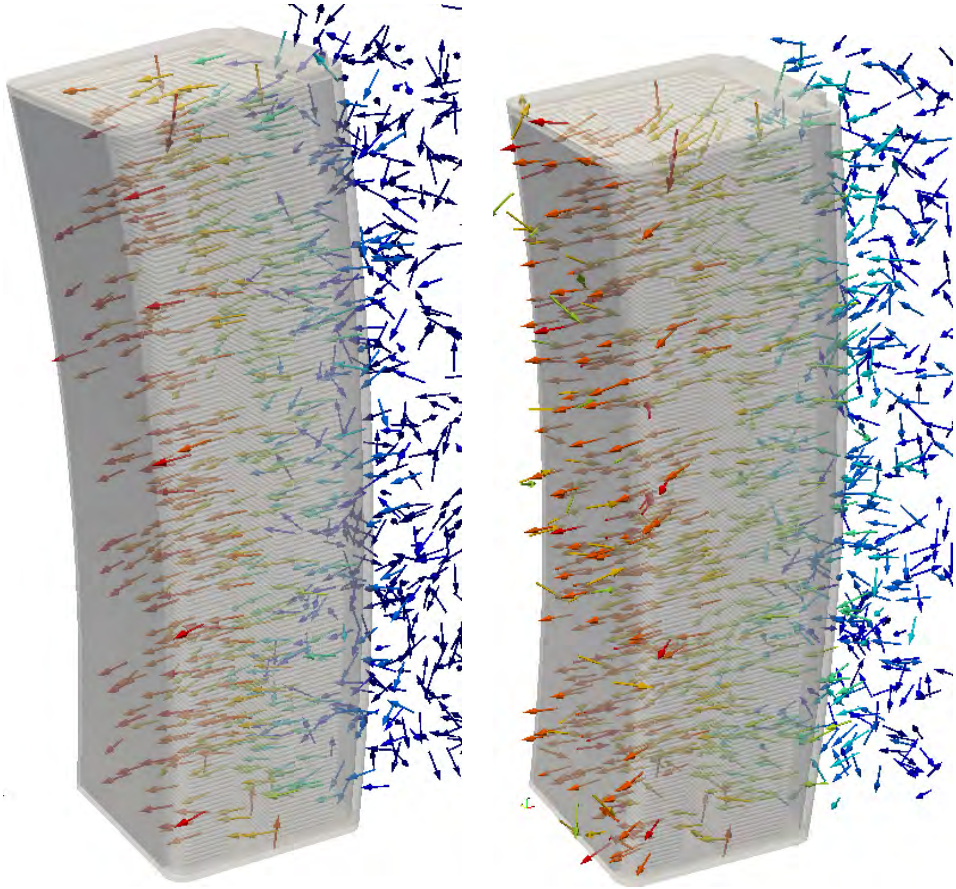

(a) (b)

Figure 4.2.10: MCNP 3D - Neutron (a) and photon (b) flux gradient vectors

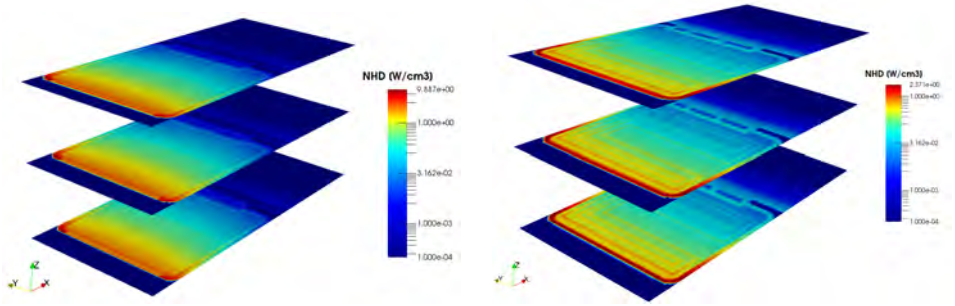

(a) (b)

Figure 4.2.11: MCNP 3D - Neutron (a) and photon (b) NHD

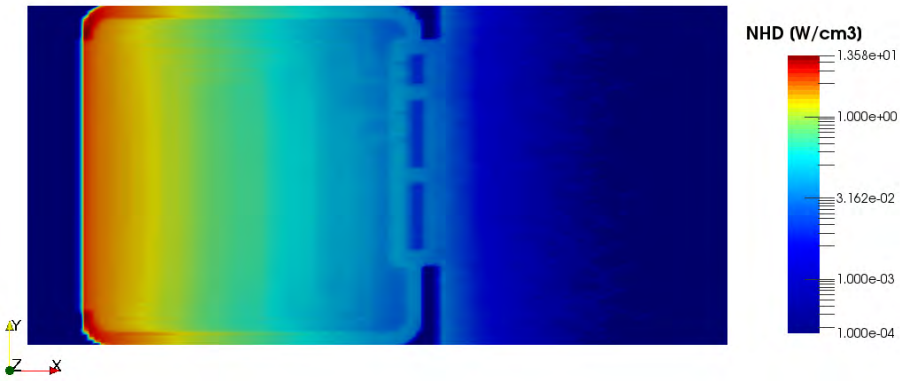

Figure 4.2.12: MCNP 3D - Total NHD

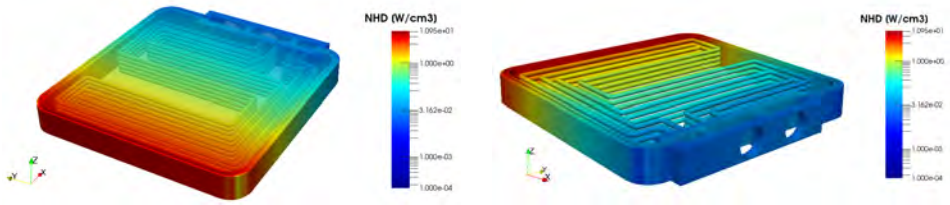

Figure 4.2.13: MCNP 3D - Total NHD 3D

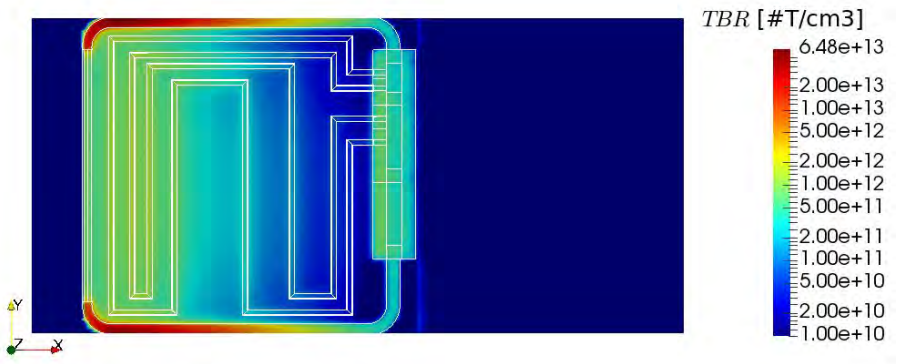

Figure 4.2.14: MCNP 3D - Tritium production

Tritium production The production of the Tritium has been assessed by means of an explicit FMESH considering the whole composed by mixed breeder, Fig.4.2.14. The results, which are computed using the neutron flux energy spectra in the specific voxel, are only valid where the mesh is composed by the breeding. Indeed, the tritium production over the WCPB BB case, where hot spot appeats, are not valid.

4.2.2 Simplified 1D MCNP models

Starting from the 3D WCPB CAD representation, two 1D blanket simplified MNCP models have been manually generated without employing any intermediate software. Both are composed by forty-seven radial parallel layers to preserve the in-vessel features as far as possible, Fig.4.2.15. In the end, they differ only in material slice composition corresponding to the cooling areas as reported in Table 4.2.3. Indeed, whereas one model employs the most representative material of the segmentation, the other uses a homogenized material mixture corresponding to the effective cell composition, being therefore identified as the heterogeneous (1D-HET) and the homogeneous (1D-HOM) model. Thus, each of 1D-HOM pipes are composed by three layers: lateral MIX (F82H 69%w, MIX breeder 31%w), internal MIX (F82H 61%w, H20 22%w, mixed breeder 17%w), lateral MIX (equal to the first one), Fig.4.2.16. A simplified three layer representation of the VV has been also included in the model to preserve the back-scattering phenomena in the back region. The whole model results in almost 60 cm long with the typical WCPB front section of 60 cm x 200 cm.

The MCNP material card have been generated employing the element composition reported in Sec.4.1.2 and applying the FENDL3.1b cross section with the photon transport data from MCPLIB84 libraries. Material densities have been assumed at room temperature (300 K). Thanks to the simplicity of the

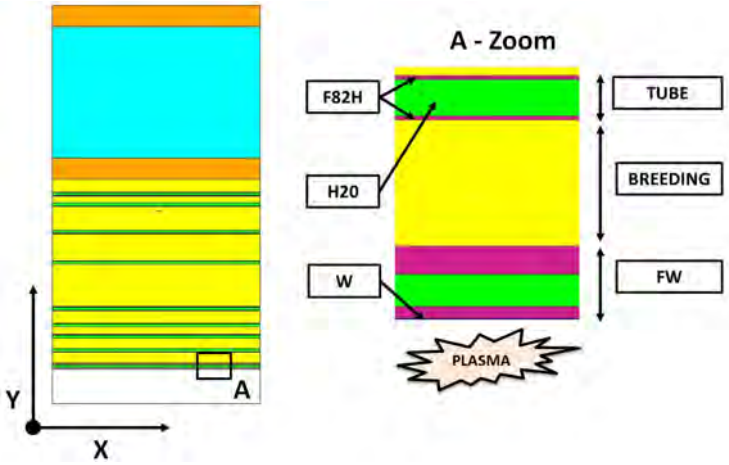

Figure 4.2.15: MCNP 1D Model layers and 1D-HET zoom

model, the MCNP universe concept has not been implemented.

In addition to this main study, further assessments about the impact of the boundary conditions (Sec.4.2.2.4), of the temperature (Sec.4.2.2.7) and of the cross sections (Sec.4.2.2.6) are hereinafter reported.

4.2.2.1 SDEF definition and normalization

A surface and isotropic Deuterium-Tritium neutron Gaussian fusion source has been assumed in front of the whole WCPB FW. The mean energy spectrum and full width at half maximum (FWHM) have been imposed equal to 14.0791 MeV and 0.53415 MeV as in [120]. The results have been normalized to a Neutron Wall Loading (NWL) of 1 MW/m^2 using the neutron current impinging FW. An optimized random number and stride have been employed according to [120] [9].

4.2.2.2 Variance reduction techniques and tally definitions

Primary nuclear responses of interest are the WCPB integral nuclear heating and detailed 3D heat deposition maps due to plasma neutrons and secondary prompt photons. These have been obtained by implementation of the MCNP tally cards described in following sections. The following tallies have been applied:

- F4[10] type to compute the FW surface neutron current and the tritium production using and 205 MT ENDF reaction within a dedicated FM

[9] RAND GEN=2 SEED=501932527452161 STRIDE=152917 HIST=5518120

[10] As explained in Sec.2.2.4.4, this estimator uses the fundamental definition of the flux as the number of particle-track lengths per unit of volume [75].

No.#	Thickness, cm	Material@1D-HET	Material@1D-HOM
1	2.00E-02	W coating	W coating
2	4.09E-01	F82H	F82H
3	5.82E-01	Water	FW MIX
4	8.09E-01	F82H	F82H
5	4.13E+00	Mixed breeder	Mixed breeder
6	1.65E-01	F82H	1D Lateral Mix
7	4.24E-01	Water	1D Internal Mix
8	1.65E-01	F82H	1D Lateral Mix
9	5.40E+00	Mixed breeder	Mixed breeder
10	1.65E-01	F82H	1D Lateral Mix
11	4.24E-01	Water	1D Internal Mix
12	1.65E-01	F82H	1D Lateral Mix
13	6.98E+00	Mixed breeder	Mixed breeder
14	1.65E-01	F82H	1D Lateral Mix
15	4.24E-01	Water	1D Internal Mix
16	1.65E-01	F82H	1D Lateral Mix
17	9.76E+00	Mixed breeder	Mixed breeder
18	1.65E-01	F82H	1D Lateral Mix
19	4.24E-01	Water	1D Internal Mix
20	1.65E-01	F82H	1D Lateral Mix
21	1.61E+01	Mixed breeder	Mixed breeder
22	1.65E-01	F82H	1D Lateral Mix
23	4.24E-01	Water	1D Internal Mix
24	1.65E-01	F82H	1D Lateral Mix
25	4.28E+00	Mixed breeder	Mixed breeder
26	1.65E-01	F82H	1D Lateral Mix
27	4.24E-01	Water	1D Internal Mix
28	1.65E-01	F82H	1D Lateral Mix
29	1.00E+00	Mixed breeder	Mixed breeder
30	1.65E-01	F82H	1D Lateral Mix
31	4.24E-01	Water	Coolant (15.5MPa)
32	1.65E-01	F82H	1D Lateral Mix
33	1.00E+00	Mixed breeder	Mixed breeder
34	1.65E-01	F82H	1D Lateral Mix
35	4.24E-01	Water	1D Internal Mix
36	1.65E-01	F82H	1D Lateral Mix
37	1.00E+00	Mixed breeder	Mixed breeder
38	9.72E-01	F82H	1D Lateral Mix
39	2.56E-01	Water	1D Internal Mix
40	1.27E+00	F82H	1D Lateral Mix

Table 4.2.3: 1D MCNP models layering

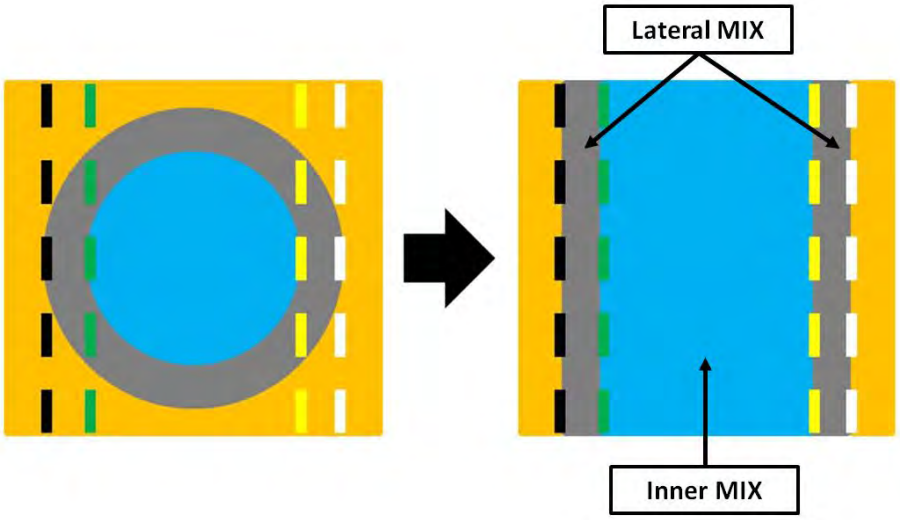

Figure 4.2.16: MCNP 1D Pipe representation

card[11]

- F6[12] tallies to determine the nuclear heating, both by neutrons and by photons, over each material layer
- Implicit FMESH to determine the local behavior of the responses as the neutron and photon flux, NHD and TBR.

Thanks to the simple geometry and the presence of reflecting boundary conditions, no specific variance reduction techniques have been employed. The results presented hereinafter are based on 1e8 histories. All the MNCP main tally statistics requirements are fulfilled.

4.2.2.3 Results

MCNP 1D-HET Model The results concerning MNCP 1D-HET model are reported in Fig.4.2.17. As expected the neutron flux experiments a exponential decrease driven by the rapid component, Fig.4.2.17-(a). Approximately at 10 cm after the FW the thermal neutron spectra overcomes the fast one thanks to

[11] It is a tally multiplier card [75]. It can be used to estimate a specific reactions or response as the d.p.a., doses or He ppm production.

[12] As explained in Sec.2.2.4.4, this estimator is a track-lengths estimators of the flux with a energy-dependent multiplier. Therefore, the F4 tallies with a proper energy dependent multiplier, FM card, can be equivalent to F6 tallies [75].

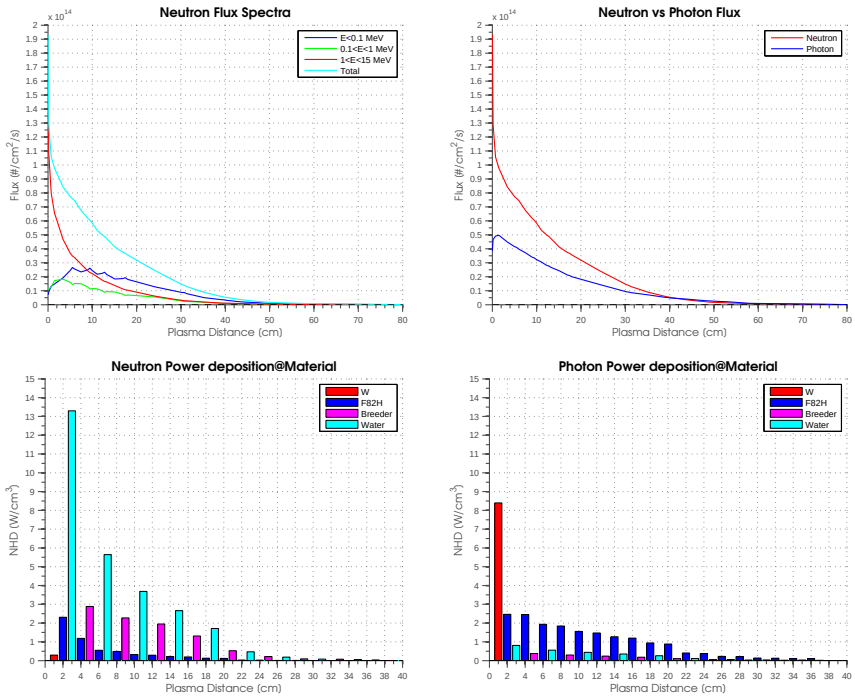

Figure 4.2.17: MCNP 1D-HET Model

the attenuation proportioned by the water layers. On the other hand, the epidermal flux is constantly the smallest part. In addition, the secondary photons, generated by radiative reaction channel along the WCPB BB, never reach the neutron population, Fig.4.2.17-(b). A photon flux peak is present close to the FW close to the Wolfram layer due to the highest neutron flux.

Moreover, depending on the material typology and especially on its atomic No., a heating particle contribution is dominant: water and breeder for neutrons whereas Wolfram and F82H for photons, Fig.4.2.17-(c,d). To conclude, accordingly to the flux distributions, the total power deposition trend has a clear decrease toward the VV region.

MCNP 1D-HOM Model The results concerning MNCP 1D-HOM model are reported in Fig.4.2.18. As expected the neutron flux experiments a exponential decrease driven by the rapid component, Fig.4.2.18-(a). Approximately at 5 cm after the FW the thermal neutron spectra overcomes the fast one thanks to the attenuation proportioned by the mixed FW layers. In contrast, the epidermal flux is constantly the smallest part. In addition, the secondary photons, generated by radiative collision along the WCPB BB, never overcome the neutron population, Fig.4.2.18-(b). A photon flux peak is observed close to the FW close to the Wolfranium layer due to the highest neutron flux.

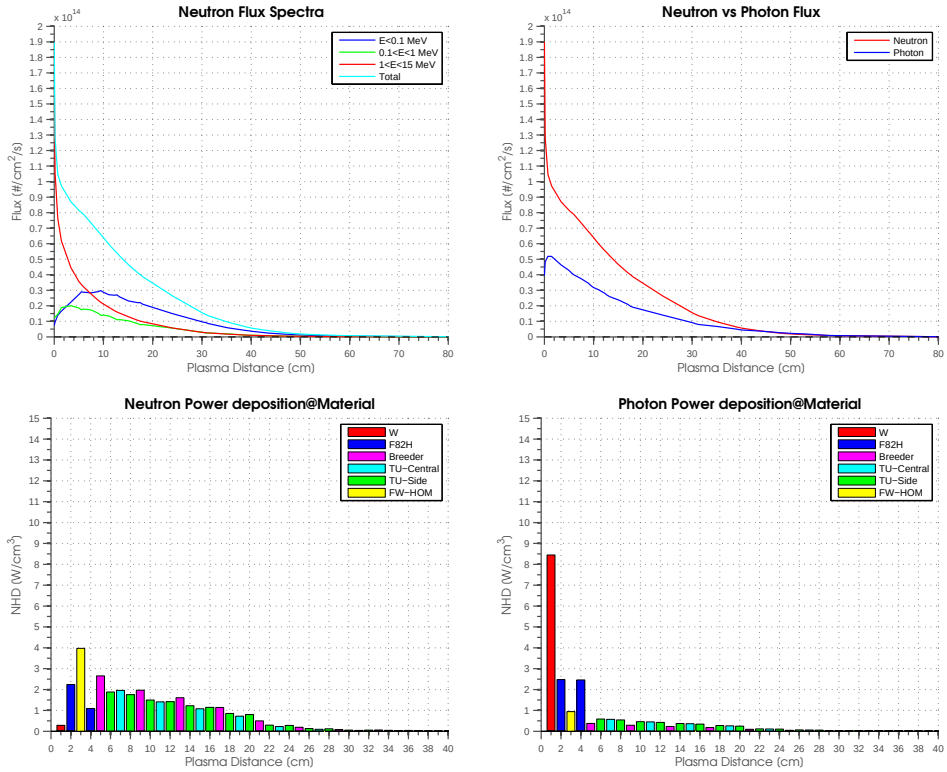

Figure 4.2.18: MCNP 1D-HOM Model

Moreover, neither the neutron nor the photon contribution are dominant in the mixed material composition. Apart from the FW layers, all the heating peaks are smeared down, Fig.4.2.18-(c,d). The neutron contrutions is clearly dominant over the photon one. To conclude, accordingly to the flux distributions, the total power deposition has a substantial decrease toward the VV region.

MCNP 1D-HOM vs 1D-HET The results comparison between the MNCP 1D-HET and 1D-HOM responses is reported in Fig.4.2.20[13]. In both cases the neutron distribution suffers an exponential decrease. In addition, the 1D-HOM total neutron flux is higher from just after the FW F82H layer up to the WCPB BB back-plate mainly due to the the lower energy bins. This effect could be mainly attributed to the increased F82H and breeder MIX contents in the mixed layers which seem to thermalize more the spectra[14]. Thus, the 1D-HET neutron

[13] All the per cent differences have been determined as (1 - 1D-HOM/1D-HET)*100

[14] This effect is generally observed passing from an heterogeneous to an homogeneous modelization of components.

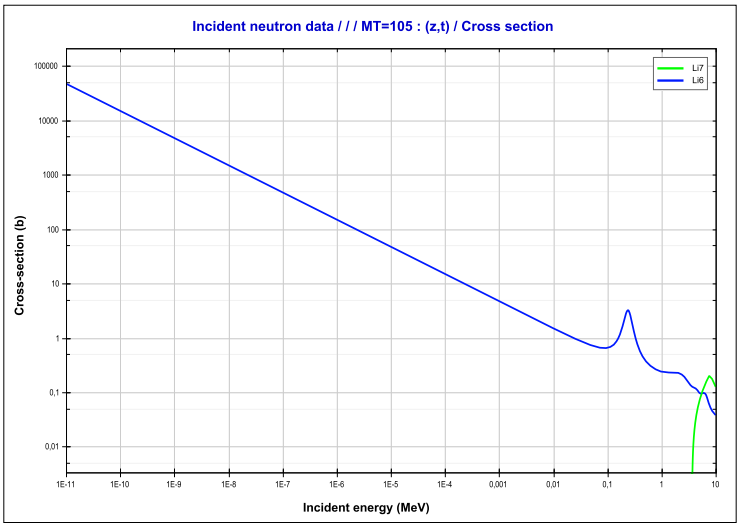

Figure 4.2.19: Lithium (n,T) cross section [18]

total flux is lower but harder. Indeed, also the Tritium production is decreased up to about -15% having less neutrons at thermal energy where the typical cross-section inversed proportionality to the velocity is observed as for Litium [39], Fig.4.2.19. On the other hand, the presence of more F82H in the 1D-HOM grows the photons populations all over the domain having a higher peak at the same plasma radial distance. For these reasons, the 1D-HET total power deposition is about 30% bigger than the 1D-HOM preserving also the NHD peaks which are of fundamental importance in the subsequent CFD analysis. The response variations are not limited locally to the single different local cells but to the entire domain due to the impact in flux, energy and reaction channels. In addition, the one to one comparison of the NHD in each cells shows how the impact is not limited to the modified regions but to the whole model mainly due to the neutron spectra modifications. In conclusion, whereas the 1D-HET model results to be more conservative regarding the NHD maintaining also the peaks distribution, the 1D-HOM has a wider Tritium production. In both cases the neutron NHD is globally dominant. Thus, depending on the project needs, the most suitable and conservative model shall be selected.

In conclusion, Taking into account the current AINA WCPB thermal-model needs, the 1D-HET responses will be considered as the reference case for the simplified radiation transport assessment.

4.2.2.4 Boundary conditions study impact

As described in Sec.2.2.4.2, four types of external boundary conditions can be imposed to the MCNP geometry surfaces. Depending on the specific applica-

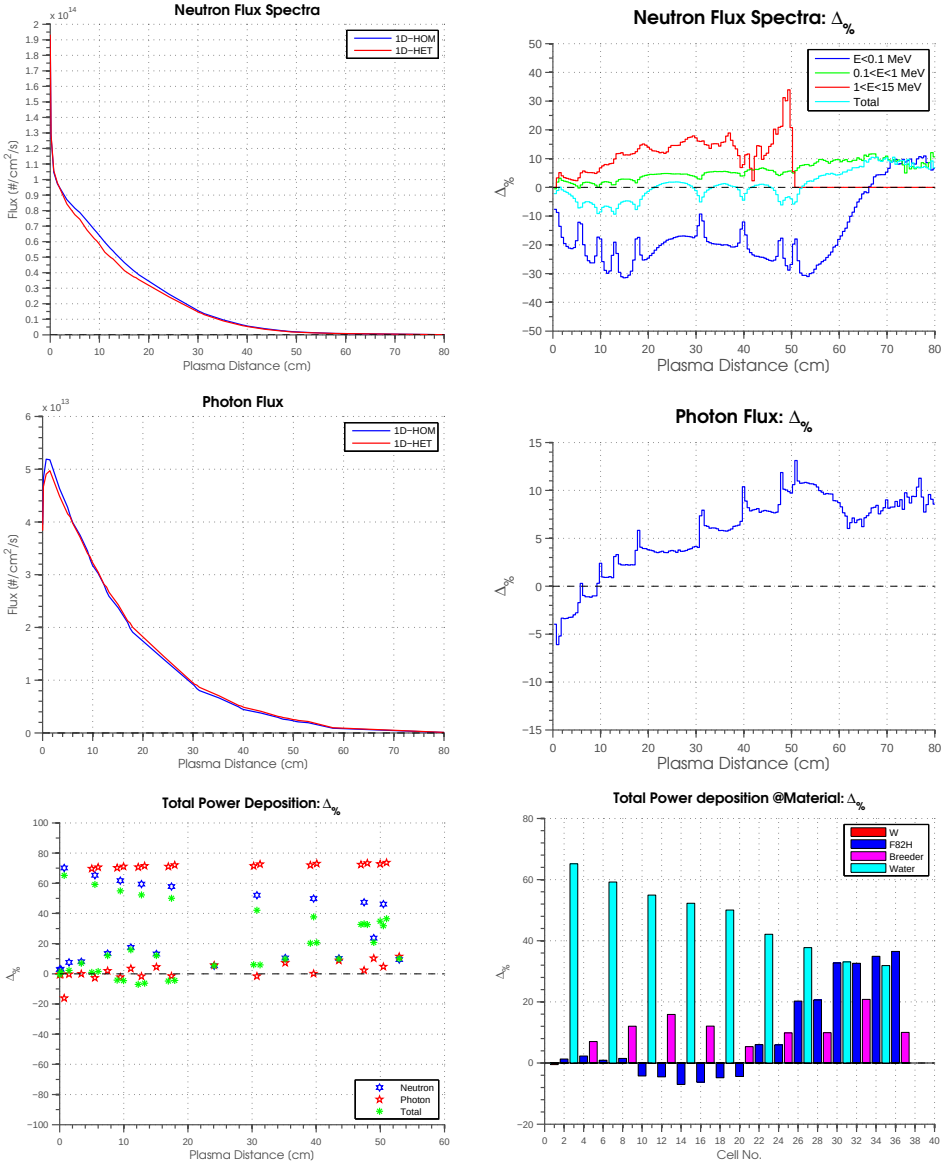

Figure 4.2.20: MCNP 1D-HET vs 1D-HOM

tion, simulation needs and mediums, one or more BC types could be applied achieving an optimized simulation and correct results. Hereinafter, the impact of the several BC (e.g. white boundary bonditions or WBC, no boundary bonditions or NBC, periodic boundary bonditions or PBC) has been assessed for the WCPB BB case to demonstrate its importance and impact on the computed responses (neutron and photon flux and heating), Fig.4.2.21. The 1D-HET model, Sec.4.2.2.3, where reflecting boundary conditions (RBC) are imposed, has been taken as baseline case[15].

Results A selection of the *boundary conditions study impact* assessment is reported in Fig.4.2.21.

The impact of BC typology has resulted relevant (e.g. differences up to 60%) hence it shall not be neglected. As expected, the case with no boundary conditions (NBC) has resulted in the lowest neutron and photon flux because the particles are killed ones the BC are reached. The white BC (WBC) are in line with the 1D-HOM results: differences up to 10% are determined and the responses are slightly more conservative starting from 30 cm of plasma distance. This effect is mainly attributed to the possibility of a particle impinging the BC to be sampled in a direction opposite to the original one having an increased flux than the RBC case which preserve the original angle of incidence. In addition, the PBC outcomes are exactly the same of the RBC because due to the geometry features (e.g. parallel and constant cell layers orthogonal to the front section), the particle tracking is exactly the same.

Furthermore, the BC assumption affects all the responses (e.g. flux and NHD) similarly and with an increasing trend with the radial distance because of the decreased flux/NHD. Overlapping the nuclear and photon NHD with the flux, minor differences over the pipe cooling areas are observed having the points slightly detached from the main distribution. This effect could be mainly attributed to the usage of F6 tally heating estimator in conjunction with the small thickness of the cells when compared with the mean free path of the particles. Indeed, the discrepancies appears to be more prominent where the ratio mean free paths/cell is larger as for photons particle or in F82H for the neutrons.

To conclude, RBC and WBC BC show a similar behavior concerning the neutron and photon flux/NHD. Having the RBC the more conservative responses in the front part of the WCPB BB where critical temperatures are foreseen, they have been preferred to the WBC for this specific application.

4.2.2.5 Model section dimensions influence

During the modelling phase of a simplified 1D MCNP model (e.g. 1D-HET), once the external boundary conditions and the material layering/thickness are selected, the last but not the least decision is about the model cross sections dimension. Should it be in the same order of magnitude of the fully detailed

[15] Per cent differences have been computed as $(1 - BC_{Case}/1D - HET) * 100$

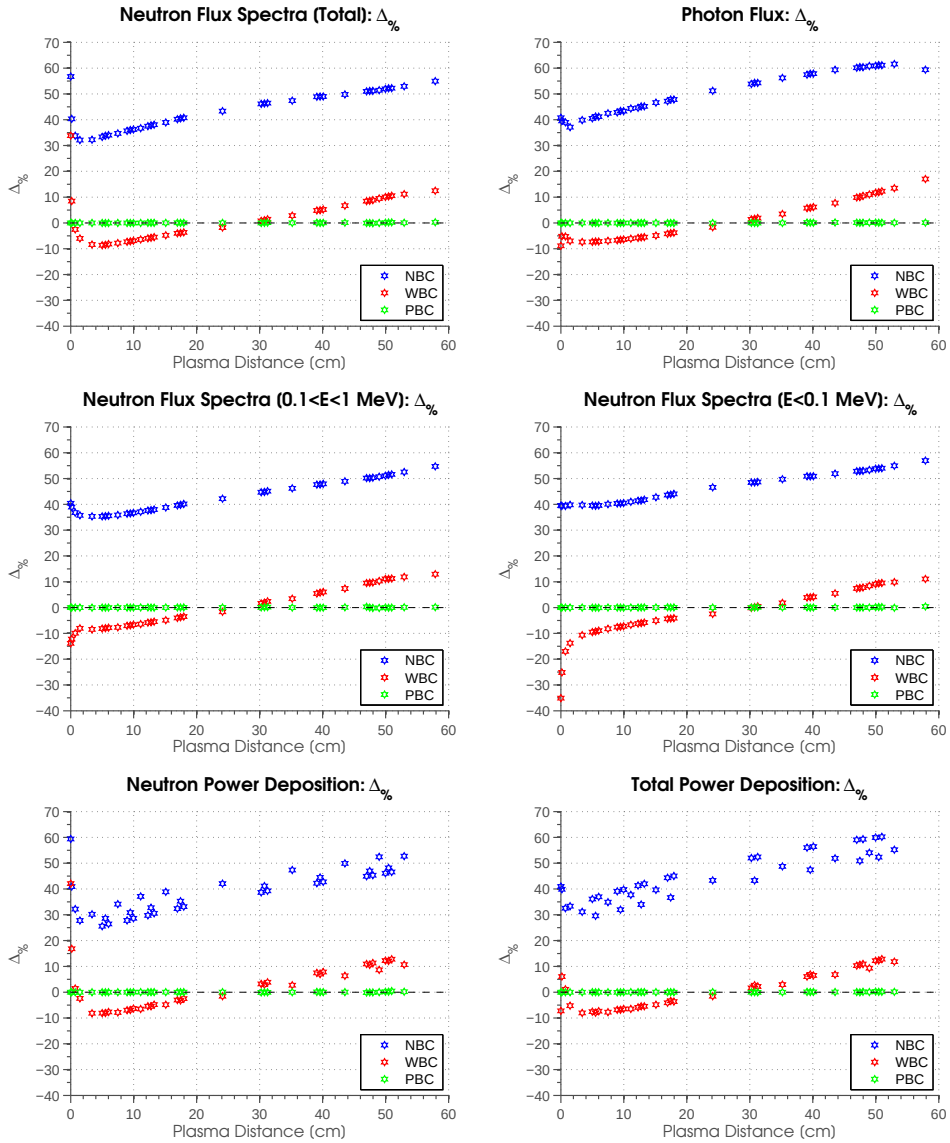

Figure 4.2.21: MCNP BC Assessment

model or could it be smaller? Are they any further differences? To assess the influence of the model section dimensions, additional simulations have been carried out taking as reference the 1D-HET case 4.2.2.3 and only modifying its cross section from $12000\,cm^2$ ($200\,x\,60\,cm$) to $120\ cm^2$ ($20\,x\,6\,cm$). No other modifications has been applied. Hereinafter, the impact of the cross section has been assessed by means of the computed responses (neutron and photon flux and heating), Fig.4.2.22, and the computational effort[16].

Results A selection of the *model section dimensions influence* responses is reported in Fig.4.2.22.

Observing Fig.4.2.22, it is evident that the model cross section dimensions does not affect at all the nuclear responses as it was expected a priori. On the other hand, using the model with reduced cross section (e.g. one order of magnitude), an improvement in the computational effort is observed : -10% decreasing in running time from 1222 min to 1121 min. These changes are mainly attributed to the smaller length of the particle tracks in the single MCNP histories hence achieving a smaller computational time for each particle run.

It is important to remark that these conclusions are limited to this model which is using the reflecting boundary conditions and cells composed by parallel constant layer of materials and it cannot be generalized to other conditions as NBC or WBC BC.

For these reasons, in future assessments the model cross section could be limited one order of magnitude in order to optimize the computational effort.

4.2.2.6 Cross section impact

Monte Carlo method relies on the nuclear cross section data which "describes" the nuclear physic processes (e.g. fusion, fission, spallation, etc...). The selection of a specific cross section is a fundamental step in the MCNP model generation thus it shall be properly justified. Unfortunately, no specific cross section is internationally recognized as the most correct and suitable for fusion application. In this thesis the FENDL v3.1b libraries [18][17] have been applied because they are the reference in the ITER project[5]. Nevertheless, there are further data available in the fusion community which could be also implemented: TALYS-based evaluated nuclear data library (TENDL)[121], the Joint Evaluated Fission and Fusion File (JEFF) [122], Japanese Evaluated Nuclear Data Library (JENDL) [123] and Russian National Library of Evaluated Neutron Data (ROSFOND) [124].

In addition, once the specific library is selected, it is very important to point to the most consolidated and recent one. Indeed, to show the importance of data improvement and evolution, the 1D-HET case 4.2.2.3 has been computed

[16] Per cent differences have been computed as $(1 - 1D - HET_{Small-Section}/1D - HET_{Standard-Section}) * 100$

[17] At room temperature.

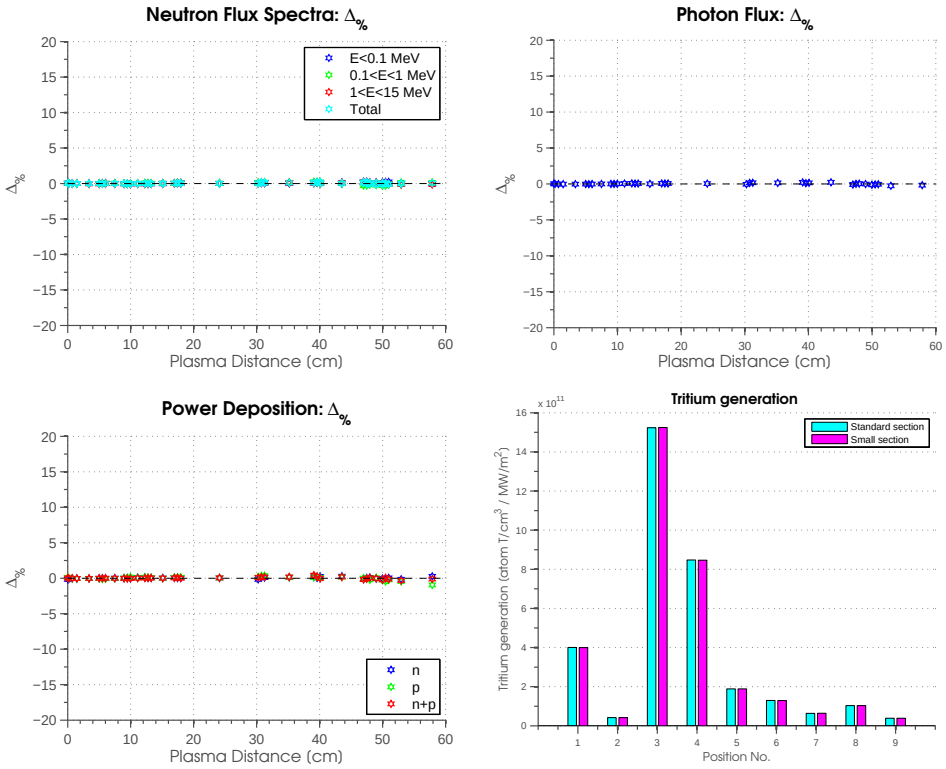

Figure 4.2.22: MCNP Section dimension assessment

by means of two subsequent versions of FENDL libraries: v2.1 and v3.1b. Hereinafter, its impact has been evaluated by the neutron and photon flux/heating), Fig.4.2.23, and the computational effort[18].

Results A selection of the *cross section impact* responses is reported in Fig.4.2.23.

The whole set of responses shows slightly differences always within the 15%. Moreover, compared to FENDL2.1, the use of FENDL3.1b produces a decrease of 2% in the total heating and of about 1% in the Tritium generation. Although, no clear response underestimation or overestimation is foreseen, the neutron flux seems to be more affected than the photon one. These results are consistent with those of the 1D ITER benchmark presented by Bohm et al. at the CSEWG 2016 meeting, (BNL, 14-16 November 2016), particularly considering that the real radial build-up of WCPB BB is different to the 1D ITER benchmark. The discrepancies found could be considered a consequence of the improvement of the nuclear data as the modification/addition of resonances or the modification of the nuclear fundamental models. For instance, the comparison of some important elements has been done using the JANIS database [39] and reported in Fig.4.2.24-4.2.25-4.2.26. Regarding, the M1 ENDF cross section (n,TOT), no difference are found in ^{56}Fe, minor in ^{1}H and ^{6}Li while relevant in ^{184}W. Indeed, further resonances aroud 3-4 MeV have been introduced as well as some at lower energy reviewed. On the other hand, the M105 ENDF cross section (n,T) has been compared also with TENDL-2015 and RUSFOND-2010 founding variation up to the 15%.

Furthermore, the usage of the FENDL3.1b instead of the previous version increases both the computational time by 30% approximately (running time from 829 min to 1222 min) and the model dimension (e.g. runtpe[19]) by almost a factor of 2. These changes are mainly associated to the enhanced accuracy of the libraries and the presence of the covariance data which are fundamental in the determination of the uncertainty propagation in the shut-down dose rate calculations. Although these computational disadvantages, more recent and consolidated data have to be preferred to improve the accuracy of the solution.

4.2.2.7 Operation condition influence

Along this thesis, the reference radiation transport simulations have been carried out using the material features at room conditions (e.g. 1 bar, 300 K). Nevertheless, the applications of effective operation conditions might have an influence on results due to the variation of the material densities and the nu-

[18] Per cent differences have been computed as $(1 - 1D - HET_{FENDLv2.1}/1D - HET_{FENDLv3.1b}) * 100$

[19] The RUNTPE file is a output file produced by MCNP during the simulation [75]. It contains all the information needed to restart a problem in the continue-run mode thus representing the dimension of the model. It can be used either to run more histories or to post-process and plot tallies. The RUNTPE file is sequential and unformatted.

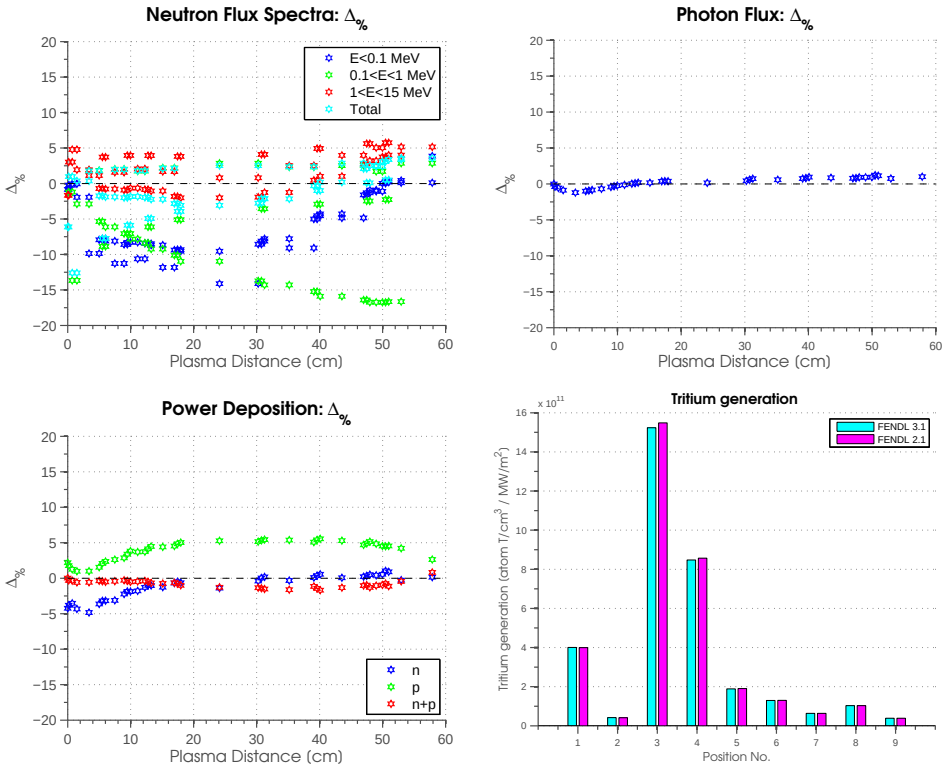

Figure 4.2.23: MCNP FENDL Assessment

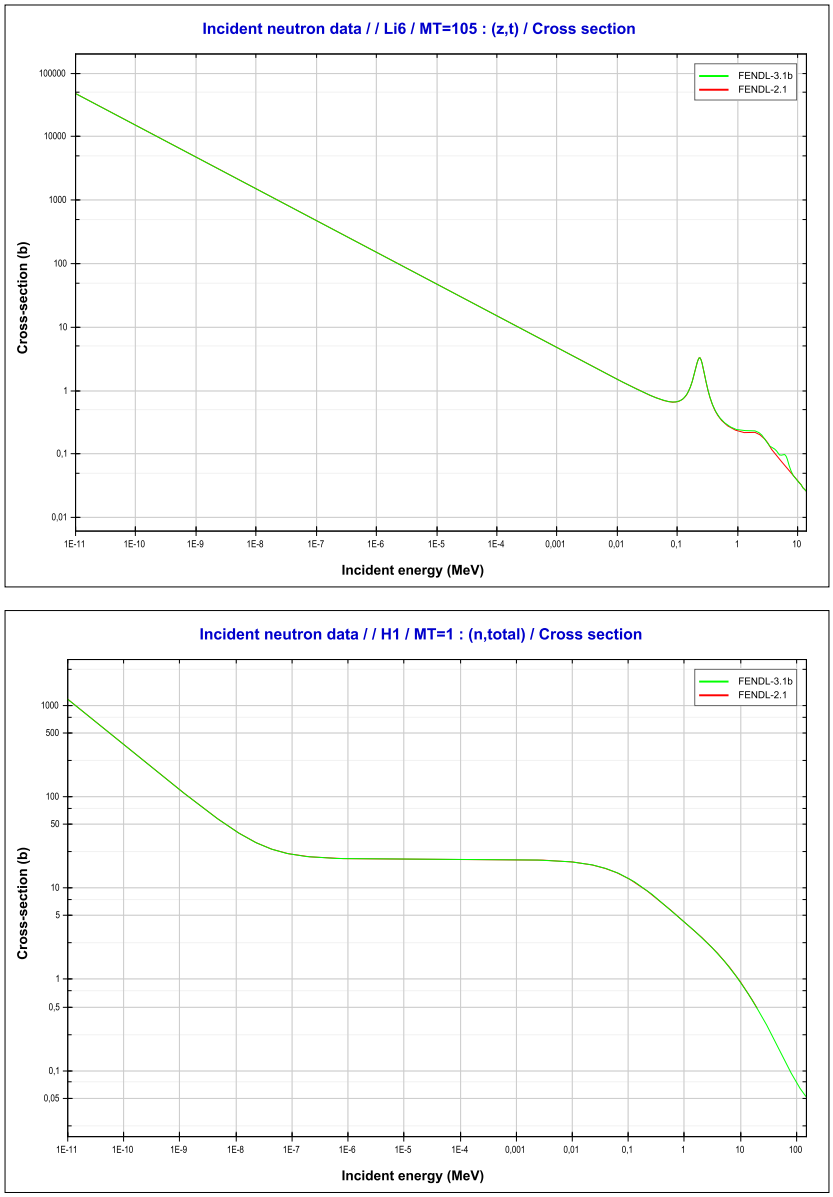

Figure 4.2.24: Nuclear cross sections - Li6 and H1

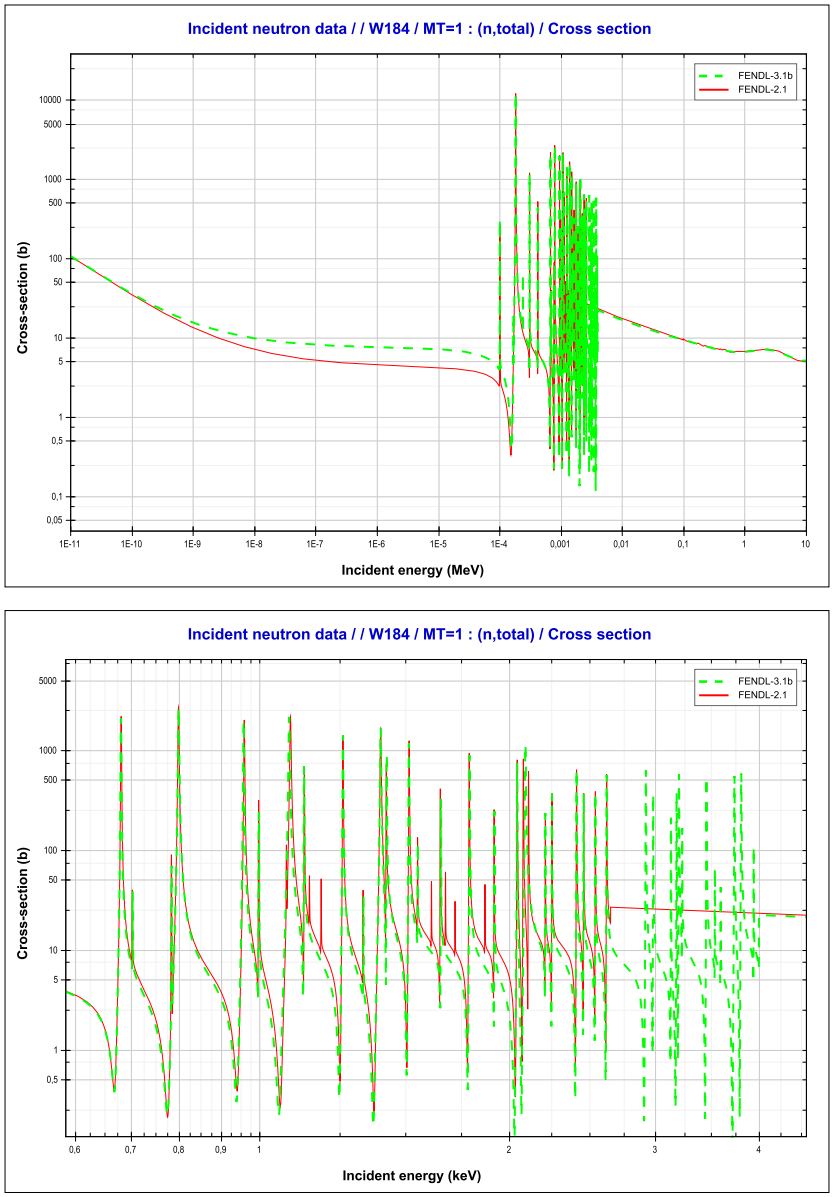

Figure 4.2.25: Nuclear cross sections - W184

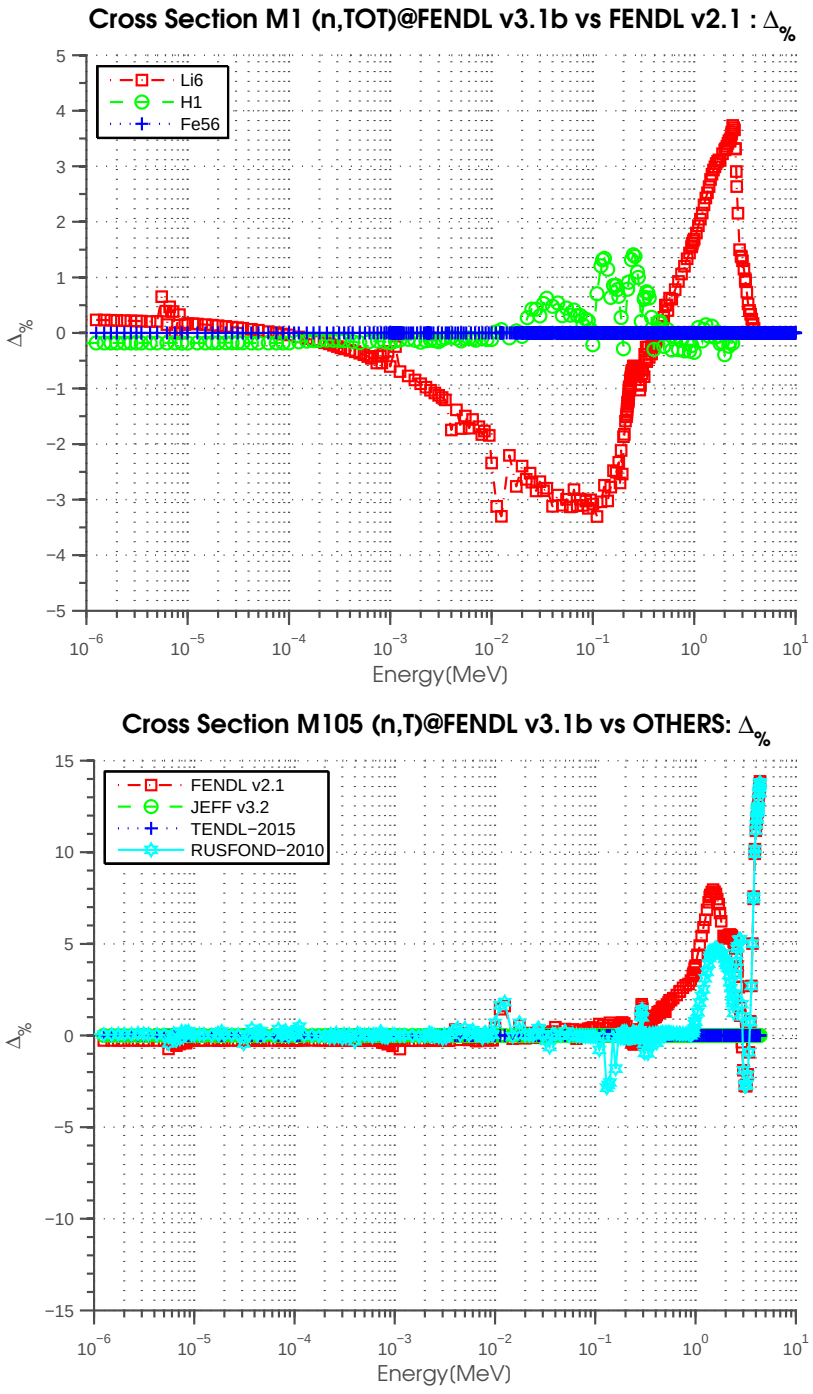

Figure 4.2.26: Nuclear cross sections - comparison

clear cross-sections due to effective pressure and temperature fields. Depending on the specific conditions and medium, these effects could have different importance. For this reason, these contributions are described hereinafter and assessed comparing the baseline case, the 1D-HET MCNP model, with a new model, named as 1D-DENS.

Densities In general terms, the material densities could be affected by the operational system temperatures and pressure (e.g. water, Helium). Changing the densities, the number of nuclear interactions per unit of volume is modified, hence changing the radiation transport inside the matter. Employing the material specifications, detailed in Sec.4.1.2 and the cell temperatures obtained from simulation, Sec.4.4.2, new material densities have been computed and reported in Table 4.2.4. Due to the combined effect of pressure and temperature, the density is equal or decreased among each layer.

Cross-sections The reaction cross-section is a measure of the probability of a particular reaction to occur. It depends on the striking particles, its energy and the nature of the target nucleus. Depending on the reactions, at least for neutrons three regions are commonly distinguished starting from lower energies:

1. *The thermal zone* which could have an inverse proportionality trend to the particle velocity
2. *The resolved resonance zon*e, where the single resonance can be appreciated
3. *The unresolved resonances area* where they are too crowd together to such an extend that the individual ones cannot be distinguished

In fact, the temperature might also influence the radiation transport by means of the *thermal scattering* and the resolved resonances modifications if the neutron energy is comparable to the thermal motion of the atom which, indeed, are in continuous motion. Thus, even a beam of mono-energetic neutrons impinging on a target could appear to the nucleus as a continuous distribution. This repercussion, which is known as *Doppler effect* [22], maintains the resonance areas but at the same time makes them shorter and wider. It is enhanced with the temperatures increase.

Application of the operation conditions In general terms in order to simulate correctly the radiation transport at a given temperature in MCNP [75], you have to change four things:

1. The material densities (see previous section)
2. Use Doppler broadened cross sections at the right temperature which can be done:

No.#	Thickness, cm	Material	$\rho_{ROOM}, \frac{g}{cm^3}$	$\rho_{OPER}, \frac{g}{cm^3}$
1	2.00E-02	W coating	19.30000	19.21094
2	4.09E-01	F82H	7.87100	7.71604
3	5.82E-01	Water	0.99821	0.66649
4	8.09E-01	F82H	7.87100	7.71664
5	4.13E+00	Mix breeder[20]	1.84000	1.84000
6	1.65E-01	F82H	7.87100	7.71661
7	4.24E-01	Water	0.99821	0.66649
8	1.65E-01	F82H	7.87100	7.72355
9	5.40E+00	Mix breeder	1.84000	1.84000
10	1.65E-01	F82H	7.87100	7.74730
11	4.24E-01	Water	0.99821	0.66649
12	1.65E-01	F82H	7.87100	7.75268
13	6.98E+00	Mix breeder	1.84000	1.84000
14	1.65E-01	F82H	7.87100	7.76760
15	4.24E-01	Water	0.99821	0.66649
16	1.65E-01	F82H	7.87100	7.76723
17	9.76E+00	Mix breeder	1.84000	1.84000
18	1.65E-01	F82H	7.87100	7.73712
19	4.24E-01	Water	0.99821	0.66649
20	1.65E-01	F82H	7.87100	7.73227
21	1.61E+01	Mix breeder	1.84000	1.84000
22	1.65E-01	F82H	7.87100	7.76860
23	4.24E-01	Water	0.99821	0.66649
24	1.65E-01	F82H	7.87100	7.77460
25	4.28E+00	Mix breeder	1.84000	1.84000
26	1.65E-01	F82H	7.87100	7.77482
27	4.24E-01	Water	0.99821	0.66649
28	1.65E-01	F82H	7.87100	7.77627
29	1.00E+00	Mix breeder	1.84000	1.84000
30	1.65E-01	F82H	7.87100	7.77634
31	4.24E-01	Water	0.99821	0.66649
32	1.65E-01	F82H	7.87100	7.77721
33	1.00E+00	Mix breeder	1.84000	1.84000
34	1.65E-01	F82H	7.87100	7.75804
35	4.24E-01	Water	0.99821	0.66649
36	1.65E-01	F82H	7.87100	7.75802
37	1.00E+00	Mix breeder	1.84000	1.84000
38	9.72E-01	F82H	7.93000	7.80400
39	2.56E-01	Water	5.12188	5.12188
40	1.27E+00	F82H	7.93000	7.80400

Table 4.2.4: 1D MCNP Material density

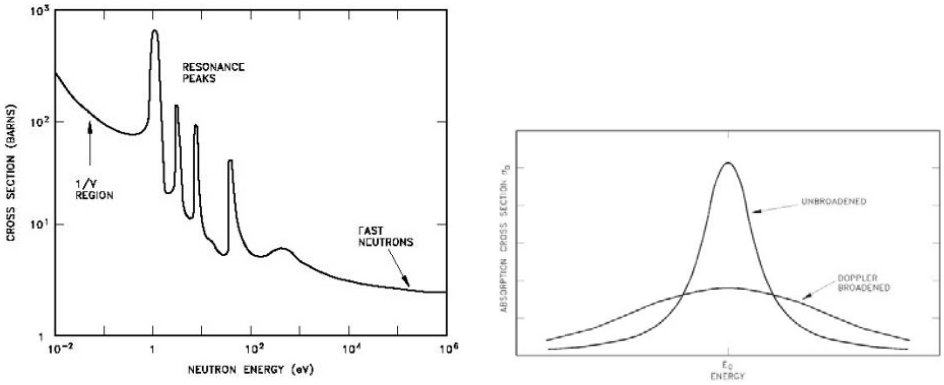

Figure 4.2.27: Cross section and Doppler Effect

(a) Interpolating existing ACE files with the MAKXSF[21] utility [126], or

(b) Generating the ACE[22] [127] file from the ENDF evaluations at the right temperature using NJOY

3. Use the thermal scattering libraries $S(\alpha, \beta)$ at the right temperature which can be done:

   (a) Interpolating existing ACE thermal files with the MAKXSF utility, or

   (b) Generating the ACE from the ENDF evaluations at the temperature given in the ENDF-6 formatted $S(\alpha, \beta)$ libraries and then interpolating with MAKXSF (is necessary), or

   (c) Creating the ACE files with NJOY [92] at the right temperature. This could require the usage, at least, of the LEAPR with the right thermal scattering model.

4. Use the "Free-gas thermal temperature card" (TMP) [75] to impose the free-gas model at the right temperature if you do not have the correspondent thermal scattering libraries.

For this specific case, the free-thermal scattering temperature card and the Doppler effect have been considered as a negligible contribution compared to the variation of the material densities. Indeed, they have been not applied for the following reasons:

[21] The MAKXSF code is a utility program for manipulating cross-section library files for the MCNP5/MCNPX Monte Carlo code. It is distributed inside the MCNP5/MCNPX package. It can be to convert ACE data files between ASCII and binary formats and to make customized libraries containing selected datasets.

[22] ACE stays for "a compact ENDF" format and originated from work on MCNP. It is used in a number of other Monte Carlo particle transport codes. ACE-format cross sections are typically generated from ENDF files through a cross section processing program like NJOY.

- *Doppler effect:* this contribution mainly affect the heavy nuclides where several resonances are present (e.g. Uranium, Plutonium). In the fusion technologies, the application of heavy material is limited as much as possible to decrease the high radioactivity waste. Indeed, considering the 1D-HET model, only Wolfram might be affected but having a thickness of less than millimeters and temperature not too far from 300 K, the computed effect could be shadowed by the uncertainty in the generation of the specific cross-sections. As proposed in [128], this contribution is neglected.

- *Free-gas thermal temperature card (TMP card):* the 1D-HET model represents the WCPB BB model from the FW up to the VV spanning over about 60 cm. As described in the Sec.4.2.2.3, only a minor fraction of the neutron spectra distribution is, so far, thermalized once the VV inner shell is reached having is average energy around 1 MeV. Moreover, the MCNP manual recommends the application of the TMP card if the neutron energy E (MeV) is minor that $E < 400^{-1} * 8.167 * 10^{-11} * T[K]$, where T is the temperature of light nuclei in the medium. So, for this specific application, this contribution is neglected as proposed in [128]. Nevertheless, if the model embraces systems which suffers a fully thermalized neutron flux (e.g. magnets, thermal shields), this effect might be taken into account or at least evaluated.

Results The comparison between the MNCP 1D-HET and 1D-DENS responses is reported in Fig.4.2.28[23]. In both cases the neutron distribution suffers an exponential decrease but less pronounced in the 1D-DENS due to the density variations. Although, all the energy bins are affected, the thermal range is the most influenced one because the down energy group scattering is less pronounced. Indeed, the decrease of the density increases the cells mean free path hence reducing the number of interactions. This effect also contracts the Tritium generation in all the breeding areas achieving about -50% loss over the total production. In addition, the photon total flux is larger because the neutron flux is less attenuated producing more secondary particles. As for neutrons, the photon distribution flux difference increases with the radial distance because of the sum up effect.

In both cases the neutron NHD is dominant. However, it is interesting to observe how the 1D-HET NHD is more prominent over the material cells where the deposition is dominated by neutrons, as the water layers, whereas it seems smaller over the F82H zones which are impinged by a larger photon flux. In addition, the breeding areas observe larger fluxes having an increased deposition peaked over the middle planes as detected by the 1cm resolution MCNP FMESH (i.e. right side NHD plot)[24]. To conclude, the 1D-DENS experiences a substantial decrease of about 50% in total power deposition and for these rea-

[23] All the per cent differences have been determined as (1 - 1D-DENS/1D-HET)*100

[24] The usage of the tally and the FMESH tools is complementary and it gives a better global understanding of the physical behavior having the averaged and the local picture of the situation.

sons it has been discarded in favor of the 1D-HET model to increase the safety margins.

4.2.3 Fully detailed vs Simplified MCNP models

The three-dimensional radiation transport responses, described in Sec.4.2.1, have been compared with those obtained employing two 1D blanket simplified MNCP models (e.g. 1D-HET and 1D-HOM), Sec.4.2.2. Hereinafter a selection of the detailed comparison is reported focusing on the neutron flux, photon flux and nuclear power density (Fig.4.2.29, Fig.4.2.30 and Fig.4.2.31). All the per cent differences have been computed as $(1 - 1D_{CASE_i}/3D) * 100$ thus having prevalence of the simplified responses over the fully detailed ones in case of negative values.

A good agreement in observed both in the photon and neutron flux in the whole set of cases endorsing the methodology generation of the 1D simplified MNCP models. The exponential decreasing neutron trend are matched as well as the photon flux which presents a peak just close to the plasma. No major differences are found. Nevertheless, minor divergence are observed, a very good agreement is obtained considering the very different models. The discrepancies increase with the radial distances having in the 1D-models higher and harder fluxes. Indeed, the neutron flux spectra analysis highlights a prevalence of the fast range with a detrimental effect over the thermal bin. This outcome, which is less prominent in the 1D-HOM, could be attributed in part to the absence of back-scattering from nearby region which is clearly absent in the simplified simulation.

The neutron and photon NHD computed have a similar trend in all the cases being the neutron contribution dominant. However, it is interesting to observe how the deposition peaks are smeared down in the 3D simulation due to the presence of different materials in the MCNP FMESH voxel which causes the averaging of the flux. This "artificial" effect, which appears both for neutron and photons, is detrimental for the CFD calculation safety margin because it decreases the temperature peak. In the same way, sensible differences are observed in the cooling areas especially for the 1D-HET case which does not employ material mixture. In addition, the NHD discrepancies increase with the radial distance having in the 1D-model more conservative results, apart from a small area close to the first wall.

To conclude, after a meaningful comparison, the 1D-HET responses have been preferred to the others due to the greater integrated power deposition as well as the preservation of the NHD peaking profile. Moreover, 1D-HET results have been used as reference radiation transport data for thermal-hydraulic analyses because they imply the most conservative temperature distribution and they have been endorsed by further assessments about the boundary condition impact, Sec.4.2.2.4, the operation condition influence, Sec.4.2.2.7, and the cross section one, Sec.4.2.2.6.

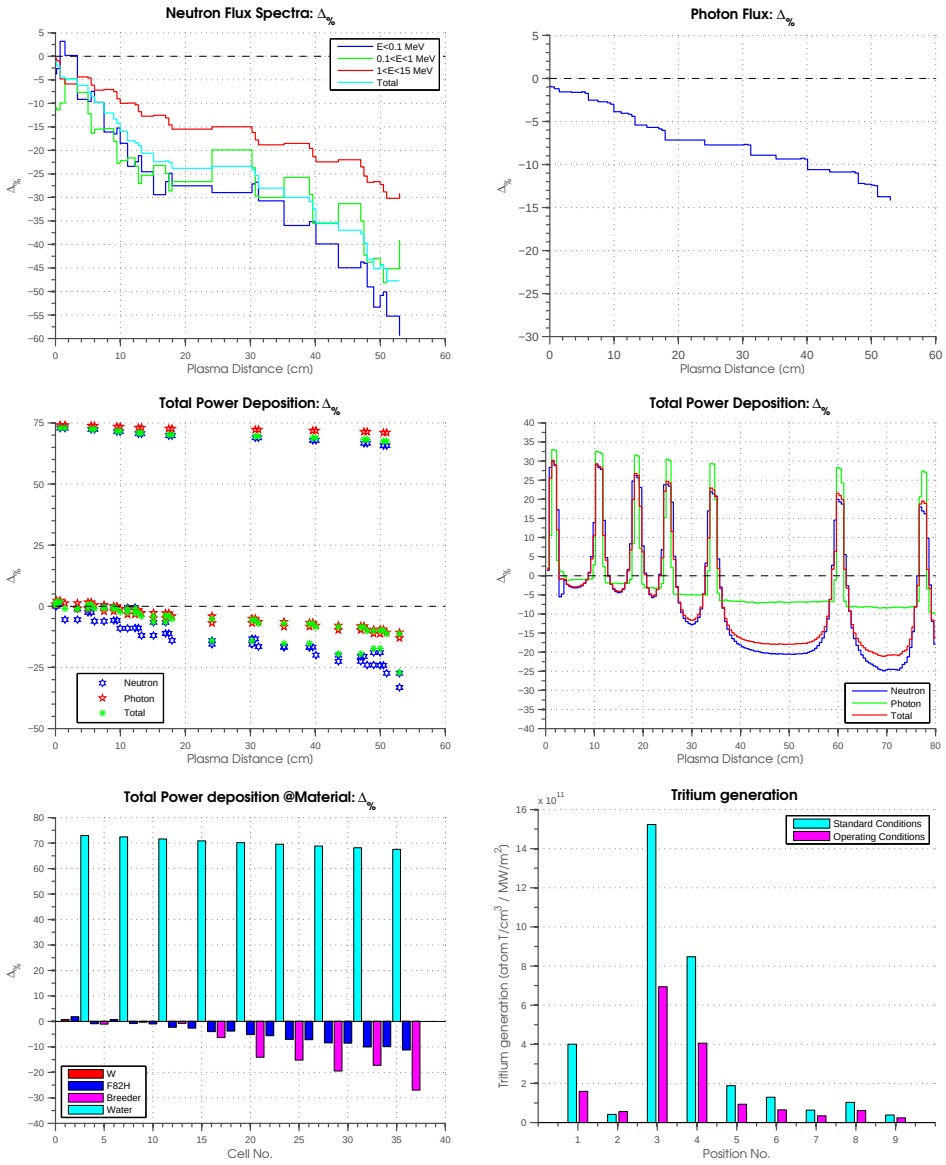

Figure 4.2.28: MCNP Operation Conditions Assessment

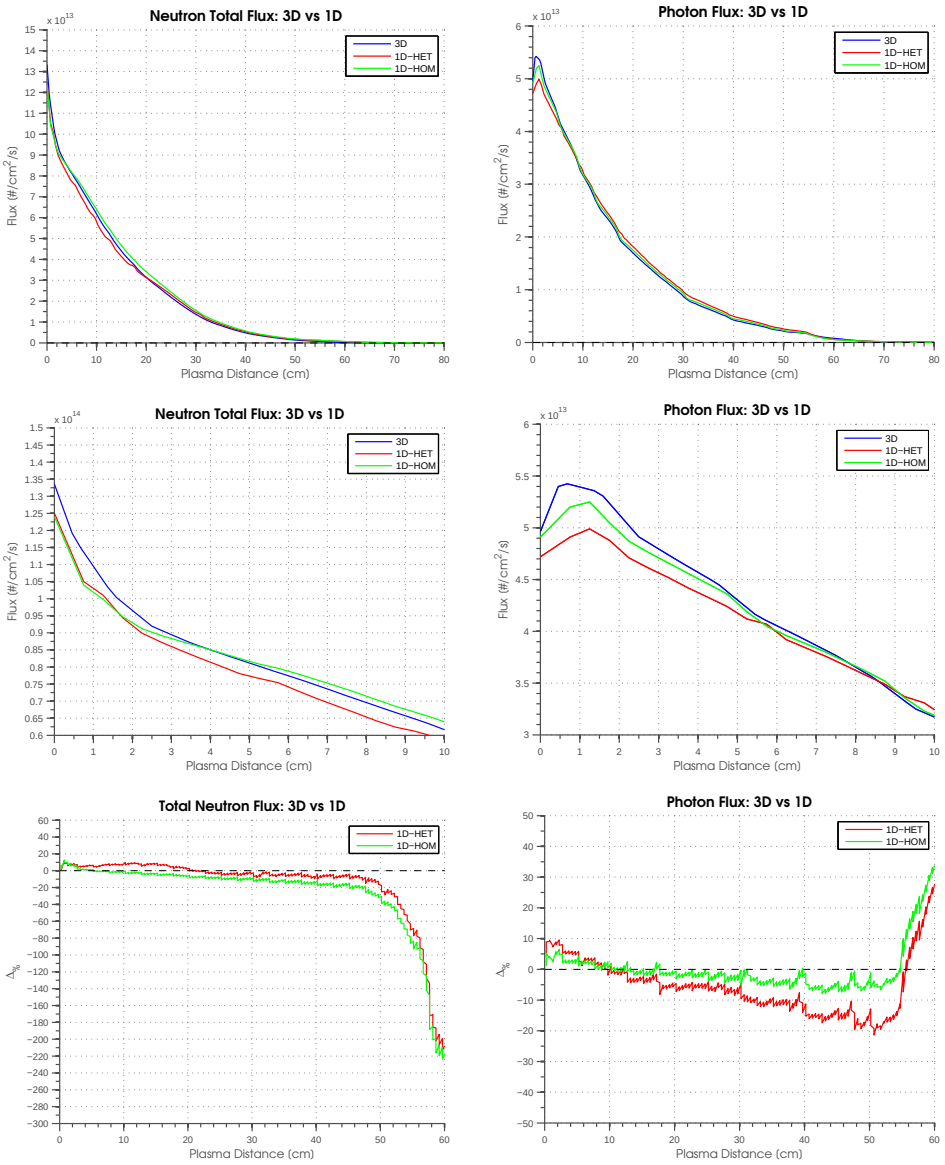

Figure 4.2.29: MCNP 3D vs 1D comparison - flux

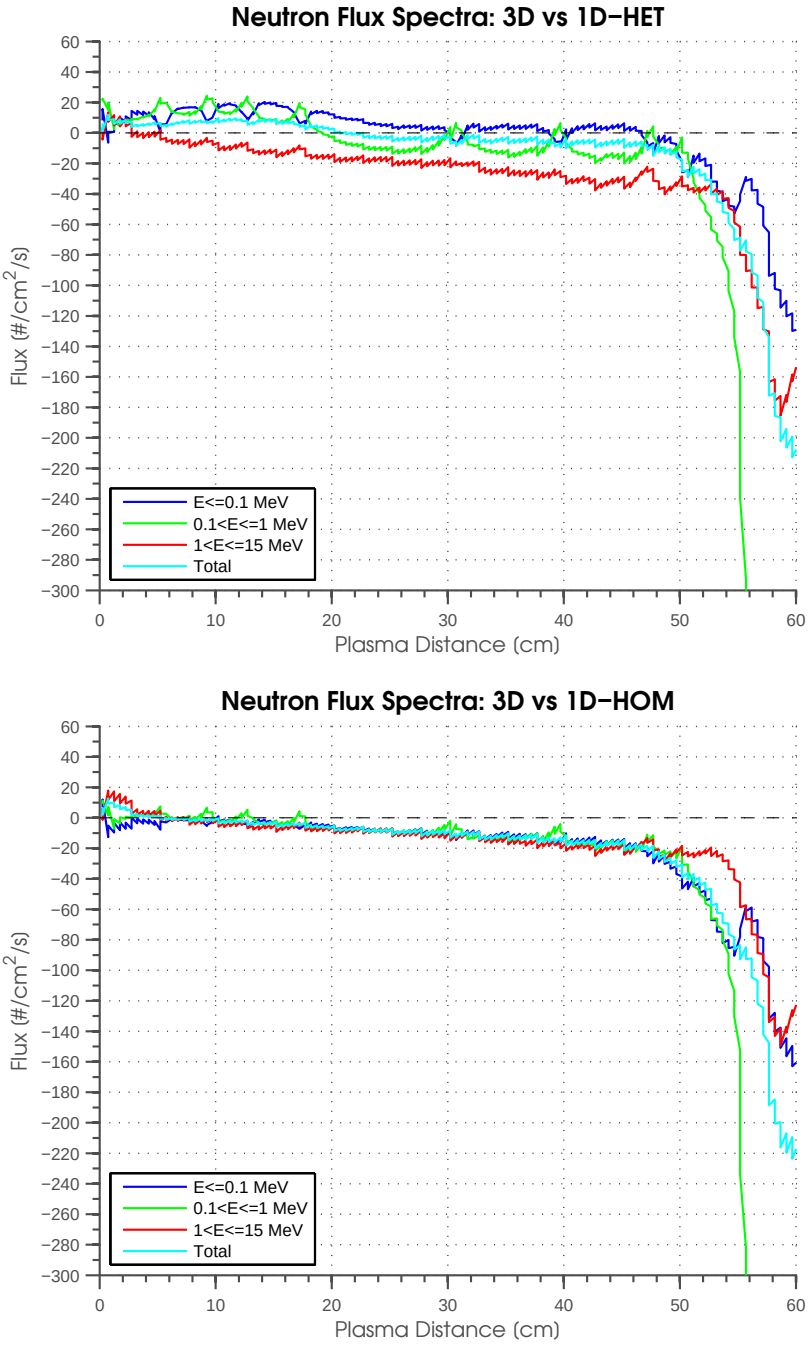

Figure 4.2.30: MCNP 3D vs 1D comparison - neutron spectra

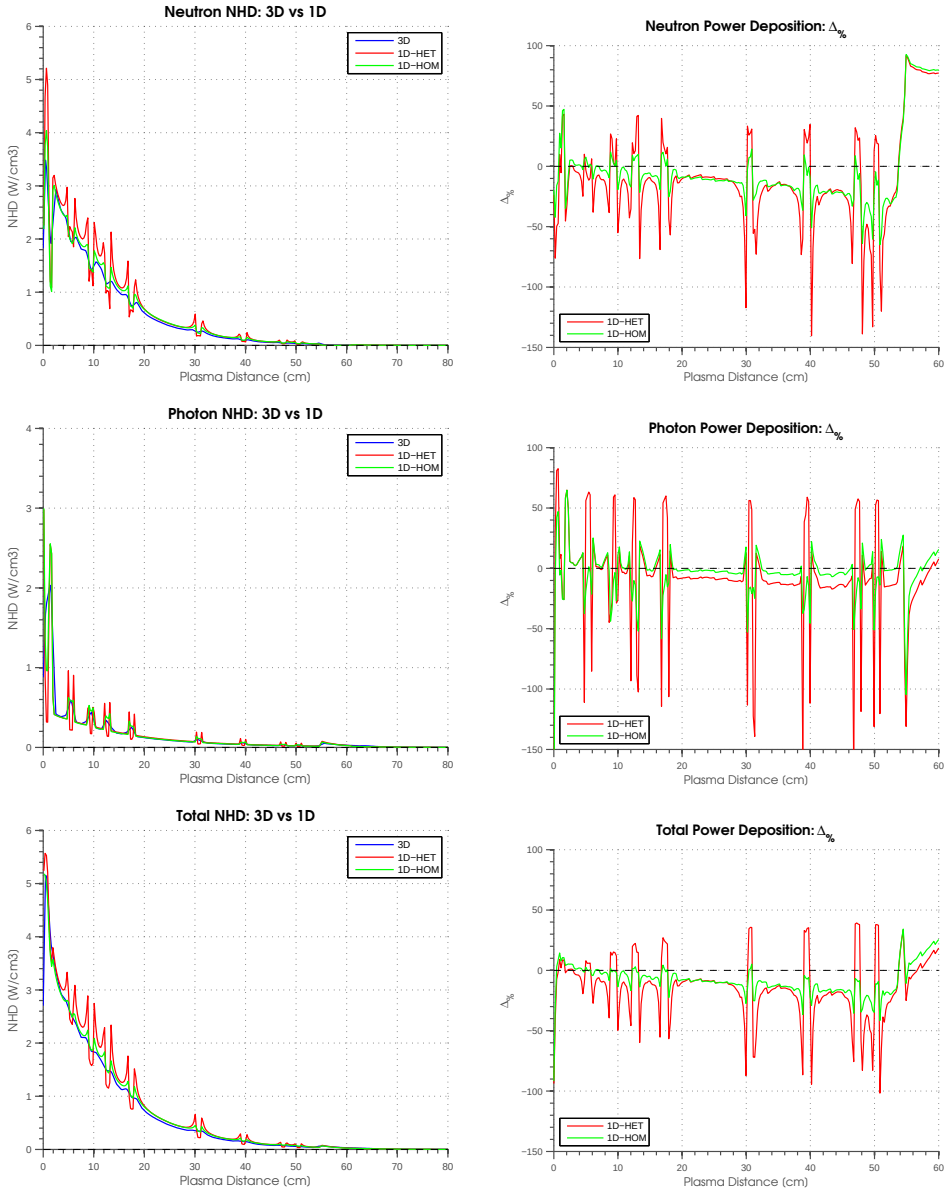

Figure 4.2.31: MCNP 3D vs 1D comparison - NHD

4.3 Thermal-hydraulics Analyses

Fully detailed 3D thermal-hydraulic analyses, Sec.4.3.1, have been computed by means of the computational fluid dynamics (CFD) ANSYS® Fluent® v17.2 [98] following the methodology described in Sec.2.3. The original blanket geometrical model [113] has been simplified using SpaceClaim [90] and CATIA [91] software in order to remove non-relevant details for meshing proposal. Within this work, the use of automatic meshing has been discarded in favor of manual meshing in order to achieve a better control of mesh over small details such as the first wall (FW) channels and the pipes. Therefore, Pointwise software has been employed. Hence boundary conditions, material temperature dependent properties and NHD have been introduced using in-house developed ANSYS® Fluent® User Defined Functions, Sec.2.3.2. Then, thermal responses have been post-processed by Paraview software [104, 105] and distribution extracted for further comparisons. Moreover, more refined and polyhedral meshes have also been tested to comply with the Richardson theorem to confirming the independence of the mesh results. To consolidate this study named as CFD-3D, further assessments have been performed changing the NHD, CFD-NHD in Sec.4.3.3, to verify the results sensibility as well as the domain dependence using a 2D very refined domain model, CFD-DOM in Sec.4.3.4.

4.3.1 Fully detailed 3D Thermal-hydraulics analysis

4.3.1.1 Geometry simplifications

Geometrical simplifications are needed to achieve good results convergence and mesh quality. They have been limited only where strictly necessary. Using SpaceClaim [90] and CATIA [91] non-relevant details, as tangent surfaces and small angles, has been removed. In addition, the back plate inlet has been removed in order to apply a uniform BC among all the surface. Thanks to the poloidal simmetry of the system, the domain of simulation has been limited along the Z directions to achieve an optimized computational effort. Despite the applied modifications, no significant impact on the system behavior is expected as the geometry has been kept very close to the real one. Indeed, this can be appreciated comparing the baseline geometry, Fig.4.3.1, with the simplified one, Fig.4.3.2. Moreover, several views have been reported in Fig.4.3.2 to even better observe the level of details preserved in the FW, in the back plate and in the pipes.

4.3.1.2 Meshing

Within this work, despite the very time consuming operation, the use of automatic meshing has been discarded in favor of manual meshing, in order to achieve a better control of mesh over small details such as the first wall (FW) channels and the pipes. Therefore, Pointwise software [102] has been employed, resulting in a domain of 6.7 M tetrahedra subdivided in the following ZoneID:

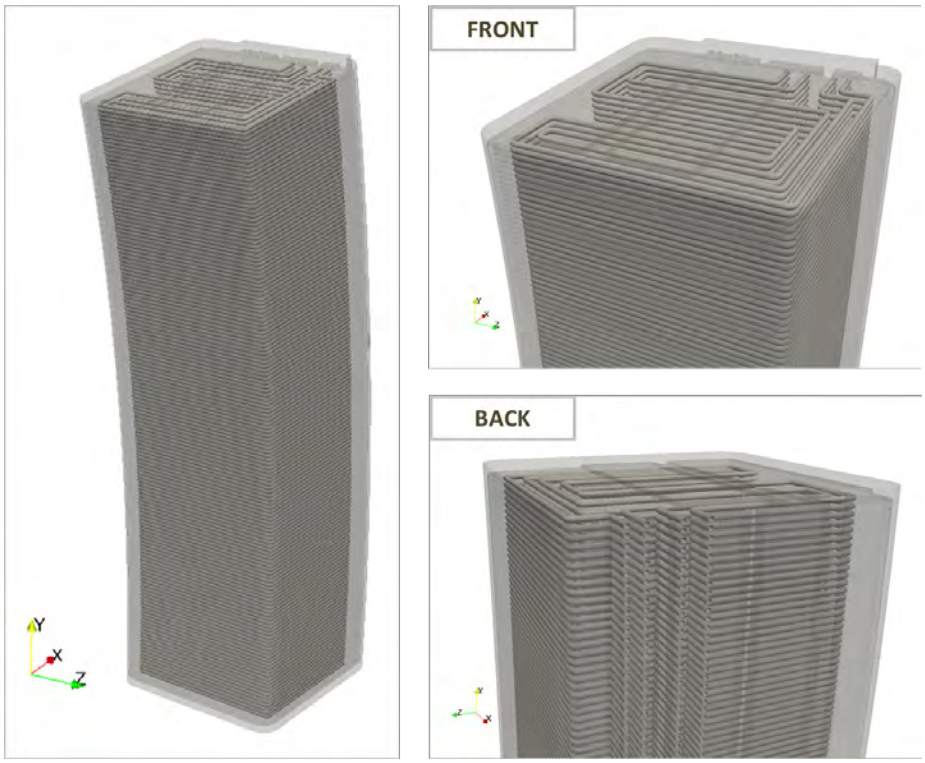

Figure 4.3.1: WCPB Baseline geometry

(a) Front view

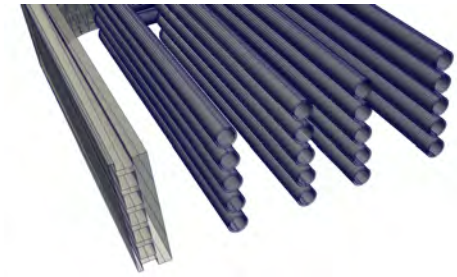

(b) Zoom over the first wall

(c) Back view

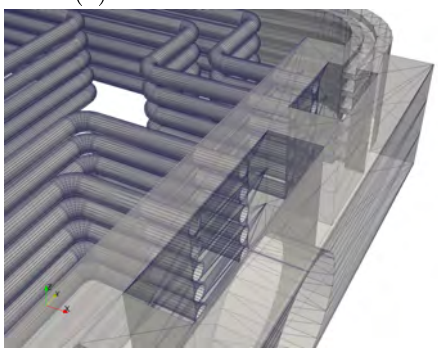

(b) Zoom over the back plate

Figure 4.3.2: WCPB simplified geometry

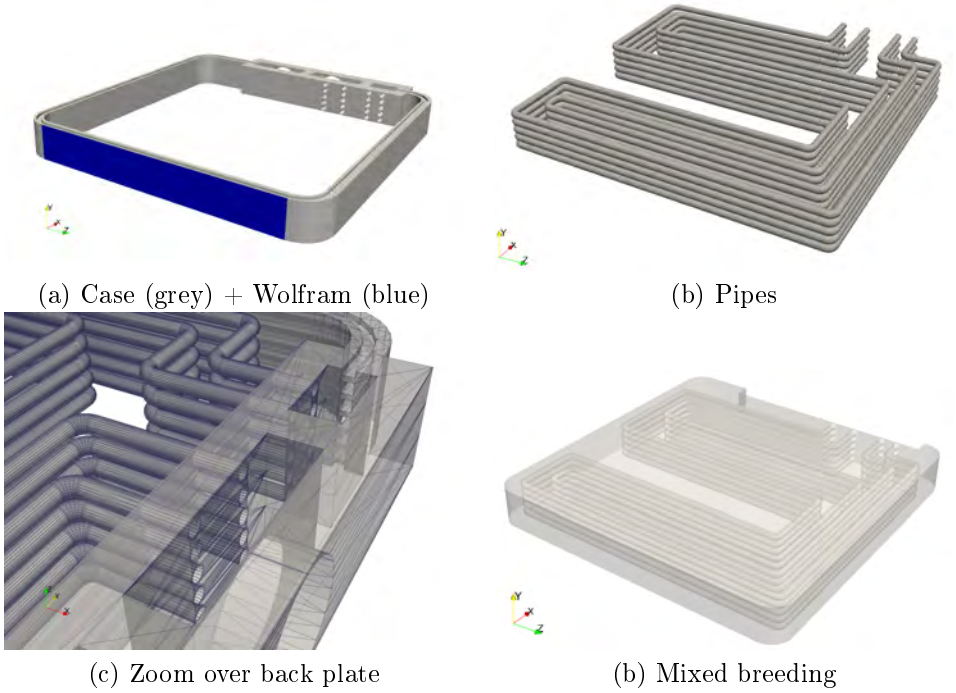

(a) Case (grey) + Wolfram (blue)

(b) Pipes

(c) Zoom over back plate

(b) Mixed breeding

Figure 4.3.3: WCPB ZoneID

- Wolfram, Fig.4.3.3-(a): 37400 wedge
- Case, Fig.4.3.3-(a): 1089414 tetrahedra
- Pipes[25], Fig.4.3.3-(b): 895012 tetrahedra
- Breeding material, Fig.4.3.3-(d): 4740291 tetrahedra

A hybrid mesh has been used to cope with the small thickness of the Tungsten. In fact, all the components are composed by tetrahedra apart from the Wolfram which is represented by wedge element obtained by extrusion from the case mesh along the FW surface normal direction.

The very fine mesh employed over all the components can be denoted in Fig.4.3.4. A more refined grid has been used over the FW and over the breeding material to achieve a enhanced resolution of the results. All the mesh statistics fulfills the CFD standards supporting the results obtained.

[25]One region for each pipe has been generated in order to allow future assessments regarding the impact of a single pipe operation conditions.

(a) Case

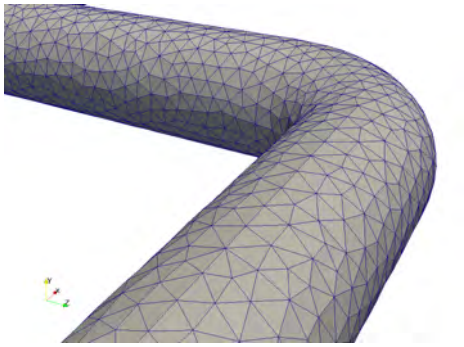

(b) Pipes

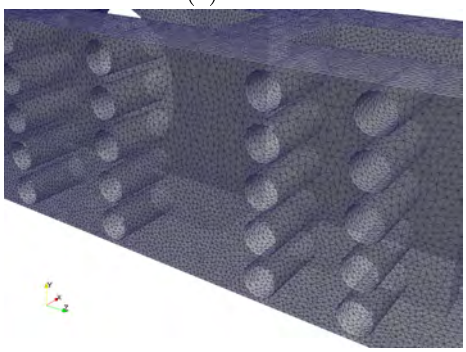

(c) Back plate holes (case only)

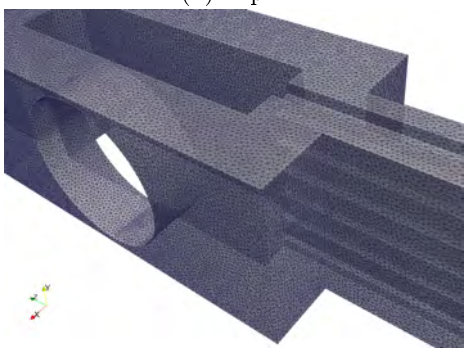

(b) Back plate (case only)

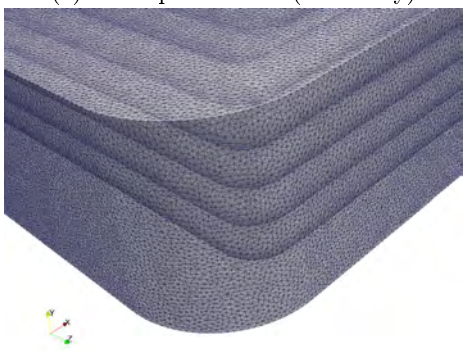

(e) Front side (pipes and breeding)

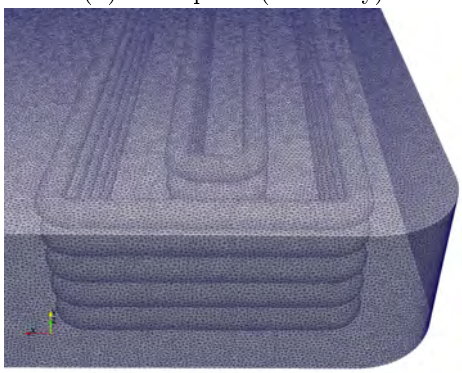

(f) Lateral side (pipes and breeding)

Figure 4.3.4: WCPB Mesh zoom

4.3.1.3 Boundary conditions and assumptions

The boundary conditions and assumptions adopted in the thermal hydraulic simulation of WCPB BB have been reported in Table 4.3.2. The single BC are identified in Fig.4.3.5. Regarding the NHD implementation please refer to Sec.4.3.1.4.

Type	Description
BC@Back Plate	Temperature imposed at 598 K
BC@FW or X-	1 MW/m^2
BC@Y- & Y+	Adiabatic
BC@Z- & Z+	Periodical
Pipe[14]	$T_{Bulk} = 593\ K$; $HTC = 13285\ W/m^2/K$
Water Case [14]	$T_{Bulk} = 593\ K$; $HTC = 13285\ W/m^2/K$
Solution type	Steady-state
Solver	Double precision
Energy Equation	Solved in coupled in all the domains
Material properties	As specified in Sec.4.1.2
	Temperature dependent

Table 4.3.2: Boundary conditions

4.3.1.4 Nuclear heating

The nuclear heat deposition computed by the MCNP fully detailed 3D radiation transport calculation, Sec. 4.2.1, has been employed and set by means of the ANSYS Fluent routines developed, Sec.2.3.2. A combination of implicit and explicit tally has been used to increase the margins, Sec.4.3.4. Indeed, the mere usage of the FMESH of 1 cm resolution over a very small thickness component is not sufficient to preserve the NHD due to to the volume smearing. For this reason the Wolfram NHD has been adjusted to match the total power deposition computed by tally. In addition, the case and pipe ZoneID NHD has been filled by the explicit F82H FMESH to maximize the nuclear hot-spot particularly close to the FW, as described in Sec.2.2.4.4.

The NHD macroscopic responses (e.g.minimum, maximum, average and integral) in each Zone ID has been reported in Table 4.3.5 and the several contour plots in Fig.4.3.6. As expected, the NHD set is according the MCNP fully detailed 3D radiation transport calculation NHD hence validating once more the ANSYS Fluent routines developed , Sec.2.3.2.

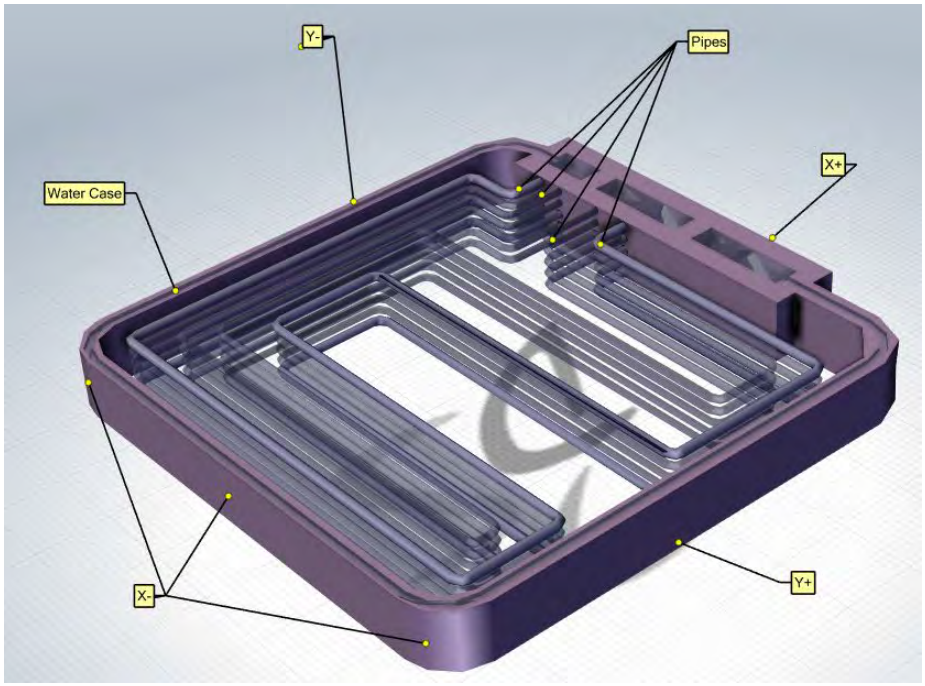

Figure 4.3.5: CFD Boundary condition identification

ZoneID	Input
Wolfram Layer	Power adjusted to the tally value
Case	Explicit F82H FMESH
Breeding	Implicit FMESH
Pipes	Explicit F82H FMESH

Table 4.3.4: Nuclear Heating Assumptions

ZoneID	NHD_{min} $[W/m^3]$	NHD_{max} $[W/m^3]$	NHD_{ave} $[W/m^3]$	$\int\int\int NHD$ $[W]$	$[\%]$[26]
Wolfram Layer	10375000	10375000	10375000	14	0.08
Case	19569	5340143	961308	3064	17.6
Breeding	16057	8457355	740516	13553	78.1
Pipes	50588	2363204	848494	733	4.2

Table 4.3.5: Nuclear heating implemented

4.3.1.5 Results

The macroscopic CFD WCPB BB responses are reported in Table4.3.6 whereas a selection of the microscopic ones in Fig.4.3.7. In addition, the temperature gradients have been reported in Fig.4.3.9.

As expected, the WCPB temperature responses are influenced by the presence of water cooling patterns and by its distance. Indeed, at about 25 cm from the FW a large hot-spot is observed in the breeding material which reaches the maximum temperature of the case, 962.3 K. This peak of temperature is almost constant along Z while experiments sensible changes along the Y direction, as showed by temperature distribution, Fig.4.3.8, and its gradients, Fig.4.3.9, generating a sort of Gaussian bell. Indeed, just moving away about 10 cm along Y direction, the maximum temperature decreases almost 100 K. This behavior is induced in one side by the proximity of the pipe bend while in the other by the case cooling. Apart from this region, constant breeding temperatures along Y axis are extensively observed and confirmed by the gradient.

In addition, the case temperature increases up to a maximum close to the Y sides because of the conjunctions of adiabatic BC and Neumann BC whereas it has a almost constant temperature in the central part beyond the Wolfram layer. This effect could be generated by the conservative BC. Indeed, it will disappear once a more accurate heat exchange is modeled either by the introduction of nearby BB or by an imposed thermal flux.

To conclude, the temperature distribution computed seems to be almost constant toroidally. This support the approach used which allows limits the

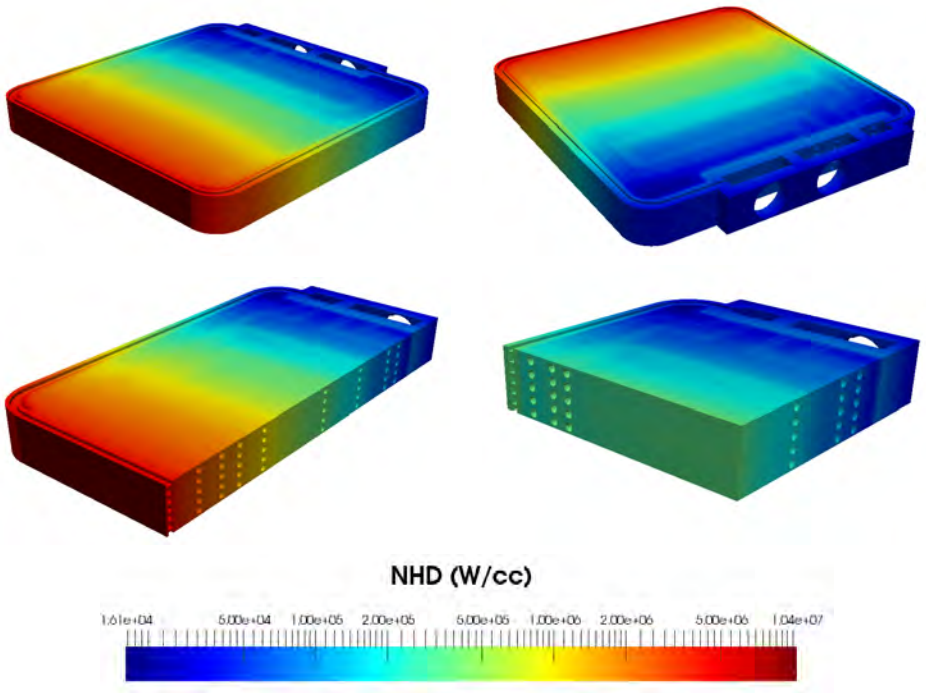

Figure 4.3.6: WCPB NHD Source term

ZoneID	T_{min} $[K]$	T_{max} $[K]$	T_{ave} $[K]$
Wolfram Layer	764.8	797.8	770.8
Case	598.1	915.5	607.8
Breeding	598.2	962.3	666.6
Pipes	598.1	606.9	598.2
WCPB BB	598.1	962.3	655.6

Table 4.3.6: WCPB BB Macroscopic results

model in the Z direction taking advantage of the periodical boundary conditions. On the other hand, sensible variation in the radial direction are observed as cross-checked by the analysis of the temperature gradient, which is close to zero over the temperature peaks. Moreover, the case maximum temperatures are placed close to the lateral side and in the middle part of the breeding. Further assessments about NHD, Sec.4.3.3, domain, Sec.4.3.4, and mesh independence, Sec.4.3.2, have confirmed and endorsed this behavior.

4.3.2 Mesh independence

An additional 3D WCBP BB model case (or CFD-POLY) based the same simplified geometry but with different mesh element type and resolution has been developed.

It aims to fulfill the the Richardson theorem demonstrating the response mesh independence. In the following sections the assessment has been described starting from the geometrical simplification up to the response justifications in comparison with those of CFD-3D.

4.3.2.1 Geometry simplifications

The geometry simplified is equal to the one used in Sec.4.3.1.1. Please refer to Sec.4.3.1.1 for more details.

4.3.2.2 Meshing

Starting from previous the 6.7 M tetrahedral mesh, Sec.4.3.1.2, polyhedra mesh has been obtained by means of the internal ANSYS Fluent conversion function (e.g. Mesh –> Polyhedra –> Convert Domain). Thanks to the usage of these innovative elements, the total No. of cells decrease about a -21%up to the 5.35 M. The ZoneID are preserved and hereinafter detailed:

- Wolfram, Fig.4.3.3-(a): 23496 polyhedra, -37 %
- Case, Fig.4.3.3-(a): 504585 polyhedra, -54 %

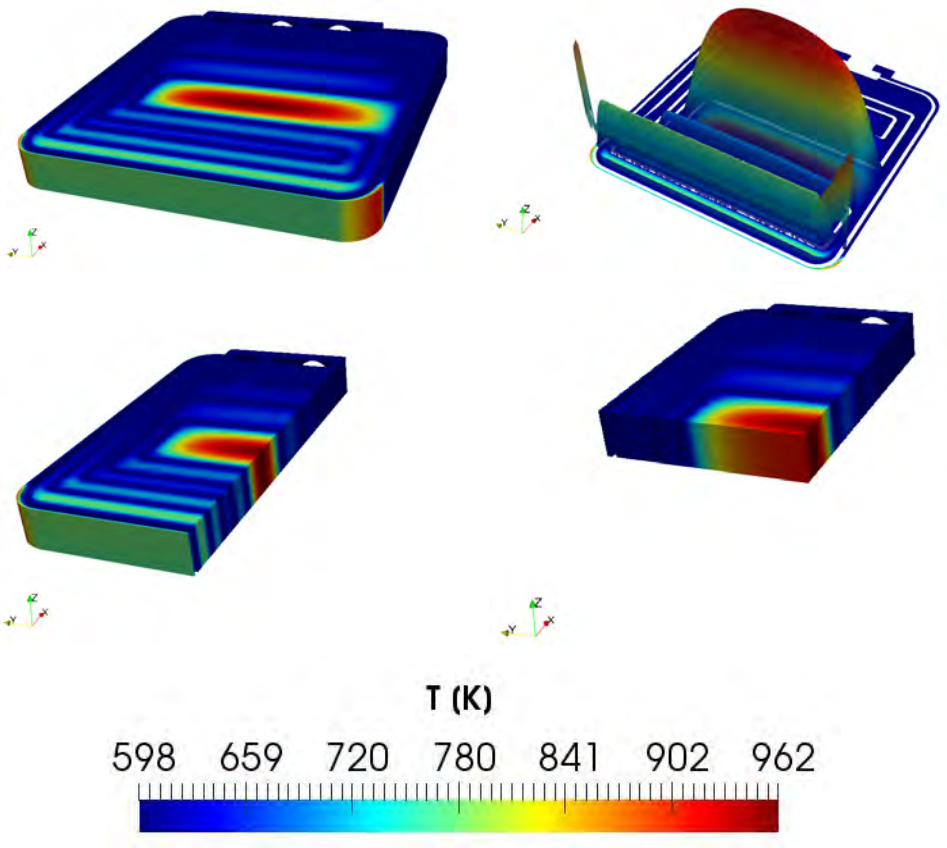

Figure 4.3.7: WCPB BB Microscopic temperature results

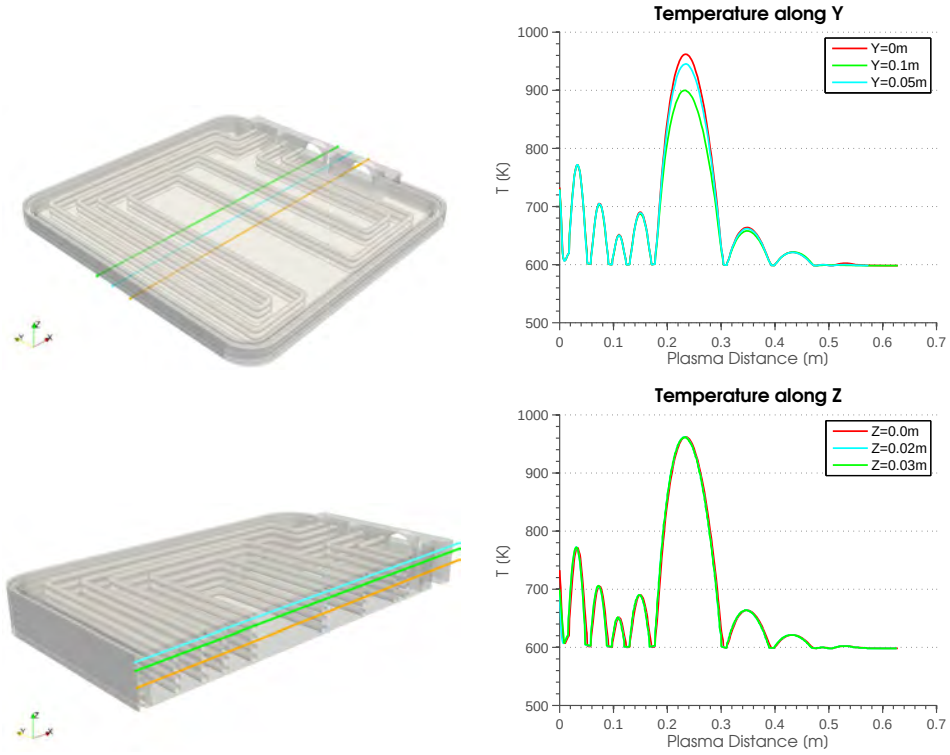

Figure 4.3.8: WCPB BB analysis

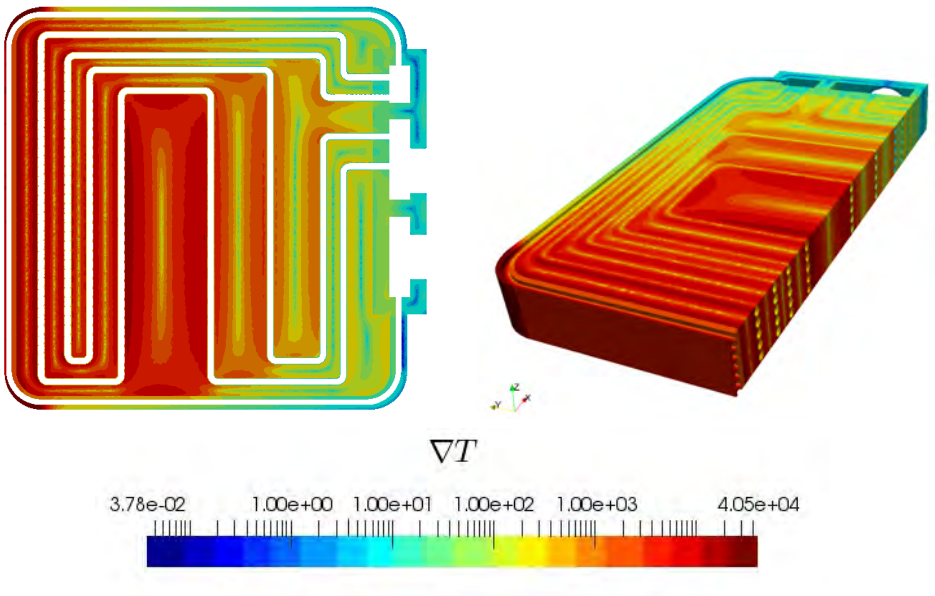

Figure 4.3.9: WCPB BB Temperature gradient

- Pipes[27], Fig.4.3.3-(b): 2524184 polyhedra, -182 %
- Breeding material, Fig.4.3.3-(d): 2300531 polyhedra, -52 %

In Fig.4.3.10 several zooms over the components have been reported to highlight the quality of the mesh and its details. The whole set of ZoneID are composed by polyhedra and fulfill the mesh statistics supporting the results obtained. In this case, the mesh quality analysis has been carried out using the ANSYS Fluent internal utilities because the deficiency of Paraview to work with this kind of element.

4.3.2.3 Boundary conditions and assumptions

The boundary conditions and assumptions match those used in Sec.4.3.1.3. Please refer to Sec.4.3.1.3 for more details.

4.3.2.4 Nuclear heating

The nuclear heat deposition computed by the MCNP fully detailed 3D radiation transport calculation, Sec.4.2.1, has been employed and set by means of the ANSYS Fluent routines developed, Sec.2.3.2, according to Sec.4.3.1.4. Besides the same assumptions and baseline data used, minor local differences are present

[27] One region for each pipe has been generated in order to allow future assessments regarding the impact of a single pipe operation conditions.

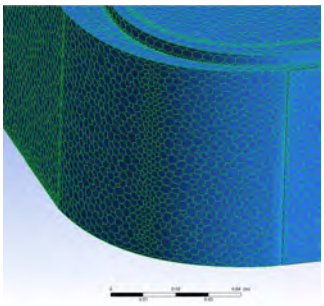

(a) Mesh - Case & Breeding left side

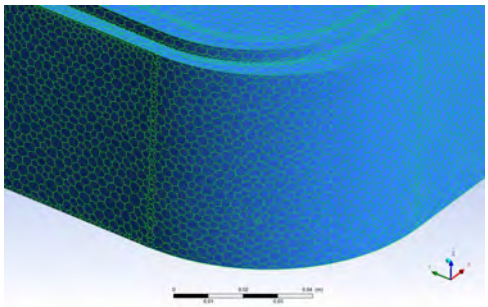

(b) Mesh - Case & Breeding right side

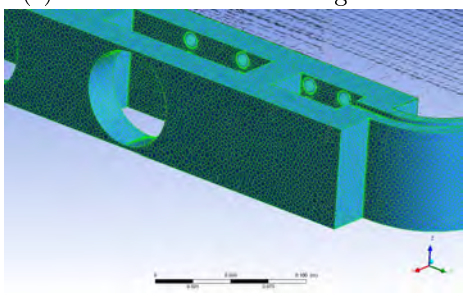

(c) Mesh - Case back plate

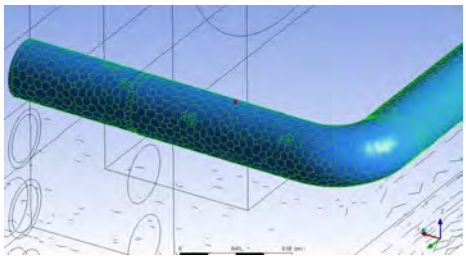

(b) Mesh - Pipe

Figure 4.3.10: WCPB CFD-POLY mesh

in the NHD implemented (e.g. minimum, maximum and average) due to the discrepancies of the mesh resolution and typology. Having this discrepancies always within 1%, the detailed description of the macroscopic and microscopic NHD is not duplicated here thus please refer to Sec.4.3.1.4.

4.3.2.5 Results

The macroscopic CFD responses are reported in Table 4.3.7 while microscopic in Fig.4.3.11.

As foreseen, the macroscopic responses are in line with those of the CFD-3D case. Apart from the Wolfram layer, difference are within 1% thus validating the mesh independence of the results. The Tungsten discrepancy should be not considered as a showstopper because the decreased resolution of the mesh could have smeared down the temperature peak as well as the usage of a polyhedra mesh instead of a wedge one.

The microscopic results[28] appears completely in line with those of the CFD-3D case, Sec.4.3.1, confirming the hot spot positions. Again, no major discrepancies have been discovered neither analyzing the temperature gradient nor the

[28] Due to the polyhedra mesh which is not usable in Paraview, the post-processing have been carried directly inside ANSYS Fluent. For this reason the pictures could result in a different aspect.

ZoneID	T_{min} $[K]$	T_{max} $[K]$	$[\%_i]$	T_{ave} $[K]$
Wolfram Layer	682.1	699.4	11.0	685,0
Case	598.2	759.6	0.7	604.0
Breeding	598.2	979.8	-0.3	668.7
Pipes	598.2	607.5	-0.1	600.0
WCPB 3D-NHD	598.2	979.8	11.0	657.0

Table 4.3.7: WCPB CFD-POLY Macroscopic results

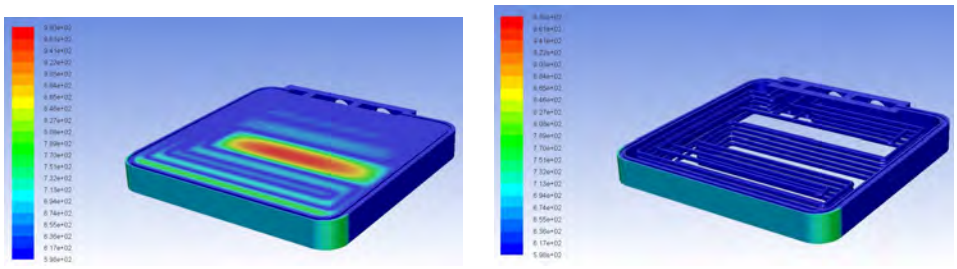

Figure 4.3.11: WCPB CFD-POLY Microscopic results

temperature distribution along the mayor axis. To conclude, thanks to the CFD-DOM case, the CFD-3D case responses have been verified as mesh independent.

4.3.3 Nuclear heating sensitivity

An additional 3D WCBP BB case (or CFD-NHD) has been carried out to verify the sensitivity of the NHD and its impact. It has been based upon the same model used in Sec.4.3 but employing the NHD computed by the simplified MNCP model In the following sections the assessment has been described starting from the geometrical simplification up to the response justifications in comparison with those of CFD-3D.

4.3.3.1 Geometry simplifications

The geometry simplified is equal to the one used in Sec.4.3.1.1. Please refer to Sec.4.3.1.1 for more details.

4.3.3.2 Meshing

The mesh corresponds to the employed in Sec.4.3.1.2. Please refer to Sec.4.3.1.2 for more details.

4.3.3.3 Boundary Conditions and assumptions

The boundary conditions and assumptions match those used in Sec.4.3.1.3. Please refer to Sec.4.3.1.3 for more details.

4.3.3.4 Nuclear Heating

The nuclear heat deposition computed by the MCNP simplified heterogeneous model, 1D-HET, Sec.4.2.1, has been employed and set by means of the ANSYS Fluent routines developed, Sec.2.3.2. This has been computed by an implicit FMESH, which is absence of void materials works as an explicit one.

The NHD macroscopic responses (e.g. minimum, maximum, average and integral) in each Zone ID has been reported in Table 4.3.8 and the several contour plot in Fig.4.3.12. The several discrepancies appreciated are hereinafter detailed and justified:

- Wolfram layer: it suffers a clear decrease in the total power deposition due to the usage of a FMESH instead of a tally power deposition value. Anyhow, this contribution is order of magnitude than the others.
- Case: it experiments a small increase in the total power deposition because of the usage of breeding data over the F82H components. Local effects are also observed: NHD profiles parallel to the FW are present remarking the peculiar input data used.
- Breeding: it undergoes a sensible overestimation of the total power deposition due to the usage of the simplified 1D-HET data as described in Sec.4.2.3. The main contributors of this effect are the simplified geometry, the difference material mixture set-up and the application of a NHD which does not correspond to the breeding zone area due to the presence of bends.
- Pipes: it experiments an increase of the NHD as for the "Breeding" area. In addition to the main contributions explained previously, the discrepancy is also justified by the object dimension. Being small components their deposition is influenced by the FMESH resolution which is higher in the 1D-HET than the 3D fully detailed one.

As expected, the NHD set is according the MCNP 1D-HET NHD endorsing the usage of ANSYS Fluent routines developed, Sec.2.3.2.

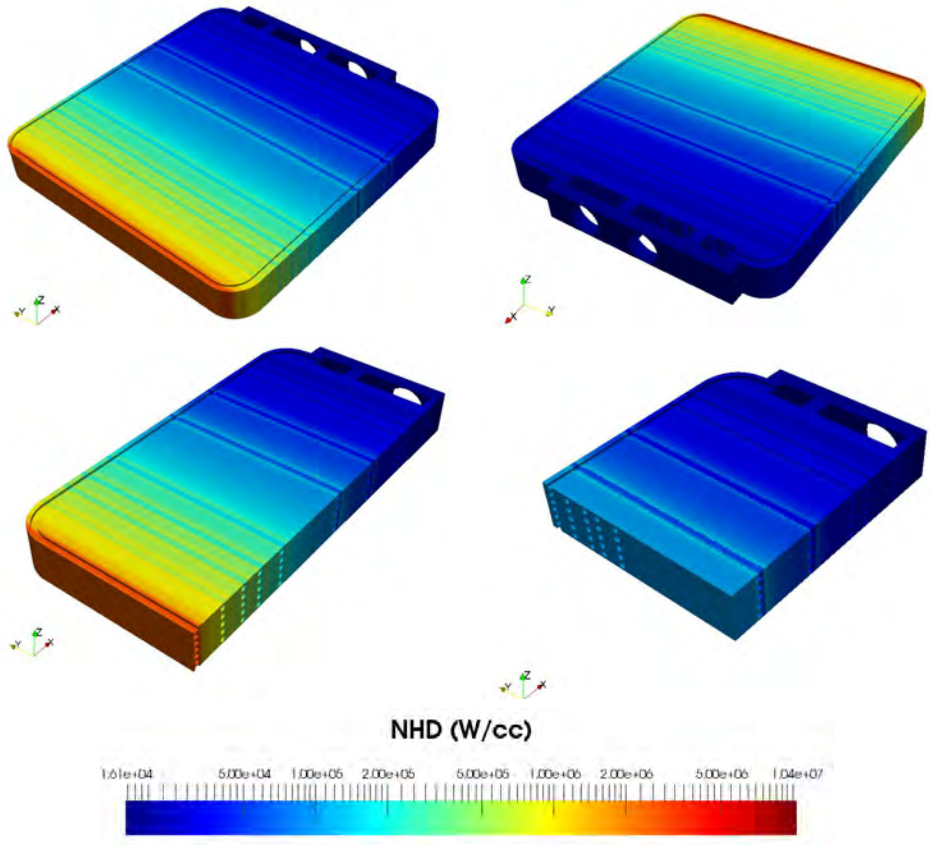

Figure 4.3.12: NHD Source term

ZoneID	NHD_{min} $[W/m^3]$	NHD_{max} $[W/m^3]$	NHD_{ave} $[W/m^3]$	$\int\int\int NHD$ $[W]$	$[\%_i]$	$[\%_{Diff}]$[29]
Wolfram layer	5239000	5239000	5239000	7	0.04	49.5
Case	18170	5570000	994263	3169	16.1	-3.4
Breeding	33680	3796000	855073	15650	79.7	-15.5
Pipes	33680	3109000	935190	809	4.1	-10.1

Table 4.3.8: Nuclear heating implemented

ZoneID	T_{min} $[K]$	T_{max} $[K]$	$[\%_i]$	T_{ave} $[K]$
Wolfram layer	764.9	797.8	0.0	770.8
Case	598.2	915.1	0.05	607.9
Breeding	598.2	1015.0	-5.5	679.8
Pipes	598.2	607.2	-0.3	599.9
WCPB 3D-NHD	598.2	1015.0	-5.5	666.5

Table 4.3.9: WCPB BB Macroscopic results

4.3.3.5 Results

The macroscopic CFD-NHD responses are reported in Table 4.3.9 whereas a selection of the microscopic ones in Fig.4.3.13. In addition, the temperature gradients have been included in Fig.4.3.15.

The analysis of the macroscopic highlights temperatures similar to those of the CFD-3D case apart from the "Breeding" domain. The "Breeding" maximum temperature experiments an increase of about 5% (e.g. 962.3 K vs 1015 K). It can be mainly attributed to the NHD input used. Indeed, comparing the CFD-3D vs CFD-NHD, a constantly higher NHD over the breeding areas is emphasizes. Nevertheless, the temperature CFD-NHD distribution is very similar to the CFD-3D one but more peaked over the breeding area, Fig.4.3.14.

Apart from this aspect, the thermal behavior as well as the temperature gradients of the CFD-NHD are very similar to those of the CFD-3D case, Fig.4.3.7-4.3.9. No major differences are discovered. The temperature distribution computed seems to be almost constant in the Z direction while to suffer sensible variation in the radial direction as confirmed by the analysis of the temperature gradient. Moreover, the case maximum temperature is placed close to the lateral side confirming that it is caused by the conjunction of the application of adiabatic BC on Y+/- and the Neumann BC on the FW and not by the NHD itself.

To conclude, the CFD-NHD case endorses the previous results confirming the possibility to employ the NHD computed by simplified models preserving the main responses of the system and giving a further conservatism to the breeding area responses.

4.3.4 Domain independence

A 2D WCBP BB model (or CFD-DOM) has been developed to verify the domain independence of the results, so to demonstrate that the thermal responses are not biased by the usage of different discretization approach (e.g. 1D or 2D model). In addition, the usage of a reduced domain allows increasing the mesh resolution hence obtain results with higher accuracy. In the following sections

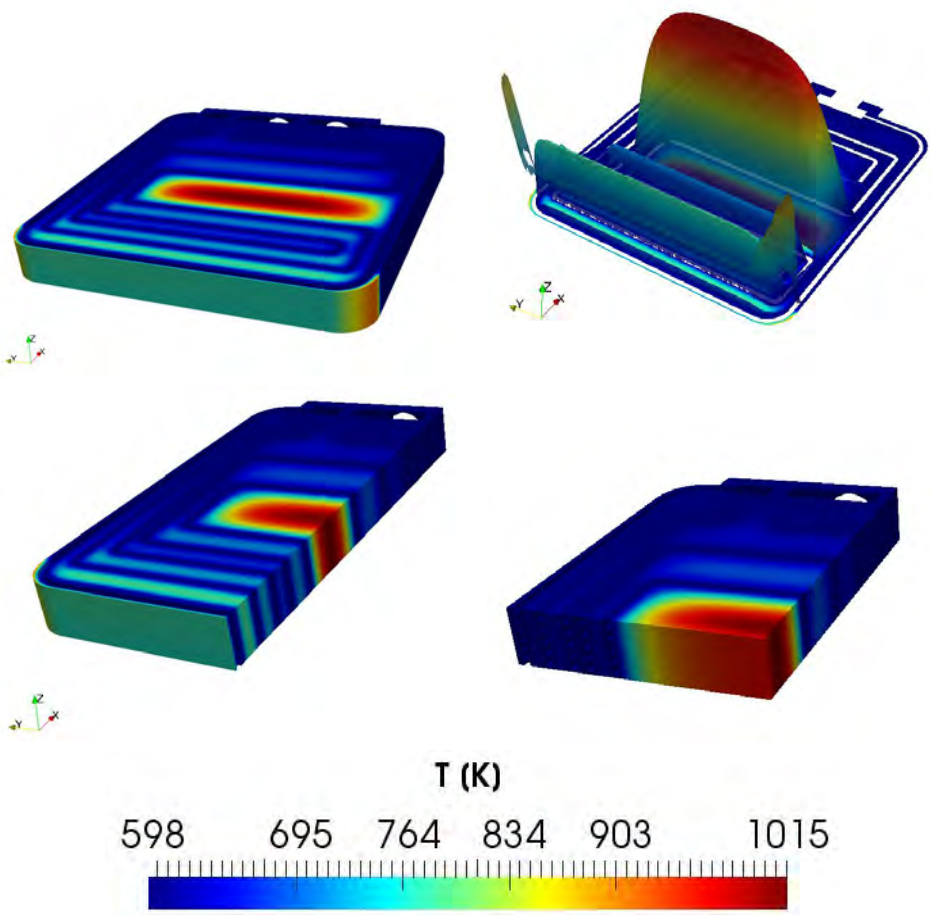

Figure 4.3.13: WCPB BB Microscopic temperature results

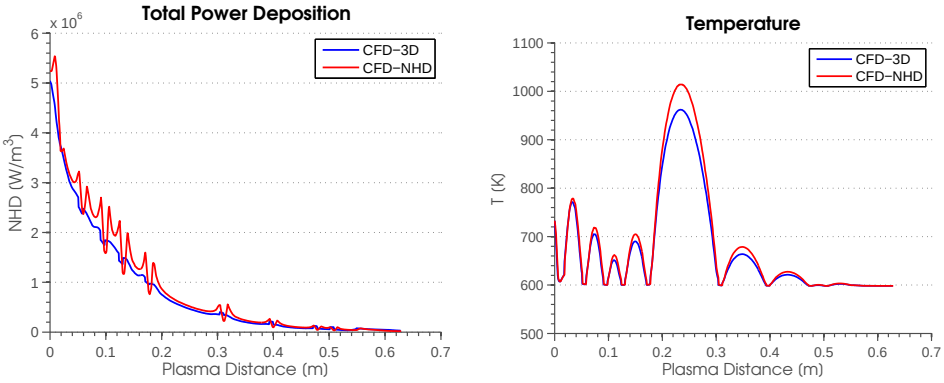

Figure 4.3.14: CFD-DOM vs CFD-3D along Y=0 m

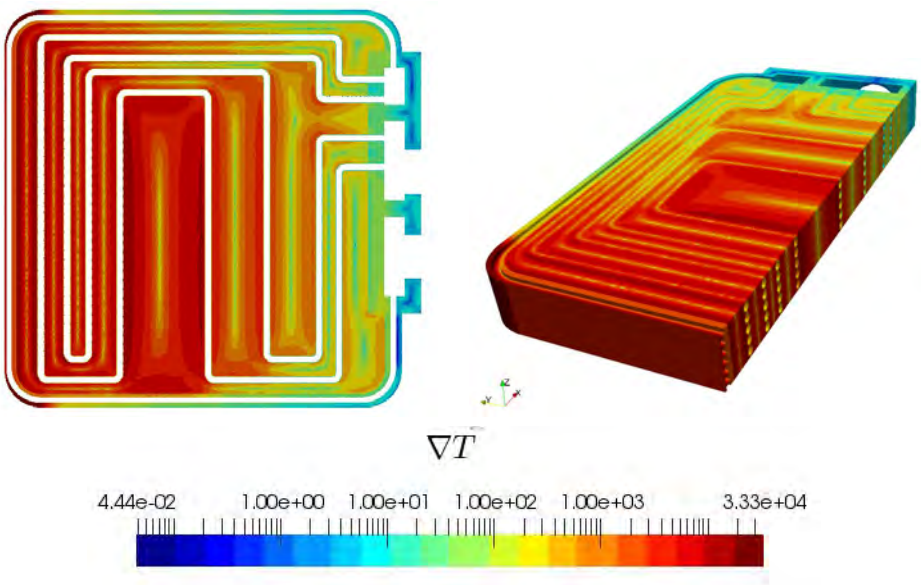

Figure 4.3.15: WCPB BB Temperature gradient

the assessment has been described starting from the geometrical simplification up to the response justifications in comparison with those of CFD-3D.

4.3.4.1 Geometry simplifications

Starting from the simplified geometry, Sec.4.3.1.1, a 2D slice along X has been created using CATIA [91] software, Fig.4.3.16. The obtained domain spans from the FW to the front end of the back plate covering all the breeding sections analyzed in all the previous cases. In addition, it is placed over to the breeding hot-spot section found in CFD-3D case. Doing this, a representative plane of the whole model is used. No further simplifications have been carried out over the baseline geometry.

4.3.4.2 Meshing

The use of automatic meshing has been discarded in favor of manual meshing, despite the very time consuming operation, in order to achieve a better control of mesh over small details such as the first wall (FW) channels and pipes. Therefore, Pointwise software [102] has been employed, resulting in a domain of 107340 triangular cells, Fig.4.3.17-4.3.18, subdivided in the following eleven ZoneID:

- Wolfram[30], magenta area in Fig.4.3.17-(b): 272 quadrilateral cells

[30] This region has been obtained by the radial extrusion of the FW cells distributed in four layers.

Figure 4.3.16: WCPB 2D Geometry

- Case, grey region in Fig.4.3.17-(b): 2508 triangular cells
- Pipes[31], Fig.4.3.17-(c): 5040 triangular cells
- Breeding Material, red zone in Fig.4.3.17-(a): 99520 triangular cells

Although, this hybrid mesh has almost two orders of magnitude less of cells than the CFD-3D case, the resolution is finer thanks to the domain simplification allowing a faster resolution and post-processing. The level of mesh detail can be appreciated in Fig.4.3.18, which contains zooms over the WCPB front part and FW. For instance, you can observe the presence of at least six triangular cells between the FW and the FW-water holes allowing an improved determination of the temperature peaks and gradients. This improvement is not limited only to the front part whereas it is extended to the whole simulation area.

4.3.4.3 Boundary conditions and assumptions

The boundary conditions and assumptions adopted for the thermal hydraulic simulation of WCPB BB have been included in Table 4.3.10. The single BC are identified in Fig.4.3.5. Regarding the NHD implementation please refer to Sec.4.3.4.4.

[31] Eight regions, one for each pipe radial area, have been generated in order to allow future assessments regarding the impact of a single pipe operation conditions.

(a) ZoneID general view

(b) ZoneID - zoom over FW

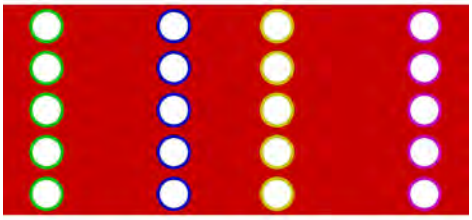

(c) ZoneID - zoom over breeding zone

Figure 4.3.17: WCPB 2D ZoneID

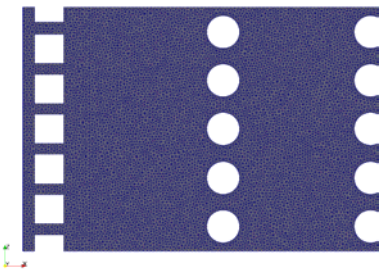

(a) Mesh - general view

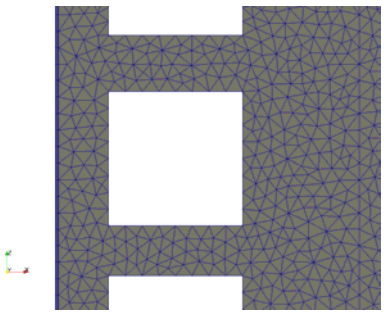

(b) Mesh - zoom over FW

Figure 4.3.18: WCPB 2D Mesh

Type	Description
BC@Back Plate	Temperature imposed at $598\,K$
BC@FW or X-	$1\,MW/m^2$
BC@Z- & Z+	Adiabatic
Pipe[14]	$T_{Bulk} = 593\,K$; $HTC = 13285\,W/m^2/K$
FW [14]	$T_{Bulk} = 593\,K$; $HTC = 13285\,W/m^2/K$
Solution type	Steady-state
Solver	Double precision
Energy Equation	Solved in coupled in all the domains
Material properties	As specified in Sec.4.1.2
	Temperature dependent

Table 4.3.10: Boundary conditions

4.3.4.4 Nuclear Heating

The nuclear heat deposition computed by the MCNP simplified heterogeneous model, 1D-HET, Sec.4.2.1, has been employed and set by means of the ANSYS Fluent routines developed, Sec.2.3.2. This has been computed by an implicit FMESH, which is absence of void materials works as an explicit one.

The NHD macroscopic responses (e.g.minimum, maximum, average and integral) in each Zone ID has been reported in Table 4.3.11 and the several contour plot in Fig.4.3.19.

ZoneID	NHD_{min} $[W/m^3]$	NHD_{max} $[W/m^3]$	NHD_{ave} $[W/m^3]$	$\int\int NHD$ $[W]$	[%]
Wolfram layer	5.3	5.3	5.3	70.3	0.2
FW/Case	3.5	5.6	4.6	3748.1	11.4
Breeding	0.03	3.8	0.9	28062.0	85.0
Pipes	0.05	410.3	142.3	1138	3.4

Table 4.3.11: Nuclear heating implemented

4.3.4.5 Results

The macroscopic CFD-DOM responses are reported in Table 4.3.12 whereas a selection of the microscopic ones in Fig.4.3.20. In addition, the temperature gradients have been reported in Fig.4.3.21.

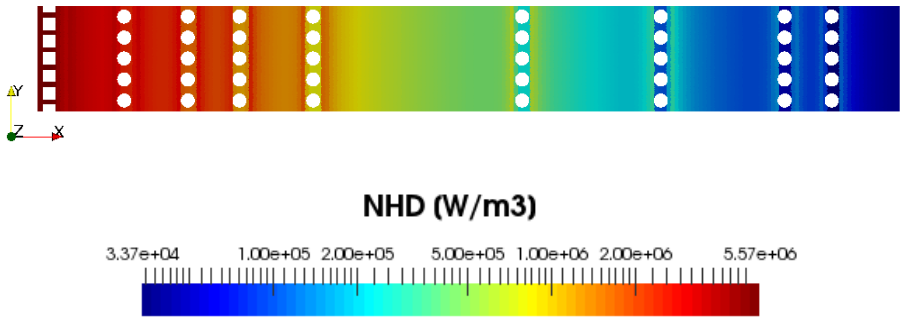

Figure 4.3.19: WCPB 2D NHD source term

The temperature distribution computed seems to be almost constant in the Z direction while to have sensible variation in the radial direction as confirmed by the analysis of the temperature gradients. In addition, the pipe surrounding areas appear to be slightly influenced by the presence of the nearby pipes having a smaller temperature variations. On the other hand, the adiabatic Z-/+ side BC do not alter the response, so the domain could be considered sufficiently large.

The analysis of the macroscopic responses highlights temperatures similar to those of the CFD-3D case apart from the "FW" and "Breeding" domain. The "Breeding" maximum temperature experiments an increase of about 5%. It can be mostly attributed to the NHD input used and to the improved resolution but not to the domain dimensions. Indeed, this CFD-DOM response is very close to the CFD-NHD one (e.g. 1015.0 K vs 1010.6 K).

In addition the "Pipes" temperature is almost the same of previous case, because it is driven by the water imposed condition (e.g. HTC and bulk temperature). On the other hand, the FW temperature peak is about 140 K less than the CFD-3D case, which is placed close to the Y-/+ BC not present in this case. Actually, the CFD-DOM employs a 2D section which could be considered as representative of the whole domain but not substitute of all positions. For these reasons, the CFD-DOM case supports the validity of previous results. It confirms the possibility to employ a further simplified model preserving the main responses of the system.

4.4 AINA WCPB BB model

Once fully detailed radiation transport calculation, Sec.4.2.1, and computational thermal-hydraulic studies, Sec.4.3.1, have been performed and consolidated by means of further assessments (e.g. Sec.4.2.2.4, 4.2.2.6, 4.2.2.7, 4.3.3, 4.3.4), the first AINA wall model concept has firstly drafted hence iterated reaching a

ZoneID ZoneID	T_{min} $[K]$	T_{max} $[K]$	$[\%]$	T_{ave} $[K]$
Wolfram Layer	779.0	781.8	2.0	780.0
FW	603.7	774.5	15.4	642.4
Breeding	598.1	1010.6	-5.0	706.0
Pipes	598.0	606.3	0.1	602.2
WCPB 2D	598.0	1010.6	15.4	700.5

Table 4.3.12: WCPB 2D Macroscopic results

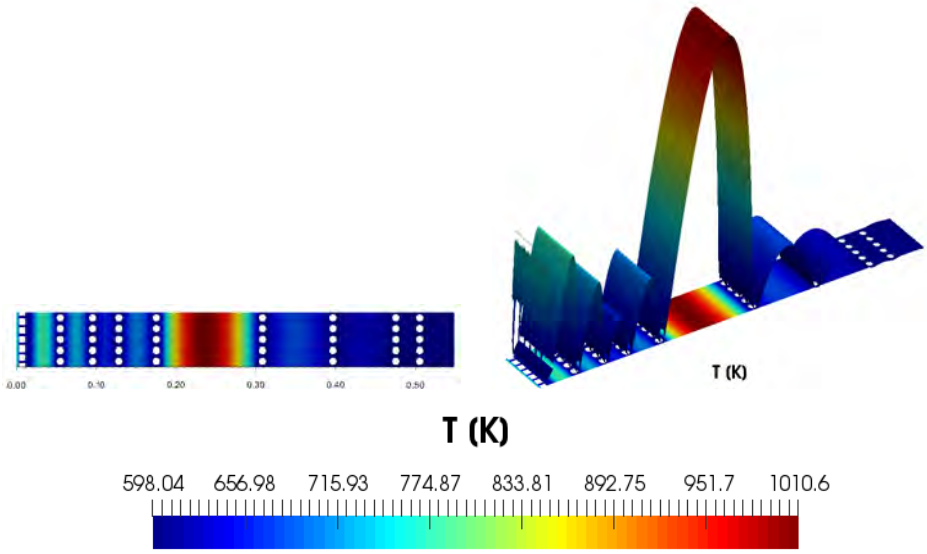

Figure 4.3.20: WCPB 2D Microscopic temperature results

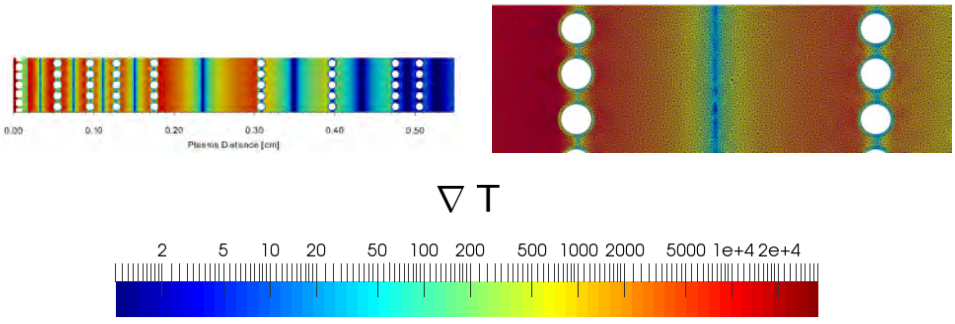

Figure 4.3.21: WCPB 2D Temperature gradient

consolidated configuration which best represents the detailed behavior[32].

Thanks to the good poloidal symmetry (both in NHD, geometrical and temperature responses), a 1D configuration has been finally selected and validated by the good temperature agreement with the fully detailed simulation. These differences, which are within the 10%, largely fulfils the initial requirement, supporting the methodology proposed.

Nevertheless, the AINA wall model was not conservatively representing the detailed behavior of the components due to the simplifications carried out, the diverse thermal response and due to intrinsic modeling features which cannot be adjusted by further iterations. To cope with these contributions, the AINA temperature field distribution once computed has to be compensated by the application of the so called scaling functions determined as $T_{3D}(x,y,z)/T_{1D}(x)$ [33] ratios for different operational levels (e.g. NWL equal to 80%, 100%, 120% of the nominal power) which are interpolated depending on the scenarios. To enhance the safety margin, the temperature field distribution is adjusted only if the simplified temperature is smaller than the more accurate one, $T_{3D}(x,y,z) > T_{1D}(x)$.

The following sections describes the AINA WCPB BB model features, the steady state cases and its comparison with the fully detailed CFD simulations. To conclude, the scaling function determination approach and its calculations is reported.

4.4.1 WCPB AINA Model description

Thanks to the good poloidal symmetry observed in the fully detailed simulations (both in NHD, geometrical and temperature responses), a 1D configuration has been selected to represent the most representative thermal response of the WCPB BB.

The AINA simplified 1D model spans radially all over the WCPB BB components starting from the First Wall up to the Vacuum Vessel for a total length of almost 55 cm. It is composed by thirty-seven parallel layers, Table 4.4.2, which have been obtained using the 3D WCPB CAD representation[34] [113]. Each slice employs the most representative material of the segmentation and the correspondent temperature dependent features which are described in Sec.4.1.2. Initial material conditions (e.g. density, thermal conductivity) are imposed at room conditions.

The cooling pipes and FW channel have been represented by *Type A-Unique-node* layers at different depths parallel the first wall, Sec. 3.3.1.1 [51]. They are considered as planar and occupying only one node. Their f_{COOL} factors, which

[32] This operation is defined as *"blanket collapse"* because it aims to obtain to move from the a fully detailed model to a simplified one retaining the characteristic features of the systems as much as possible.

[33] $T_{3D}(x,y,z)$ represents the fully detailed temperature distribution whereas $T_{1D}(x)$ the simplified one generated by the AINA WCPB BB model.

[34] The 1D layer discretizations employed matched the 1D-HET, Sec.4.2.2.3, apart from the VV part which here it is not represented.

are equal to the relative surface of the coolant tubes to the total surface of the module section, has been determined geometrically. A perfect contact has been applied between the layers with no thermal contact resistance.

The water conditions are been proposed and validated by IFERC:

- Heat transfer coefficient equal to $13285\,W/m^2/K$
- Coolant bulk temperature of $598\,K$

Thanks to development of the thermal routines, all the BC types can be applied to the FW and to the VV side. By the way, the studies reported hereinafter employ the Neumann BC at the FW and temperature imposed for the VV side. In the same way, the model has been prepared to employ NHD as equation or bin description to allow additional assessments.

4.4.2 AINA 1D-HET case

The BC reported in Table 4.4.3 have been applied to the model characterized in Sec.4.4.1. The baseline case of the AINA WCPB BB is hereinafter described and named as 1D-HET because it utilizes the NHD determined by the 1D-HET radiation transport case, Fig.4.4.1-(a), which is the most conservative and peaked one, Sec.4.2.2.3.

Type	Description
BC@FW	$1\,MW/m^2$
BC@Back Plate	Temperature imposed at $598\,K$
Domain	1D
Pipe[14]	$T_{Bulk} = 593\,K$; $HTC = 13285\,W/m^2/K$
Water Case [14]	$T_{Bulk} = 593\,K$; $HTC = 13285\,W/m^2/K$
Solution type	Steady-state
Solver	Sec.3
Nuclear Heating	1D-HET case 4.2.2.3
Material properties	As specified in Sec.4.1.2
	Temperature dependent

Table 4.4.3: Boundary conditions

The AINA WCPB 1D-HET solution is computed by the thermal-routines developed and presented in Sec.3. The running time is very limited and less than 1 minute. Starting from an initial guess of all the material at 598 K, the solution determined is based over an iterative procedure which is stopped once the all the nodes at iteration i+1 has less than 0.1 K of difference than iteration

No.#	Thickness, cm	Material	f_{COOL}
1	2.00E-02	W coating	-
2	4.09E-01	F82H	-
3	5.82E-01	Water	0.727
4	8.09E-01	F82H	-
5	4.13E+00	Mixed breeder	-
6	1.65E-01	F82H	-
7	4.24E-01	Water	0.600
8	1.65E-01	F82H	-
9	5.40E+00	Mixed breeder	-
10	1.65E-01	F82H	-
11	4.24E-01	Water	0.600
12	1.65E-01	F82H	-
13	6.98E+00	Mixed breeder	-
14	1.65E-01	F82H	-
15	4.24E-01	Water	0.600
16	1.65E-01	F82H	-
17	9.76E+00	Mixed breeder	-
18	1.65E-01	F82H	-
19	4.24E-01	Water	0.600
20	1.65E-01	F82H	-
21	1.61E+01	Mixed breeder	-
22	1.65E-01	F82H	-
23	4.24E-01	Water	0.600
24	1.65E-01	F82H	-
25	4.28E+00	Mixed breeder	-
26	1.65E-01	F82H	-
27	4.24E-01	Water	0.600
28	1.65E-01	F82H	-
29	1.00E+00	Mixed breeder	-
30	1.65E-01	F82H	-
31	4.24E-01	Water	0.600
32	1.65E-01	F82H	-
33	1.00E+00	Mixed breeder	-
34	1.65E-01	F82H	-
35	4.24E-01	Water	0.600
36	1.65E-01	F82H	-
37	1.00E+00	Mixed breeder	-

Table 4.4.2: AINA 1D Layers

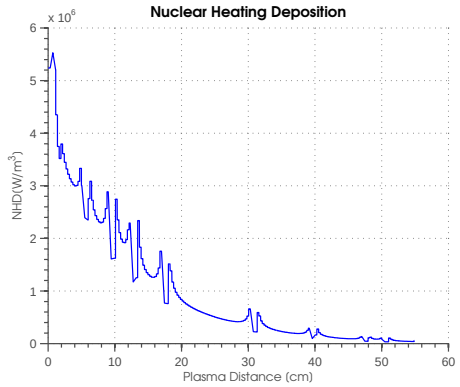

(a) NHD applied

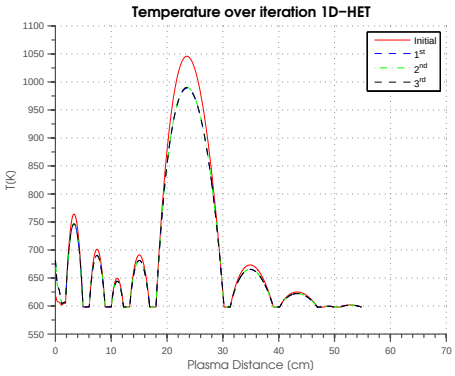

(b) Temperature iteration

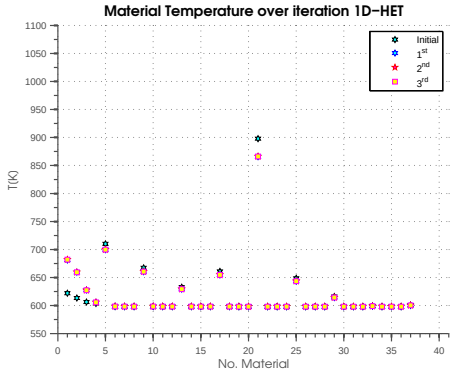

(c) Material temperature cell convergence

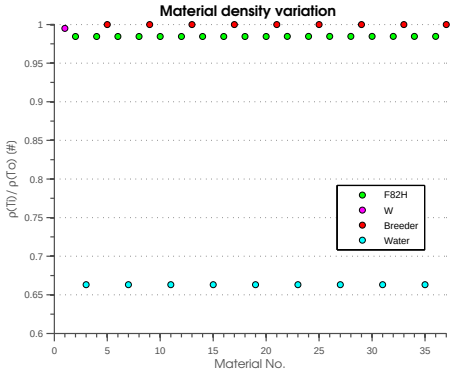

(c) Material density variation[35]

Figure 4.4.1: AINA 1D-HET

i, Fig.4.4.1-(b). Because of the material features dependence on temperature, the nodal temperatures converge step by step, which in this specific case are in total four, Fig.4.4.1-(c).

Indeed, discrepancies between the initial guesses and the final responses have been observed in particular for water (e.g. up to 35% decrease of density), Fig.4.4.1-(d).

The maximum temperatures computed per material type are reported in Table 4.4.4. Several peaks are observed in the breeding material. They are placed in the central plane between tubes. Having conditions correspondence between the set of coolant nodes, the maximum temperatures depends both from the NHD and the breeding thickness. For this reason the highest temperature found, 990 K, it is placed a 25 cm from the FW and not just after the FW.

On the other hand, minimum temperatures are observed in proximity of the coolant position which act as cold focus driving down the distribution and also influencing the earby positions. Due to the very thin thickness (e.g. few

	$T_{max}[K]$
Wolfram Layer	682
FW	680
Breeding	990
Pipes	599

Table 4.4.4: AINA 1D-HET Temperature maximum

millimeters), the pipes have almost the same thermal conditions imposed to the water node. In addition, very lower temperatures are observed close to the VV because of the lower NHD and the presence of the imposed temperature BC which drives the distribution over the area.

The responses computed are based on the 1D AINA WCPB layer FD solution which relies upon 700 nodes per material[36], for a total of almost 19000, because time constrains are not present in this specific application. The discretization criteria has been selected after a proper convergence analysis, Sec.3.5.1. The study shows how the temperature integral, so the truncation error, Sec.3.5.2, is reduced using finer discretization. Although, the node increases linearly the computational time has a exponentially running time due to the necessity to compute the inverse matrix.

Nevertheless, the employment of a reduced number of nodes, three hundreds for instance, could be a also a proper choice because it appears to compute consolidated temperature distribution. Dedicated plots over the FW and the maximum temperature are reported to show the importance of the nodal mesh in particular in the FW region. Results obtained by courser meshes are completely inaccurate and they shall be spotted by proper error analysis as in this case. Therefore it is evident the importance of the methodology applied which allows the model debugging and improvements.

4.4.3 AINA 1D vs 3D Fully detailed CFD analysis

At this stage of the development, once the 3D fully detailed thermal-hydraulic calculations and the thermal-block AINA model are consolidated, a duly comparison of the results is required. The fully detailed thermal-hydraulic case used to evaluate the impact of the nuclear sensibility (CFD-NHD, Sec.4.3.3) has been hereinafter employed thanks to the similarity of the BC employed (e.g. equal NHD distribution and BC) and to its conservatism of the responses. Indeed, apart from the 2D thermal-hydraulic domain independence case (CFD-DOM, Sec.4.3.4), it has determined the higher temperatures among the different materials.

[36]The Wolfram layer employs a reduced number of nodes because it is very thin. In this specific case, it is divided in five zones.

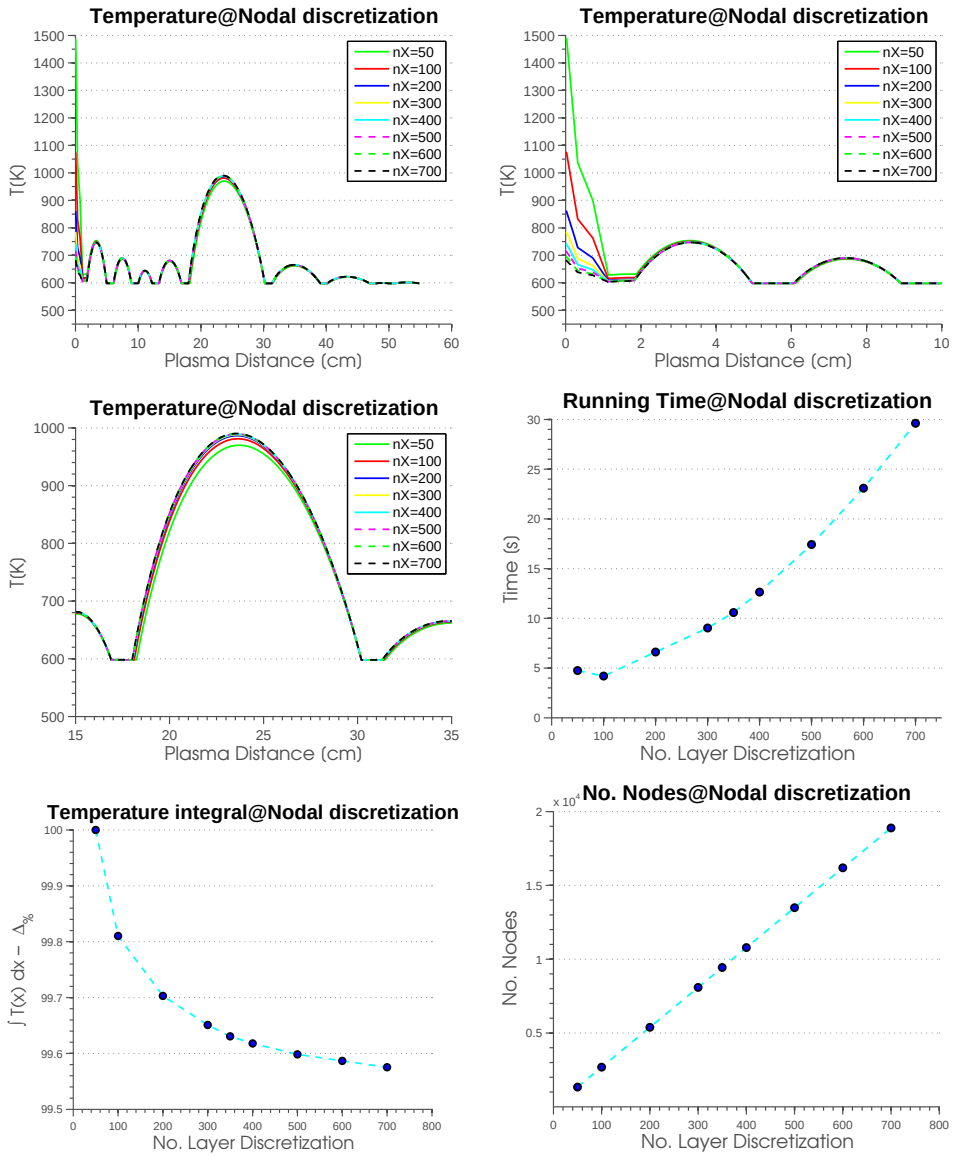

Figure 4.4.2: AINA 1D-HET Error Analysis

The detailed temperature comparison along the radial direction[37], Fig.4.4.3 and in Table 4.4.5, shows a very good agreement of the distributions, both over the coolant zones and the breeding peaks. No major discrepancies are observed. Depending upon which radial plane is under evaluation, the AINA distribution could be or not a conservative estimation, because, as observed in Sec.4.3.1, the 3D thermal-hydraulic calculation computes a temperature Gaussian over the breeding area. For this specific reason and to enhance the safety margin, from now on we refer to the most conservative 3D distribution (e.g. along Y plane). Nevertheless it is worth reminding that the AINA WCPB thermal-block matches the temperature range founded in more complex simulations.

Specific attention has been given to the FW and the breeding maximums: minor differences are observed which can be considered minor taking into account the model differences. Whereas an excellent agreement is obtained with a maximum difference of 8% close to FW and with peaks over the cooling channel areas, a consistent temperature underestimation is observed over the breeding areas. This effect is mainly attributed to the 1D bigger cooling surface/volume ratio, the major distance between the cooling tubes apart from the axis plane and the one node coolant channel representation, Fig.4.2.16. The non-conservatism discovered is intrinsic to the 1D approach and thus unfortunately cannot be directly resolved. To cope with these effects, a scaling approach is proposed instead, Sec.4.4.4. The determination and coherence of the temperature distribution obtained using independent tools and approaches, ANSYS® Fluent® vs AINA thermal-hydraulic routines, justifies the proposed methodology, and hence validating the results.

On the other side, the macroscopic analysis reports a sensible difference over the "case" domain. By the way as observed in Sec.4.3.4, the F82H peak in question is placed close to the Y-/+ BC, which are not present in the AINA case, so not really representative. Actually, the AINA thermal-block employs a 1D representation which could be considered as representative of the whole domain but not a substitute of all positions.

Furthermore, in contrast to the AINA distribution, the 3D temperature reported appears more a piecewise function. This behavior, which of course influences the temperature per cent difference, is caused by CFD the mesh discretization on which the results are computed. In addition, the difference seems to be more pronounced over the pipe regions because of temperature "averaging" of AINA thermal-block in the radial cooling node, as detailed in Sec.2.1.

4.4.4 Scaling function

The non-conservatism observed is intrinsic to the 1D approach and thus unfortunately cannot be directly resolved. To cope with these effects, a scaling approach is proposed instead. The use of simplified models instead of fully detailed ones could lead to an underestimated response and must be avoided. The innovative approach proposed here is based on the application of scaling

[37] Of course, no other directions can be analyzed because it is a 1D model.

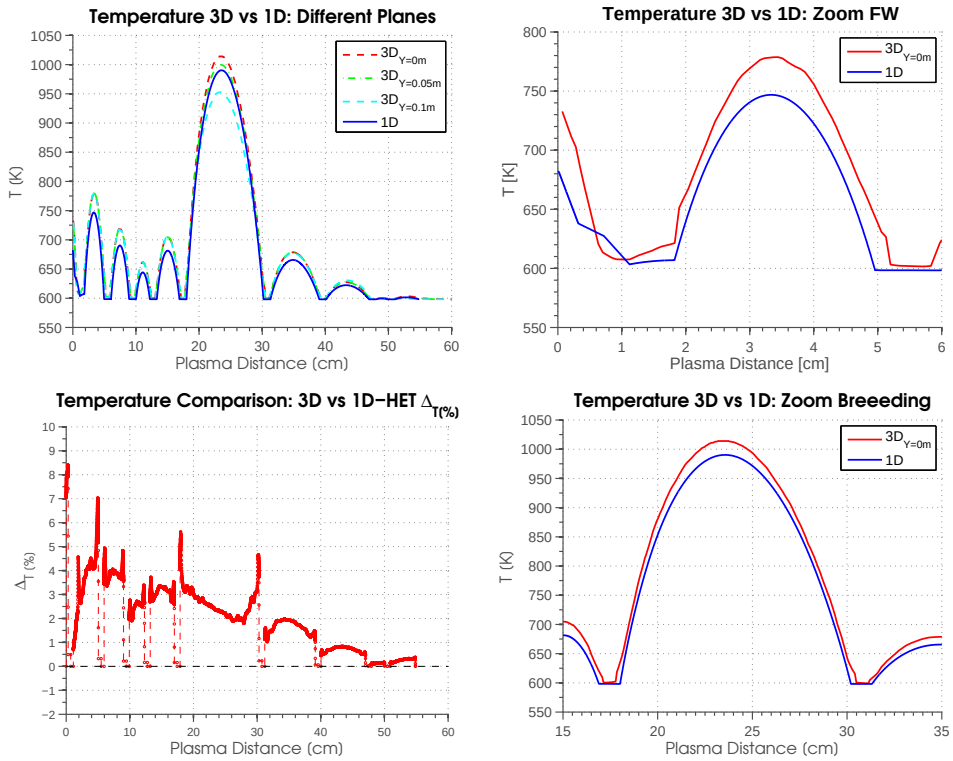

Figure 4.4.3: AINA 1D-HET vs 3D

ZoneID	$AINA$ $[K]$	$3D-NHD$ $[K]$	$\|\Delta\|$ [%]
Wolfram Layer	682	797.8	14.4
Case	680	915.1	25.0
Breeding	990	1015.0	2.5
Pipes	599	607.2	1.1

Table 4.4.5: Macroscopic results comparison

functions (SF) which compensate the AINA wall model responses (e.g. the temperature) only where the distribution results are less conservative than those of the fully detailed one. By doing this, an equal or more conservative response is obtained, thus enhancing the safety margins. For this purpose, several SF have been computed, covering different conditions simulated by the AINA code. Due to the mesh discretization and resolution of the two vectors, specific routines have been developed to compare the results and generate automatically the SF, per cent difference and the corrected vectors. For instance, the LOPC functions are determined as a ratio between the most conservative radial temperature distribution computed by fully detailed 3D CFD and the 1D simplified model at steady-state condition using the same BC. Two additional simulations of the 1D WCPB AINA, Sec.4.4.2, and the 3D-NHD assessment, Sec.4.3.3, have been carried out scaling properly the NWL to 0.8 and $1.2 MW/m^2$, hence the NHD distribution. The distribution obtained in both cases, and its the per cent difference from the baseline one, are reported in Fig.4.4.4-4.4.5. Again the distributions found are very similar and no major discrepancies are observed. Fig.4.4.6 reports the LOPC SF obtained, which are a linear function of the NWL, with the exception of those from the breeding area around 25cm, where the maximum thermal conductivity value is reached. The SF have higher values close to the cooling area where more differences are present both for the mesh CFD courser discretization and for the AINA thermal-routine assumption to compute the effect of the radial cooling effect. Again, the determination and coherence of the temperature distribution obtained and the minor differences found (e.g. 12% close to the FW) using independent tools and approaches, ANSYS® Fluent® vs AINA thermal-hydraulic routines, justifies the proposed methodology, and hence validating the results. To conclude, the comparison of the scaled WCPB distributions and the 3D fully detailed thermal-hydraulic calculations is reported in Fig.4.4.6 highlighting the perfect match. It should be noted that in case of intermediate conditions the SF are linearly interpolated.

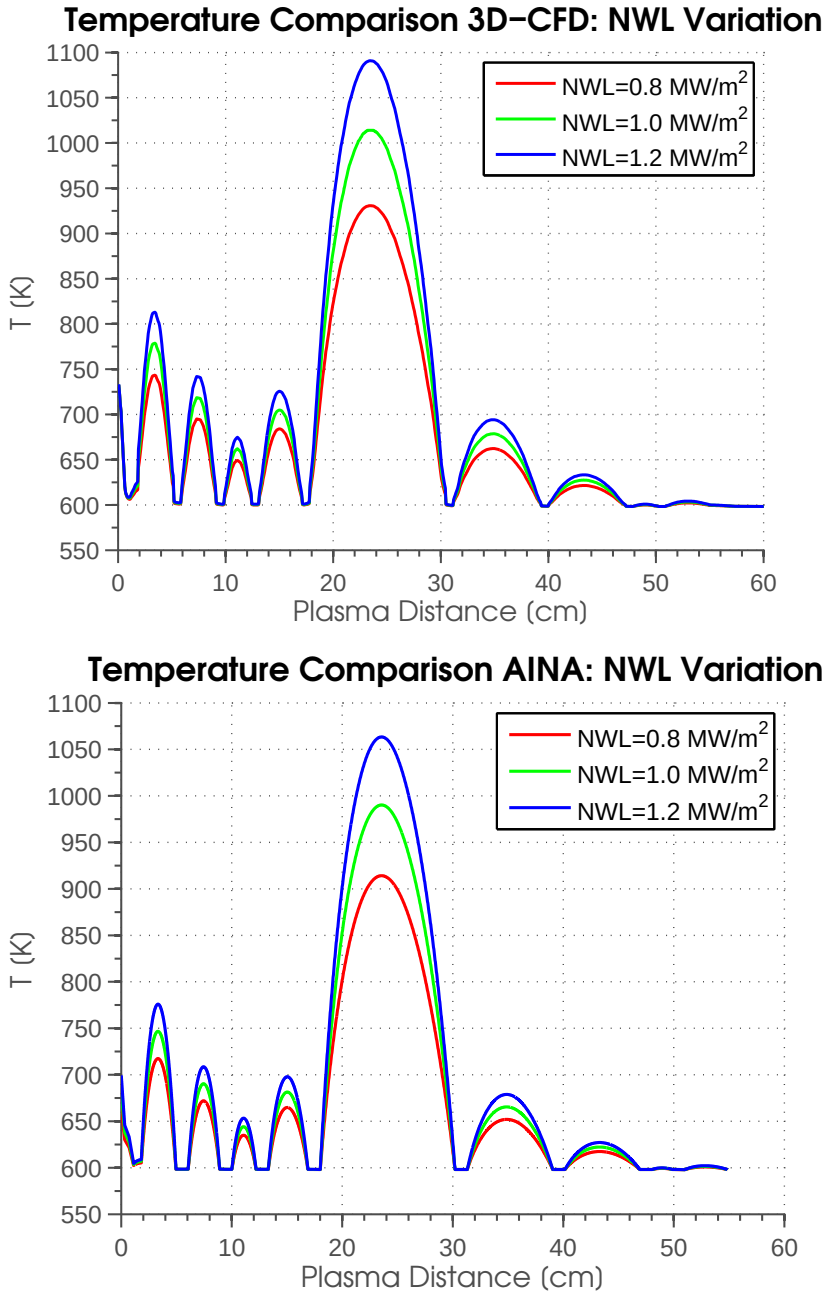

Figure 4.4.4: AINA 1D-HET vs 3D@NWL

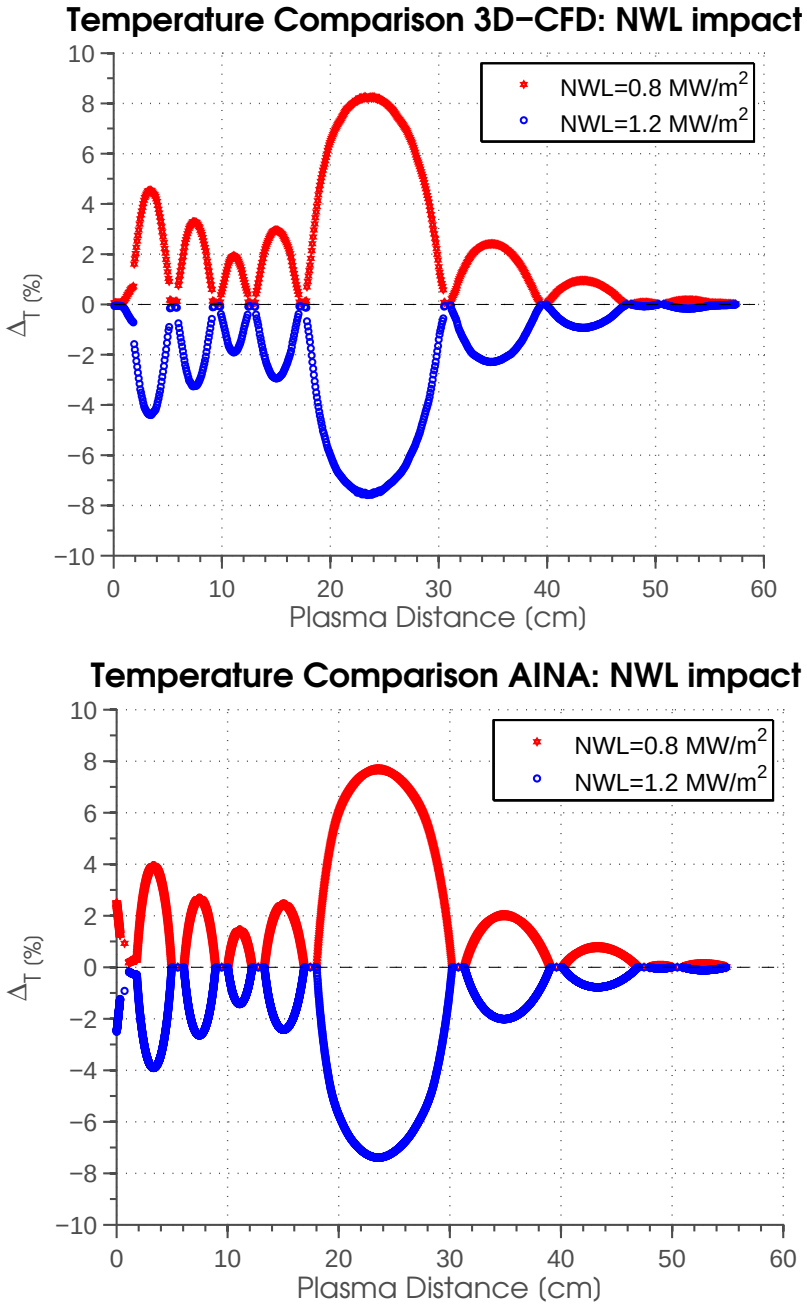

Figure 4.4.5: AINA 1D-HET vs 3D@NWL-Variation

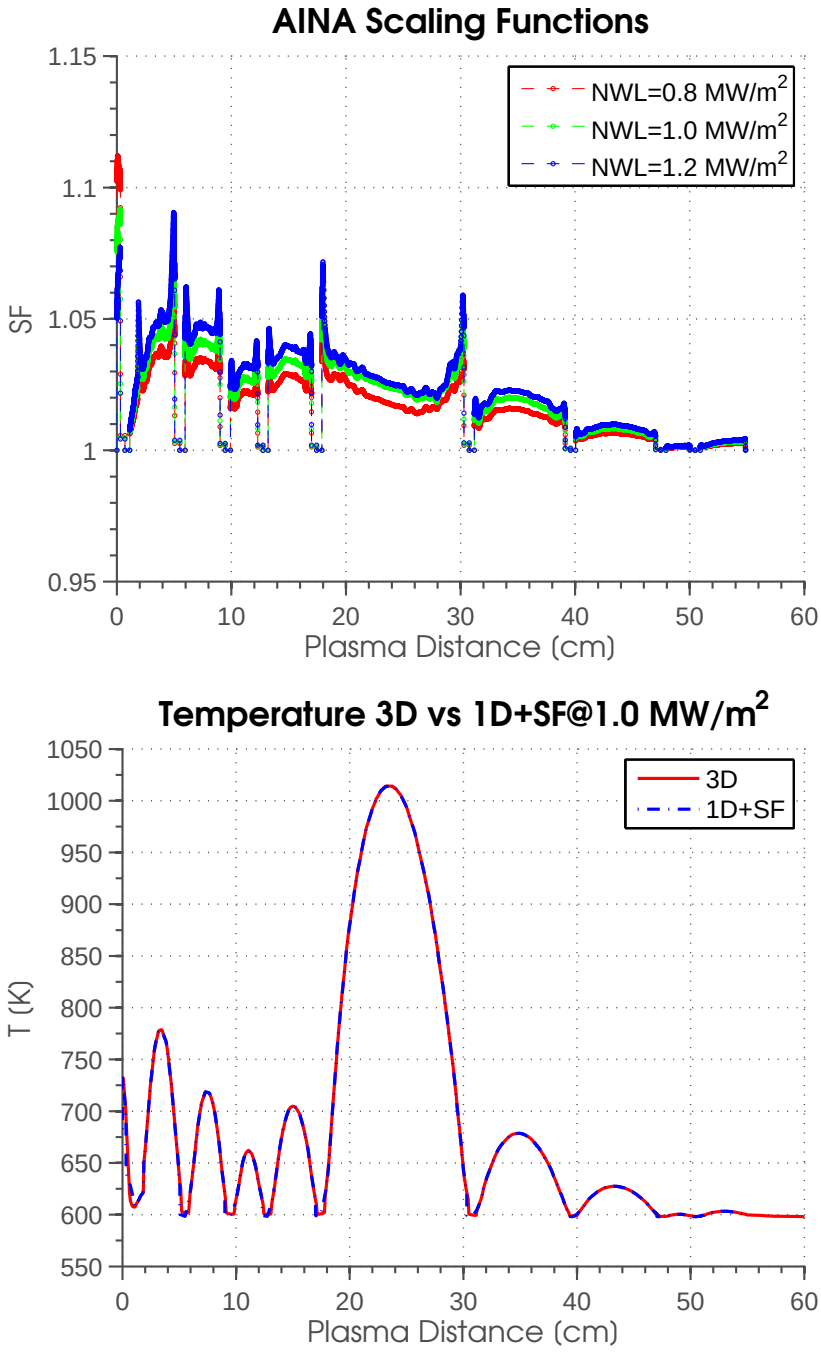

Figure 4.4.6: AINA 1D-HET vs 3D-Scaling Functions

4.5 Conclusions

The methodology for the development of a new AINA code version has been described and its application to the Japanese DEMO WCPB wall-model generation reported. Three-dimensional radiation transport calculations by means of MCNP6.1 code, Sec.2.2, have been carried out and compared with the 1D simplified models, Sec.4.2.2, which are valuable for future sensibility assessments. Nuclear responses have been detailed, compared and justified. The NHD and the neutron/photon flux show good agreement, within 10%: the major differences are located in the cooling areas due to different approaches and the absence of back-scattering phenomena from the surroundings areas. Furthermore, TBR have been computed and are available for future applications.

Using the computed NHD, the WCPB 3D thermal hydraulic simulations have been carried out and their results exposed, Sec.4.3.1. As expected, the temperature peaks are located between the cooling tubes. Moreover, further assessments have been done to consolidate the results obtained: (i) mesh independence and its compliance with Richardson theorem, Sec.4.3.3, (ii) domain dimension influence, Sec.4.3.4, (iii) the impact of the NHD, Sec.4.3.2.

Thanks to very limited gradients along the Z direction, a 1D simplified model, Sec.4.4, has been iteratively built and adjusted, achieving a good agreement with the fully detailed simulation and yielding a maximum absolute temperature difference of about 12%. The determination and coherence of the temperature distribution obtained using independent tools and approaches, ANSYS® Fluent® vs AINA thermal-hydraulic routines, supports the proposed methodology, hence validating the results, Sec.4.4.3. Nevertheless, the 1D non-conservative temperature field, where present, is compensated by the application of scaling functions, Sec.4.4.4, obtaining a perfect match with the most conservative 3D distribution. The scaling functions correspond to the ratios between the most conservative radial distribution in the fully detailed and the 1D simulations. They have been computed to cover the whole operational areas including accidental scenarios. For intermediate conditions, the SF are linearly interpolated.Thanks to this robust methodology, starting from fully detailed neutronics and thermal-hydraulic results, a simplified and conservative wall model will be implemented in AINA from now on, obtaining reliable results in a short calculation time. It is worth remembering that the formulation of simplified models without the full and rigorous comparison with the fully detailed model could result in non-conservative results, which are avoided using this methodology. Future developments will be focused on the impact of the variation of NHD (due to temperatures, different cross sections, boundary conditions influence and Doppler effect broadening) as well as the determination of the effect of this methodology on the AINA safety analysis.

Chapter 5

Helium Cooled Pebble Bed Blanket (European-DEMO)

5.1 Introduction

In this chapter, the work done regarding the Helium Cooled Pebble Bed European DEMO blanket concept is presented and its main features described, Sec.5.2. In the frame of a specific EuroFUSION contract, a new version of AINA code containing the HCPB European DEMO concept has been developed. This has allowed the realization of preliminary safety studies and the publication of several contributions as papers/posters to main conferences (e.g. *"Development of the safety code AINA for the European DEMO designs"* [129], *"Desarrollo del código de seguridad para reactores de fusión AINA 4 para DEMO"* [130]) and EuroFUSION technical reports (e.g. "*Report on development of new AINA code for DEMO HCPB models and numerical methods*" [131], "*AINA plasma physics module development for DEMO*" [132]).

Within the several tasks carried out, my support has been mainly focused on:

- Blanket collapse toward the creation of the AINA HCPB thermal-wall model
- Support to the development of a new AINA 4.0 version and the blocks assembly
- Contribution to the preliminary assessment of the AINA HCPB Safety Analysis

As described in Sec.2.1, the development of a new AINA wall model envisages, as first stages, the determination and consolidation of the nuclear heating density by means of fully detailed radiation transport calculations, Sec.4.2, therefore the computation of detailed 3D CFD model to understand the thermal behavior of the system. Considering that these phases had already been carried out

by further EuroFUSION parties thus the UPC-FEEL tasks were focused on the generation of AINA HCPB thermal-wall model employing the input data provided.

Therefore, having a consolidated he 3D HCPB BB temperature field and nuclear power deposition, the first AINA Wall model concept has firstly drafted hence iterated reaching a configuration which best represents the detailed behavior[1]. Indeed, thanks to the toroidal symmetry and the modular concept, a 1D configuration has been finally selected obtaining at nominal conditions a good temperature agreement within the 5% and so largely within the initial requirement and expectation endorsing the new approaches implemented. These discrepancies could be not attributed to a specific factor but more of sum-up of effect due to the different methodology, algorithms and boundary conditions. In addition, although, in some materials the temperature distribution computed by the AINA HCPB thermal-model resulted slightly not conservative if compared with the outcomes obtained for the 3D fully-detailed CFD ones, the application of a scaling function was considered not appropriate due to the early stage of the HCPB design and the predominance of the several uncertainty accumulated along the process. Nevertheless, neither the application of scaling functions nor the usage of 2D AINA model approach is discarded a priori in next phases.

Besides, sensitivity study of the AINA Wall model temperature distribution versus NHD type, HTC variation and water bulk temperature have been carried out as well as the preliminary assessments regarding LOCA and LOFT accidents.

To conclude, it is worth reminding that all the analysis here reported has employed the HCPB-2015 BB v3 concept [19]; further assessments which were done with previous version are not included in this thesis for sake of simplicity. Recently the EuroFUSION project leader has announced the release of a new DEMO baseline model which is guaranteed now to remain unchanged until 2020 [133]. For this reason, an update of this model is foreseen in 2018.

5.2 System description

The Helium Cooled Pebble Bed (HCPB) Breeding Blanket (BB) is one of the selected blankets for the DEMO fusion reactor. During the last years, the BB has been significantly evolved and simplified to improve the tritium breeding ratio (or TBR) increasing the quantity of BB and reducing that of steel. For instance, the vertical stiffening grids have been removed and the ceramic bridge (U-shape cooling plates bend) eliminated remaining now only the horizontal cooling plates in the breeding zone and the Helium coolant flows directly from the Back Supporting Structure (BSS) into the BB instead of passing from the manifold box. For this reasons all the HCPB thermal studies carried out in the

[1] This operation is defined as *"blanket collapse"* because it aims to obtain to move from the a fully detailed model to a simplified one retaining the characteristic features of the systems as much as possible.

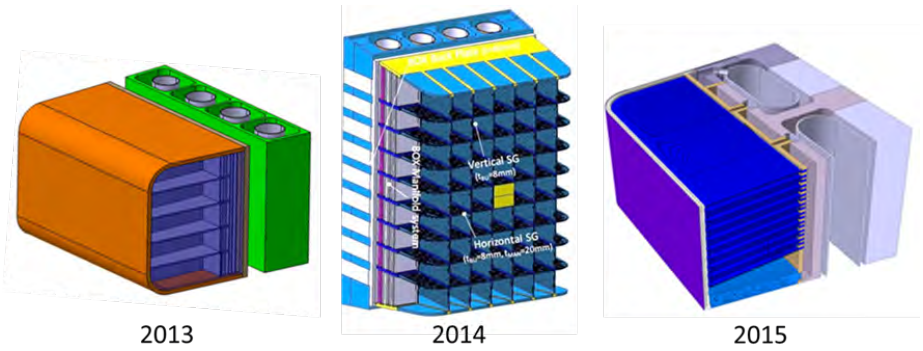

Figure 5.2.1: HCPB BB Evolution Concept

past by UPC-FEEL are not valid. The main design of HCPB BB evolution is reported in Fig.5.2.1.

Moreover, three main HCPB design iteration has been performed in 2015 in order to fulfill the material design limits, to further increase the TBR optimizing at the same time the manufacturing cost thanks to the experience of HCPB ITER TBM. This report considers only the HCPB latest version: HCPB-2015 v3 briefly described in the Sec.5.2.1.

5.2.1 General architecture

In order to describe the specific peculiarity of the AINA wall model, the general architecture of the HCPB-2015 v3 "sandwich" concept for an outboard segment is hereinafter described and reported in Fig.5.2.2.

A 2 mm W-armour layer is assumed for all the modules at the plasma facing side of the FW whereas in the internal part the cooling plates subdivide the Be and the Li_4SiO_4 bed zone which are arranged perpendicularly to the first wall and alternated. The double caps are placed on the top and bottom part of the BB, the bed nearby filled by Be pebble. The breeding blanket back structure (BSS)is used as the Helium collecting zone both for input and output. For more information please refer to EFDA_D_2LHS3F [19].

5.2.2 Cooling flow scheme

The HCPB BB is provided by two Helium redundant, fully symmetric, purely counter flow, coolant schemes which provide 50% of the cooling performance each, see Fig.5.2.3 and Fig.5.2.4. Beginning from the BSS at 300°C, the redundant cooling loop A cools the first wall (50%) and then the cooling plates (50%), exiting the breeding zones and entering again the BSS, where the flow at about 500°C is routed out of the vacuum vessel. At the same time, the redundant cooling loop B also beginning form the BSS at 300°C cools the first wall (50%) and then the cooling plates, exiting the breeding zones at 500°C to the BSS.

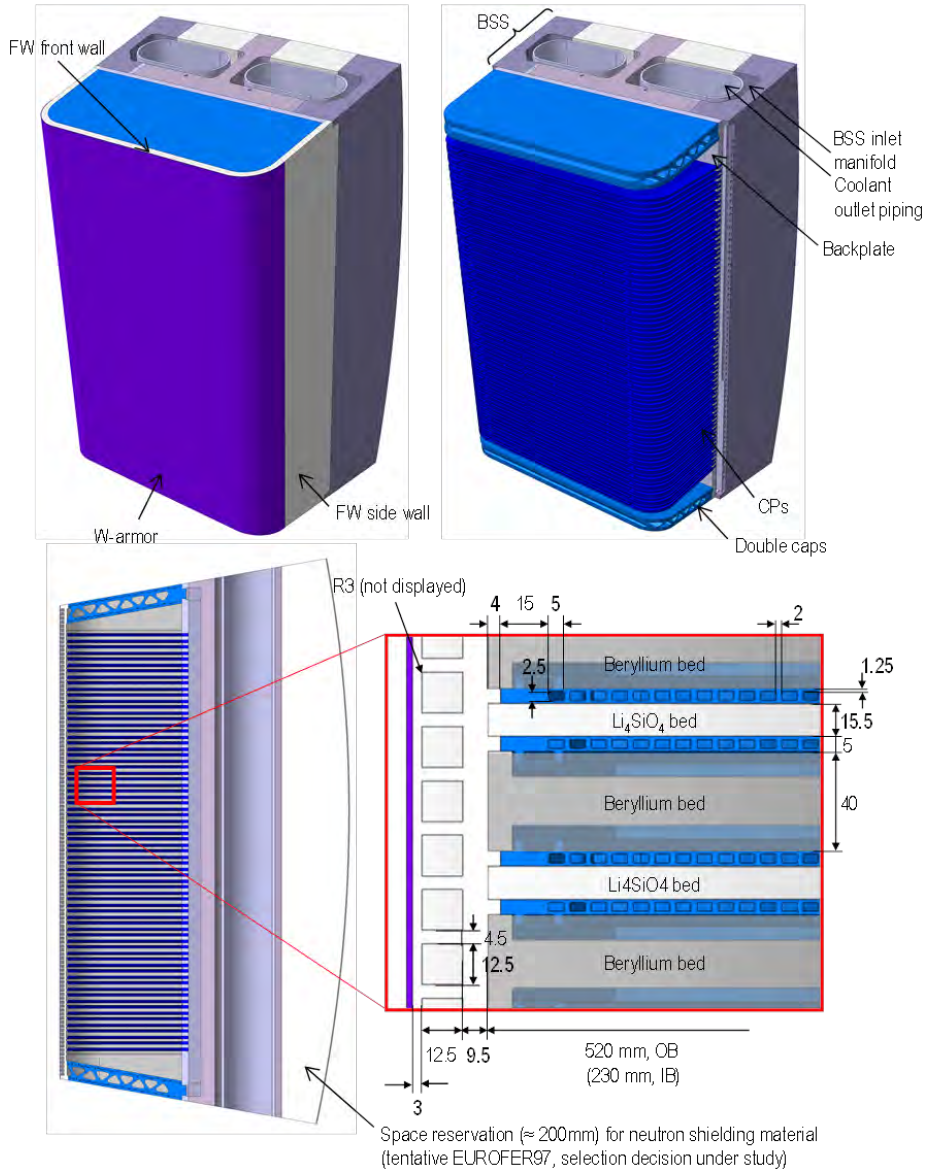

Figure 5.2.2: HCPB-2015 BB v3 concept scheme [19]

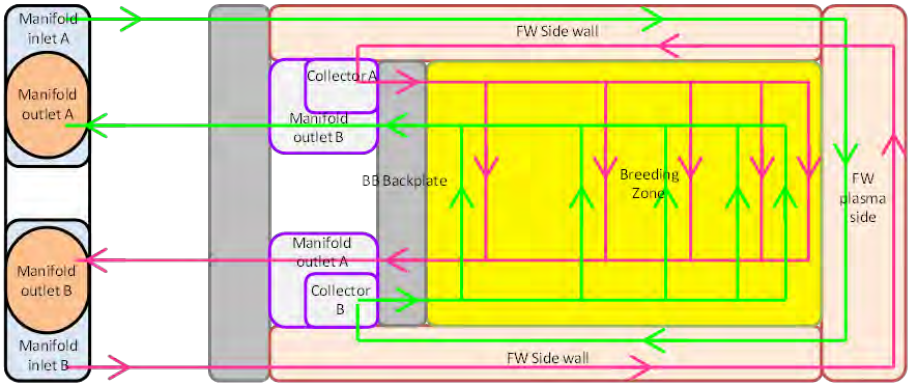

Figure 5.2.3: HCPB BB Helium cooling scheme

Even though the distance between nearby coolant channel is fixed, a toroidal cooling channel arrangement has been obtained closing some cooling channels and converting them to "dummy" or "blind". In this way the thermal behaviour of the BB is optimized minimizing at the same time the steel volume fraction in the breeding zone hence the TBR.

As result of the assessment, the density of the "functional" cooling channels is higher in the front part of the BB where the NHD is higher. In addition to the main BB Helium cooling scheme, a Helium purge gas system is present. Please for more information refer to [19].

5.2.3 Design HCPB limits

The following material temperature limits are considered.

Material	*Temperature Limit*
EUROFER	550°C
Beryllium	650°C
Tungsten	TBD[2]
Li_4SiO_4	920°C

Table 5.2.2: Material Temperature Limits

5.2.4 Thermo-hydraulic analyses of HCPB BB segment

As commented in Sec.5.1, the determination of the thermal-hydraulic behavior of the HCPB BB in normal operation was carried out by a another EuroFUSION supplier by means of a fully detailed 3D CFD analyses hence it is considered as

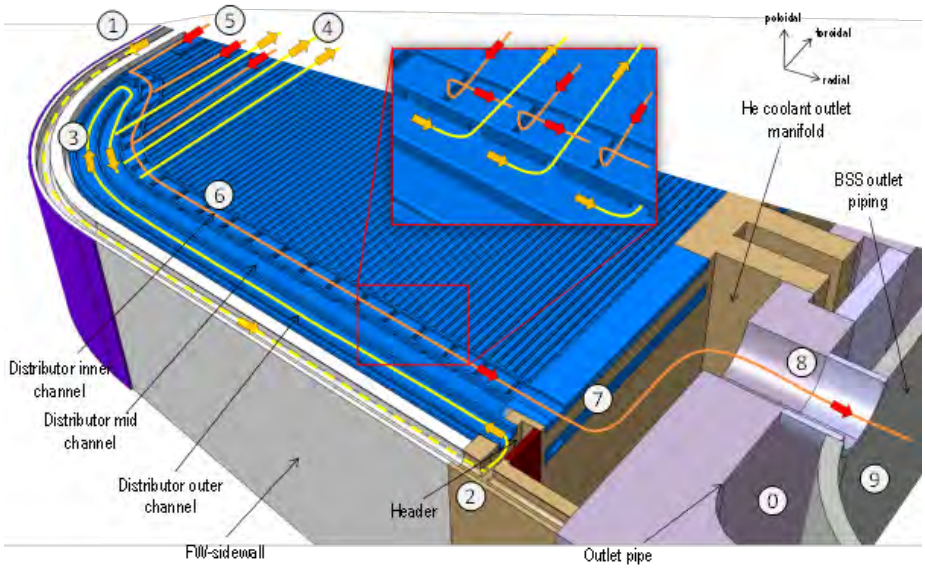

Figure 5.2.4: Thermo-hydraulic working principle of the CP

an input to this thesis. Nevertheless, for completeness, an executive summary of the hypothesis and results is reported hereinafter, while for more detailed information please refer to [134].

The domain used was a mid-plane slice segment of an equatorial outboard HCPB breeder blanket module that suffers the maximum load . It is approximately 30 mm thick (e.g. 7.75 mmLi_4SiO_4 plus 20 mm of Be), which should be considered as representative of the wholes modules thanks to the modular concept employed. It spans radially all over components starting from the First Wall up to the Vacuum Vessel and divided in four main areas, Fig.5.2.5-a,c:

- Helium domains
- Eurofer structure
- Lithium orthosilicate Li_4SiO_4 (LiOS) volume
- Beryllium domain

Two redundant Helium loops connected directly to the BSS are present as well as the purge gas channel, Fig.5.2.5-b. In addition, to the first, the blue colored, and the second loop, the red one, there are dummy (blind) channels in the cooling plate, which are closed so the Helium coolant cannot enter into them. To optimize the temperature distribution and the tritium breeding ration, more dummy channels, which are marked in green, are located close to VV plasma side.

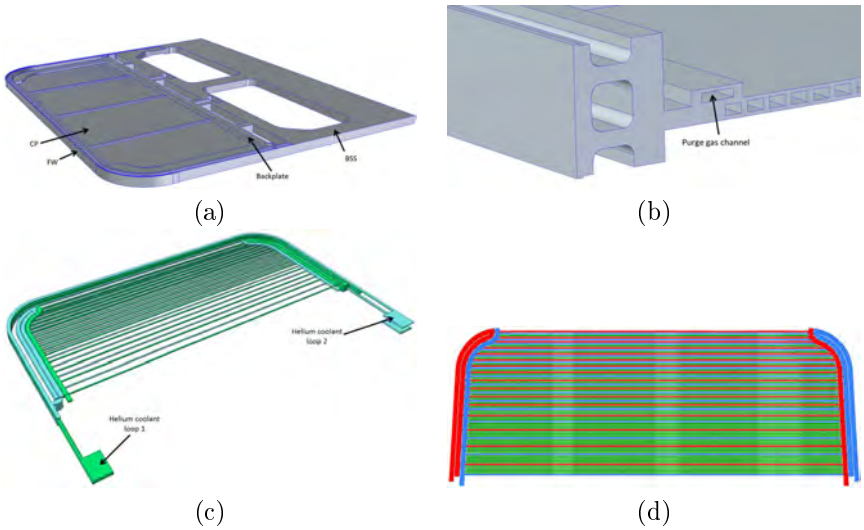

(a) (b)

(c) (d)

Figure 5.2.5: HCPB BB thermal-hydraulic model

This is the boundary condition configuration employed: periodic boundary condition are used on bottom/top, adiabatic on the sides, Neumann on the FW and temperature imposed in the VV side.

Although, the thermal-hydraulic analysis contains several assessments (e.g. mesh independence, different design configuration and cooling conditions), we refer to the final configuration labeled as case No.12 reported in Fig.5.2.6-5.2.7. The steady-state analysis highlights close to the design limits, Sec.5.2.3, in particular for the BZ and the FW. In addition the Be and Li_4SiO_4 temperatures increase proportionally with the distance from the CP reaching a maximum in the bed middle plane where the BC are placed because the deeper zones are less sensitive to the effect of the convention proportioned by the Helium flow. A rather symmetric temperature layout along the poloidal direction is observed for all the material. Similar temperature distribution between Be and Li_4SiO_4 can be observed having in the second material bigger temperature due to the lower thermal-conductivity. As expected, more elevated temperature are present close to the FW due to the enhanced volumetric nuclear power deposition whereas the BZ back zone temperatures are mainly driven by the Helium coolant outlet conditions and the BSS temperatures which are lower.

5.3 Material Properties

The material properties employed in the AINA DEMO HCPB code are hereinafter detailed. When needed the properties have been interpolated. To obtain comparable temperature distribution, the properties employed match those in [19],

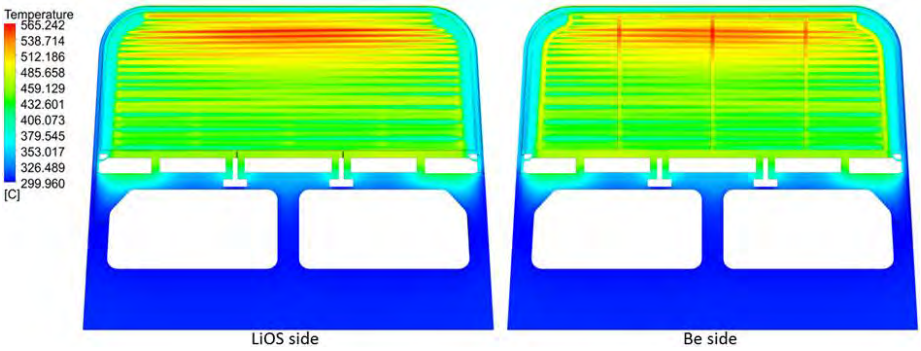

(a) Eurofer temperature distribution

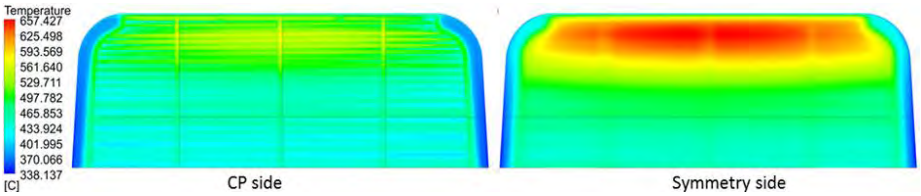

(b) Beryllium temperature distribution

Figure 5.2.6: HCPB BB thermal-hydraulic results - Part-II

(b) Beryllium temperature distribution

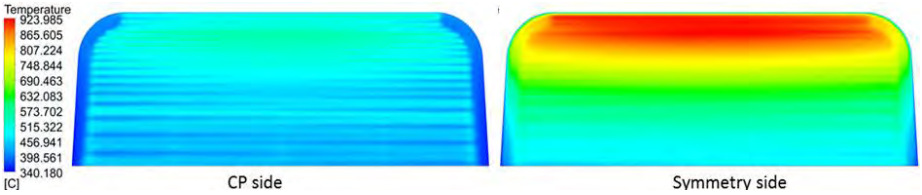

(c) Li_4SiO_4 temperature distribution

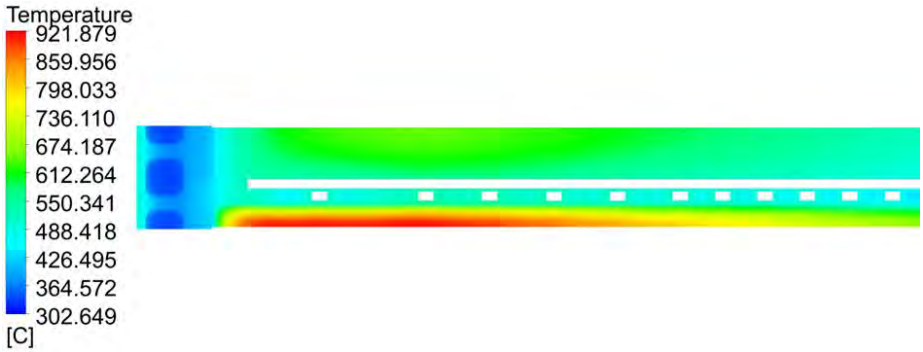

(d) XY Mid-plane temperature distribution

Figure 5.2.7: HCPB BB thermal-hydraulic results - Part-II

5.3.1 Helium

The Helium properties are extracted from Petersen [135] and the same employed in [19]. The Helium is considered as pure because the quantity of the purge gas dopant, H_2, is too low (1‰).

Mass density

$$\rho^{He}(T,p) = 48.14\,\frac{p}{T}\,\left(1 + 0.4446\,\frac{p}{T^{0.5}}\right)^{-1}\left[\frac{kg}{m^3}\right] \tag{5.3.1}$$

with the pressure p expressed in [bar] and the absolute temperature T in [K].

Dynamic viscosity

$$\mu^{He}(T) = 3.674 * 10^{-7} T^{0.7}\left[\frac{kg}{m^3}\right] \tag{5.3.2}$$

with the absolute temperature T expressed in [K].

Thermal conductivity

$$k^{He}(T,p) = 2.682{*}10^{-3}\,\left(1 + 1.123 * 10^{-3}\,p\right) T^{0.71-\left(1-2*10^{-4}\,p\right)}\left[\frac{W}{m\,K}\right] \tag{5.3.3}$$

with the pressure p expressed in [bar] and the absolute temperature T in [K].

5.3.2 EUROFER97 structural steel

The following table summarizes the thermo-mechanical properties for the EUROFER97, namely the coefficient of thermal expansion α^{E97}, the density ρ^{E97}, the specific heat capacity cp^{E97}, the thermal conductivity k^{E97}, which have been extracted from [19, 136].

5.3.3 Tungsten armor

The material properties of the Tungsten armor are taken from the ITER Materials Properties Handbook [137]:

Mass density

$$\rho^{W}(T) = 19302.7 - 203786 * 10^{-1}\,T - 2.2448\,10^{-5}\,T^2\left[\frac{kg}{m^3}\right] \tag{5.3.4}$$

with T in [°C].

$T\,[°C]$	$\alpha^{E97}\ \left[\frac{10^{-6}}{K}\right]$	$\rho^{E97}\ \left[\frac{kg}{m^3}\right]$	$cp^{E97}\ \left[\frac{J}{kg\,K}\right]$	$k^{E97}\ \left[\frac{W}{m\,K}\right]$
20		7750	448	31.5
100	10.70	7753	460	32.2
150			477	
200	11.20	7713	494	32.7
250			510	
300	11.60	7685	527	33.2
350			544	
400	11.90	7655	565	33.3
450			586	
500	12.20	7625	611	32.8
550			644	
600	12.50	7594	682	32.3
650			728	
700			866	44.,8

Table 5.3.2: Thermo-mechanical properties of EUROFER97

Heat Capacity

$$c_p^W(T) = 128.308 + 93.2797 * 10^{-2}\,T - 3.4097 * 10^{-6}\,T^2 \left[\frac{J}{kg\,K}\right] \tag{5.3.5}$$

with T in [°C].

Thermal conductivity

$$k^W(T) = 174.9274 - 0.1067\,T + 5.0067 * 10^{-5}\,T^2 - 7.8349 * 10^{-9}\,T^3 \left[\frac{W}{m\,K}\right] \tag{5.3.6}$$

with T in [°C].

5.3.4 Li_4SiO_4 pebble bed

The coefficient of the thermal expansion α^{LOS}, the density ρ^{LOS}, the specific heat capacity cp^{LOS} of the Li_4SiO_4 pebble beds have been obtained from Sena [138] and Petukhov [139].The following table summarizes these properties.

The expression for the effective thermal conductivity of the Li_4SiO_4 pebble beds is given by the following expression [138]:

$$k^{Li_4SiO_4}(T,\,\varepsilon_{vol}^{in}) = 0.768 + 4.96 * 10^{-4}\,T + 0.045\,\varepsilon_{vol}^{in} \left[\frac{W}{m\,K}\right] \tag{5.3.7}$$

where T is the pebble bed local temperature [°C] and ε_{vol}^{in} is the inelastic volumetric strains in [%], which is the sum of the 3 principal strains. The ε_{vol}^{in} parameter has been considered 0 as a conservative approximation.

5.3.5 Beryllium pebble bed

The coefficient of thermal expansion α^{Be}, the density ρ^{Be}, the specific heat capacity $cp^{Be}$of the Beryllium pebble beds have been obtained from Sena [138] and Petukhov [139]. The following table summarizes these properties.

The expression for the effective thermal conductivity of the Beryllium pebble beds is given by the following expression [19]:

$$k^{Be}(T,\,\varepsilon_{vol}^{in}) = 1.81 + 0.0012\,T - 5 * 10^{-7}\,T^2 + \left(9.03 - 1.386 * 10^{-3}\,T - 7.6 * 10^{-6}\,T^2 + 2.1 * 10^{-9}\,T^3\right)\varepsilon_{vol}^{in} \left[\frac{W}{m\,K}\right] \tag{5.3.8}$$

where T is the pebble bed temperature [°C] and ε_{vol}^{in} is the inelastic volumetric strains in [%], which is the sum of the 3 principal strains.

In the case of the Be pebble beds, the effect of ε_{vol}^{in} in the conductivity of the Be pebble beds is not negligible. This parameter is influenced by thermal

$T\,[^{\circ}C]$	$\alpha^{LOS}\ \left[\frac{10^{-6}}{K}\right]$	$\rho^{LOS}\ \left[\frac{kg}{m^3}\right]$	$cp^{LOS}\ \left[\frac{J}{kg\,K}\right]$
0	1.881E-05	1526.4	1392.4
50	1.965E-05	1526.4	1450
100	2.048E-05	1526.4	1513.4
150	2.131E-05	1526.4	1580
200	2.214E-05	1526.4	1648.5
250	2.298E-05	1526.4	1718.2
300	2.381E-05	1526.4	1788.8
350	2.464E-05	1526.4	1859.9
400	2,548E-05	1526.4	1931,4
450	2,631E-05	1526.4	2003.3
500	2.714E-05	1526.4	2075.3
550	2.798E-05	1526.4	2147.5
600	2.881E-05	1526.4	2219.8
650	2.964E-05	1526.4	2292.3
700	3.048E-05	1526.4	2364.8
750	3,131E-05	1526.4	2437,4
800	3,214E-05	1526.4	2510,1
850	3,298E-05	1526.4	2582,8
900	3,381E-05	1526.4	2655,5
950	3.464E-05	1526.4	2728.3
1000	3.548E-05	1526.4	2801.1

Table 5.3.4: Thermo-mechanical properties of Li_4SiO_4

$T\,[°C]$	$\alpha^{Be}\ \left[\frac{10^{-6}}{K}\right]$	$\rho^{Be}\ \left[\frac{kg}{m^3}\right]$	$cp^{Be}\ \left[\frac{J}{kg\,K}\right]$
0	1.134E-05	1166.72	1741.8
50	1.182E-05	1166.72	1900.97
100	1.229E-05	1166.72	2045.53
150	1.275E-05	1166.72	2176.44
200	1.319E-05	1166.72	2294.66
250	1.361E-05	1166.72	2401.14
300	1.402E-05	1166.72	2496.83
350	1.442E-05	1166.72	2582.71
400	1.480E-05	1166.72	2659.71
450	1.516E-05	1166.72	2728.79
500	1.551E-05	1166.72	2790.93
550	1.585E-05	1166.72	2847.05
600	1.617E-05	1166.72	2898.14
650	1.648E-05	1166.72	2945.13
700	1.667E-05	1166.72	2988.99
750	1.704E-05	1166.72	3030.68
800	1.731E-05	1166.72	3071.14
850	1.755E-05	1166.72	3111.34
900	1.778E-05	1166.72	3152.22
950	1.800E-05	1166.72	3194.76
1000	1.820E-05	1166.72	3239.9

Table 5.3.6: Thermo-mechanical properties of Beryllium pebbles

expansion between the BB module box and the pebble beds. Thanks to thermo-mechanical models a correlation between pebble beds temperature and ε_{vol}^{in} has been derived in HCPB Test Breeding Material Breeding Unit [19] and applied in AINA models:

$$\begin{cases} 0.2\% & T\,\epsilon\,[20, 500[\,^oC \\ 0.3\% & T\,\epsilon\,[500, 600[\,^oC \\ 0.5\% & T \geq 600^oC \end{cases} \tag{5.3.9}$$

5.4 AINA HCPB Wall model

Since early 2016, a HCPB AINA BB thermal-wall model has been developing hence introduced in AINA 4.0 to perform the preliminary HCPB DEMO Safety Analysis. Thanks to the HCPB modular concept and the good poloidal symmetry observed in the fully detailed thermal-hydraulic simulations, Sec.5.2.4, a 1D configuration has been selected to represent the most representative and conservative thermal response of the WCPB BB. Indeed, differences are observed along the Y sections in the fully detailed CFD analyses, Fig.5.2.7, due to the presence of Helium loop on the sides which cool down the material. As first approximation a 1D simplified model has been built and consolidated using the steady state results provided by Eurofusion [19, 134] and summarized in Sec.5.2.4. For time being, the 1D AINA HCPB wall model seems to well represent the behavior of the more complex 3D CFD model however a further development toward the 2D approach is not discarded a priori [51].

Furthermore, the former AINA thermal wall model solver was not suitable to adapt to the HCPB-2015 design because it was not able to take into consideration the influence of coolant channels not in line with the 1D segment. For this reason, new capabilities, Sec.3, have been developed to consider this effect as a weighted convective negative flux as:

$$\dot{q} = h\,(T - T_\infty) \tag{5.4.1}$$

Where:

- $\dot{q}$ is the convective negative flux $\left[\frac{W}{m^2}\right]$
- h is the heat transfer coefficient $\left[\frac{W}{m^2\,K}\right]$
- T is the material temperature [K]
- $T_\infty$is the bulk coolant temperature [K]

The analytical methodology for the computation of the Helium HTC is detailed in Sec.5.4.2, the 1D model description in Sec.5.4.1 and the boundary conditions in Sec.5.4.3. To conclude, in order to have a correct comparison and cross-check of the model, the results refer to the steady-state behavior of the 1D AINA HCPB wall model not integrated in AINA and so without the loads to due BLK irradiation, corrosion, radiative flux etc.

5.4.1 Model description

Thanks to the HCPB modular concept and the good poloidal symmetry observed in the fully detailed thermal-hydraulic simulations Sec.5.2.4, a 1D configuration has been selected to represent the most conservative thermal response of the WCPB BB.

The AINA 1D thermal-wall model spans radially all over the HCPB BB components: it starts from the First Wall ending in the Vacuum Vessel for a total length of almost 54 cm. It is composed by five parallel layers, Table 5.4.2, which have been derived from the HCPB drawings [19, 134]. Each slice employs the most representative material of the segmentation and the correspondent temperature dependent features which are described in Sec.5.2.4. Moreover, the routines give either the possibility to compute either the temperature distribution in the three parallel materials present in layer No.5 or only for one, speeding up the calculation. In both cases the initial material conditions (e.g. density, thermal conductivity) are assumed at room conditions for the first iteration. A perfect contact has been applied between the layers without thermal contact resistance.

No.#	Thickness, cm	Material
1	2.00E-02	W coating
2	3.00E-02	EUROFER
3	1.35E-01	Helium Coolant
4	8.50E-01	EUROFER
5	51.6E+00	$Be/Li_4SiO_4/EUR$

Table 5.4.2: AINA 1D HCPB Layers

In addition, the complete set of HCPB cooling systems are included and hereinafter described:

- *FW channel:* they are modeled by *Type A- unique-node*, Sec.3.3.1.1 [51]. They are considered as planar and occupying only one node. Their f_{COOL} factors, which are equal to the relative surface of the coolant tubes to the total surface of the module section, has been determined geometrically.
- *Cooling plate channels:* they are modeled by *Type-B node*, Sec.3.3.1.1, to consider the effect of convention provided by the cooling plate channels using a negative weighted heat flux. Indeed, to take into consideration the detrimental response in function of the radial distance from the coolant and from poloidal distance from the 1D discretization line two factor are used: $f_{WGT,R}$ and $f_{WGT,P}$. The $f_{WGT,P}$ is a material dependent parameter which depends on the thermal features and the material thickness,Table 5.4.4-5.4.6. On the other hand, $f_{WGT,R}$ is a pure geometrical

value which changes on the distance of the node to the closest no dummy cooling plate Helium channel, x in Table 5.4.4: more distance corresponds to smaller values so a decreased cooling capability.

Material	$f_{WGT,P}$
EUROFER	0.5
Beryllium	0.004
Li_4SiO_4	0.005

Table 5.4.4: AINA 1D HCPB - $f_{WGT,P}$

No. Dummy CP channels	$f_{WGT,R}$
$x < 1$	0.8
$1 \leq x < 2$	0.7
$2 \leq x < 3$	0.6
$3 \leq x < 4$	0.5
$4 \leq x$	0.4

Table 5.4.6: AINA 1D HCPB - $f_{WGT,R}$

Thanks to development of the thermal routines, all the BC types can be applied to the FW and to the VV side. By the way, the studies reported hereinafter employ the Neumann BC at the FW and temperature imposed for the VV side. In the same way, the model has been prepared to employ NHD as equation or bin description to allow additional assessments.

Furthermore, after a dedicated sensibility, Sec.5.4.5.1, study three-thousands nodes per layer and a time step of 0.5 s have been employed as a the best compromise between computational effort and accuracy of the model.

5.4.2 Methodology to compute the Helium heat transfer coefficients

The analytical procedure used to compute the heat transfer coefficient is described hereinafter. The bulk coolant temperature of the CP cooling channels has been extracted from Fig.50 of [134]. Imposing a coolant pressure, p, equal to 80 bar [134] and knowing the bulk coolant temperature, T_∞, the Helium coolant density has been obtained in the following way (Equ.3-19 [135] and Equ.2.1 [19]):

$$\rho^{He}(T_\infty, p) = 48.14\,\frac{p}{T_\infty}\left(1 + 0.4446\,\frac{p}{T_\infty^{1.2}}\right)^{-1}\left[\frac{kg}{m^3}\right] \tag{5.4.2}$$

The mass flow rate, $\dot{m}\left[\frac{kg}{s}\right]$, of each CP cooling channels has been extracted from Fig.52 [13] and used to compute the Helium coolant velocity, $v\left[\frac{m}{s}\right]$:

$$\dot{m} = \rho^{He}\,A\,v \tag{5.4.3}$$

where A is the CP section $[m^2]$. The Reynolds Number is derived as:

$$Re_D = \frac{\rho^{He}\,A\,v}{\mu^{He}} \tag{5.4.4}$$

where:

- D is the coolant diameter for circular pipes [m]
- μ is the dynamic viscosity $\left[\frac{kg}{s}\right]$ obtained as follow (Equ.6-1 [135]):

$$\mu^{He}(T_\infty) = 3.674 * 10^{-7}\,T_\infty^{0.7} \tag{5.4.5}$$

Having a rectangular cross sections, the D is substituted by the hydraulic diameter D_H [m]:

$$D_H = 4\,\frac{A}{P} \tag{5.4.6}$$

where P is the wetted perimeter [m].
Moreover, the Prandlt number, Pr, is obtained (Equ.8-1 [135]) as:

$$Pr = \frac{0.7177}{1 + 1.123 * 10^{-3}\,p\,T_\infty^{-(0.01 - 1.42 * 10^{-4}\,p)}} \tag{5.4.7}$$

Depending on the Reynold Number the Nusselt No. has been obtained in two different ways:

- *Laminar Flow* [Re_D<3000]: according to [13] and assuming a constant heat flux along the pipe length and a CP channel dimension ratio a/b equal to 2, the Nu_d is set to 4.12.
- *Turbulent Flow* [Re_D≥ 3000]: following the Gnielinski correlation [140]:

$$Nu_D = \frac{\frac{f}{8}\,(Re_D - 1000)\,Pr}{1 + 12.7\,\left(\frac{f}{8}\right)^{0.5}\,-\left(Pr^{2/3} - 1\right)} \tag{5.4.8}$$

where Re_D is the Reynolds number, Pr is the Prandlt number and f is the Darcy-Weisbach friction factor, which can be approximated as:

$$f = \left(0.79\,ln\left(Re_D\right) - 1.64\right)^{-2} \tag{5.4.9}$$

after the correlation by Petukhov (Equ2.7 [19, 139]).

Finally, the Helium heat transfer coefficient for each CP channel is computed as:

$$h = \frac{Nu_D\, k^{He}}{D_H} \tag{5.4.10}$$

where k^{He} is the Helium thermal conductivity $\left[\frac{W}{m\,K}\right]$ (Equ.7-1 [135])

$$k^{He}(T_\infty, p) = 2.682 * 10^{-3}\ \left(1 + 1.123 * 10^{-3}\, p\right)\ T_\infty^{0.71-\left(1-2*10^{-4}\, p\right)} \left[\frac{W}{m\,K}\right] \tag{5.4.11}$$

Where:

- p is the pressure expressed in [bar]
- T is the absolute temperature in [K]

5.4.3 Boundary conditions

5.4.3.1 FW Helium channel

For the FW Helium channel according to EuroFUSION technical report [134], you have assumed a temperature of 400°C and a mass flow rate equal to $0.054\,kg/s$ which corresponds to the total mass flow rate of a cooling plate Helium loop. This data has been taken from the detailed 3D CFD modelling result [134].

5.4.3.2 Helium purge gas system

In a conservative approach, the Helium purge gas system has been not taken into account decreasing the coolant capability of the BB hence increasing the safety factor of the model.

5.4.3.3 Cooling plate Helium channels

The mass flow rates of each both cooling plate channels have been extracted from Fig.52 [134] and their temperature from Fig.50 [134] and reported hereinafter in Fig.5.4.1. Their complex layout has been reported in Fig.5.2.5-d.

5.4.3.4 First-wall and vacuum-vessel conditions

According to EuroFUSION technical report [134] a neutron wall loading (NWL) of $0.5\,MW/m^2$ is assumed. Robin BC is implemented over the last node which represents the VV with a heat transfer coefficient of $1000\,W/m^2/K$ and a bulk temperature of $450\,K$.

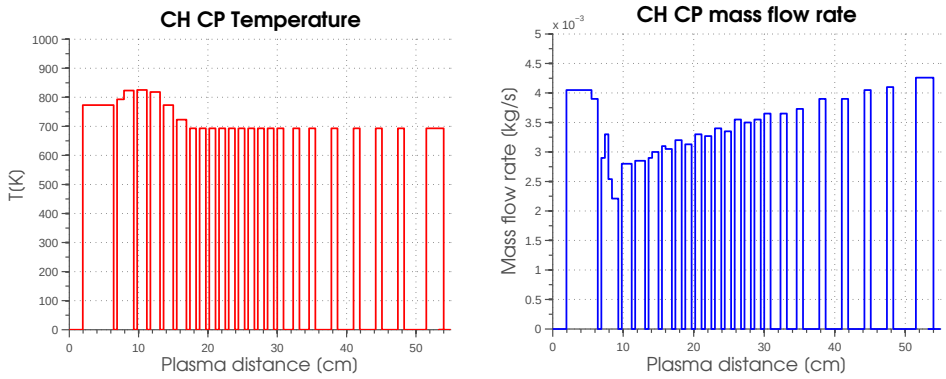

Figure 5.4.1: CH He channel temperatures and mass flow rates

5.4.3.5 Pebble bed interfaces

In a simplified approach the 1D toroidal interfaces between the Pebble bed and the EUROFER have been considered a pure conductive.

5.4.4 Heat load

At the time of the study, no official and updated nuclear heat data was available for the HCPB-2015 baseline. For this reason in line with what performed in the EuroFUSION technical report [134], the previous data has been adapted scaling proportionally them to a NWL of 0.5 MW/m^2 and approximated to an exponential function. Due to the diverse macroscopic cross sections and densities, a different nuclear heating density for each material is applied. Depending on the material and the plasma distance the AINA code applies the correspondent value. In Fig.5.4.2 the input NHD material distributions (left side) and the 1D depositions implemented (right side) are reported [3]. In the heat load implemented, we can distinguish between a shared area which is fixed for all the material configurations and one which depends upon the input selected (e.g. Eurofer, Beryllium and Li_4SiO_4).

5.4.5 Thermal-hydraulic analyses

Using the boundary conditions described in Sec.5.4.3-5.4.4, the AINA HCPB thermal-hydraulic analyses, both in state-state and transient scenarios, have been performed and hereinafter reported. In addition, the layer discretization has been properly selected and justified by dedicated analyses, Sec.5.4.5.1.

[3] Unfortunately, the Wolfram NHD was not included in the documentation provided, so the Eurofer one has been applied.

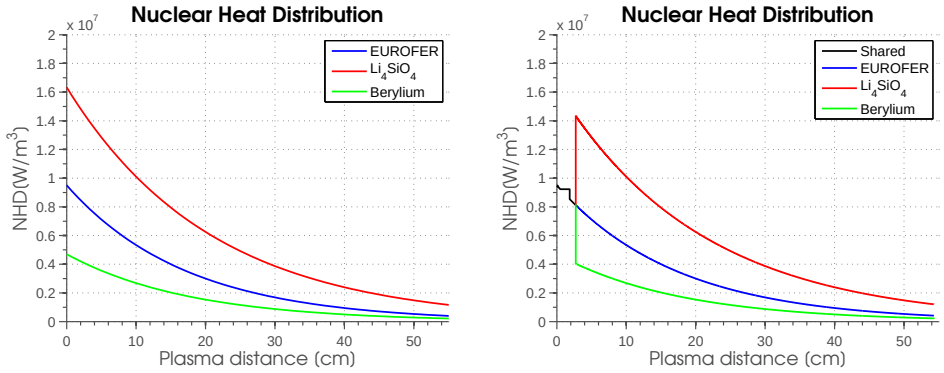

Figure 5.4.2: Nuclear Heat Distribution: Material vs AINA 1D

5.4.5.1 Truncation error and model discretization

As described in Sec.3.5, the AINA finite-element solution is computed and depends over a nodal net which covers the whole domain, averaging the solution over the single element of dimension, Δx, and in time, Δt. The source of errors which could be involved in the application of the FD have been listed and rated in Table 3.5.1. Having already selected the simplified simulation domain and its boundary conditions, the main source of errors is the problem discretization, both in time and space. Indeed, although the stability criteria is fulfilled (Sec.3.5.5), the model could lead to very inaccurate if the model nodal mesh is not fine enough to couch the variation of the response functions as the temperature distributions. For these reasons, two main cases have been assessed:

1. Steady-state case changing the space node distribution to determine the optimized single element of dimension, Δx, optimizing accuracy and computational effort. The boundary conditions described in Sec.5.4.3 are applied. Beryllium is assumed in the layer No.5.

2. Over-fuelling transient accident scenario doubling the nuclear heating density is increased as well as the power flux over the first wall. The steady-state solution computed in the previous case is employed as initial conditions. In addition, the Helium bulk temperature has been adjusted according to the methodology reported in Sec.5.4.5.4. In this assessment, the Δt is varied to minimize the truncation error of the solution maintaining a total transient duration of 40 s. As done previously, Beryllium is assumed in the layer No.5.

CASE-I: Steady-state The steady-state analysis results have been reported in Fig.5.4.3. The solutions obtained appear to be rather sensible to the No. of node per layer employed. The distribution with No. minor than four hundred are discarded because they are clearly too inaccurate (e.g. peak temperature up

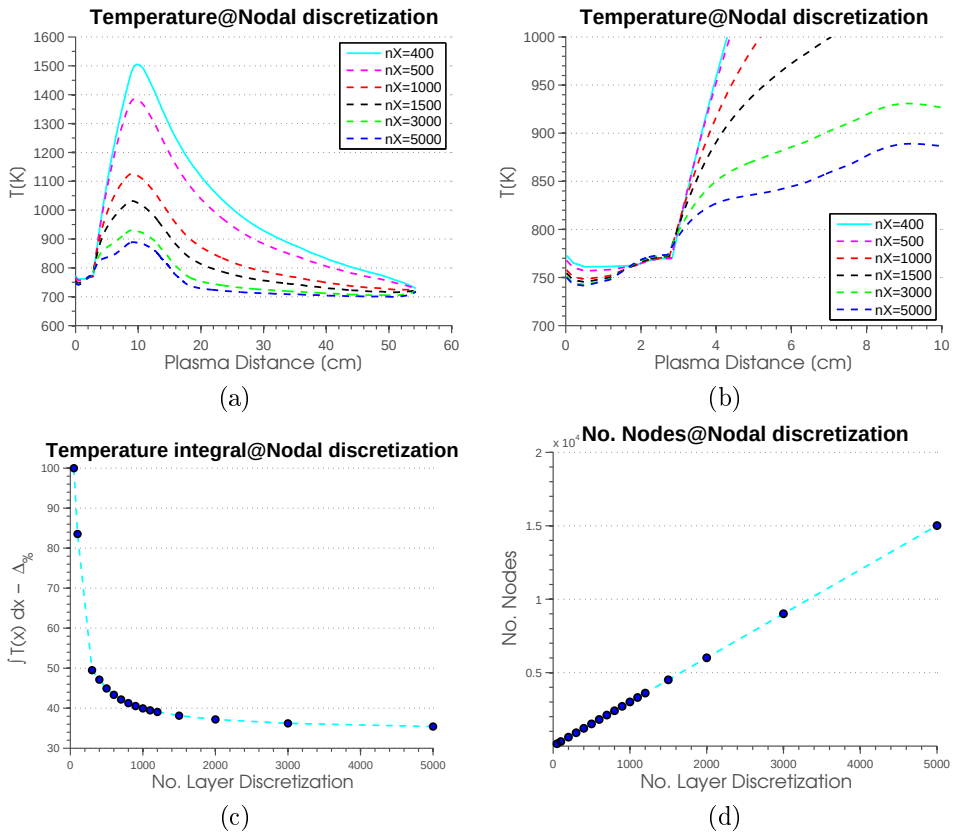

Figure 5.4.3: HCPB - Steady-state - mesh sensibility

to 3000 K). On the other hand, increasing the No. of discretization, the temperature distribution approximately maintains the shape while the temperature integral decreases up to an asymptote justifying the solution convergence. In addition, minor changes are observed close to the FW where the FW channel drives the temperature down. To conclude, the three thousand node option has been selected because it reflects the reference temperature distribution, its maximum and at the same time has a smaller computational time than the five thousand one. It is worth reminding that the cooling parameters $f_{WGT,R}$ and $f_{WGT,P}$ have been tuned to match the solution function in shape and magnitude.

CASE-2: Overfueling accident The overfuelling accident transient scenario responses have been reported in Fig.5.4.4. The several assessments done employs different time discretizations (e.g. 0.5 s, 1 s, 5 s, 10 s, 20 s) but the same spatial one selected previously (e.g. three thousand node per layer). The initial conditions imposed are the steady-steady state distribution obtained in Sec.5.4.5.1 and the variation is imposed as a step function.

The transient evolution determined with the smallest time step (i.e. 0.5 s) is reported in Fig.5.4.4-a. As expected, the temperature distribution suffers a progressive increment due to the increased power deposition. The variation seems to be more prominent in the first 20 s hence to move progressively to another steady-state point around 40s. This effect can be observed also in the time truncation-error which decreases with the time increase thanks to the limited time derivatives, Fig.5.4.4-c. Whereas, minor time truncation errors are computed for smaller Δt these assessments require more running time because of the increased number of time steps, Fig.5.4.4-b. On the other hand, moving from a interval of 0.5 s to 20 s you can increase the speed by an order of magnitude but generating a detrimental effect over the accuracy of the solution. This is noticed plotting the maximum Beryllium temperature in function of the Δt at different time, Fig.5.4.4-d, and observing how the maximum temperature computed decrease using bigger Δt.

To conclude, the smallest time step,$\Delta t = 0.5\,s$, has been selected for the transient analysis in this thesis. Besides the largest computational time, it limits the time TE, computes the most accurate and conservative temperature distributions. In future studies, other space/time discretizations could be employed depending on the computational and time constraints thus compensating the non-conservative effects by scaling functions, Sec.2.1.

5.4.5.2 Steady-state results

Using the thermal-hydraulic routine developed, the AINA HCPB steady-state temperature distribution are computed in few seconds, Fig.5.4.5. As observed in Sec.5.4.5.1, independently from layer No.5 material type, the first four layer has a similar temperature which is driven by the blanket cooling channels. In the BU zone, the Eurofer has smaller temperature thanks to its proximity to the cooling channels and the relative small material thickness. On the other hand, the $Li_4SiO_4$and the Beryllium has bigger temperature because of the increased distance from the cold focus and their smaller thermal conductivity. Moreover, a sort of saw effect is denoted in the distribution due to the discretization of the cooling channels in the cooling plate: this behavior increases toward the the blanket supporting structure due to the presence of more dummy channels.

All the materials presents a peak temperature around 9 cm. An improved design is foreseen and planned by EuroFUSION in the next year to solve this issue.

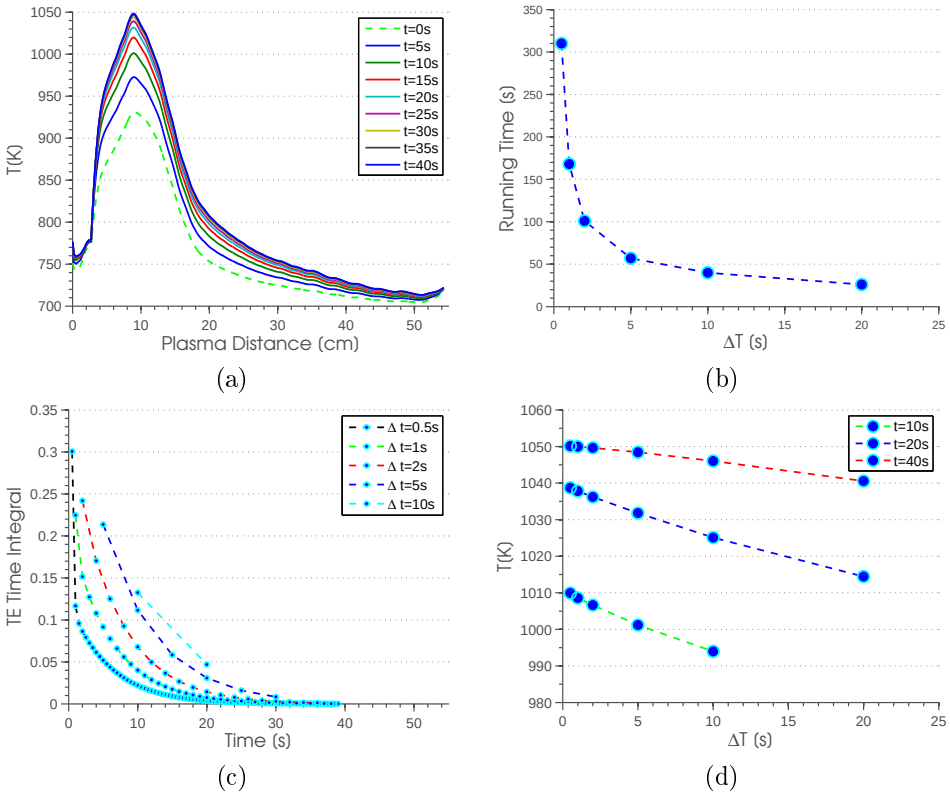

Figure 5.4.4: HCPB - Transient OFx2 - time sensibility

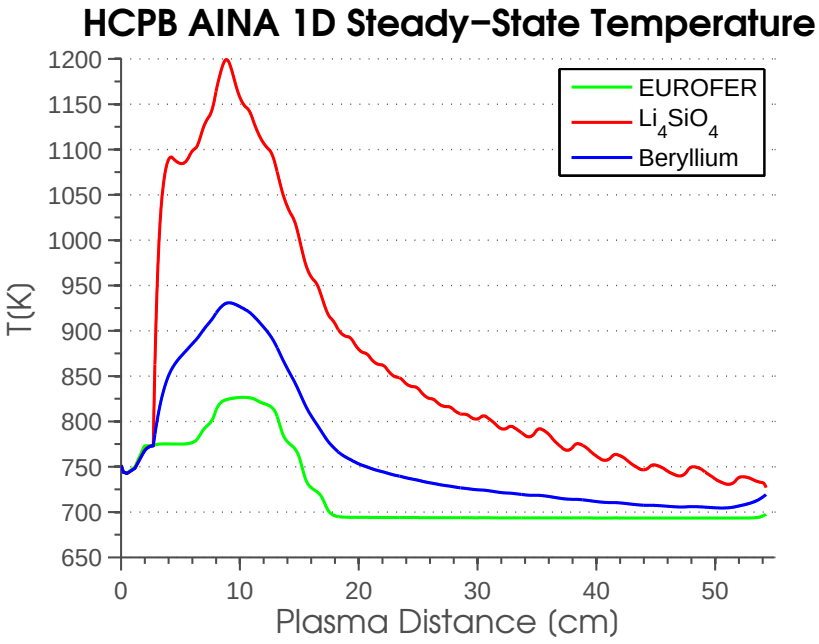

Figure 5.4.5: HCPB - Steady-State

The computed CP cooling channel heat transfer coefficients and velocities are reported in Fig.5.4.6.

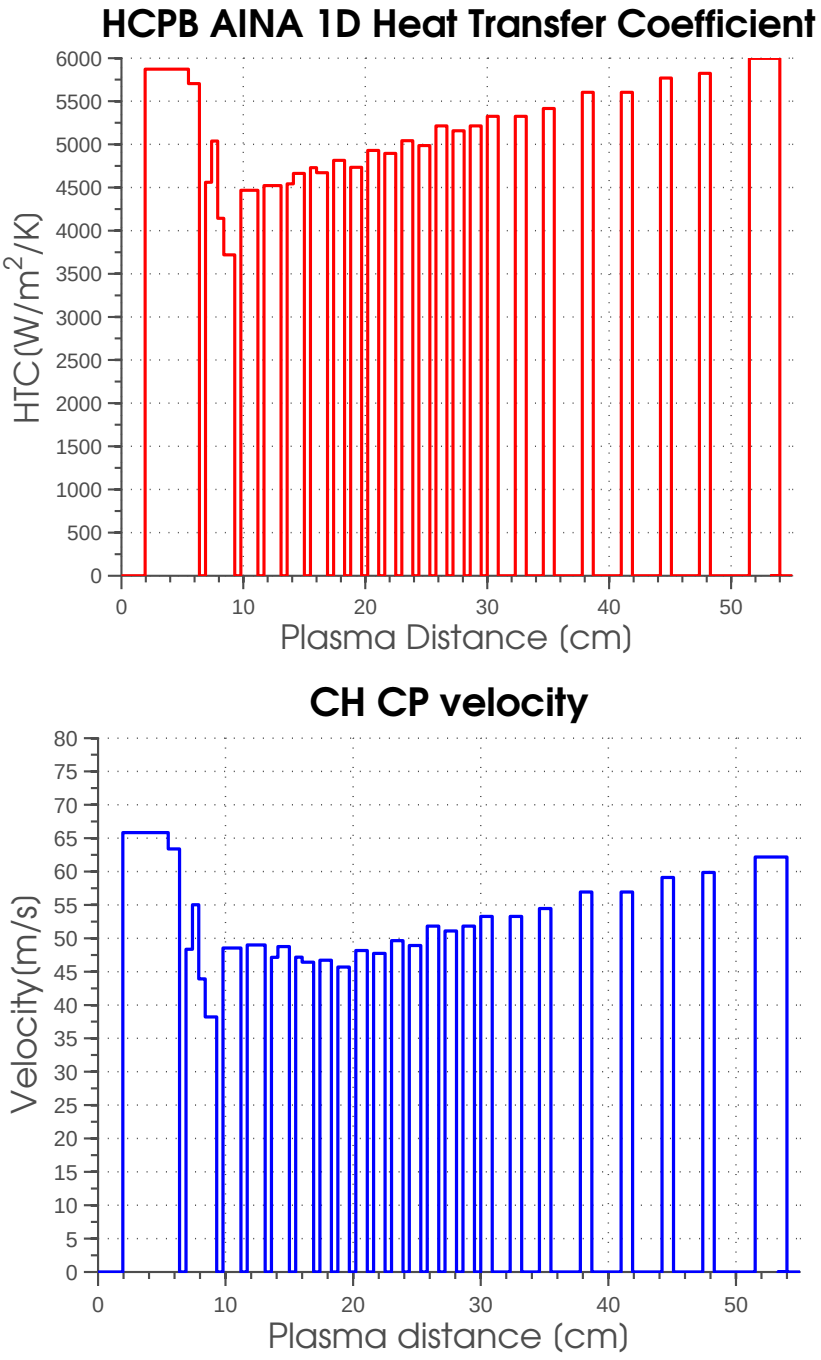

Figure 5.4.6: HCPB - CP CH heat transfer coefficients (left) and velocities (right)

Material	3D CFD [134]	*AINA*	*Temp. Limit [K]*
First Wall/WT $[K]$	~ 780	751	-
EUROFER T_{max} $[K]$	~ 837.5	827	823
BerylliumT_{max} $[K]$	~ 930.5	930	923
Li_4SiO_4 T_{max} $[K]$	~ 1196	1199	1193
FW CH velocity [m/s]	~ 55	56.2	-
CP 1st CH velocity [m/s]	~ 65	65.83	-
Temp. profile along X	Fig.5.2 [134]	Very similar	-

Table 5.4.8: AINA 1D HCPB results cross-check

A detailed response evaluation and comparison is reported in the next section.

5.4.5.3 Model verification and cross-checks

To validate and cross-check the 1D HCPB AINA thermal-hydraulic behavior responses have been compared with those obtained form 3D CFD detailed assessments ([134] reference case No.12) and reported in the Table 5.4.8. In addition, the material design limits are reported.

The 1D AINA thermal-hydraulic behavior has resulted coherent and representative of the HCPB BB global behavior analyzed by mean of 3D detailed CFD [134]. No meaningful discrepancies have been found. Indeed, the maximum temperature relative difference is less than 1.0%[4]. The HCPB material operating temperatures almost correspond to the design limits. Considering all the simplifications done, the results and the development stage, the model fulfills the current work proposal. Unfortunately, the one-to-one temperature distribution along X-axis comparison has not been carried out because the data was not provided by EuroFUSION and so the verification has been limited to graphical analysis.

Moreover, EuroFUSION has planned a HCPB design improvement in the near future in order to limit the material temperatures, increase the margin hence accomplishing the requirements also in case of accidents scenarios. Having this data, further HCPB design or modifications, they might be easily implemented in the AINA HCPB model.

[4]From this evaluation the Wolfram has been excluded because it was not include in the [134]assessment.

5.4.5.4 Suited steady-state conditions for each blanket conditions

The DEMO HCPB is composed by 18 sectors and organized in multi-module segment (MMS) arrangement with seven OB and seven IB BB modules per segment. The design employed in all the IB blanket positions is the same as well for the OB ones. Depending on the poloidal position each blanket faces a different NWL hence a different integral power deposition, so a different temperature fields. Due to the computational cost and effort required, the detailed 3D study is usually computed for only specific blanket and locations by means of CFD. On the other side, AINA DEMO HCPB wall model has not these limitation and it can compute the complete set of temperature in a short notice. It only requires as input the Helium temperature fields for the whole set of blanket locations which for the time being are not available. Then, the following methodology is proposed and implemented.

The total power deposition, P [W], in a BB module is:

$$P_\alpha = \int_{T_1}^{T_2} \dot{m}\, cp(p,T)\, dT \tag{5.4.12}$$

where $\dot{m}$ is the total Helium mass flow rate, cp [J/kg/K] is specific heat at constant pressure and T [K] is the Helium coolant temperature at the inlet, T_1, and at the outlet, T_2. The total power deposition is proportional to the NWL hence the Nuclear Heating Density. Considering two different locations, named α and β, with similar design we can affirm:

$$\frac{P_\alpha}{P_\beta} = \frac{NWL_\alpha}{NWL_\beta} = \frac{NWL_{\alpha,x}}{NWL_{\beta,x}} \tag{5.4.13}$$

Knowing the condition at BB@α we approximate the conditions at location β as:

$$P_\beta = \frac{NWL_\beta}{NWL_\alpha} * P_\alpha = \int_{T_1}^{T_2} \dot{m}\, cp(p,T)\, dT\rfloor_\alpha \tag{5.4.14}$$

The total power deposition extracted from a BB module is the sum of the contributions of each single CP channel and the FW one which are known for the location α. The temperature condition at a specific CP channel j can be obtained as:

$$P_{\beta,j} = \frac{NWL_\beta}{NWL_\alpha} * P_{\alpha,j} = \frac{NWL_\beta}{NWL_\alpha} * \int_{T_1}^{T_j} \dot{m}\, cp(p,T)\, dT\rfloor_\alpha \tag{5.4.15}$$

Hence:

$$T_{\beta,j} = \frac{\frac{NWL_\beta}{NWL_\alpha} * \int_{T_1}^{T_j} \dot{m}\, cp(p,T)\, dT\rfloor_\alpha}{\dot{m}_\beta} + cp(p_{\beta_1}, T_{\beta_1}) \over cp(p_\beta, T_\beta) \tag{5.4.16}$$

We observe that the temperature at location β and position j is increased if the NWL_β is greater than NWL_α(assuming $T_{\beta_1} = T_{\alpha_1}$). Raising the Helium

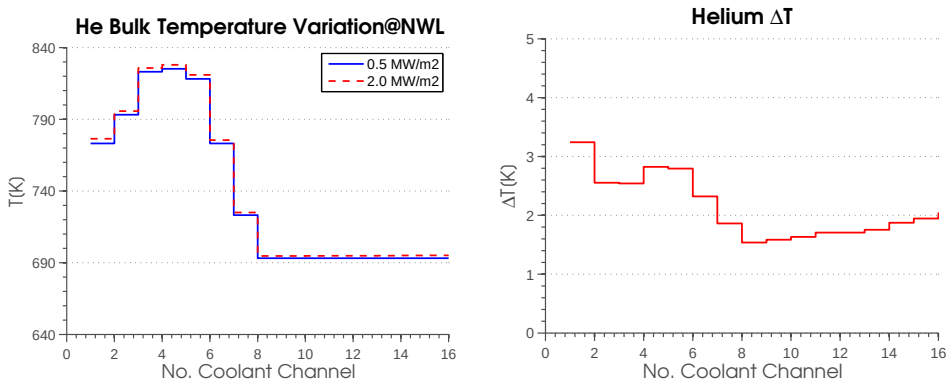

Figure 5.4.7: Suited Helium conditions

bulk temperature we decrease the convection obtaining a more conservative temperature field. To be conservative, the AINA wall model modified the Helium bulk temperature only if $NWL_\beta > NWL_\alpha$, where in this specific case $NWL_\alpha$is $0.5\,MW/m^2$ [134]. For instance, setting the NWL equal to at $2.0\,MW/m^2$ the Helium bulk temperature and its variation computed are reported in Fig.5.4.7.

5.4.5.5 Transient evolution

As part of the planned methodology for the new AINA version, Sec.2.1, several transient accidents scenarios have been assessed employing as initial condition the steady-state distribution and configuration described previously, Sec.5.4.5.2:

- Over-fuelling accident (or OF):
  - OFx1.5, Sec.5.4.5.5: the nuclear heating density is increased by 150% as well the power flux over the first wall. Helium bulk temperature has been adjusted according to the methodology reported in Sec.5.4.5.4. The overall scenario time is 40 s.
  - OFx2.0, Sec.5.4.5.5: the nuclear heating density is increased by 200% as well the power flux over the first wall. Helium bulk temperature has been adjusted according to the methodology reported in Sec.5.4.5.4. The overall scenario time is 40 s.
- Loss Of Cooling Accidents (or LOCA):
  - LOCA 25%, Sec.5.4.5.5[a small LOCA simulation]: the He loop No.2 has lose 25% of the mass flow rate as well as the loop No. 1 and the FW channel. The perturbation is applied using a step function. The progressive decrease of the mass flow rate has been not taken into account to be conservative. The overall scenario time is 40 s.

- LOCA 50%, Sec.5.4.5.5 [a medium LOCA simulation]: the He loop No.2 has lost 100% of the mass flow rate. The He Loop No.2 is working at the nominal conditions as the FW channel. The perturbation is applied by means of a step function. The progressive decrease of the mass flow rate has been not taken into account to be conservative. The overall scenario time is 40 s.

For each scenario, the temperature evolution for each material and the time frame is reported as well as the macroscopic value. The optimized space and time discretization determined is employed (e.g. 3000 nodes/layer, 0.5 s); the overall running time of the simulation is about 5 min. No material design limits are imposed even if the program is capable. These cases aim only to indicate the thermal-hydraulic response of the HCPB BB once a perturbation is imposed not a rigorous safety analysis because of the too limited temperature margins between the maximum temperature values and the steady-state one.

As this is the first accident evaluation of the HCPB transient behavior, no direct comparison is possible.

Over-fuelling accident 150% The evolution of the material temperature radial distribution and its maximum during the OFx1.5 scenario is reported in Fig.5.4.8-5.4.9.

Moreover some observations are following:

- The temperature distribution, as logic, is affected mostly in magnitude not in shape and close to the temperature peak. Reduced variation than OFx2 scenario.
- Maximum temperature increase in 40 s
  - Wolfram: $\sim 13\,K$
  - EUROFER: $\sim 5\,K$
  - Li_4SiO_4: $\sim 188\,K$
  - Beryllium: $\sim 59\,K$
- The spatial position of the material temperature peaks is unchanged.
- Li_4SiO_4 is more sensitive to changes than other materials due to the lower thermal conductivity; bigger gradients are found in the first time-steps. On the other hand, the Beryllium temperature increase is more progressive. For instance, the Beryllium distribution at 20 s can be distinguished from that at 40 s while the Li_4SiO_4 has the 5 s and the 40 s lines almost overlapped.
- The Eurofer distribution experiments some variation close to the FW due to the adjustments of the FW Helium bulk temperature, Sec.5.4.5.4.

- As observed in the steady-state, the Beryllium and Li_4SiO_4 suffers higher temperature because the effect of the convention in less effective far away from the cooling channel lines.
- The Wolfram experiences a limited increase thanks to the effective cooling of the Helium which flows in the first wall.
- At about 40 s a new SS seems to appear.
- Apart for Eurofer, all the material temperature overpass the design limit.

Over-fuelling accident 200% The evolution of the material temperature radial distribution and its maximum during the OFx2 scenario is reported in Fig.5.4.10-5.4.11.

Moreover some observations are following:

- The temperature distribution, as logic, is affected mostly in magnitude not in shape and close to the temperature peak. Enhanced variation than OFx1.5 scenario but a similar behavior is discovered.
- Maximum temperature increase per material in 40 s which approximately doubles those in OFx1.5 scenario
  - Wolfram: $\sim 25\,K$
  - EUROFER: $\sim 10\,K$
  - Li_4SiO_4: $\sim 375\,K$
  - Beryllium: $\sim 119\,K$
- The spatial position of the material temperature peaks is unchanged.
- $Li_4SiO_4$is more sensitive to changes than other materials due to the lower thermal conductivity; bigger gradients are found in the first time-steps. On the other hand, the Beryllium temperature increase is more progressive. For instance, the Beryllium distribution at 20 s can be distinguished from that at 40 s while the Li_4SiO_4 has the 5 s and the 40 s almost overlapped.
- EUROFER distribution experiments variation close to the FW due to the adjustments of the FW Helium bulk temperature, Sec.5.4.5.4.
- As observed in the steady-state, the Beryllium and Li_4SiO_4 suffers higher temperature because the effect of the convention in less effective far away from the cooling channel lines.
- The Wolfram experiences a limited increase thanks to the effective cooling of the Helium which flows in the FW.
- At about 40 s a new steady-state seems close.
- Apart for EUROFER, all the material temperature overpass the design limit.

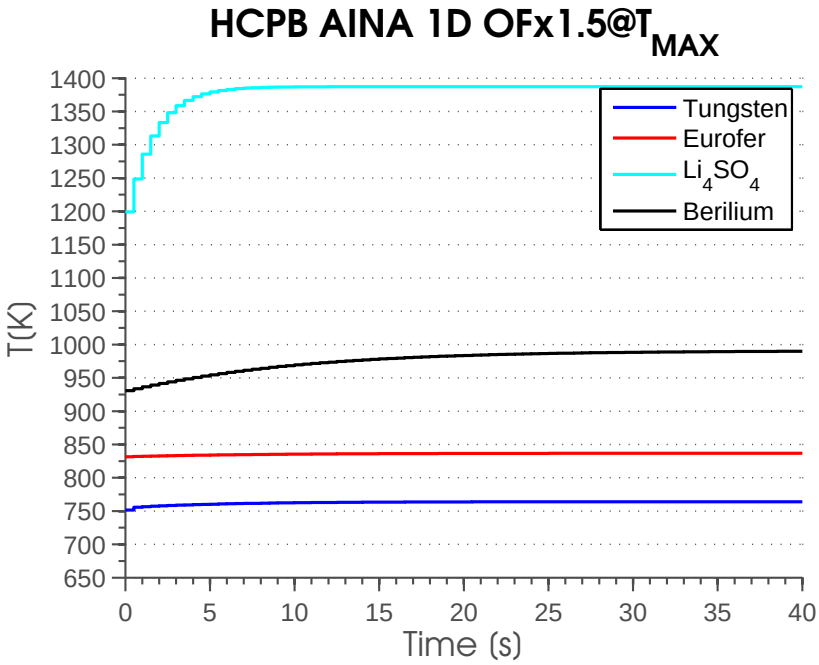

(a)

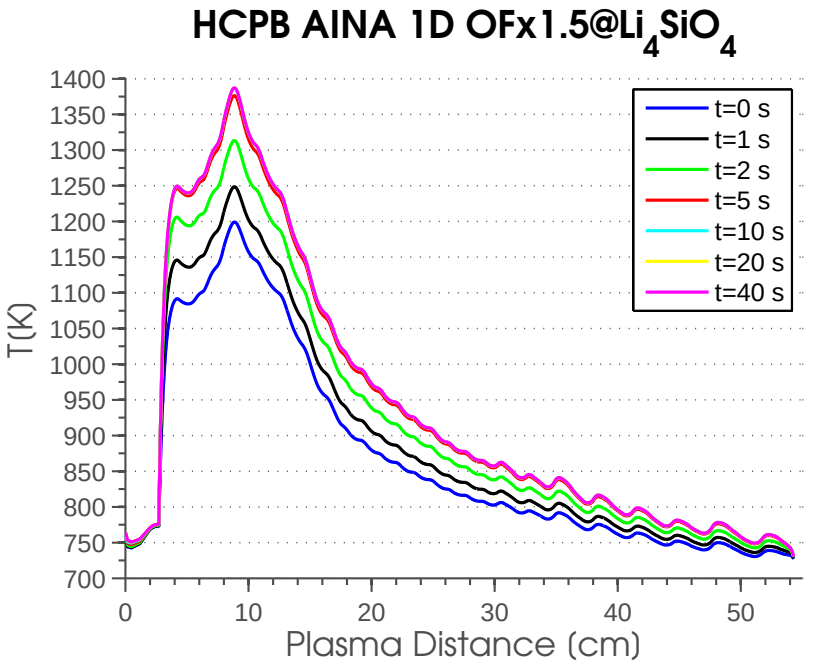

(b)

Figure 5.4.8: HCPB - Transient OFx1.5 - Part-I

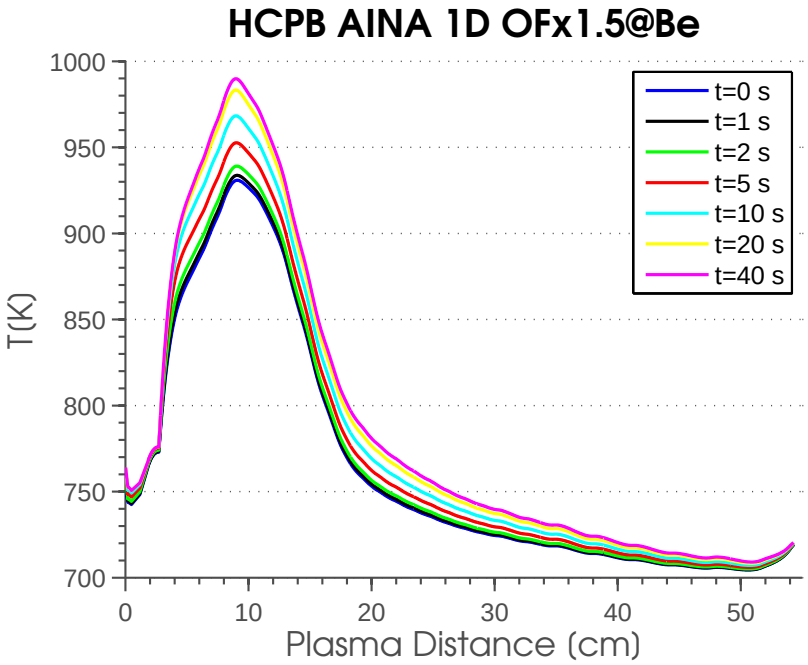

(c)

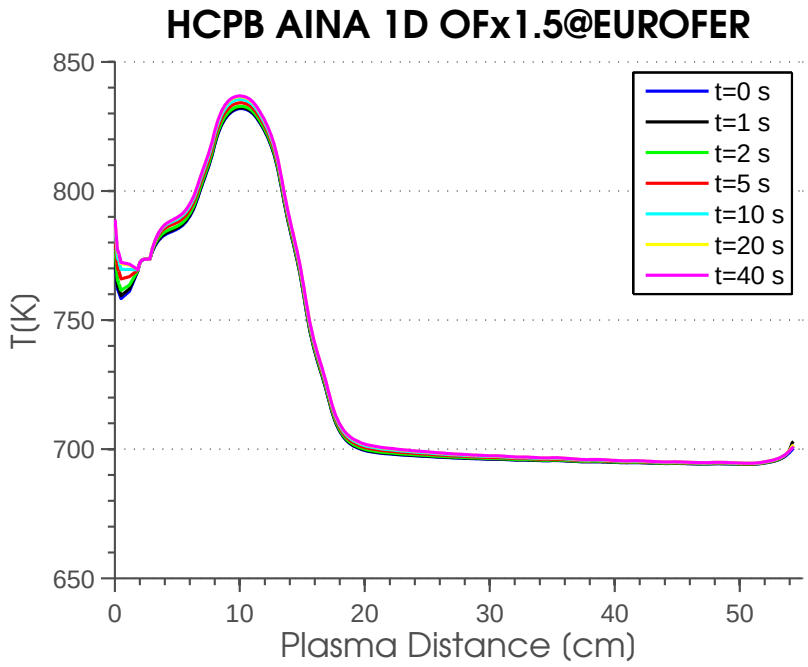

(d)

Figure 5.4.9: HCPB - Transient OFx1.5 - Part-II

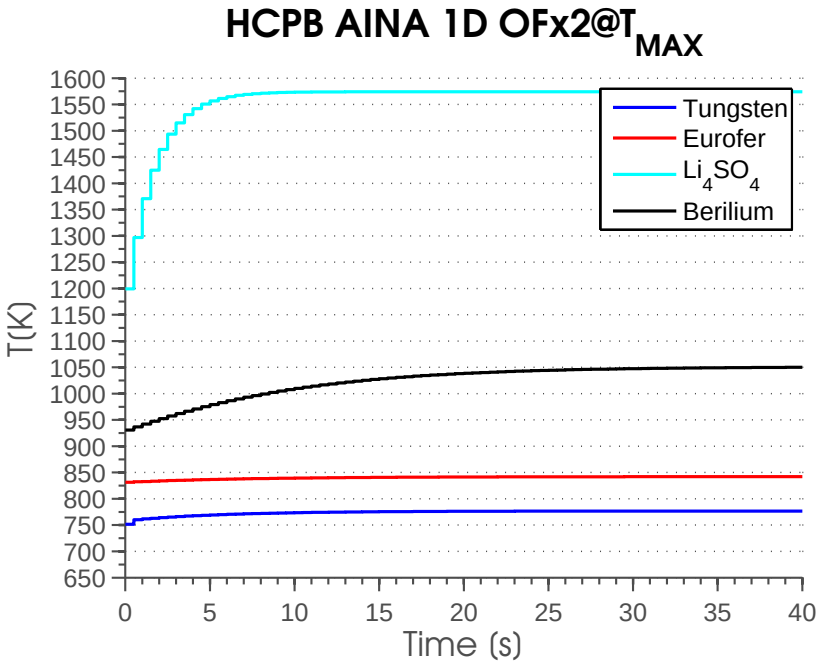

(a)

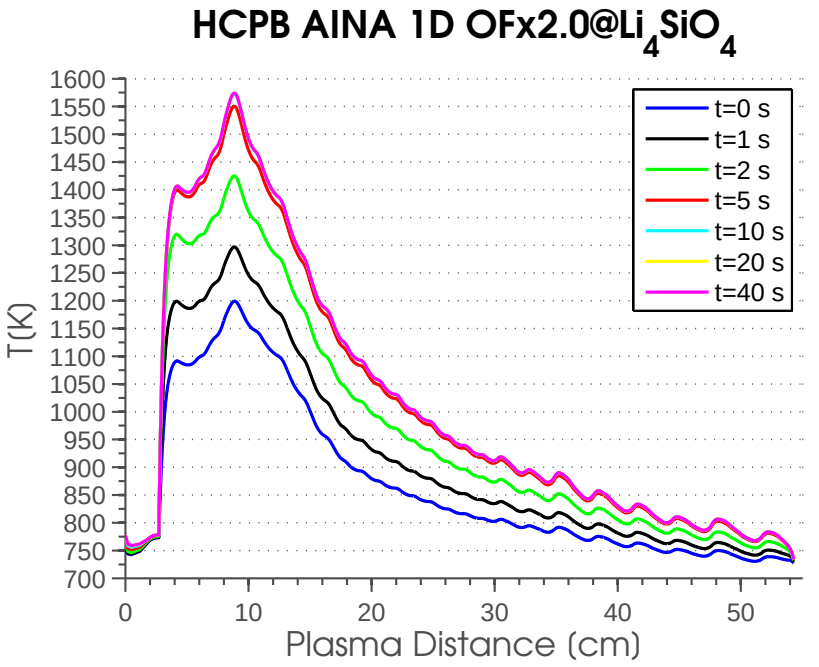

(b)

Figure 5.4.10: HCPB - Transient OFx2 - Part-I

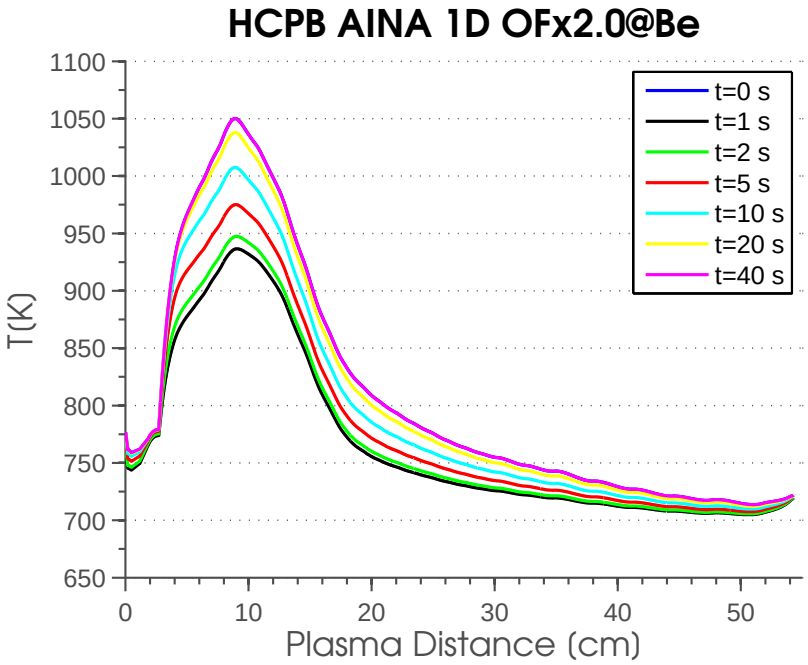

(c)

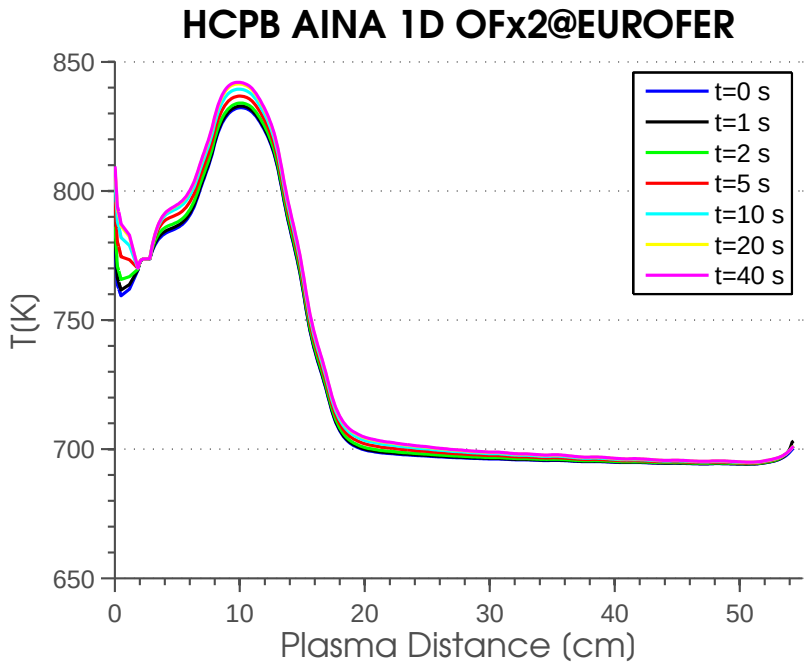

(d)

Figure 5.4.11: HCPB - Transient OFx2 - Part-I

LOCA 25% The evolution of the material temperature radial distribution and its maximum during the LOCA-25% scenario is reported in Fig.5.4.12-5.4.13.

Moreover some observations are following:

- The temperature distribution, as logic, is affected both in magnitude and in shape due to the modification of the cooling features. Enhanced variations are placed in most loaded areas. Reduced variation than LOCA-50% and OF case are highlighted.
- Maximum temperature increase per material in 40 s
  - Wolfram: $\sim 4\,K$
  - EUROFER: $\sim 1\,K$
  - Li_4SiO_4: $\sim 25\,K$
  - Beryllium: $\sim 9\,K$
- The spatial position of the material temperature peaks is unchanged. Besides, the Li_4SiO_4temperature peak around $\sim 8\,cm$ experience a higher increment due to the proximity to the coolant loop affected.
- Li_4SiO_4 is more sensitive to changes than other materials due to the lower thermal conductivity; bigger gradients are found in the first time-steps. Nevertheless, minor changes are found highlighting the importance of having two separated and independent loops in case of LOCA accidents.
- As observed in the steady-state, the Beryllium and Li_4SiO_4 suffers higher temperature because the effect of the convention in less effective far away from the cooling channel lines. EUROFER distribution is almost unchanged.
- The Wolfram experiences a relative small increase thanks to the effective cooling of the Helium which flows in the FW.
- A new steady-state seems to be reached around 30 s. The material temperature is just within the design limit.

LOCA 50% The evolution of the material temperature radial distribution and its maximum during the LOCA-50% scenario is reported in Fig.5.4.14-5.4.15.

Moreover some observations are following:

- The temperature distribution, as logic, is affected both in magnitude and in shape due to the modification of the cooling features. Enhanced variations are placed in most loaded areas. Increased variation than LOCA-25% but smaller that the OF scenarios.
- Maximum temperature increase per material in 40 s

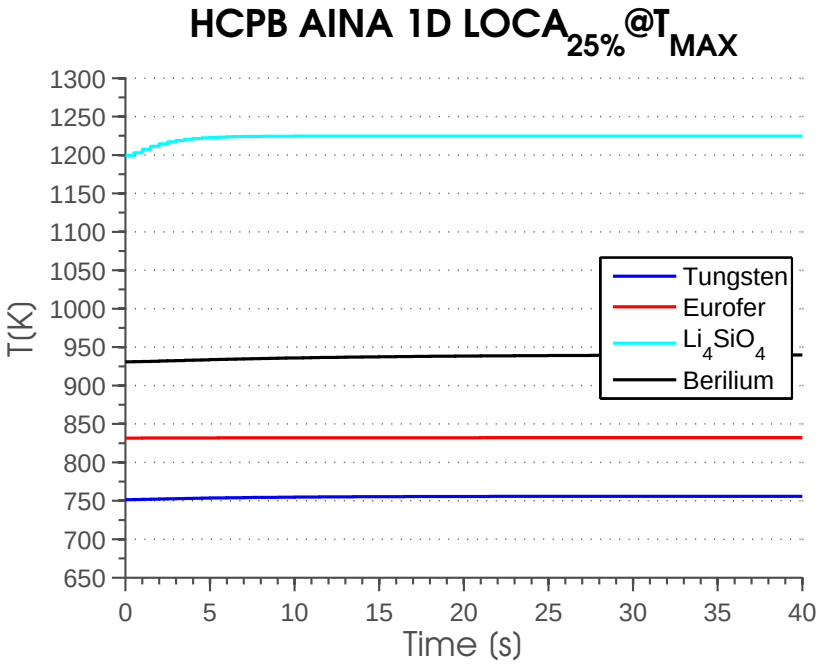

(a)

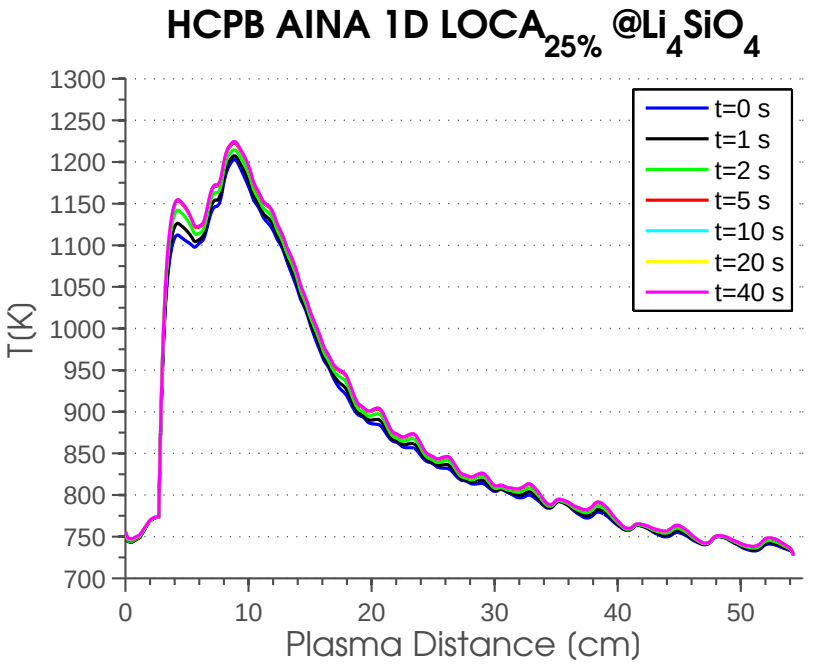

(b)

Figure 5.4.12: HCPB - Transient LOCA 25% - Part-I

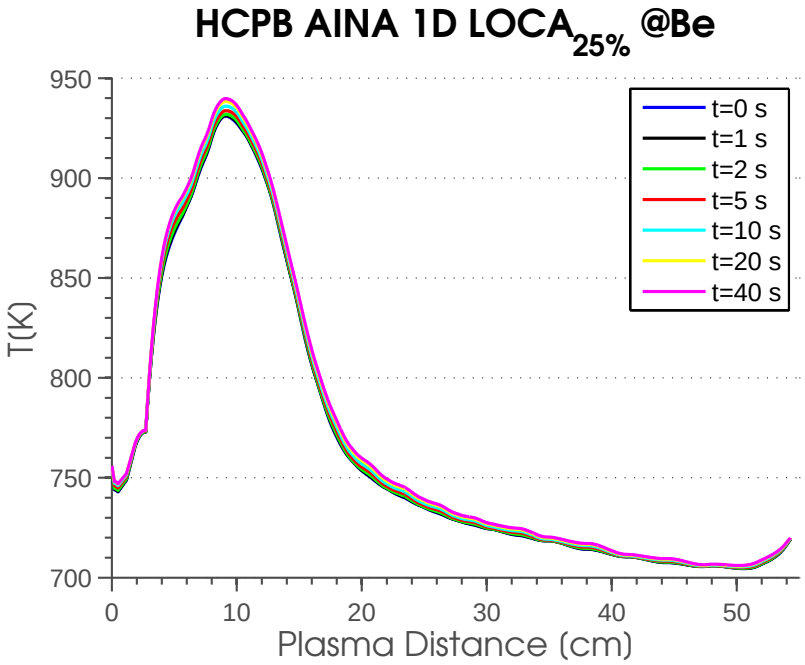

(c)

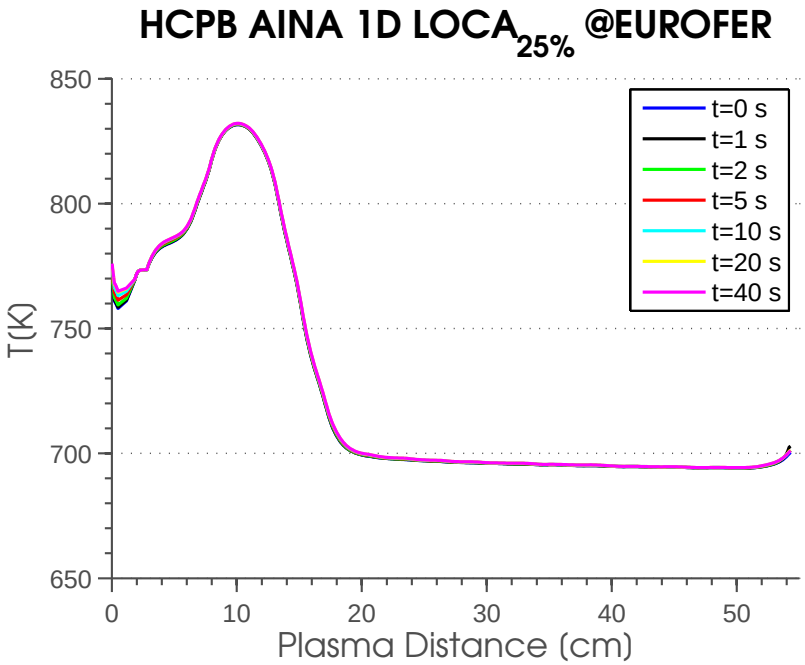

(d)

Figure 5.4.13: HCPB - Transient LOCA 25% - Part-II

  - Wolfram: $\sim 12\,K$
  - EUROFER: $\sim 1\,K$
  - Li_4SiO_4: $\sim 64\,K$
  - Beryllium: $\sim 21\,K$

- The spatial position of the material temperature peaks is unchanged. Besides, the Li_4SiO_4temperature peak around $\sim 8\,cm$ experience a higher increment due to the proximity to the coolant loop affected.
- Li_4SiO_4 is more sensitive to changes than other materials due to the lower thermal conductivity; bigger gradients are found in the first time-steps. Nevertheless, minor changes are found highlighting the importance of having two separated and independent loops in case of LOCA accidents.
- A sort of saw effect appears in the Li_4SiO_4temperature distribution due to the discretized cooling channel in the EUROFER CP. Thus the valleys correspond to the closer points to the operative CH whereas the peaks to the farthest ones.
- As observed in the steady-state, the Beryllium and Li_4SiO_4 suffers higher temperature because the effect of the convention in less effective far away from the cooling channel lines. EUROFER distribution is almost unchanged.
- The Wolfram experiences a relative small increase thanks to the effective cooling of the Helium which flows in the FW.
- A new steady-state is not reached in 40 s.
- Only the Li_4SiO_4 overpasses the material design limits.

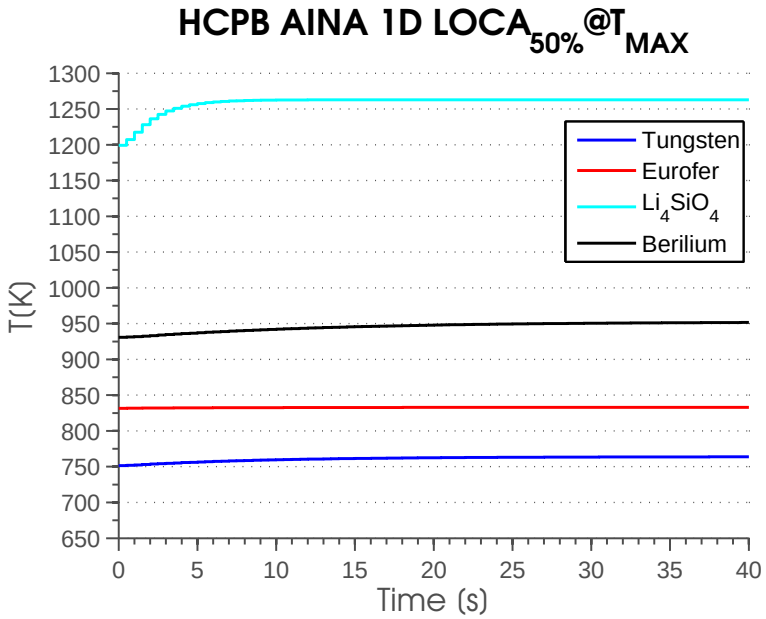

(a)

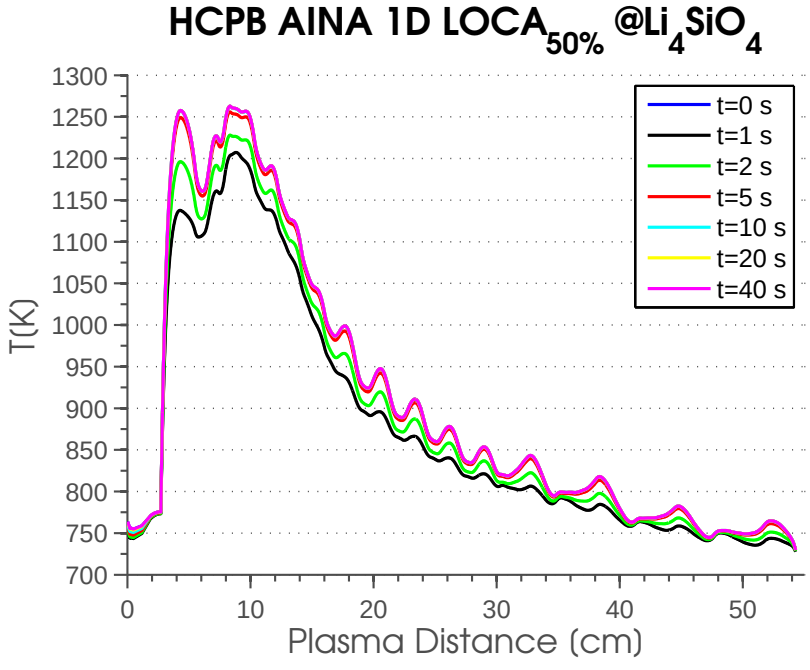

(b)

Figure 5.4.14: HCPB - Transient LOCA 50% - Part-I

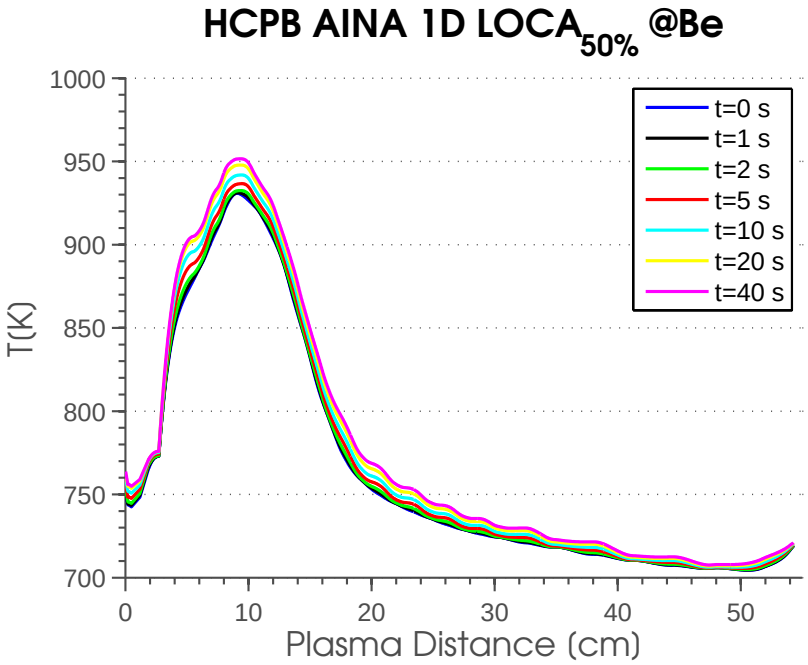

(c)

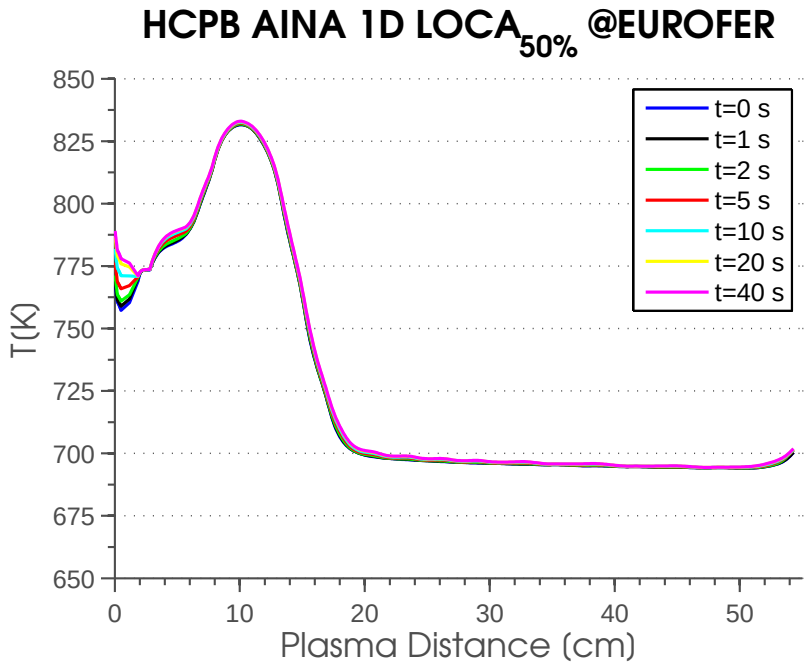

(d)

Figure 5.4.15: HCPB - Transient LOCA 50% - Part-II

5.5 Conclusion

The HCPB AINA thermal-wall model development has been detailed and properly justified. The model has been described in Sec.5.4.1. It is worth reminding that the former AINA solvers was not suitable to adapt to the HCPB-2015 design because it was not able to take into consideration the influence of coolant channels not in line with the 1D segment [51]. Hence, new capabilities have been inserted to take into consideration lateral channel as a weighted convective negative flux, Sec.3.3.1.1. The 1D AINA thermal-hydraulic steady state behavior has been computed and the outcomes reported in Sec.5.4.5.2. Its outcomes have been consolidated using the steady state results obtain by means of the detailed 3D CFD analysis done by EuroFUSION [134]. It has resulted coherent and a conservative representation of the HCPB BB SS global behavior: the material temperature maximums agree within 5%. No meaningful discrepancies are found. In addition, in contrast to the CFD approach, the blanket conditions and behavior (e.g. NWL, heating, coolant, distributions...) can be easily extrapolated to all the BB regions thanks to the methodology detailed in Sec.5.4.5.4.

For the time being, a more complex model is not needed, however a further development towards the 2D model is not discarded a priori. Indeed, due to the small margin between the HCPB BB operation and the material design limit, EuroFUSION consortium has planned for the next year a substantial re-design of the HCPB BB. Nevertheless, due to the AINA modularity concept future modifications could be easily implemented.

In addition, four transient scenarios have been preliminary assessed to understand how the HCPB BB could react to the perturbation externally imposed: two over-fuelling at 150% and 200% and two LOCA (25% and 50%) scenarios which affect the both the first coolant loop and the FW.

In the OF cases, the temperature distributions is affected mostly in magnitude and close to the temperature peak. Scenario OFx2 has a similar behavior than OFx1.5 but with bigger variation due to the enhanced power deposition. Apart from EUROFER, all the material temperature overpass the design limit.

On the other hand, in the LOCA cases, the material behavior is affected both in magnitude and in shape due to the modification of the cooling features. Enhanced variations are placed in most loaded areas. Indeed, the Li_4SiO_4 temperature peak around $\sim 8\,cm$ experience a higher increment due to the proximity to the coolant loop affected. In line with the perturbation applied, the LOCA-50% has increased variation than LOCA-25% but smaller that the OF scenarios. So, minor variations are found highlighting the importance of having two separated and independent loops in case of LOCA accidents. Only the Li_4SiO_4 overpasses the material design limits in the LOCA-50% case.

Moreover the analysis confirm the Li_4SiO_4 sensibility to the perturbation imposed because of the lower thermal conductivity; bigger gradients are always found in the first time-steps whereas the Beryllium has a more progressive variation.

To conclude, a specific and conservative Helium Cooled Pebble Bed AINA

thermal-model has been developed to estimate the thermal-hydraulic conditions for any specific boundary condition, BB loads and coolant conditions both in steady-state and transient regimes. Standard workstation (e.g. $<$ 2 GB) are suitable to run the 1D HCPB AINA thermal-hydraulic model. The run time is very short: less than 10 s to obtain the steady-state solution and less than 1 s for transient time step iteration.The developed model has been successfully introduced in AINA DEMO 4.0 to perform the preliminary HCPB DEMO Safety Analysis [129][129], which are going to be presented in the next International Symposium of Fusion Nuclear Technology (Kyoto, Japan) ISFNT-13.

Chapter 6

Conclusion

By 2050 the energy consumption is expected to increase considerably (about +40% [141]) due to the world population growth, better living standards and the further industrialization of developing countries. Furthermore, considering also the environmental requirements for zero or low CO_2 emission sources, the worldwide community needs to invest in a sustainable, balanced and efficient energy mix. This might be driven by nuclear fusion because unlike other renewable sources it could deliver continuous, large-scale long-term power without harming the environment. Unfortunately, nuclear fusion is not a mature technology and there is still a lot of work to do. Nowadays, numerous developments are undergoing around the world to prove the design feasibility and to evaluate the safety aspects embraced also in this thesis. Safety analyses cover multiple disciplines (i.e. dose calculation, waste inventory, material design fulfillment ...) and they shall be considered and embedded in all stages of the fusion power plant life-cycle from the conceptual design up to the final decommission. Indeed, numerous, independent and extensive investigations have already been performed for ITER and partially for DEMO. Consequently, numerous computer codes and models, depending on the application area, are developed and used to perform safety analyses of the fusion facilities. Before their application, they have to a pass a rigorous Validation & Verification process. In addition, if their calculations are part of the plant safety file, the usage of the specific methodology/tool shall also be endorsed by the correspondent nuclear security agency.

In light of this, during the last ten years, the Fusion Energy Engineering Laboratory (FEEL), a division of the Nuclear Engineering Research Group (NERG) of the Technical University of Catalonia (UPC) has being developing a safety code called AINA (acronym of Analyses of IN-vessel Accidents). It evaluates the magnetic fusion reactor plasma-wall transients in case of ex-vessel LOCA and overfuelling, determining thermal wall profiles as well as checking the integrity of in-vessel components (melting). The code, which is part of the European and Japanese reference software to perform the DEMO safety analyses [41], has already been successfully applied in numerous projects to different fusion reactor

designs such as ITER [42, 43, 44, 45, 46, 47, 8] and the Japanese DEMO design WCPB [48, 8, 49]. It is based on simplified models derived from more complex ones and thanks to its modularity concept it is fully adaptable to the reactor design, materials and plasma physics.

The AINA code is composed of three main core sections linked one to one another: (i) plasma block, (ii) plasma-wall interaction and (iii) thermal block. In a very simplified manner, the plasma model computes the radiative energy fluxes over the plasma wall components, at the same time, the wall-model determines the thermal profile and so the first wall temperature which influences the impurities fluxes produced by erosion processing and sputtering into the plasma, perturbing the plasma balance. With the computed input, the thermal analysis of in-vessel components is computed using suited finite difference approach and considering separately first wall and divertor modules and performing a thermal analysis for each one retrofitting back to the first wall temperature and restarting the loop again. Furthermore, the short AINA running time (a question of minutes) allows to perform multiple simulations and establish boundaries for the worst scenarios thus supporting the safety analysis.

For almost ten years now, the AINA safety code has been constantly evolved and improved. Several PhD candidates and Master Thesis students with a diverse know-how had given their meaningful support to improve/correct specific features of the routines. These have led to numerous international and peer reviewed publications [42, 43, 53, 44, 45, 46, 47, 54]. Unfortunately, the development was done in a not fully harmonized way, missing a clear and coherent roadmap. Considering also the evolution of technologies and related methodologies, a substantial renewal plan was established for the whole AINA code. For these reasons, in late 2014, the kick-off of the Safety studies for DEMO with AINA code project within the EUROfusion framework triggered a critical and peer review of the whole AINA Safety Code. Then, the foremost development areas had been listed, prioritized and shared within the research group. In addition to the contribution to the general development of AINA code by means of assistance to periodical technical meetings, production of intermediate/ final reports and task management, the NERG group leader decided to embed two specific development tasks within this PhD:

- The re-design, generalization and optimization of thermal-hydraulics routines for the determination of the AINA thermal-wall distributions both in normal and accident scenarios to substitute the former unverified /unqualified /uncommented ones. In addition, a main requirement was their endorsement against commercial software as ANSYS Fluent. This task has been described in Chapter No.3 hereinafter named as AINA thermal-hydraulic routines.

- The definition, standardization and validation of an enhanced methodology to develop new AINA versions, Sec.2.1, to obtain robust models, estimating as accurately as possible the behaviour of the studied systems. This task has been described in Chapter No.2 hereinafter named as AINA methodology and validations.

Consequently, the code has practically been rewritten, improved and consolidated. In addition, a great effort has been dedicated to documenting, commenting and Validation & Verification (when possible) in line with the current software standard requirement. Indeed, Chapter No.3 covers the work carried out within this thesis: special attention has been given to the peer review, development, consolidation and validation of the code focusing on the thermal-block which computes the temperature distribution in normal and accident operations. For the first time in the developing process, numerous validation cases with different configurations have been set-up, performed and properly recorded. Parameters as the boundary conditions, the spatial and time discretization, the nuclear heating and the domain pattern have been sequentially changed to check the routine responses and performances. When discrepancies between the AINA code and the commercial software ANSYS Fluent/analytical solutions were found, the routines have been debugged and improved. Therefore, the complete set of features was validated thanks to the limited differences found (e.g. +/-10%) which have been specifically justified.

Moreover, considering the previous AINA thermal-wall block solver limitations (i.e. possibility to represent only 1D model and coolant channel parallel to the first wall layer, limited user options and difficulty to interface with other software/tools ...), several innovative features have been specifically developed and introduced to increase the design options and the routine capabilities giving to the AINA safety code to approximate almost all blanket designs:

- Implementation of 1D or 2D computational spatial domain
- Verification of all the finite difference thermal-hydraulic solvers by direct comparison to an CFD commercial solver
- Capability to introduce the nuclear heating density by equation, discretized bins or by interpolations
- Detailed evaluation of the source of errors and their impact over the responses
- Introduction of routine for the error treatment (e.g. convergence, truncations ...)
- Possibility to introduce any boundary conditions
- Capability to variate the spatial and time discretization
- Modelling of any cooling channel types thanks to the implementation of two different model approaches
- Automatic response post-processing to standardized format as the VTK to improve the interconnection with further codes

Afterwards, once the AINA code had been renewed and verified, two specific AINA blanket thermal-wall models were created. These novel and important contributions to the EUROfusion community included:

- The complete process of design, improvement and validation of the Water Cooled Pebble Bed JAPANESE-DEMO AINA blanket thermal-block model. This also included the complete set of compulsory radiation transport analyses, thermal-hydraulic studies and AINA thermal-wall model tuning. This task has been described in Chapter No.4 hereinafter named as Water Cooled Pebble Bed (JAPANESE-DEMO).

- The generation, set-up and endorsement of the European Helium Cooled Pebble Bed DEMO AINA blanket thermal-block model. Furthermore, a preliminary assessment of the HCPB AINA safety analysis and sensibility study was required. This task has been described in Chapter No.5 hereinafter named as European Helium Cooled Pebble Bed (EUROPEAN-DEMO).

The elaboration, improvement and validation of the WCPB and the HCPB models has been largely described in Chapter 4-5 so not duplicated here. They have driven several international and peer-reviewed publications endorsing the innovative and skillful work done listed in the scientific production section. Furthermore, they are complemented by additional numerous technical projects/publications undertaken outside the PhD thesis whilst in the same period of time. The development of an AINA blanket thermal-wall model is a comprehensive and large process as detailed in Sec.2.1. Thanks to this robust methodology, starting from fully detailed neutronics and thermal-hydraulic results, a simplified and conservative wall model has been implemented in AINA, obtaining reliable results in a short calculation time validating the approach proposed. Indeed, simplified models have been iteratively built and adjusted, achieving a good agreement with the fully detailed simulation and yielding maximum absolute temperature differences of approximately 10%. The determination and coherence of the temperature distribution obtained using independent tools and approaches, ANSYS® Fluent® vs AINA thermal-hydraulic routines, supports the proposed methodology, hence validating all the results obtained. Nevertheless, the 1D non-conservative temperature field, where present, could be compensated by the application of scaling functions, obtaining a perfect match with the most conservative 3D distribution. In this innovative approach, the scaling functions correspond to the ratios between the most conservative radial distribution in the fully detailed and the 1D simulations. They have been computed to cover the whole operational areas including accidental scenarios. Moreover, thanks to the simplified and endorsed model, sensitivities and screening assessment can be easily performed showing how the system reacts as a consequence of loads, boundary conditions and perturbations. In light of this, the detailed number of studies can be extensively reduced. Therefore, the development and the implementation of a standard methodology is obviously an improvement over previous work, which was unbounded and sometimes rather untraced. This multidisciplinary activity has requested the establishment of a specific framework, including skills and tool. The knowledge has been widely extended across many different fields also thanks to the numerous technical courses attended [142]:

- Finite difference techniques:
  - Type, assessment and implementation
  - Error estimation and convergence
  - Numerical solution
- Thermal-hydraulic analyses:
  - Model preparation: usage of large CAD model, manage and simplification using the CATIA and the SpaceClaim software
  - Meshing techniques, both automatic and manual, optimizing the usage of structure and unstructured options
  - Proficient use of CFD features as models, boundary conditions and solver techniques
  - Set-up and improvement of mapping schemes and interpolation using the User Defined Function capabilities
- Radiation transport calculations based on probabilistic code (i.e. MCNP software):
  - Model preparation: usage of large CAD model, manage and simplification using the CATIA and the SpaceClaim software
  - Model conversion from CAD to MCNP specific thanks to the tool SuperMC kindly provided by INES team (Democratic Republic of China)
  - Cross-section analysis and comparison (e.g. JANIS and NJOY)
  - Application of innovative MCNP model concepts and features as the mesh tally and the universe concepts.
  - Implementation of proficient variance reduction technique
- Generation of MCNP advanced variance reduction weight windows based on deterministic solver as ADVANTG
- Handling of pre-processing tools as numjuggler to manipulate the MCNP input
- Usage of post-processing toolkits and format as VTK, Paraview, mt2vtk or ANSYS CFD post
- Design of specific routines (e.g. MATLAB and C++) for the semi-automatic implementation of new cross-sections, weight windows analysis and "softening", monitor of the solution time
- Establishment of specific Linux environment to compile and run for the nuclear software as NJOY

The entire set of activities carried out within this PhD are part of the NERG research plan related to AINA. Indeed, they were direct contributions to the following tasks/projects:

- Safety studies for DEMO with AINA code (2014-2018, EUROFusion, still on-going)
- Secondment expert from UPC-FEEL to IFERC Japan, development of AINA code for Japan DEMO (2014, Fusion for Energy)
- Secondment expert from UPC-FEEL to IFERC Japan, development of AINA code for Japan DEMO (2015, Fusion for Energy)

The specific framework and the know-how developed should be used as baseline for subsequent improvements. A continuous enhancement of the AINA code is foreseen as a consequence of the sponsor demands and technology advances as mentioned in Sec.2.1. Possible future developments have been listed and prioritized. Regarding the AINA wall thermal-model, the next tasks should be focused on the impact of the variation of NHD (due to temperatures, different cross sections, Doppler effect broadening) on the thermal-wall field as well as the determination of the effect of this methodology on the AINA safety analysis.

To conclude, five thousand hours within almost five years have been invested in this PhD. The knowledge has been extended in many different fields obtaining a more complete perspective of the fusion technologies and related research areas. An extended feedback between the research and the industrial aspects has been present supporting and improving the quality of the work done, enlarging the know-how and compensating the project risks.

Appendix A

Analytic solutions of 1D heat equation

Where possible, the analytic solution of the heat equation has been determined in order to validate and cross-check the in-house developed thermal routines.

Starting from the generic 3D heat transfer equation (Eq. 3.3.1) and considering a 1D slab of thickness x, with constant thermal conductivity k and constant heat generation $\dddot{q}$ along the domain and in time, we obtain:

$$\rho(T,x)c(T,x)\frac{\delta T(x,t)}{\delta t} - k\frac{d^2T(x)}{dx^2} = +\dddot{q} \tag{A.0.1}$$

Moreover, imposing a steady-state solution Eq.A.0.1 it is further simplified to

$$\frac{d^2T(x)}{dx^2} = -\frac{\dddot{q}}{k} \tag{A.0.2}$$

Hence integrating in x twice, the generic solution is obtained, where $C_1$and C_2 are constants:

$$T(x) = -\frac{\dddot{q}}{k}\frac{x^2}{2} + C_1x + C_2 \tag{A.0.3}$$

In the following sections the analytic solution of Case#03, Case#04 and Case#05 has been determined imposing the correspondent assumptions into Equ. A.0.3.

A.1 Case#03

The Case#03 assumptions are reported in Table A.1.1.

Type	Description
BC@X-	T imposed at 600K
BC@X+	T imposed at 300K
Nuclear Heating	Equally distributed $10W/m^3$

Table A.1.1: Case#03-Assumptions

Applying the Case#03 assumptions into Equ. A.0.3 we obtain:

$$T(x) = -\frac{q}{k}\frac{\overset{\cdots}{x^2}}{2} + \frac{1}{L}\left(+\frac{q}{k}\frac{L^2}{2} - T_{x-} + T_{x+}\right) \tag{A.1.1}$$

A.2 Case#04

The Case#04 assumptions are reported in Table A.2.1.

Type	Description
BC@X-	T imposed at 300K
BC@X+	Flux imposed, $10^4W/m^2$
Nuclear Heating	Equally distributed $10^5W/m^3$

Table A.2.1: Case#04-Assumptions

Applying the Case#04 assumptions into Equ.A.0.3 we obtain:

$$T(x) = -\frac{q}{k}\frac{\overset{\cdots}{x^2}}{2} + \frac{1}{k}\left(f + qL\right)x + T_{x+} \tag{A.2.1}$$

A.3 Case#05

The Case#05 assumptions are reported in Table A.3.1.

Type	Description
BC@X-	T imposed at 300 K
BC@X+	Adiabatic
Nuclear Heating	Equally distributed $10^5W/m^3$

Table A.3.1: Case#05-Assumptions

Applying the Case#05 assumptions into Equ.A.0.3 we obtain:

$$T(x) = -\frac{q}{k}\frac{\overset{\cdots}{L^2}}{2} + \frac{1}{k}\left(qL\right)x + T_{x+} \tag{A.3.1}$$

Bibliography

[1] John Wesson. *Tokamaks*. Claredon Press-Oxford, 2004.

[2] EUROfusion. Progress in fusion: triple product evolution, https://www.euro-fusion.org/2011/09/progress-in-fusion/.

[3] National ignition facility & photon science, https://lasers.llnl.gov, 2017.

[4] 2017. Eurofusion, https://www.euro-fusion.org.

[5] ITER IO. www.iter.org, 2017.

[6] EUROfusion. Demo plant.

[7] J.C. Ribas. *AINA DEMO User Manual*. FEEL, 2014.

[8] M. Fabbri et al. Methodology for the improvement of the aina code wall-model applied to demo wcpb blanket, 29th symposium on fusion technology (soft 2016). 2016.

[9] R. A. Pitts. Burning plasma diagnostics workshop. Technical report, Centre de Recherches en Physique des Plasmas-EURATOM, 2017.

[10] John C. WAGNER et al. Review of hybrid (deterministic/monte carlo) radiation transport methods, codes, and applications at oak ridge national laboratory. *Progress in NUCLEAR SCIENCE and TECHNOLOGY*, Vol.2:808–814, 2011.

[11] *SuperMC/MCAM 5.2 User Manual*.

[12] F. Hernández et al. Solutions presently proposed in the hcpb concept. In *WPBB Design Progress Review Meeting No. 2 BB DR02*, 2015.

[13] Frank P. Incropera. *Fundamentals of Heat and Mass Transfer*. John Wiley & Sons, 2006.

[14] IFERC. Data for neutronics calculation. Technical report, 2014.

[15] Barabash V. Appendix a, materials design limit data, iter-d-222rln v3.3. Technical report, ITER IO, 2013.

[16] Takanori Hirose, Takashi Nozawa, R.E. Stoller, Dai Hamaguchi, Hideo Sakasegawa, Hiroyasu Tanigawa, Hisashi Tanigawa, Mikio Enoeda, Yutai Katoh, and L.L. Snead. Physical properties of {F82H} for fusion blanket design. *Fusion Engineering and Design*, 89(7-8):1595 – 1599, 2014.

[17] P. Gierszewski. Review of properties of lithium metatitanate. *Fusion Engineering and Design*, 1998.

[18] R. Capote Noy D. Lopez Aldama. Fendl-3.0: Processing the evaluated nuclear data library for fusion applications. Technical report, International Atomic Energy Agency, 2011.

[19] F. A.Hernandez. Design engineering / hcpb design report efda-d-2lhs3f v1.0. Technical report, EuroFusion, 2015.

[20] United Nations. http://www.un.org/en/development/desa/news/population/2015-report.html, 2015.

[21] W. Gulden, J. Raeder, and I. Cook. Seafp and seal: safety and environmental aspects. *Fusion Eng. Des.*, 2000.

[22] J.R. Lamarsh and A.J. Baratta. *Introduction to Nuclear Engineering*. Pearson Education, Limited, 2017.

[23] M. Keilhacker, A. Gibson, C. Gormezano, P.J. Lomas, P.R. Thomas, M.L. Watkins, P. Andrew, B. Balet, D. Borba, C.D. Challis, I. Coffey, G.A. Cottrell, H.P.L. De Esch, N. Deliyanakis, A. Fasoli, C.W. Gowers, H.Y. Guo, G.T.A. Huysmans, T.T.C. Jones, W. Kerner, R.W.T. KAnig, M.J. Loughlin, A. Maas, F.B. Marcus, M.F.F. Nave, F.G. Rimini, G.J. Sadler, S.E. Sharapov, G. Sips, P. Smeulders, F.X. SAdner, A. Taroni, B.J.D. Tubbing, M.G. von Hellermann, D.J. Ward, and JET Team. High fusion performance from deuterium-tritium plasmas in jet. *Nuclear Fusion*, 39(2):209, 1999.

[24] ITER IO. Tore supra plasma duration record, https://www.iter.org/sci/beyoplasma, 2016.

[25] L. J. Perkins, R. Betti, K. N. LaFortune, and W. H. Williams. Shock ignition: A new approach to high gain inertial confinement fusion on the national ignition facility. *Phys. Rev. Lett.*, vol. 103(no. 4):p. 045004, July 2009.

[26] OAK Ridge Laboratory. Stellarators around the world http://web.ornl.gov/info/stelnews/world-stellarators.html, 2017.

[27] ITER IO. Iter press release 17/11/2016.

[28] European Union. https://www.euro-fusion.org/eurofusion/, 2017.

[29] F. Hernandez, P. Pereslavtsev, Q. Kang, P. Norajitra, B. Kiss, G. Nadasi, and O. Bitz. A new {HCPB} breeding blanket for the {EU} demo: Evolution, rationale and preliminary performances. *Fusion Engineering and Design*, 2017.

[30] G. Aiello, J. Aubert, N. Jonquares, A. Li Puma, A. Morin, and G. Rampal. Development of the helium cooled lithium lead blanket for {DEMO}. *Fusion Engineering and Design*, 89:1444 – 1450, 2014. Proceedings of the 11th International Symposium on Fusion Nuclear Technology-11 (ISFNT-11) Barcelona, Spain, 15-20 September, 2013.

[31] Sergey Smolentsev, Neil B. Morley, Mohamed A. Abdou, and Siegfried Malang. Dual-coolant lead-lithium (dcll) blanket status and r&d needs. *Fusion Engineering and Design*, 100:44 – 54, 2015.

[32] A. Del Nevo, E. Martelli, P. Agostini, P. Arena, G. Bongiova, G. Caruso, G. Di Gironimo, P.A. Di Maio, M. Eboli, R. Giammusso, F. Giannetti, A. Giovinazzi, G. Mariano, F. Moro, R. Mozzillo, A. Tassone, D. Rozzia, A. Tarallo, M. Tarantino, M. Utili, and R. Villari. {WCLL} breeding blanket design and integration for {DEMO} 2015: status and perspectives. *Fusion Engineering and Design*, pages –, 2017.

[33] European Union. http://fusionforenergy.europa.eu/, 2017.

[34] N. Taylor. General safety principles, efda-d-2ljvz7 v1.0. Technical report, EFDA, 2014.

[35] J. Knaster, F. Arbeiter, P. Cara, S. Chel, A. Facco, R. Heidinger, A. Ibarra, A. Kasugai, H. Kondo, G. Micciche, K. Ochiai, S. O'hira, Y. Okumura, K. Sakamoto, and E. Wakai. Ifmif, the european-japanese efforts under the broader approach agreement towards a li(d,xn) neutron source: Current status and future options. *Nuclear Materials and Energy*, 9:46 – 54, 2016.

[36] Alban Mosnier et al. The accelerator prototype of the ifmif/eveda project. *Conf. Proc.*, C100523:MOPEC056, 2010.

[37] Broader Approach. http://www.ifmif.org, 2017.

[38] U Colombo (chair). Fusion programme evaluation, commission of the european communities. Technical report, European Union, 1990.

[39] IAEA. Janis database, http://www.oecd-nea.org/janis/download.html. 2017.

[40] E. Urbonavicius. Identify required safety analysis code, efda-d-2mh2pz v1.0. Technical report, Eurofusion, 2015.

[41] M. Porfiri. Review of modelling codes and identifications of development needs. Technical report, ENEA. EFDA D 2MBJ86 v1.1.

[42] J.C. Rivas and J. Dies. Iter safety studies: The effect of two simultaneous perturbations during a loss of plasma control transient. *Fusion Engineering and Design*, 89:2043 – 2047, 2014. Proceedings of the 11th International Symposium on Fusion Nuclear Technology-11 (ISFNT-11) Barcelona, Spain, 15-20 September, 2013.

[43] J.C. Rivas, A. de Blas, J. Dies, and L. Sedano. Fusion neutron source model for the systems analysis of a tokamak power plant. *Fusion science and technology*, 64(3):687–691, Sep 2013.

[44] J. Dies, M. Dapena, M. Ramon, R. Lopez, J. Garcia, J.C. Rivas, A. Calvo, and S. Reyes. Aina safety code, a review of loss of plasma control transients in iter: Sudden increase in fuelling rate, sudden increase of auxiliary heating. *Fusion science and technology*, 56(1):31–37, Jul 2009.

[45] J.C. Rivas, J. Dies, and X. Fajarnes. Revisiting the analysis of passive plasma shutdown during an ex-vessel loss of coolant accident in iter blanket. *Fusion engineering and design*, 98-99:2206–2209, Oct 2015.

[46] J.C. Rivas and J. Dies. Safety studies: Review of loss of plasma control transients in iter with aina 3.0 code. *Fusion engineering and design*, 88(9-10):2709–2713, Oct 2013.

[47] J. Izquierdo, J. Dies, J. Garcia, C. Tapia, G. Cortes, and L. Rodriguez. Safety assessment of energy fluxes on in-vessel components with safaly. *Fusion engineering and design*, 82(15-24):2856–2860, Oct 2007.

[48] R. Wenninger. Scenario modelling, efda-d-2lmsdr. Technical report, EUROfusion, 2014.

[49] R. Wenninger. Demo1 reference design "eu demo1 2015", efda-d-2mdkfh. Technical report, EUROfusion, 2015.

[50] T. Honda et al. Development of safety assessment method for plasma anomaly events in fusion reactors. *J. Fusion Energy*, 16(1-2):175–179, 1997. doi:10.1023/A:1022593803350.

[51] JOSE CARLOS RIVAS REGUERA. *Development of AINA code for the study of loss of plasma control events in ITER and DEMO, and contribution to the systems study of DEMO.* PhD thesis, Departament de Física i Enginyeria Nuclear (FEN), 2016.

[52] JESUS IZQUIERDO VILLENA. *Iter Safety Assessment: In-vessel simulation of tokamak events and component reliability approach.* PhD thesis, Departament de Física i Enginyeria Nuclear (FEN), 2008.

[53] J.C. Rivas and J. Dies. Upgrading of plasma wall interaction model for tokamak transient modeling code aina 2.0, used in safety studies of iter plasma instability events. *Fusion science and technology*, 60(2):825–829, Aug 2011.

[54] J.C. Rivas, M. Nakamura, Y. Someya, K. Hoshino, N. Asakura, H. Takase, Y. Miyoshi, H. Utoh, K. Tobita, J. Dies, A. de Blas, A. Riego, and M. Fabbri. Safety studies of plasma-wall events with {AINA} code for japanese {DEMO}. *Fusion Engineering and Design*, 109-111, Part B:1653 – 1657, 2016. Proceedings of the 12th International Symposium on Fusion Nuclear Technology-12 (ISFNT-12).

[55] M. Kovari, R. Kemp, H. Lux, P. Knight, J. Morris, and D.J. Ward. Process: A systems code for fusion power plants - part 1: Physics. *Fusion Engineering and Design*, 89(12):3054 – 3069, 2014.

[56] Fontanet Saez Joan. *Simulación de plasmas de dispositivos de fusión por confinamiento magnético tipo tokamak y stellarator. Validación experimental y aplicación al estudio del Heliac Flexible TJ-II.* Universitat Politècnica de Catalunya. Departament de Física i Enginyeria Nuclear, 2001.

[57] Javier Dies, Alfredo de Blas, Jose Carlos Rivas, Albert Riego, and Marco Fabbri. Progress in aina development for demo, efda d2m4p9j v1.0. Technical report, Universidad Politecnica de Catalunya - FEEL, 2014.

[58] IFERC. Helios super computer http://www.iferc.org/csc-scope.html, 2017.

[59] H. D. Benington. Production of large computer programs. *Annals of the History of Computing*, 5(4):350–361, Oct 1983.

[60] Oleg N. Vassiliev. *Monte Carlo Methods for Radiation Transport.* 2016.

[61] M.Z. Youssef. Summary of the up-to-date 3-d nuclear analyses of iter diagnostics generic equatorial port plug (gepp) performed with the attila design code. *Fusion Science and Technology,Vol. 64, No. 3*, 2013.

[62] P.J Coelho. The role of ray effects and false scattering on the accuracy of the standard and modified discrete ordinates methods. *Journal of Quantitative Spectroscopy and Radiative Transfer*, 73(25):231 – 238, 2002. Third International Symposium on Radiative Transfer.

[63] Eugene Butkov. *Mathematical Physic.* ADDISON-WESLEY PUBLISHING COMPANY, 1973.

[64] *TRIDENT; A two-dimensional, multigroup triangular mesh discrete ordinates explicit neutron transport code*, volume LA-6735-M. LANL, 1977.

[65] OECD. The vitamin-j.

[66] Mahmoud Z. Youssef, Russell Feder, and Ian M. Davis. Neutronics analysis of the international thermonuclear experimental reactor (iter) mcnp "benchmark cad model" with the attila discrete ordinance code. *Fusion Engineering and Design*, 83:1661 – 1668, 2008. Proceedings of the Eight International Symposium of Fusion Nuclear TechnologyISFNT-8 {SI}.

[67] Jong Sung Park, Sungjin Kwon, and Kihak Im. Comparison study on neutronic analysis of the k-demo water cooled ceramic breeder blanket using {MCNP} and {ATTILA}. *Fusion Engineering and Design*, 109:801 – 808, 2016. Proceedings of the 12th International Symposium on Fusion Nuclear Technology-12 (ISFNT-12).

[68] Alissa S. Stafford Thomas M. Evans. Denovo: A new three-dimensional parallel discrete ordinates code in scale. *Nuclear Technology*, 171(2):171–200, Agust 2010.

[69] N. Metropolis. The beginning of the monte carlo method. Technical report, 1987.

[70] Serge. *From X-Rays to Quarks: Modern Physicists and their Discoveries.* Dover-Mineola, 2007.

[71] Von Neumann Richtmyer. Statistical methods in neutron diffusion. (LAMS-551), 1947.

[72] R. Eckhardt. *Stan Ulam, John von Neumann, and the Monte Carlo Method.* Number No. 15 in 131-137. 1987.

[73] N. Metropolis et al. Equation of state calculations by fast computing machines. *The Journal of Chemical Physics*, Vol.21(No.6):pp. 1087–1092, 1953.

[74] Marconi-fusion, https://wiki.u-gov.it/confluence/display/scaius/marconi-fusion+environment, 2016.

[75] X-5 Monte Carlo Team. *MCNP A General Monte Carlo N-Particle Transport Code, Version 5.* LANL, April 2003.

[76] Allison J. et al. Geant4 developments and applications. *IEEE Trans. Nucl. Sci.*, 53(1):270–278, 2006.

[77] F. Salvat. The penelope code system:specific features and recent improvements. *Ann. Nucl. Energy*, (82):98–109, 2015.

[78] Y. Wu. Cad-based interface programs for fusion neutron transport simulation. *Fusion Engineering and Design*, 84:1987 – 1992, 2009. Proceeding of the 25th Symposium on Fusion Technology(SOFT-25).

[79] Yican Wu, Jing Song, Huaqing Zheng, Guangyao Sun, Lijuan Hao, Pengcheng Long, and Liqin Hu. Cad-based monte carlo program for integrated simulation of nuclear system supermc. *Annals of Nuclear Energy*, 82:161 – 168, 2015. Joint International Conference on Supercomputing in Nuclear Applications and Monte Carlo 2013, {SNA} + {MC} 2013. Pluri- and Trans-disciplinarity, Towards New Modeling and Numerical Simulation Paradigms.

[80] A.M. Bevill S. W. Mosher. *ADVANTG An Automated Variance Reduction Parameter Generator*. OAK Ridge National Laboratory, November 2013.

[81] F.B. Brown. Fundamentals of monte carlo particle transport. *LA-UR-04-8817*, 2004.

[82] H. Iida et al. Iter nuclear analysis report. Technical report, 2004. ITER IDM G 73 DDD 2 W.

[83] P. F. Rose. Endf-201, endf/b-vi summary documentation. Technical report, 1911. BNL-NCS-17541.

[84] F. Moro et al. The mccad code for the automatic generation of mcnp 3-d models: Applications in fusion neutronics. *The McCad code for the automatic generation of MCNP 3-D models: Applications in fusion neutronics*, 42(4):1036–1041, 2014.

[85] F. Moro et al. Applications of mccad for the automatic generation of mcnp 3d models in fusion neutronics. 2013.

[86] Dassault Systèmes. Abaqus, 2017.

[87] R. A. Forster et al. Mcnp capabilities for nuclear well logging calculations. In *IEEE Transactions on Nuclear Science*, volume 37, 1990.

[88] A. Trkov D. L. Aldama. Fendl-2.1: Update of an evaluated nuclear data library for fusion applications. Technical report, IAEA, 2004. Report INDC(NDS)-467.

[89] Hank Childs, Eric Brugger, Brad Whitlock, Jeremy Meredith, Sean Ahern, David Pugmire, Kathleen Biagas, Mark Miller, Cyrus Harrison, Gunther H. Weber, Hari Krishnan, Thomas Fogal, Allen Sanderson, Christoph Garth, E. Wes Bethel, David Camp, Oliver Rübel, Marc Durant, Jean M. Favre, and Paul Navrátil. VisIt: An End-User Tool For Visualizing and Analyzing Very Large Data. In *High Performance Visualization–Enabling Extreme-Scale Scientific Insight*, pages 357–372. Oct 2012.

[90] ANSYS. *ANSYS SpaceClaim, http://www.spaceclaim.com*, 2017.

[91] Dass. *CATIA V5, https://www.3ds.com/es/productos-y-servicios/catia*, 2017.

[92] LANL. *NJOY 2016, https://www.oecd-nea.org/dbprog/njoy-links.html*, 2017.

[93] D. Große et al. Status of the mccad geometry conversion tool and related visualization capabilities for 3d fusion neutronics calculations. *Fusion Engineering and Design*, October 2013.

[94] LANL. Compressible flows: Particles in cells: Eularian-lagrangian method where particles move through a fixed grid. 1955.

[95] ASME Committee PTC 61. Standard for verification and validation in computational fluid dynamics and heat transfer. In *ASME V&V 20-2008*. 2008.

[96] NASA. Nparc alliance cfd verification and validation, 2012.

[97] Ansys cfx, http://www.ansys.com/products/fluids/ansys-cfx.

[98] ANSYS. *ANSYS Fluent (C) V17.2 User Manual*, 2015.

[99] Star-ccm+, http://mdx.plm.automation.siemens.com/star-ccm-plus.

[100] Hrvoje Jasak, Ar Jemcov, and United Kingdom. Openfoam: A c++ library for complex physics simulations. In *International Workshop on Coupled Methods in Numerical Dynamics, IUC*, pages 1–20, 2007.

[101] J. Fradera, C. Colomer, M. Fabbri, M. Martin, E. Martinez-Saban, I. Zamora, A. Aleman, J. Izquierdo, R. Le Barbier, and Y. Utin. Thermal-hydraulic analysis of an irregular sector of the {ITER} vacuum vessel by means of {CFD} tools. *Fusion Engineering and Design*, 92:69 – 74, 2015.

[102] Pointwise, http://www.pointwise.com/pointwise/, 2017.

[103] NAFEMS. Nafems: Verification and validation master class. 2016.

[104] Ahrens James. Paraview: An end-user tool for large data visualization. *Elsevier*, 2005. ISBN-13: 978-0123875822.

[105] Utkarsh Ayachit. The paraview guide: A parallel visualization application. *ISBN 978-1930934306*, 2015.

[106] J. Dies et al. Progress in aina development for demo-january 2016. Technical report, UPC-FEEL, 2016.

[107] B. Bigot. Progress in iter construction, manufacturing and r&d. *IAEA Procedings*, 2016.

[108] KITWARE. Vtk libraries, 2017.

[109] Steven T. Karris. *Numerical Analysis Using MATLAB and spreadsheet*. Orchard Publications, 2015.

[110] EUROfusion. Final 2016 task meeting. 2017.

[111] J.C. Rivas, M. Nakamura, Y. Someya, K. Hoshino, N. Asakura, H. Takase, Y. Miyoshi, H. Utoh, K. Tobita, J. Dies, A. de Blas, M. Fabbri, and A. Riego. Safety studies for japanese {DEMO} design with{AINA} code. *Plasma Conference 2014 , Nigata(Japon)*, 2014.

[112] M. Fabbri, A. de Blas, A. Riego, J. Dies, I. Zamora, and E. Baeza. Methodology for the improvement of the {AINA} code wall-model applied to {DEMO} {WCPB} blanket. *Fusion Engineering and Design*, pages –, 2017.

[113] IFERC. Wcpb blanket cad model. Technical report, 2014.

[114] Mikio Enoeda, Hisashi Tanigawa, Takanori Hirose, Satoshi Suzuki, Kentaro Ochiai, Chikara Konno, Yoshinori Kawamura, Toshihiko Yamanishi, Tsuyoshi Hoshino, Masaru Nakamichi, Hiroyasu Tanigawa, Koichiro Ezato, Yohji Seki, Akira Yoshikawa, Daigo Tsuru, and Masato Akiba. Development of the water cooled ceramic breeder test blanket module in japan. *Fusion Engineering and Design*, 87(7-8):1363 – 1369, 2012. Tenth International Symposium on Fusion Nuclear Technology (ISFNT-10).

[115] *A feasible DEMO blanket concept based on water cooled solid breeder,*, 2012.

[116] K. Tobita et al. Compact demo, slimcs: design progress and issues. *Nuclear Fusion*, 2009.

[117] X-steam database, www.x-eng.com, 2006.

[118] Hiroyasu Tanigawa, Yoji Someya, Hideo Sakasegawa, Takanori Hirose, and Kentaro Ochiai. Radiological assessment of the limits and potential of reduced activation ferritic/martensitic steels. *Fusion Engineering and Design*, 89(7-8):1573 – 1578, 2014. Proceedings of the 11th International Symposium on Fusion Nuclear Technology-11 (ISFNT-11) Barcelona, Spain, 15-20 September, 2013.

[119] Farhad Tavassoli. Eurofer steel, development to full code qualification. *Procedia Engineering*, 55:300 – 308, 2013.

[120] D. Leichtle et al. The iter tokamak neutronics reference model c-model. *SOFT 2017 (Submitted)*, 2017.

[121] A.J. Koning and D. Rochman. Modern nuclear data evaluation with the talys code system. *Nuclear Data Sheets*, 113(12):2841 – 2934, 2012.

[122] *"Status of the JEFF Nuclear Data Library", Proceedings of the International Conference on Nuclear Data for Science and Technology*, 2017.

[123] Japanese Nuclear Data Committee (JNDC). http://wwwndc.jaea.go.jp/jendl/jendl.html. Technical report, Japan Atomic Energy Agency, 2010.

[124] http://www.ippe.ru/podr/abbn/english/libr/pdf/00intr.pdf. Technical report, Departament of Nuclear Power Plants, ABBN Laboratory, 2010.

[125] Mohamed Abdou, Neil B. Morley, Sergey Smolentsev, Alice Ying, Siegfried Malang, Arthur Rowcliffe, and Mike Ulrickson. Blanket/first wall challenges and required r&d on the pathway to {DEMO}. *Fusion Engineering and Design*, 100:2 – 43, 2015.

[126] F.B. Brown. The makxsf code with doppler broadening, la-ur-06-7002. Technical report, LANL, 2006.

[127] Lee Young-Ouk Kim Do Heon, Gil Choong-Sup. Current status of ace format libraries for mcnp at nuclear data center of kaeri. *J Radiat Prot Res*, 41(3):191–195, 2016.

[128] A.Davis. *RADIATION SHIELDING OF FUSION SYSTEMS*. PhD thesis, CCFE, 2010.

[129] Alfredo de Blas Albert Riego Marco Fabbri Eduard Baeza and Alvaro Cubi. Development of the safety code aina for the european demo designs. In *13th International Symposium on Fusion Nuclear Technology*, 2017.

[130] Alfredo de Blas Albert Riego Marco Fabbri Eduard Baeza and Alvaro Cubi. Desarrollo del código de seguridad para reactores de fusión aina 4 para demo. In *Sociedad Nuclear Española (SNE)*, 2017.

[131] Alfredo de Blas Albert Riego Marco Fabbri Eduard Baeza and Alvaro Cubi. Report on development of new aina code for demo hcpb (models and numerical methods), sae-2.13.7-t01-d01. Technical report, FEEL - UPC, 2016.

[132] Javier Dies et al. Aina plasma physics module development for demo, sae-2.13.1-01 and sae-2.13.2-01. Technical report, FEEL - UPC, 2015.

[133] Neill Taylor. June-2017 demo reference configuration model, June 2017.

[134] F.A. Hernandez. Thermo-hydraulic analyses of hcpb bb segment, efda-d-2hf7ku v1.1. Technical report, EuroFUSION, 2016.

[135] H.Petersen. The properties of helium: density, specific heats, viscosity, and thermal conducdivity at pressures from 1 to 100 bar and from room temperature to about 1800 k. Technical report, Danish At. Energy Com. Res. Establ. Riso, 1970.

[136] F. A.Hernandez et al. Material property handbook on eurofer97, 2015-mta. mat-1.2.1.02, d-2mrp77. Technical report, 2016.

[137] P.D. Smith. J. W. Davis. Iter material properties handbook. j. nucl. mater. *Journal of Nuclear Materials*, 233(1593-1596), 1996.

[138] A. Abou-Sena et. al. Measurements of the purge helium pressure drop across pebble beds packed with lithium orthosilicate and glass pebbles. *Fusion Eng. Des.*, 89(1459 -1463), 2017.

[139] B. S. Petukhov. Heat transfer and friction in turbulent pipe flow with variable physical properties. *Adv. Heat Transf.*, 6(503 564), 1970.

[140] V. Gnielinski. New equations for heat and mass transfer in turbulent pipe and channel flow. *Int. Chem. Eng.*, 16(359-368), 1976.

[141] International Energy Agency. Annual energy outlook 2017 https://www.eia.gov/outlooks/aeo/pdf/0383(2017).pdf, 2017.

[142] M. Fabbri. Documento de actividad del doctorando. Technical report, ETSEIB, 2017.

[143] KIT. modelling report row 12 (omf-466-03-05 d1). Technical report, 2016.